Terahertz time resolved spectroscopy of Intersubband Polaritons and Spintronic Emitters

Jacques Hawecker

Sorbonne Université

Ecole doctorale 397 : Physique Et Chimie Des Matériaux

Laboratoire de Physique de l'Ecole Normale Supérieure / Equipe Nano-THz

Terahertz time resolved spectroscopy of Intersubband Polaritons and Spintronic Emitters

Par **Jacques Hawecker**

Thèse de doctorat de Physique de la Matière Condensée

Dirigée par Sukhdeep S. Dhillon

Présentée et soutenue publiquement le 30 juin 2021

Devant un jury composé de :

Prof. LANGE Christoph	Rapporteur
Prof. DELEPORTE Emmanuelle	Rapporteur
Dr. VITIELLO Miriam	Examinateur
Dr. TESTELIN Christophe	Examinateur
Dr. JAFFRES Henri	Membre invité
Dr. COLOMBELLI Raffaele	Membre invité
Dr. DHILLON Sukhdeep	Directeur de thèse

Résumé de la Thèse

Le térahertz (THz) est un domaine spectral de rayonnement électromagnétique situé entre les micro-ondes et l'infrarouge moyen, correspondant à des fréquences comprises entre environ 0.1 et 10 THz. Ce domaine fréquentiel a été nommé « fossé des térahertz » due aux performances déclinantes des sources et détecteurs électroniques et photoniques spectralement situés de part et d'autre de ce domaine. Malgré cela, une multitude d'applications en astronomie, en sécurité ou encore en télécommunication peuvent être développées autour de ces fréquences. Le THz est également un domaine spectral précieux pour l'étude de phénomènes fondamentaux de basses énergies : les phonons, les dynamiques de spins, les transitions intersous-bandes des puits quantiques, les niveaux de Landau, etc. Ce fossé des térahertz commence à se remplir avec le perfectionnement et l'élaboration de nouveaux dispositifs tels que : les lasers à cascade quantiques (QCL), les antennes photoconductrices, les émetteurs basés sur des phénomènes spintroniques, les réseaux de bolomètres ou encore les nano-antennes, pour n'en citer que quelques-uns. Afin de généraliser les applications THz il est nécessaire d'étudier et de concevoir d'autres sources et détecteurs. Dans ce but, cette thèse présente les résultats de mes recherches qui à terme pourront permettre l'élaboration de nouvelles sources efficaces de rayonnements THz, ainsi que l'exploration d'interactions fondamentales.

Cette thèse s'articule autour de la spectroscopie THz résolue en temps (TDS) qui est une méthode de caractérisation sans contact et rapide bénéficiant d'une détection cohérente. Décrite avec précision dans le chapitre I, cette technique est basée autours d'un laser femtoseconde Ti:Sa émettant des impulsions ultra-rapides de 100fs centrées à une longueur d'onde de $\sim 800nm$. Ces impulsions sont divisées en deux bras optiques, un dirigé vers le système de détection et le second sur l'émetteur THz : l'antenne photoconductrice. Le faisceau THz est ensuite dirigé à l'aide de miroirs parabolique sur le système de détection. Via une ligne à retard placé sur le chemin optique du premier bras, il est possible de changer la phase relative de ces deux faisceaux, et par phénomènes électro-optique, d'échantillonner (de reconstruire) le champ électrique THz incident sur la détection. Ainsi, la spectroscopie THz résolue en temps donne accès à l'amplitude et la phase – une détection cohérente - d'une onde THz dû à cette relation de phase entre les deux bras optiques. Cette caractéristique est particulièrement attractive dans l'étude des polaritons intersous-bande présenté dans le

chapitre V où une pompe THz puissante, sans lien de phase avec le système TDS, n'éblouit pas le sonde THz de l'antenne photoconductrice.

Au sein du chapitre II, la technologie des antennes photoconductrices THz est discutée, plus précisément, d'une structure basée sur une géométrie d'électrodes interdigitées incluant un plan d'or enterré à une distance sous longueur d'onde de la surface active du dispositif. Cette structure réalise une cavité THz et a permis précédemment de supprimer les échos temporels dues à la propagation de l'onde THz à travers le substrat. Cependant, aucune caractérisation de la puissance absolue THz ni simulations électromagnétiques précisant le rôle de ce plan d'or n'ont été montrée. De ce fait, j'ai établi des modèles de simulations électromagnétiques pour comparer deux structures, avec et sans cavité, par lesquelles il a été établi que la cavité augmente par un facteur 3 le champ électrique THz émit par la structure (voir Figure 1). De plus, des variations de la profondeur du plan d'or ont mis en évidence que cette structure se comporte tel une cavité tout en conservant un caractère large-bande sur les fréquences THz émises. Il est donc possible d'élaborer de nouvelles structures en modifiant la profondeur de ce plan d'or pour augmenter le champ électrique THz (pour des profondeurs plus grandes) ou d'ajuster la profondeur pour changer la fréquence centrale d'émission du dispositif (ce qui a également été prouvé expérimentalement). J'ai également montré des caractérisations de la puissance THz absolue des deux structures mettant en évidence un facteur 7.5 en faveur du dispositif en cavité (voir Figure 1). En optimisant les paramètres de fonctionnement, l'antenne photoconductrice a atteint une puissance de 240µW, dépassant largement les antennes classiques généralement capable d'émettre quelques dizaines de µWs. Cette optimisation a permis de montrer la première démonstration d'imagerie THz large bande en temps réel sur une surface large (faisceau non focalisé) avec l'aide d'une camera THz basée sur un réseau de micro-bolomètres à température ambiante (voir Figure 1). Cette démonstration est importante car contrairement à l'imagerie monofréquencielle basée sur des QCL, l'imagerie large bande ne comporte pas d'artefact due à la diffraction. Cette étude a également donné lieu à une publication dans le journal *Photonic research*.

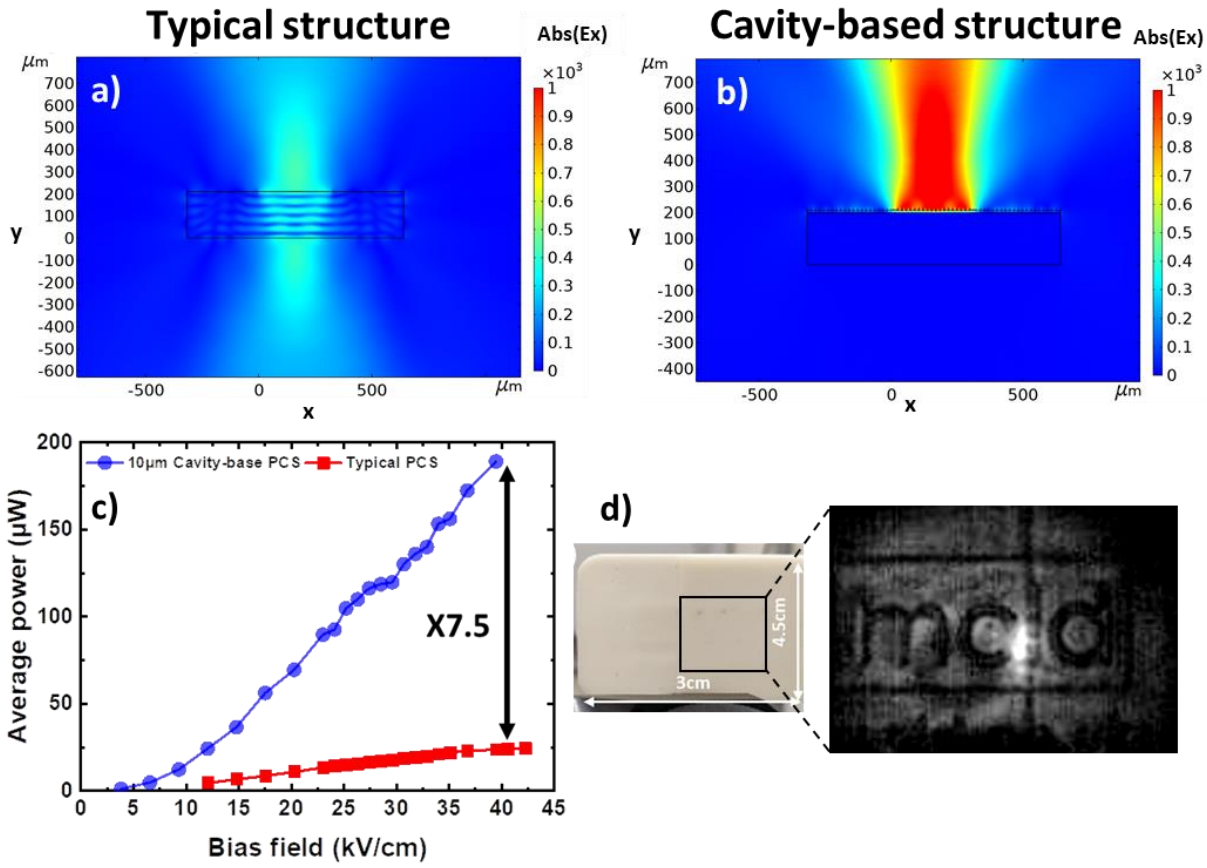

Figure 1 : a) Simulation électromagnétique d'une structure typique (sans cavité) b) avec cavité, représentée à leurs fréquences centrales, présentent le maximum de champ électrique THz. c) Mesures de puissance absolue THz des deux dispositifs. d) Première démonstration d'imagerie THz large en temps réel utilisant une antenne photoconductrice.

Le chapitre III est dévoué à l'étude de sources THz basées sur des phénomènes spintroniques ultra-rapides dans des hétérostructures d'épaisseurs nanométriques constituées de matériaux ferromagnétiques (FM) et métaux de transitions (HM). Ces sources THz relativement récentes constituent actuellement un domaine de recherche très actif par le fait de leur simplicité et de leur spectre d'émission non limité par des phonons. Ces structures sont en effet capable d'émission THz par démagnétisation ultra-rapide du FM induite par le laser femtoseconde créant un courant de spin ultra-rapide. Lorsque celui-ci diffuse dans le HM, une conversion de courant de spin en courant de charge (SCC) génère une impulsion THz (voir Figure 2). Cette SCC, due à l'effet Hall de spin inverse intervenant dans le volume du HM, est quantifiée par l'angle de Hall (SHA) représentant « l'efficacité » de la conversion. Dans ce chapitre, la physique liant les paramètres fondamentaux de ces hétérostructures à l'amplitude du champ électrique THz émis est établie à l'aide de la technique de pompage de spin en résonnance ferromagnétique (FMR-SP) couplée à la TDS en émission. De ce fait, en faisant

intervenir un SHA diffèrent pour plusieurs structures FM/HM, il est mis en évidence que le SHA en lui-même n'est pas suffisant à prédire l'émission THz. En effet, des phénomènes d'interfaces limitent la diffusion des porteurs du FM vers le HM (transmission électronique). Ces effets sont quantifiés au sein des simulations ab-initio réalisées par nos collaborateurs, et mettent à jour que les transmissions électroniques ne sont pas équivalentes pour des excitations de différentes énergies (TDS vs FMR-SP). De plus, l'intensité du champ électrique THz semble proportionnelle au produit de l'angle de Hall, de la conductivité du HM, de la longueur de relaxation du spin dans le HM et de la transmission électronique à l'interface de la structure. Cette étude a donné lieu à une publication dans le journal Applied Physics Reviews.

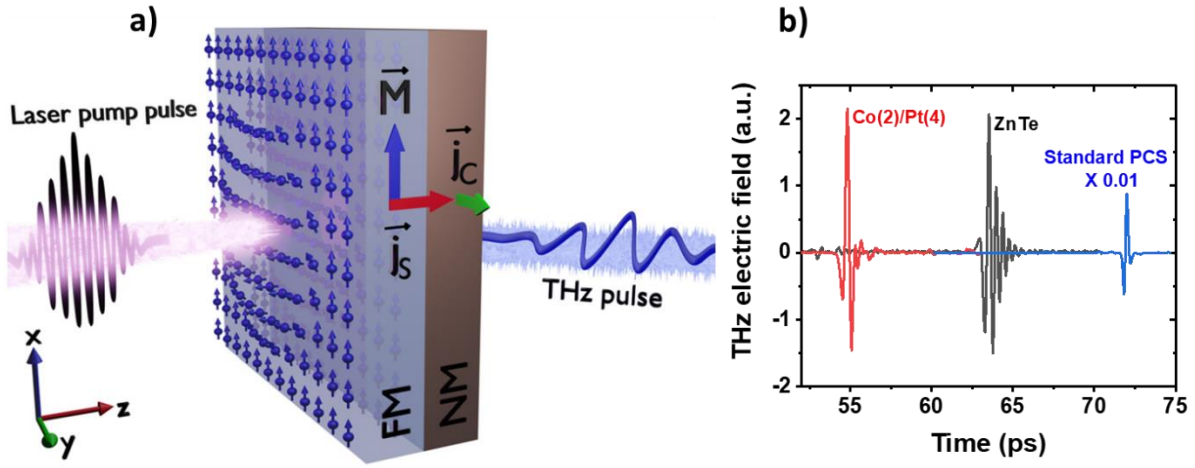

Figure 2 : a) Représentation d'émission THz par démagnétisation ultra-rapide du FM induite par un laser fs, source [1]. b) Champ électrique THz d'une hétérostructure Co/Pt montrant un signal équivalent au cristal électro-optique ZnTe. Pour comparaison, un signal issu d'une antenne photoconductrice est également représenté.

Dans un second temps, j'ai également étudié un système composé de Co/X/Pt où X représente une variation d'épaisseur de Ti, Au et AuW. La structure Co/Pt est en effet connue pour son excellente transmission électronique à l'interface, et l'insertion de X au sein de cette structure a pour effet de dégrader cette interface. Il est montré que la transmission électronique à l'interface, typiquement extraite à l'aide de la FMR-SP est également accessible via des mesures TDS. Un modèle élaboré par nos collaborateurs permet de quantifier un autre effet d'interface, les pertes mémorielles de spins (« spin memory loss » SML). En effet, il est montré qu'un champ électrique Rashba due à la rupture de symétrie d'inversion à l'interface participe à la diffusion électronique responsable du SML. Celle-ci est

quantifiée à 40% dans Co/Pt. Cette étude a été soumise dans le journal *Advanced Optical Materials.*

Ce chapitre se termine par la preuve du concept du « spin-sink » où il est montré que l'épaisseur des structures FM/HM peuvent être réduites par l'ajout d'un HM possédant de faibles longueurs de relaxations de spin, augmentant l'émission THz par la diminution de l'absorption.

Le chapitre IV donne des perspectives de recherche pour dépasser l'état de l'art de la spintronique THz (FM/HM) par des hétérostructures basées sur des matériaux quantiques. L'élaboration d'émetteur THz à base de matériaux de type Heusler et Weyl semi-métal est présentée et étudiée via des échantillons de Co_2MnGa issue de collaborations. Ce matériau a un fort potentiel pour la conception d'applications spintroniques par son caractère semi-métallique et ferromagnétique, lui conférant une forte polarisation de spin. De plus, son caractère Weyl, provenant d'une phase de Berry importante, peut également lui permettre une « self SCC ». Afin de valider la possibilité de réaliser des structures bénéficiant de cette « self-SCC » une structure basée sur Co_2MnGa/Pt est étudiée par TDS. Une variation de l'épaisseur de Co_2MnGa au sein de cette structure révèle un signal THz dépassant d'un facteur 1.33 la référence HM/FM Co/Pt pour de faibles épaisseurs (voir Figure 3), ce qui est corroboré par le signe de son SHA apporté par la littérature. En effet, le Co_2MnGa possède un SHA plus large mais surtout, de signe opposé par rapport au Pt, prouvant ainsi que ce matériau a un fort potentiel pour la réalisation d'émetteurs THz via l'adjonction d'autres matériaux en tri couches.

Dans ce chapitre, nous étudions aussi les matériaux quantiques, où un autre mécanisme de SCC - l'effet inverse Rashba Edelstein (IEE) – est capable de dépasser l'efficacité de conversion par effet inverse Hall de spin. Afin d'étudier ce phénomène, des systèmes Rashba, comportant un gaz bidimensionnel d'électrons, ainsi qu'un isolant topologique sont étudiés par TDS. Pour analyser l'émission THz dû au IEE, des matériaux Rashba composés d'oxydes $LaAlO_3/SrTiO_3$ (LAO/STO) et $AlO_3/SrTiO_3$ (AlO/STO), permettant à leur interface un gaz bidimensionnel d'électrons (2DEG), sont étudiés. Ces hétérostructures, couplés à un matériau ferromagnétique ont prouvé, via des études FMR-SP antérieur, des efficacités records de SCC. En effet, à températures cryogéniques, des efficacités de conversion jusqu'à 100 fois supérieures aux interfaces à base de Pt ont été démontré avec l'adjonction d'une grille permettant d'augmenter l'interaction spin-orbite du 2DEG. La possibilité de contrôler le SCC

via une grille est attractive car cela pourrait permettre le développement de sources THz spintroniques électriquement modulées. Dans le but d'observer ces hautes efficacités de SCC et sa variation permise par la grille sur le signal THz, des échantillons de NiFe/LAO/STO et NiFe/AlO/STO sont étudiés par TDS, préliminairement à basse températures sans grille. Une émission THz est détectée pour les deux systèmes, plus faible que Co/Pt d'un facteur 20 et 100 pour NiFe/LAO/STO et NiFe/AlO/STO, respectivement. Une variation en épaisseur de la barrière du AlO/STO ne montrant pas d'augmentation importante du signal THz, suggère une tendance des électrons chauds induits par le laser femtoseconde à passer au-dessus la barrière et non au travers. Ceci explique la différence de signal THz importante entre LAO/STO et AlO/STO avec ce dernière possédant une barrière plus haute en énergie. Les mesures cryogéniques ont montré une augmentation de ~50% en signal THz de LAO/STO mais également la présence d'un phonon dont la fréquence change avec la température. Les mesures en grilles ont montré un effet sur le signal THz (~15%) mais des optimisations, notamment au niveau du dispositif expérimental pourrait permettre l'observation d'augmentations plus importantes.

Le IEE est également possible sur des plateformes à bases d'isolants topologiques. Ces matériaux sont potentiellement plus attractifs par leur unique surface de Fermi par rapport aux matériaux Rashba, leur conférant ainsi une SCC plus efficace. Pour cela des échantillons de Si(111)/InAs(35nm)/Bi_2SnTe_4(x)/Co(4)/Al(2nm) sont étudiés par TDS. Une émission THz d'origine spintronique est clairement observé dans ces structures. Une variation d'épaisseurs (x) révèle un signal THz plus intense pour de faibles épaisseurs (voir Figure 3, le Bi_2SnTe_4 est appelé BST) avec une corrélation avec les états de surface mesuré par ARPES à SOLEIL. (Il est montré que le substrat Si/InAs contribue faiblement à l'émission THz). Cependant, de par la difficulté importante que représente une croissance parfaitement contrôlée de ces échantillons, des états de volume peuvent également permettre une conversion basée sur l'effet inverse Hall de spin. Des études complémentaires sont nécessaires afin de décorréler l'émission due aux états de volume des états de surface.

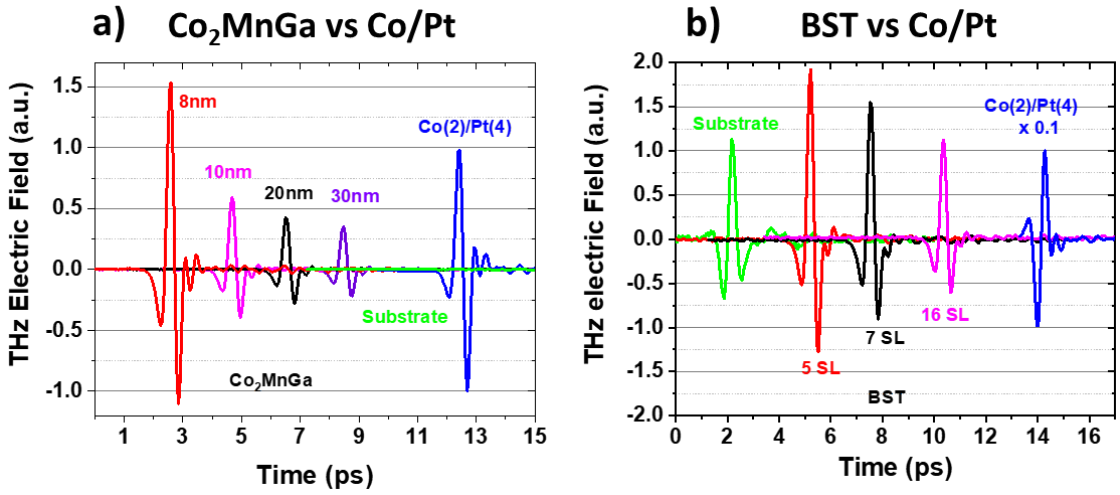

Figure 3 : a) Champ électrique THz des hétérostructures basées sur une variation d'épaisseur de Co2MnGa comparé à la référence Co/Pt b) Champ électrique THz des hétérostructures basées sur une variation d'épaisseur de Bi_2SnTe_4 (BST) comparé à la structure Co/Pt de référence (signal divisé par 10).

Le chapitre V de ce manuscrit aborde un autre sujet et se concentre sur l'étude des polaritons intersous-bande dans la gamme THz. Les polaritons sont des quasi-particules résultant d'une interaction lumière-matière forte. Un tel couplage est possible en ajustant les transitions d'un émetteur (tel un puit quantique) et d'une cavité optique afin qu'un photon d'énergie résonante avec le système puisse interagir de façon significative. Ainsi, le système est défini par deux nouveaux états couplés : les polaritons inférieur et supérieur. De nombreux systèmes peuvent êtres couplés de cette manière. Au sein des semiconducteurs, les polaritons les plus étudiés sont les polaritons excitoniques résultant du couplage fort d'une transition excitonique (d'une transition interbande) et d'une microcavité. Les polaritons sont des bosons et suivent donc une statistique bosonique où il est possible de stimuler leur population a l'état final. Cette propriété a été exploitée au sein des polaritons excitoniques en cavité dispersive par la démonstration de diffusion polariton-polariton, déclenchée par pompage optique. Celle-ci stimule une population polaritonique à l'état final, donnant lieu à une émission cohérente due à un condensat de polaritons similaire à un condensat de Bose-Einstein. Cependant, ce processus ainsi que les non-linéarités qui lui sont associées n'ont jamais été démontrés expérimentalement pour les polaritons intersous-bandes. Ces polaritons résultent du couplage fort entre une transition intersous-bande d'un puit quantique et d'une microcavité. La nature intersous-bande de la transition permet d'accéder au couplage fort dans la gamme THz. Un condensat issu de ce type de polariton permettrait le développement de nouveaux dispositifs optoélectronique THz. Dans ce projet, notre approche utilise 53 puits quantiques incluant une transition intersous-bande à 2.7 THz couplé à une cavité métal-isolant-métal dispersive. Cette

cavité développée par nos collaborateurs offre un confinement sous longueur d'onde du champ électrique et garantie un bon recouvrement avec les puits quantiques. La stimulation et l'observation de ce processus de diffusion polariton-polariton requière une pompe THz, résonant avec une des branches polaritoniques, et injectée à un vecteur d'onde précis (correspondant à un angle) permettant une conservation du vecteur d'onde et de l'énergie des polaritons sur la dispersion. Si l'interaction est suffisamment forte, deux nouveaux états de lumière peuvent être crées - le signal et l'idler - séparés par le même vecteur d'onde et la même énergie (voir Figure 2). En investiguant la réflectivité de l'échantillon polaritonique à incidence normale avec une sonde THz issue d'un système TDS, il est possible de caractériser et étudier l'accumulation de polaritons à l'état final pour un faisceau de pompe THz.

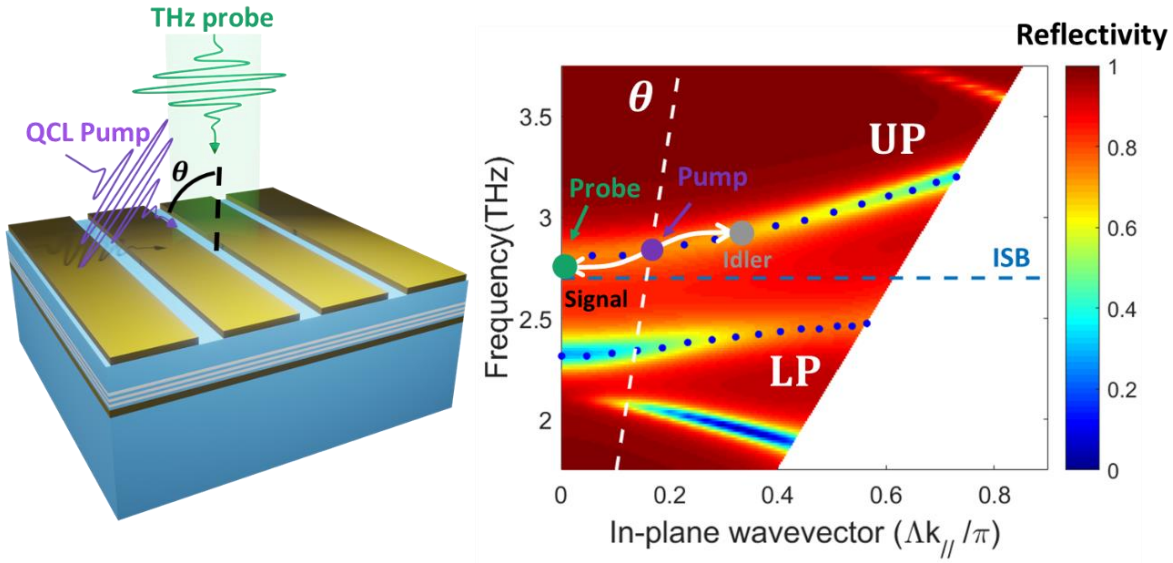

Figure 2 : Gauche -Représentation de la cavité MIM avec la sonde THz à incidence normale issue de l'antenne photoconductrice et de la pompe QCL à l'angle résonant θ. Droite – Dispersion polaritonique où le mécanisme de diffusion polariton-polariton est explicité par des flèches blanches pour un angle de la pompe QCL θ sur la branche polaritonique haute (UP).

La pompe choisie pour cette étude est un laser à cascade quantique (QCL) THz résonant en énergie avec la branche polaritonique haute, que j'ai intégré au sein du système THz résolue en temps où le faisceau de sonde THz large-bande est issue de l'antenne photoconductrice introduite précédemment. Les premiers résultats présentés soulignent une augmentation de la réflectivité à incidence normale pour une augmentation de la puissance de la pompe. Des variations de températures sur l'échantillon polaritonique ainsi qu'une variation en angle de la pompe QCL ont amené la preuve que le changement de réflectivité caractérisé est dû à un processus résonant. Ce résultat n'est cependant pas suffisant à prouver

une diffusion polariton-polariton. Pour cela une autre cavité montrant un mode replié par le réseau d'or à sa surface est réalisée ; ce mode replié peut assister la diffusion polariton-polariton. Les expériences de pompage THz réalisées sur cette cavité, ont montré des variations de réflectivités plus importantes mais surtout des changements non-linéaires de fréquences des branches polaritoniques hautes et basses, la branche haute étant la plus affectée. Avec l'aide de nos collaborateurs, nous soutenons l'hypothèse que ces décalages fréquentiels sont dus à la modulation des effets collectifs des électrons dans la transition intersous-bande par le faisceau de pompe intense, induisant un effet de dépolarisation couplé à une réduction de l'interaction lumière-matière. La dernière partie de ces travaux consiste à étudier sur le même échantillon la réflectivité non-linéaire où le ratio de lumière réfléchie/injectée mesuré avec un détecteur pyroélectrique large bande, montre une non-linéarité qui a été reproduite par les calculs de nos collaborateurs via la théorie des modes couplés, confirmant ainsi nos expériences.

Abstract

The terahertz (THz) domain provides a rich playground for many practical and fundamental applications, where the low energy of THz photons permits to probe novel light-matter interactions. This work investigates two recent and emerging scientific areas where ultrafast THz spectroscopy can be used as a probe of fundamental phenomena, as well as potentially enabling the conception of new THz sources. In the first case, ultrafast THz spintronics are studied where ultrafast excitations of spintronic heterojunctions result in efficient pulse generation. These structures consist of nanometer thick ferromagnetic - heavy metal junctions, where an optically generated spin-charge in the former is converted to a charge-current in the latter via the Inverse Spin Hall Effect. This permits to generate a THz field, with efficiencies comparable or greater than hundreds of micron thick nonlinear crystals. This work also shows that THz spectroscopy permits to determine several key parameters that strongly influence the THz emission, from the spin-hall angle to the spin interface transmission. Beyond these metal-based junctions, ultrafast THz spintronics based on "quantum" materials is also investigated, where THz pulses are generated using quantum phenomena such as the Inverse Edelstein Effect in Topological Insulators. This is shown to be a promising research direction where THz spectroscopy can probe efficiently the spin-to-charge conversion in these materials.

The second subject area is focused on THz intersubband polaritons, quasi-particles that emerge from the strong light-matter coupling of a THz photonic cavity and an intersubband transition. Here we are interested in the bosonic nature of the intersubband polaritons, as a long-term aim of realizing a novel THz laser based on Bose-Einstein condensation. In this work, we investigate resonant narrowband pumping of a polariton branch and probe using spectrally broad THz pulses. This shows strong indications of nonlinear effects and potential signatures of scattering processes that could eventually lead to the demonstration of THz polaritonic gain.

Finally, to support our work in the above subject areas, technological developments were made in existing THz sources. This included high power THz photoconductive switches using cavities, which permitted the first demonstrations of real time THz imaging with such devices, and high power THz quantum cascade lasers as narrowband laser pumps.

Table of contents

Preface

This manuscript addresses a rich variety of subjects focused on the terahertz (THz) range, ranging from high performance photoconductive switches, THz spintronics to THz intersubband polaritons. To this end, this thesis is divided into VI chapters that each include the introduction of the relevant physics. More specifically:

Chapter I-Introduction defines the context of this thesis by introducing the THz domain, along with the THz time domain spectroscopy extensively used in this work.

Chapter II-Cavity based photoconductive switch: In this chapter I will show high performance THz photoconductive switches, where the THz output powers can be enhanced by almost an order of magnitude when compared to standard devices. This is realized by the application of a quarter wavelength THz cavity using an embedded Au plane placed below the top surface of the switch. Modeling of a THz photoconductive switch shows the role of the cavity, in agreement with the experimental data. High absolute THz powers of ~ 240μW are measured with which I demonstrate the first real time THz imaging using a photoconductive switch.

Chapter III-Heavy metal based spintronic THz emitters: THz spintronics is a relatively new field of research from which a new generation of THz technology could be realized. This chapter focuses on optically excited Ferromagnetic/Heavy metal heterostructures for THz pulse generation via spintronic concepts. Here the effect is based on ultrafast spin to charge conversion using the Inverse Spin Hall Effect (ISHE). I will introduce the relevant physics linking their THz emission to their fundamental properties, along with modeling highlighting the critical material parameters directly impacting the THz emission amplitude. This is compared experimentally to a range of FM/HM junctions that show the spin-to-charge conversion for THz generation efficiency depends on a several parameters.

Chapter IV-Quantum materials based spintronic emitters: This second chapter on THz spintronics investigates the application of recent ‘quantum’ materials beyond the use of FM/HM heterostructures for THz pulse generation. In the first case Heusler alloys, half-metals that are expected to possess high spin polarization, are investigated where spin to charge conversion is expected to be enhanced using the ISHE. Secondly, Rashba materials

and Topological Insulators are studied where the spin to charge conversion is expected at the interface between the ferromagnetic and the material in question. In contrast to the use of HMs which relies on bulk effect, this is an entirely a 2D effect where the spin-to-charge conversion is via the Inverse Rashba Edelstein Effect (IREE). The samples investigated, provided by a wide collaboration network, shows potential for THz technology as well as using THz emission to understand in detail the processes occurring at these novel material interfaces.

Chapter V-Resonant pumping and broadband probing of THz intersubband polaritons: This chapter is focused on THz intersubband polaritons, more specifically, on scattering mechanisms that can potentially lead to THz gain, as demonstrated in exciton polaritons in the optical domain. This is investigated by a specially developed THz spectroscopy system capable of resonant pumping with quantum cascade lasers and a broadband probe of the polaritonic sample. The reflectivity is studied for a range of parameters (pump angle, sample temperature, polariton coupling) that clearly shows resonant effects with the pump. Most importantly I highlight nonlinearities associated with the intersubband dynamics that can potentially be associated with the precursor of gain. Finally, I performed preliminary nonlinear reflectivity experiments showing polariton nonlinearities on the reflected pump beam and supported by our collaborators modeling of the system.

Chapter VI – General conclusions: Summarize the main conclusions of each chapters.

Chapter

I

I Introduction

Owing to the diversity of the physics discussed in this work, each experimental chapter includes a detailed introduction to the relevant subject area. However, one important thread links the subjects together - the terahertz (THz) domain, and the application of THz time domain spectroscopy (TDS). This brief chapter therefore provides an introduction to the THz domain along with few practical and fundamental applications. Importantly, TDS, which has become one of the most powerful techniques for the THz range, is presented in detail.

Chapter I

I.1 The THz domain

Terahertz (THz) is a frequency metric corresponding to a frequency of 10^{12}Hz translating to 300µm in wavelength, $\sim 4.1 meV$ in photon energy or $1ps$ in time. The THz domain however is loosely defined as a region of the electromagnetic spectrum between 0.1 and 10 THz [2] (see Figure I-1). This spectral area lies between the typical operation of electronics and optical technology and has often been labelled as the THz gap due the lack of efficient sources and detectors [3].

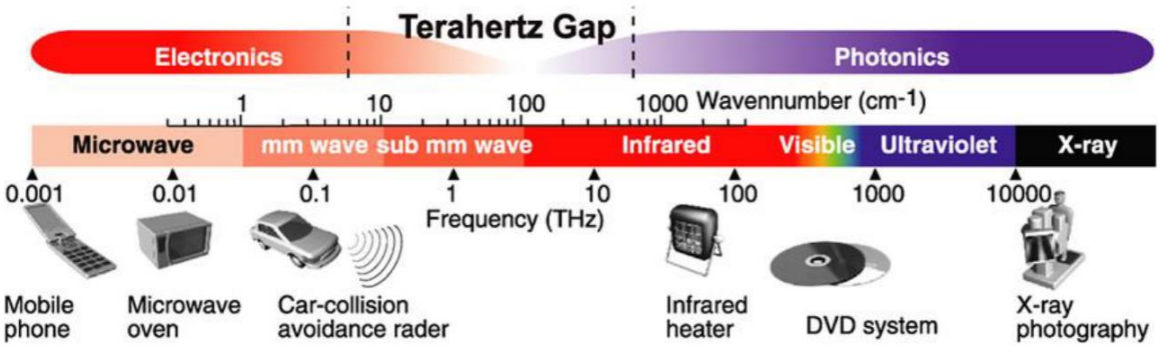

Figure I-1: Electromagnetic spectrum highlighting the THz gap bridging electronic to photonic technologies. Illustration from [4]

However, owing to the tremendous research effort carried by the scientific community, this gap is being filled with innovative source and detector technologies, such as quantum cascade lasers, photoconductive switches, spintronic based emitters and bolometer arrays, nano antenna detectors to name a few. These developments are beginning to impact mostly untapped applications in a wide diversity of fields, i.e. in security owing to THz being transparent to certain materials such as clothes, where THz imaging can show hidden objects (see Figure I-2 a)), or even in bioanalysis, astronomy, non-destructive testing, telecommunication [5]. On a more fundamental level, these advances in technology has opened up a rich playground for advanced studies of low energy physics phenomena, such as Landau level transitions, plasmons, intersubband transitions in quantum wells, harmonic generations in graphene and spin dynamics [6]–[8] (as illustrated in Figure I-2 b and c)) and could enable the development of novel THz sources and detectors.

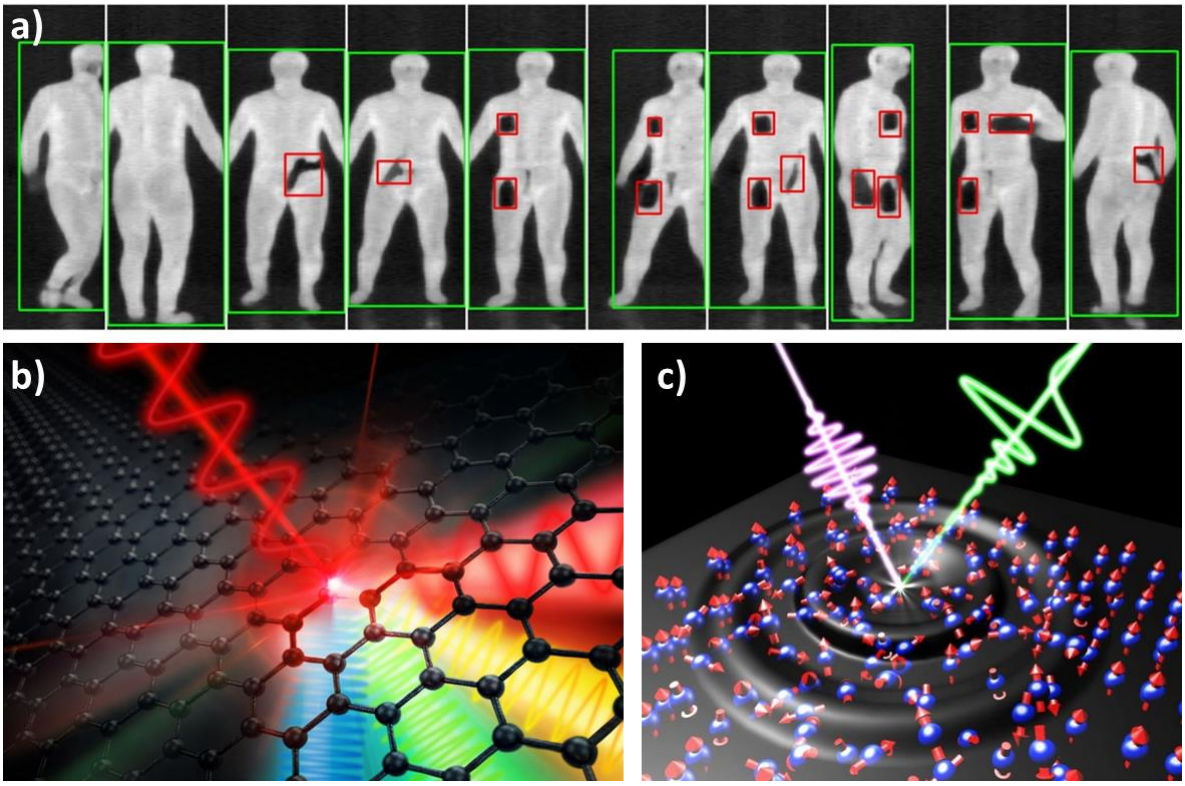

Figure I-2 : Examples of THz practical a) and fundamental b) and c) applications. a) Imaging of concealed weapons [9] b) Representation of terahertz harmonic generation in graphene [7]. c) Artist view of spin dynamics [8].

In this thesis, we will show that THz time domain spectroscopy is indeed well suited to investigate such low energy phenomena. More specifically, the physics of THz spintronics (focus of chapters III and IV) and THz intersubband polaritons (chapter V) will be probed by THz time domain spectroscopy (TDS). The latter has become one of the most important THz techniques and is the experimental core of this thesis.

I.2 THz time domain spectroscopy

THz time-domain spectroscopy (TDS) is an ultrafast and time resolved spectroscopy technique that enables non-destructive investigation of materials and interfaces with a sub picosecond resolution. Fundamental parameters such as the spectral reflectance, transmittance, optical conductivity can be investigated with TDS. Combined with a pump beam it is also possible to study the ultrafast dynamics of a system. This technique is based on ultrafast optical lasers and permits coherent detection of the amplitude and phase of a generated THz electric field. In this section, we will detail the working principle of the ultrafast THz TDS.

I.2.1 Working principle

A typical THz TDS is composed of four parts, a femtosecond near-infrared (NIR) laser, a THz generation device, THz optics, and a THz detection scheme. In the coming sections, we will describe each component.

The TDS setup considered in this manuscript is centred around a Ti:Sa oscillator (Coherent Mira pumped by a 10W Verdi pump) to generate 100fs pulses at a wavelength of 800nm with a repetition rate of 78MHz, thus emitting NIR pulses spaced by $\sim 12.8 ns$.

Using such ultrafast lasers, a range of methods are now available for THz pulse generation such as optical rectification in nonlinear crystals, plasma generation, spin currents in spintronic heterostructures (see chapter III and IV) or photoconductive switches [6], [10]–[12]. Regarding the latter, this has become the technology of choice for most TDS systems based on oscillators and is used in chapters II and V of this thesis, where a high-power cavity based photoconductive switch has been developed [13], [14]. Although specifics will be given in chapter II, a general introduction to this technology is given here for the sake of clarity. Photoconductive switches rely on semiconductor materials with ultrafast carrier lifetimes and are excited with NIR femtosecond lasers with a photon energy greater than the material bandgap. Commonly used materials include GaAs and InGaAs for a $\sim 800 nm$ or $\sim 1550 nm$ NIR excitation, respectively. The basic mechanism is as follows: i) NIR pulses generate carriers into the semiconductor material that is processed with biased metal contacts; ii) ultrafast generation and relaxation of carriers in the conduction band of the material leading to; iii) transient photocurrents between the surface electrodes that; iv) generate a linearly

polarized THz pulse. This leads to a THz electric field amplitude proportional to the photocurrent time differential as described by equation (I-1).

$$E_{THz}(t) \propto \frac{dI(t)}{dt} \qquad (I\text{-}1)$$

The simplest device consists in two metal electrodes patterned on a GaAs semiconductor substrate as described in Figure I-3. The bias is placed between Au electrodes and typically consists of a square modulation of a few tens of kV/cm and a few tens of kHz frequency. The generated THz pulse is proportional in field to the applied bias (if no optical saturation occurs). The latter is used as a reference for a lock-in amplifier to benefit from high signal-to-noise ratio. Such photoconductive switches are typically able to generate 1ps THz pulses and therefore are spectrally broad $0.2 - 4\,THz$. (Note, however, that the spectral range strongly depends upon the carrier dynamics of the semiconductor material, the near-infrared pulse length, and the detection scheme). Further details of different switches are provided with chapter II.

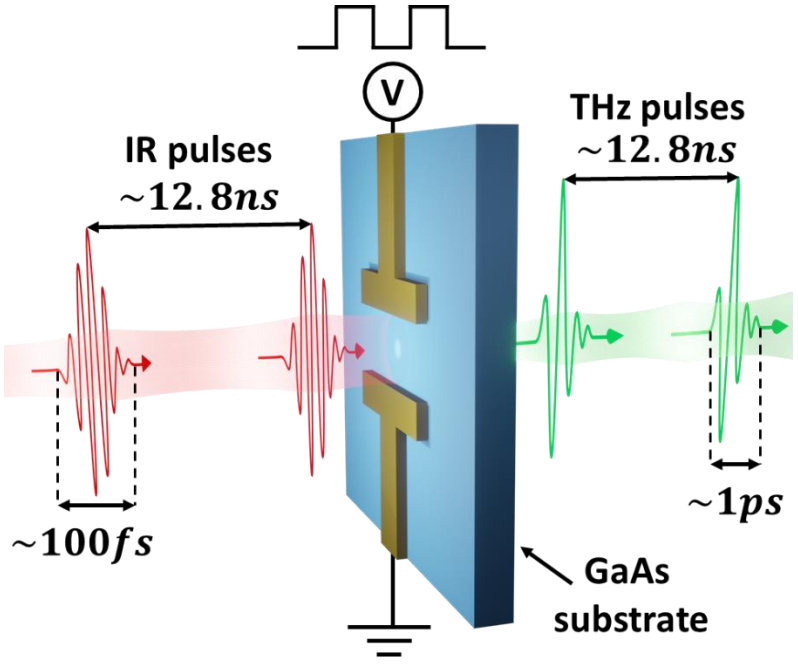

Figure I-3 : Sketch of a photoconductive switch excited by 100fs near-infrared pulses at a repetition rate of 78MHz radiating THz pulses. The semiconductor is biased by the application of a voltage between the Au electrodes and typically consists of a square modulation.

I.2.2 THz coherent detection

Several techniques can be applied to coherently detect the generated THz pulses in TDS, and mainly rely on photoconductive switches [15] or electro-optic crystals [16] with femtosecond oscillators. However, owing to their generally broader spectral bandwidth, electro-optic crystals are used for THz detection in our research group using electro-optic sampling. A sketch of the detection scheme used to reconstruct the THz wave is available in Figure I-4. It is based on using the same linearly polarized NIR probe that is used for THz generation. The THz field is incident on the crystal where, by the Pockels effect, induces a birefringence in the electro-optic crystal proportional to the field amplitude. The alters the polarisation response of simultaneous incident NIR probe. Note that an optimized spatial overlap between the THz and the NIR beam is required to maximize this phenomenon. After the electro-optic crystal, a quarter waveplate is used to transform the NIR linearly polarization into a circular/elliptical. A Wollaston prism splits the two linear components of the polarization. The horizontal and vertical polarizations components are then measured and subtracted by a balanced photodiode scheme with the resulting signal proportional to the THz field.

To illustrate this, let us consider the case where no THz field is incident on the electro-optic crystal. After the quarter wave plate, the NIR polarization is a perfectly circularly polarised. Thus, the horizontal and vertical polarisation components are equal, and their difference is zero. With an incident THz electric field, the NIR polarization rotates due to the birefringence induced by the THz field that results in different refractive indices along the crystal axis. For an electro-optic crystal of thickness L, the phase delay between the linear polarization components can be expressed by equation (I-2) [6] with n_0, the refractive index of the crystal for the NIR frequency and r_{EO} the electro-optic coefficient.

$$\Delta\phi = n_0^3 r_{EO} E_{THz} \frac{\omega L}{c} \qquad (I\text{-}2)$$

This leads to an elliptically polarized NIR beam after the quarter wave plate, where horizontal and vertical polarization intensity components expressed by equation (I-3) (with I_0, the intensity of the NIR pulse) are not equal. Their difference from by the balanced photodiode results in a signal proportional to the THz electric field, including its sign, as in equation (I-4).

$$\begin{cases} I_x = \frac{I_0}{2}(1 - sin\Delta\phi) \approx \frac{I_0}{2}(1 - \Delta\phi) \\ I_y = \frac{I_0}{2}(1 + sin\Delta\phi) \approx \frac{I_0}{2}(1 + \Delta\phi) \end{cases} \quad (I\text{-}3)$$

$$I_s = I_y - I_x = I_0\Delta\phi = n_0^3 r_{EO} E_{THz} \frac{I_0 \omega L}{c} \quad (I\text{-}4)$$

It is then possible to reconstruct the time profile of the THz pulse electric field using the NIR pulse and a delay line to sample the THz pulse. (The near-infrared pulse width (~ 100fs) can be considered a delta function when compared to the THz pulse width (~ 1ps)). As described in Figure I-4, for each step of the delay line, the NIR beam samples a different part of the THz pulse in time (orange dots in the figure), thus acquiring step-by-step the whole THz electric field time profile via a lock-in amplifier using the antenna modulation frequency as a reference. The choice of electro-optic crystal and its thickness drastically impacts the bandwidth and the signal owing to their different optical properties (phase matching, electro-optic coefficient, phonons). In general, thicker crystals yield a larger detected THz signal but a narrower spectral bandwidth. In the Nano-THz group, we commonly use either GaP or ZnTe crystals depending on the experimental requirements - a $500\mu m$ ZnTe crystal is used where larger signals are required and a $300\mu m$ GaP crystal for larger bandwidth requirements.

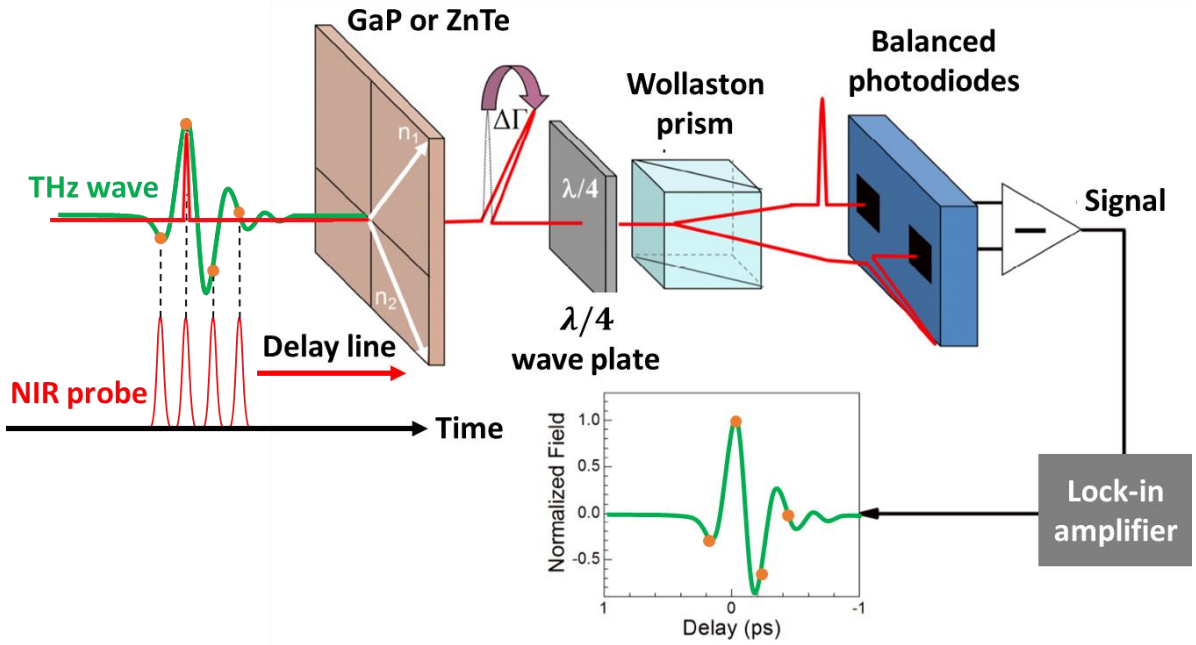

Figure I-4 : Scheme of Electro-optic sampling for the coherent detection of THz electric fields. A NIR probe and a THz wave pass through the electro-optic crystal. By the Pockels effect, the polarization of the NIR probe is rotated proportionally to the THz field amplitude, resulting in elliptical polarization after the quarter wave plate.

The Wollaston prism splits both polarizations components. The balanced photodiodes record and subtract each component resulting in a signal proportional to the THz electric field. The THz wave is sampled using a delay line on the NIR probe.

I.2.3 THz time domain spectroscopy setup

The full THz TDS setup is now displayed in Figure I-5 where the NIR ultrashort pulses generated by the Ti:Sa laser are split into two arms by a 70/30 beam spitter (BS). The higher power arm is used for the THz generation, and the other is the NIR probe used for the electro-optic sampling described above.

THz generation arm: the NIR pulses are directed and focused on the photoconductive switch by the mirror M_8. The THz pulse is then generated by the device in a reflection geometry to enhance the spectral bandwidth (no beam passes through the substrate) and collected by the parabolic mirror PM_1. The THz beam is focused between parabolic mirrors PM_2 and PM_3 (where samples are investigated in chapter V), re-collimated and then focused onto the electro-optic crystal by PM_4. Parabolic mirrors are used, permitting index-independent manipulation of the spectrally broad THz pulse, and no lens transmission loss.

The NIR probe passes through a delay-line composed of two mirrors (M_2 and M_3) on a motorized moving plate, and then focused on the electro-optic crystal via mirrors M_4, M_5. Temporally and spatially, at a given delay line position, a THz and a NIR pulse overlap on the electro-optic crystal. The relative time between the NIR and THz pulse is changed by scanning the delay line, probing different times of the THz pulse, and reconstructing its amplitude and phase.

The full THz TDS is interfaced with a Labview program coordinating the delay line and the lock-in amplifier, from where scan parameters such as acquisition speed, scanned time window, delay line step can be controlled. As THz radiation is very sensitive to water, and to avoid water absorption during measurements, a box with a dry air atmosphere is used that includes all the THz optics.

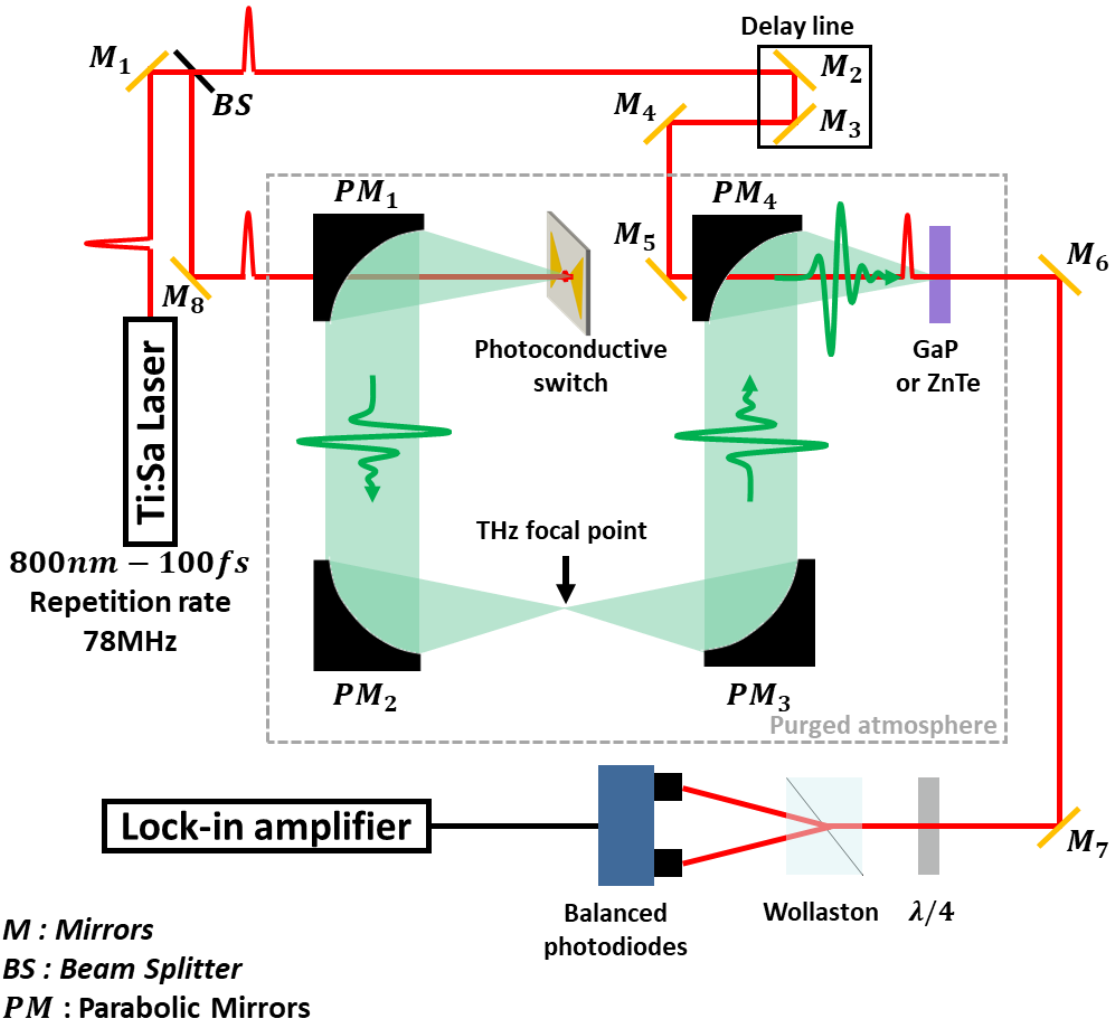

Figure I-5: Sketch of the THz-TDS experimental setup used in this work. A Ti:Sa oscillator with 100fs pulses at 800nm and a repetition rate of 78 MHz is used. The laser beam is split in two arms by the beam splitter (BS). One arm is focused and directed to the photoconductive switch, the THz is then generated by the device, collected, and collimated by the parabolic mirror PM1. The THz beam is focalized between parabolic mirrors PM2 and PM3 and then focused onto the electro-optic crystal by PM4. The other arm (the NIR probe) goes through a delay-line composed of two mirrors (M2 and M3) on a motorized plate and is then focused on the electro-optic crystal via mirrors M4, M5.

It is important note that the THz electric field and the NIR probe are locked in phase, as they originate from the same laser. Owing to this, the THz signal recorded at a given delay line position by the balanced photodiodes at a fixed time is a result of many averages of the femtosecond laser repetition rate. Combined with a lock-in amplifier this results in extremely high signal-to-noise ratio (typical value $\sim 50 - 60dB$ in spectral power). This is illustrated in Figure I-6 where four THz and NIR pulses are represented for two delay line positions, the THz pulses are fixed while the NIR shifts in time probing the THz field.

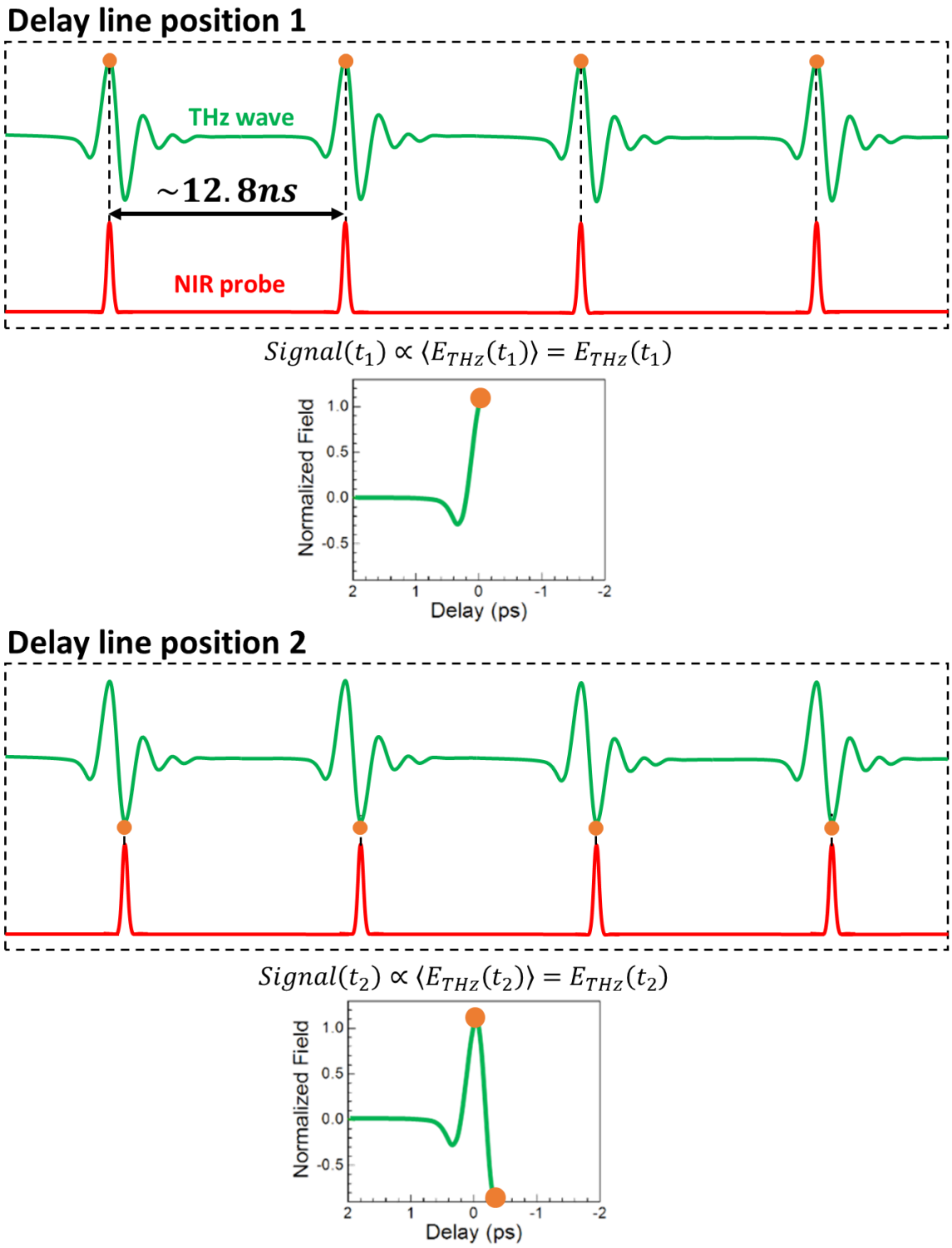

Figure I-6 : Schematic representation of four THz and NIR pulses separated by the repetition rate of the femtosecond laser with two delay line positions. The THz pulses are fixed in time while the NIR shifts by moving the delay line, thus probing the THz field. The resulting scans from each delay line position averaged by the repetition rate of the femtosecond laser are represented in the plot. Inspired from [4].

I.3 Conclusions

In this chapter we have introduced the THz range along with THz TDS, which represents the heart of the technique used in the research presented in this manuscript. We will show that THz TDS is a powerful, reliable, and versatile characterization technique capable of probing a wide range of physics.

Chapter

II

II Cavity based photoconductive switch

THz time domain spectroscopy (TDS) has become an important technique in a range of fundamental and industrial applications, from the study of low energy phenomena in condensed matter to non-destructive imaging [17]. A crucial technology is based on optically-driven photoconductive switches (PCS) [12], [15] in such THz TDS systems. These offer room temperature, spectrally broad operation, and fast electrical modulation speeds. However, their low average powers (at best tens of microwatts) have limited their use. For example, imaging is inherently limited to slow raster scanning, where the target to be imaged is physically moved to reconstruct the image. Although a variety of techniques can be implemented to increase the acquisition speed,[18] no real time imaging has been demonstrated with PCS. Although high power quantum cascade lasers have shown the possibility of real-time imaging[19], [20], these show important diffraction artefacts, operate at cryogenic temperatures and at high THz frequencies (> 2 THz), limiting their applications. Although multiplied electronic sources can reach THz frequencies, their emitted powers drop rapidly beyond a few hundred gigahertz [21]. In this chapter we will show that by placing a PCS in a cavity we can enhance the emitted electric field and power to an extent where real-time imaging is feasible. In detail we will present:

- The fundamentals of PCS.
- THz cavity-based PCS compared to standard devices.
- Electromagnetic simulations illustrating the advantages of cavity-based PCS.
- Experimental absolute power and electric field characterization.
- The first demonstration of broadband real time imaging from a cavity-based PCS.

Chapter II

II.1 Fundamentals of Photoconductive Switches

THz emission from optically pumped PCS was accomplished during the mid-1980s by David Auston`s group in Bell Laboratories [22], [23]. A typical short pulse (~1ps) from a PCS is shown in Figure II-1, along with its Fourier Transform to show the spectrally broadband nature of these devices. These sources are flexible and easily fabricated using standard photolithography. However, their typical THz average powers are typically in the range of tens of microwatts at best [15], [24], [25]. Although plasmonic based PCS have shown milliwatts THz average powers, these require electron-beam lithography [26], [27], thus complicating their fabrication.

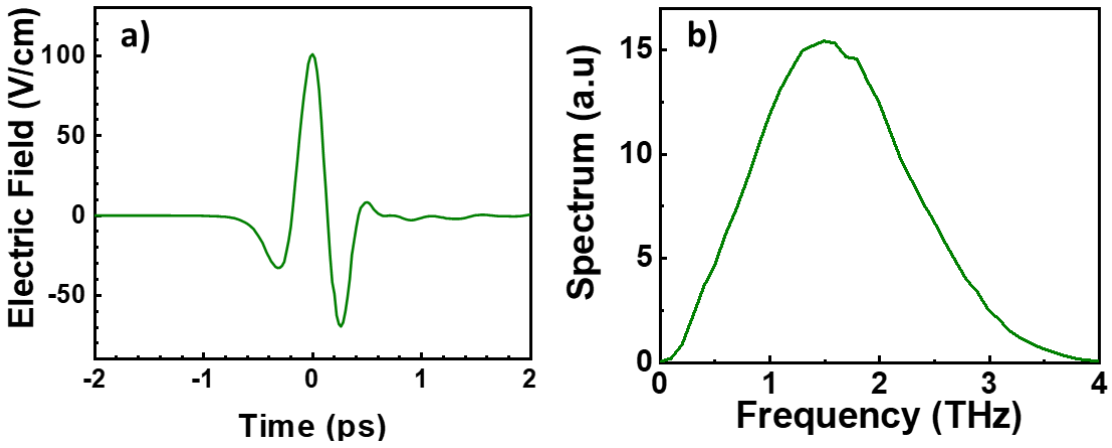

Figure II-1: a) Typical THz pulse from a photoconductive switch b) Fast Fourier transform of the pulse.

As described in chapter I, the simplest THz PCS is composed by metallic electrodes on top of a semiconductor material with short carrier lifetimes such as GaAs or InGaAs. More specifically, the process of THz radiation is described in Figure II-2 where an ultrafast (fs pulses) beam (red trace in panel b)) with an energy greater than the band gap of the semiconductor (in our case of GaAs, a 800nm excitation) generates carriers into the semiconductor. These carriers are then accelerated by an applied DC bias between the electrodes, resulting in a transient photocurrent (grey trace in panel b)). The rise and decay of this photocurrent, which depends on the duration of the excitation pulse and the decay time of the materials carriers, results in the generation of the THz pulse (grey and blue traces in panel b)). It is possible to engineer this process by tailoring the material's lifetime. For example, low temperature grown GaAs (LT-GaAs) that has much shorter lifetimes, would provide shorter THz pulses and thus a broader spectrum [28]. This PCS technology is the core of most

TDS systems discussed in section I.2 and thus it is critical to maximise its THz average power to investigate complex systems.

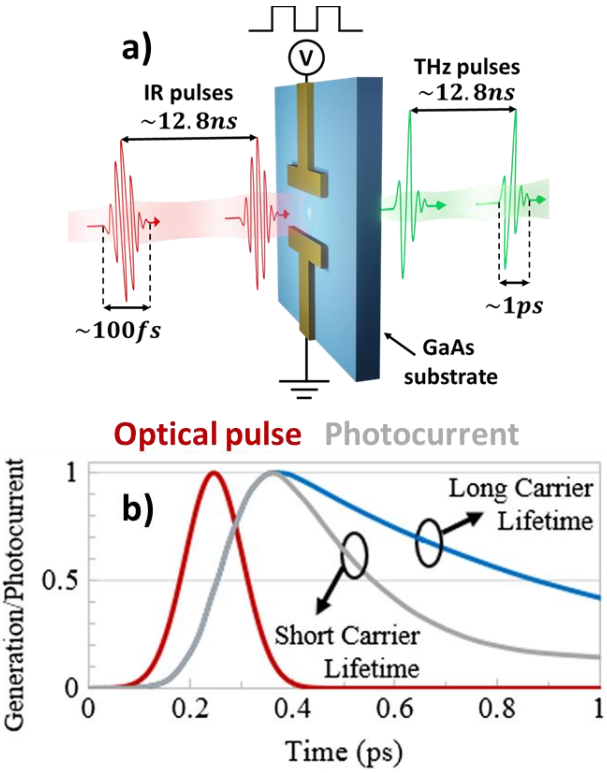

Figure II-2 General principle of THz pulse generation from optically driven PCS. a) Representation of a PCS emission b) Evolution of the Carrier generation due to the pump laser and the photocurrent over time. Figure adapted from [15]

Technologically, THz PCS have been mostly developed around III-V materials such as GaAs and InGaAs, both relying on established processing. GaAs based device are compatible with Ti:Sa oscillators as a pump-beam, while InGaAs based PCS on the other hand are compatible with $1.55\mu m$ excitations that can be coupled to optical fibre systems. Due to the strong background in GaAs based PCS and Ti:Sa lasers at the nano-THz team of the LPENS, all the work described in this manuscript is on GaAs based materials.

A range of structures of THz PCS have been designed by the scientific community [15] such as metal stripes, bow-tie, spiral to name a few. An in depth review can be found in reference [15]. In general, high average powers have been demonstrated using large area interdigitated devices [29], and has come an important component in THz TDS systems based around laser oscillators. In the next section we will introduce this PCS structure.

II.2 Interdigitated PCS

PCS based on an interdigitated geometry, demonstrated by Dreyhaupt et al [29], rely on interwoven electrodes where an alternate scheme between anode and cathode is used. This interdigitated geometry yields several advantages in respect to other structures (such as dipole, bow tie etc), namely a small spacing between the electrodes while preserving a large total PCS surface area [30]. The small spacing allows small bias fields and the large area permits: i) to scale the radiated THz power with the total area excited by the IR laser pump while avoiding optical saturation and ii) a low diverging THz beam. An illustration of this structure is available in Figure II-3 where the THz radiation mechanism along with the typical dimensions are detailed. In this picture, $4\mu m$ wide Au interleaved electrodes (digits) spaced by $4\mu m$ with a thickness of $200nm$ are directly in contact with the SI-GaAs (semi insulating) top surface. A $300nm$ thick SiO_2 layer ensures electrical insulation between the electrodes with a second Au array $8\mu m$ wide with a spacing of $8\mu m$ covering every other digit. The role of this array is to prevent destructive interferences of the radiated THz far field, by allowing optical excitation of a spaced between digits of a single bias direction ($+$ and $-$ in the figure). For an incoming ultrafast IR pulse, carriers are generated in the Si-GaAs (red and purple circles in the figure), and then accelerated by the bias field, which generate THz pulses at the repetition rate of the IR pump laser. More specifically, the THz dipolar emission (bright green arrows in the figure) radiates from the top and bottom of the device. Note that in this picture, the top THz emission is not represented for clarity. These THz waves propagating inside the device are reflected at each interface inducing “echoes” in time domain experiments. This normally limits the accessible spectral resolution of experiments where fines spectral features/changes are difficult to resolve. To give the reader a size scale of these structures, panel b) indicates typical structural dimensions ($500 \times 500\mu m$) which are larger than our IR laser waist of $300\mu m$.

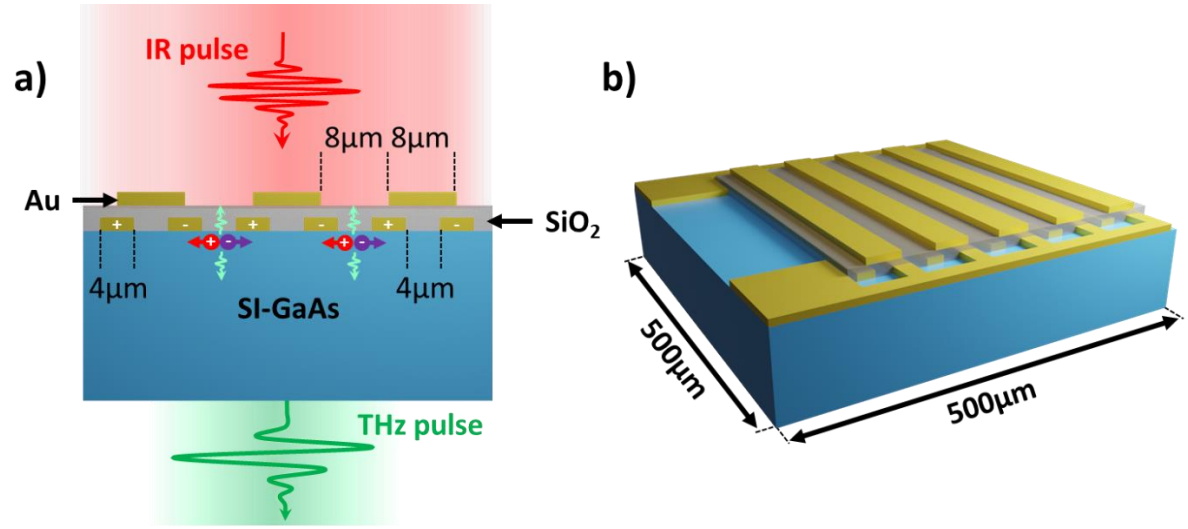

Figure II-3 : Schematic illustration of an interdigitated THz PCS along with typical dimensions. a) This geometry involves a Au interleaved digit array 4µm wide, periodic by 4µm, a SiO2 layer ensures electrical insulation with the second Au array 8µm wide periodic by 8µm to mask IR excitation of actives area with different bias field direction. Under ultrafast excitations, carriers highlighted by red and purple circles are generated in the SI-GaAs substrate and accelerated by the bias field. The rise and decay of this transient photocurrent results in THz pulses radiation periodic in time at the repetition rate of the fs laser. b) 3D view of the structure with lateral dimensions Figure inspired from [13]

For this manuscript, this interdigitated geometry will be referred as standard PCS. We will now turn to the description of a cavity-based PCS structure developed and fabricated within our team, initially to overcome time domain "echoes" and hence enhance the spectral resolution of time domain experiments.

II.3 Cavity based PCS

The concept of cavity based PCS builds on the geometry of the previous work of the Nano-THz team on "echo-less" PCS [13]. This showed how a metallic plane buried below a PCS structure can increase the spectral resolution of a THz time domain system by eliminating the THz pulses from propagating into the substrate. However, the role of the cavity was not underlined, and no measurements had been realized with the absolute power emitted or applied to real-time THz imaging. Here we show how such a structure acts as a cavity and, optimising the operating parameters in terms of electromagnetic simulations of the cavity, the applied bias field and the optical excitation to reach an important performance landmark.

The device schematic is shown in Figure II-4 where the top surface is identical to the interdigitated electrode geometry presented above, but with a thin metal plane inserted between the active GaAs layer of thickness *d* and the top surface to realize the cavity and reflect the generated THz power with no THz field transmitted through the substrate. Since the transient current photogenerated by the optical excitation pulse has its direction fixed by the interdigitated metallic layers, parallel to the buried gold plane, the structure is similar to an optical Fabry-Perot resonator. This thickness *d* ($\sim 10\mu m$) can be considered to act as a quarter wavelength resonator, enhancing the power emitted over a certain spectral bandwidth. As discussed below this resonator also preserves a broadband response. This buried Au plane now prevents the THz emission from penetrating into SI-GaAs substrate, thus suppressing time "echoes" and allowing constructive interference due to the sub-wavelength distance *d*. Note that in this picture the pump NIR beam is not represented for clarity.

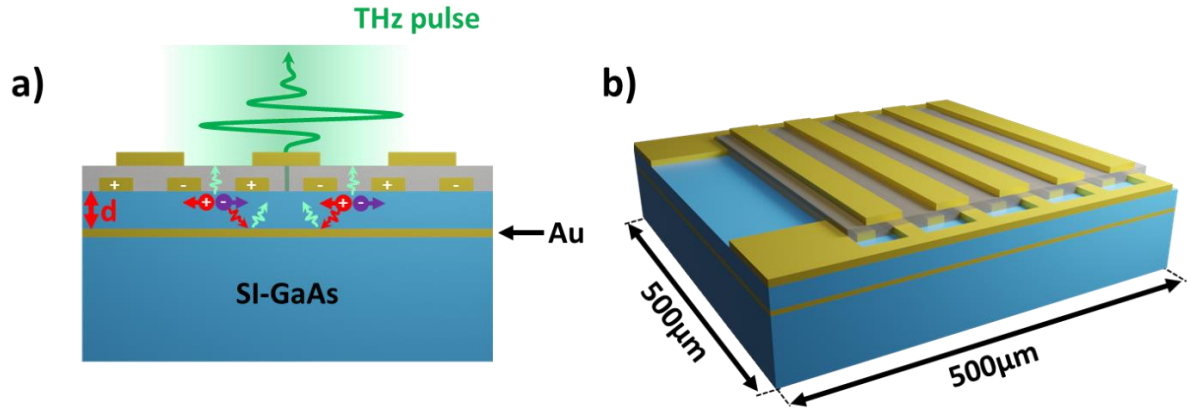

Figure II-4 1 a) Schematic of cavity-based PCS b) 3D view. The quasi-cavity structure has a buried metal plane 10µm below the surface of the interdigitated structure.

The sample is grown by metal organic chemical vapor phase deposition (MOCVD) on a SI-GaAs wafer with an AlGaAs etch stop layer, followed by the 10 µm thick undoped GaAs active layer. The sample is then wafer bonded to a gold coated host SI GaAs substrate. The original substrate and the AlGaAs layer were selectively removed, leaving the GaAs active region exposed with a metal plane 10 µm below the surface[13]. The remaining processing of the devices is performed with standard photolithography.

To investigate the potential THz power enhancement from this structure where all the generated THz is emitted from the top of the device, in respect to the standard PCS (i.e. without buried Au plane), electromagnetic simulations were performed.

II.4 Electromagnetic simulations

The propagation of the THz field from the cavity and standard PCS can be solved using COMSOL Multiphysics. With a finite difference time domain (FDTD) approach, 2D models of our different geometries along with the relevant material properties are built. Through careful meshing of the structure, COMSOL is able to resolve the Maxwell's equations for each slice of the model. Once the model achieved, by placing electromagnetic fields probe at the top and the bottom of the studied structure, we were able to determine a relative electric field value from transmission and reflection geometries.

II.4.1 Model

The simulated area was a circle with a 3 mm diameter which corresponds to 5 times the longest wavelength studied. The THz generation is modelled by surface currents between digits over $300\mu m$ (approximated spot size of our NIR excitation beam). To avoid electromagnetic reflections from the edges of the simulations, the boundaries conditions of the model were adjusted to scattering. Two identical electric field monitoring probes are placed 1.5 mm above and below the active surface of the sample to monitor the emission from the surface and through the substrate. Note that only the relevant x component of the electric field is considered here, as the THz polarization is dictated by applied DC field between the electrodes. To study the propagation of the electric field, the real and complex refractive index of each materials (n,k), we interpolated values from reference [31]. We comparatively modelled both PCS structures presented above (standard and cavity-based PCS).

II.4.2 Numerical results

The simulated electric field from the interdigitated structures are shown in Figure II-5, for a radiated frequency of 1.5 THz and 1 THz, corresponding to the frequency of highest emission of the cavity-based and standard PCS, respectively.

The cavity-based device in Figure II-5 a) and b) is modelled with a GaAs thickness d of $10\mu m$ and buried metal plane, along with a standard structure in Figure II-5 c) and d). As it can be clearly seen in the cavity-based structure, all the emission is indeed reflected from the top of the device, with no pulse that propagates into the substrate. This is in stark contrast to the standard device that radiates in both directions. Further, the buried metal switch shows an

enhanced integrated field (intensity) that is a factor 3 (9) greater than the standard equivalent PCS.

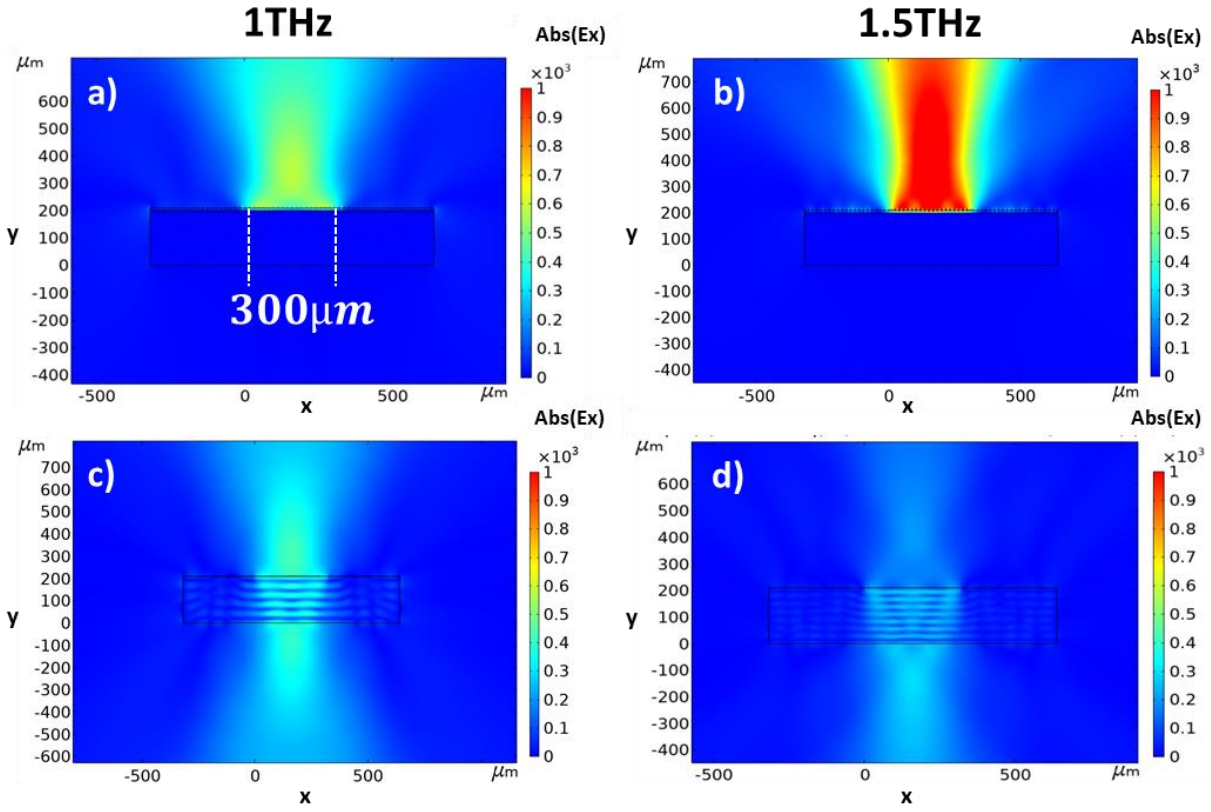

Figure II-5 Electromagnetic simulations of the 'x' polarized emitted electric field at 1 THz and 1.5 THz (maximum field emission of the standard and the cavity based PCS respectively) for the cavity (a),b)) and standard (c),d)) PCS. The whites dashed corresponds to the simulations surface currents (approximate size of our NIR beam).

The effect of the emitted frequency can be resumed in Figure II-6 that shows a contour plot of the integrated field radiated by the device as a function of frequency (y-axis) and the GaAs thickness (from the top of the GaAs layer to the buried metal (d)). As it can be seen, there is a clear resonant behaviour with the peak frequency emission shifting to higher frequencies as d is reduced that highlights the effect of the cavity. In the case of d > 10μm, higher order frequency bands are observed owing to the thick GaAs later acting as a Fabry-Perot cavity. These higher frequency contributions would result in "echoes" for time resolved experiments. As the frequency emission of these structures typically reaches 4THz, distances d of 6 and 10μm were chosen as an optimum for the PCS to avoid any generated Fabry-Perot oscillations where the first spectral dip would be expected at $\lambda \sim 2nd \sim 72\mu m \sim 4.2\ THz$ (where n is the refractive index of GaAs). For d=10μm This gives an enhancement at a central frequency of 1.5 THz that corresponds well to the central emission of these PCS. The black line corresponds to quarter wavelength condition ($\nu = c/4nd$). The deviation of the

simulated data from this line is a due to the large refractive index of the metal, that results in a larger effective index of the THz mode as the GaAs layer is reduced[32].

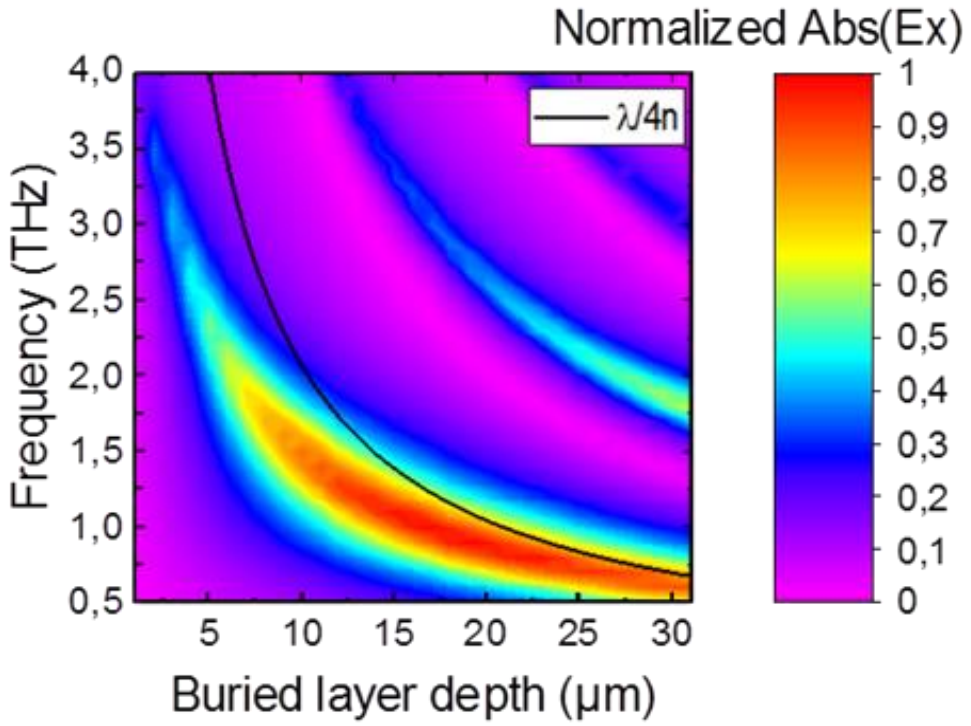

Figure II-6 2D plot of simulated electric field as a function frequency (y-axis) and GaAs active thickness d (x-axis). The black solid line corresponds to the quarter wavelength condition with a refractive index of ~3.6.

To clarify, for the standard PC switch, the digit fingers were 2 μm wide separated by 2 μm gaps instead of 4μm for the quasi-cavity. Electromagnetic simulations in appendix (Figure A 1) show that a 4μm and 2μm interdigitated distance presents no differences in emitted electric field.

In next section we will present experimental time resolved and absolute power measurements of the PCS described above (cavity-based vs standard PCS).

II.5 Time resolved measurements

Time resolved electric fields of each structure were investigated using our reflection THz TDS setup described in section I.2. First it is worth mentioning that the simulated spectrum of the cavity PCS THz pulses matches well their experimental counterparts. Figure II-7 compares the experimental to the simulated device in the case of a distance $d = 10\mu m$ with the absorption of GaAs as the single fitting parameter used to fine tune our models with experiments. The experimental data were used to determine losses for the THz pulse in the top 2µm where the optical pulse is absorbed. Fitting experimental data, a loss of a 400 cm^{-1} gives a reasonable agreement. Figure II-8 a) shows the time traces of typical structure (red) along 6 (green) and $10\mu m$(blue) thick cavity-based devices, normalized to the $10\mu m$ PCS. It is clear that the 10µm device emits stronger THz field by respectively a factor 3 and 1.6 relatively to the standard and $6\mu m$ device. Their normalized spectral fields displayed in panel b) shows a frequency response centered towards low frequencies for the standard PCS, and a good agreement with simulations (Figure II-6) for the cavity-based devices, with 6µm thick PCS being shifted towards higher frequencies. As it can be seen, a broadband response is realized despite the presence of the cavity, with only a slight reduction in bandwidth compared to a standard device.

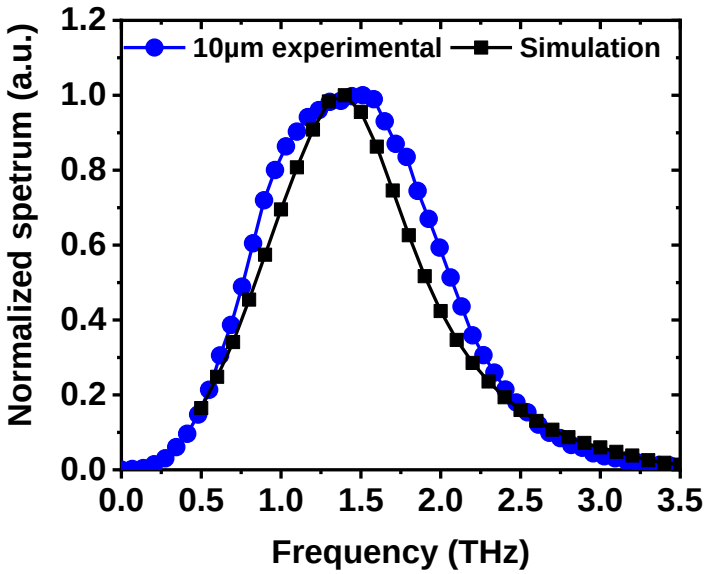

Figure II-7 shows the measured amplitude spectrum compared to the simulated profile (not considering the response of the electro-optic sampling).

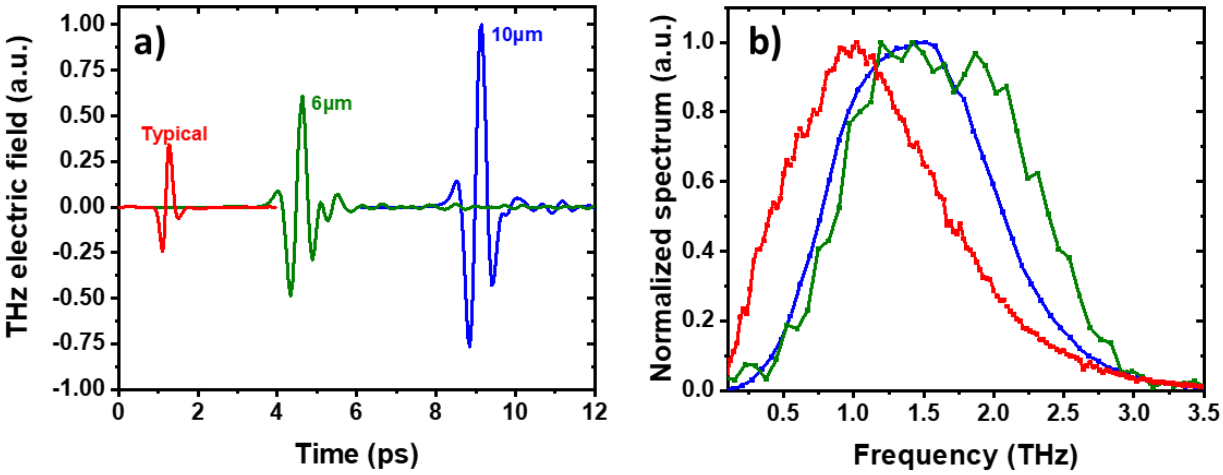

Figure II-8 a) Time trace of electric fields of typical, 6 and 10µm cavity-based PCS b) Respective spectrum.

II.6 Absolute power measurements

The coherent measurements of the THz field were followed by careful investigations of the average power using a calibrated pyroelectric detector (LP20 from SLT Sensor und Lasertechnik calibrated by the PTB Braunschweig and Berlin at 1.4 THz with a responsivity of 66 V/W). The PCS were biased up to 40 kV/cm, corresponding to an applied voltage of 16 V, and electrically modulated at 40 kHz at 50 percent duty cycle. The emission is collected and focused on the detector using two f#2 parabolic mirrors. As the switch needs to be operated in a reflection geometry with the emitted THz collected from the front of the switch, the optical pump was entirely filtered using Teflon and black plastic filters, with an infrared camera used to verify that no optical beam is incident on the detector. The results are not corrected for the absorption of the filters. To measure the power using the slow pyroelectric detector, a 20 Hz modulation is added to the device on top of the 40 kHz modulation. For the maximum applied bias, the power is read directly on an oscilloscope trace [24] through the peak-to-peak voltage. The THz response is verified by placing a metal plate in front of the detector to avoid any false reading from electromagnetic interference.

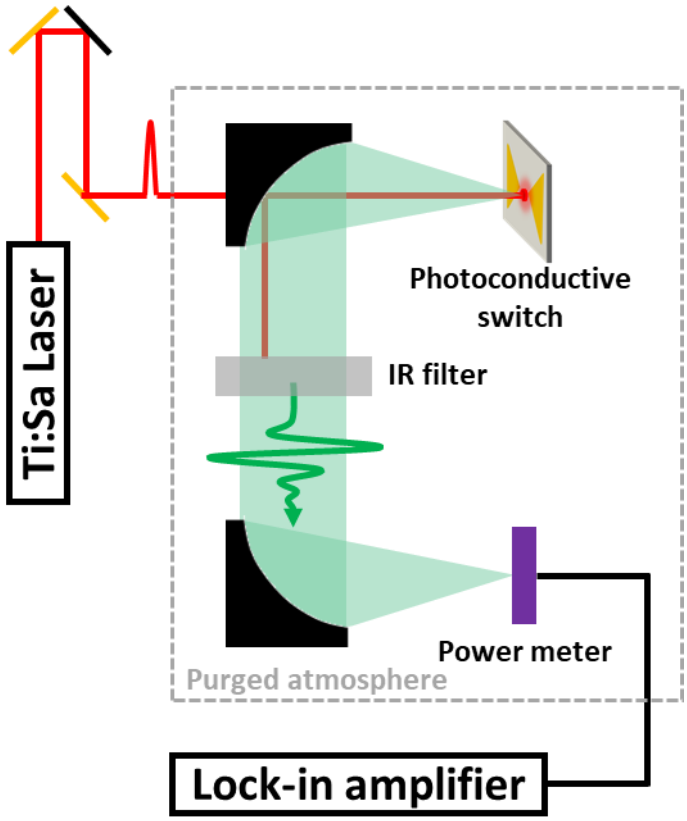

Figure II-9 TDS setup used for the power characterization of the PCs.

Figure II-10 shows the measured average power as a function of applied field for the $10\mu m$ cavity-based device and the standard switch. Here for the standard PCS, the digit fingers were 2 µm wide separated by 2 µm gaps. (Electromagnetic simulations show that a 4µm and 2µm interdigitated distance present no differences in emitted electric field, see Figure A 1 in appendix). The greatest power measured for the quasi-cavity switch was 181 µW compared to 24 µW for the standard switch at 39.5 kV/cm and 42.25 kV/cm, respectively, characterizing an enhancement of the THz power by a factor ~7.5. The former corresponds to an optical-to-THz efficiency of 0.05%. The power measured is one of the highest measured from a PCS with standard photolithography. To be noted is that the ratio between the two devices is not constant, with the contrast higher at applied fields greater than 35 kV/cm. This is possibility the result of enhanced heat dissipation in the cavity-based device where the thick buried gold layer can easily evacuate the generated heat from the excitation spot.

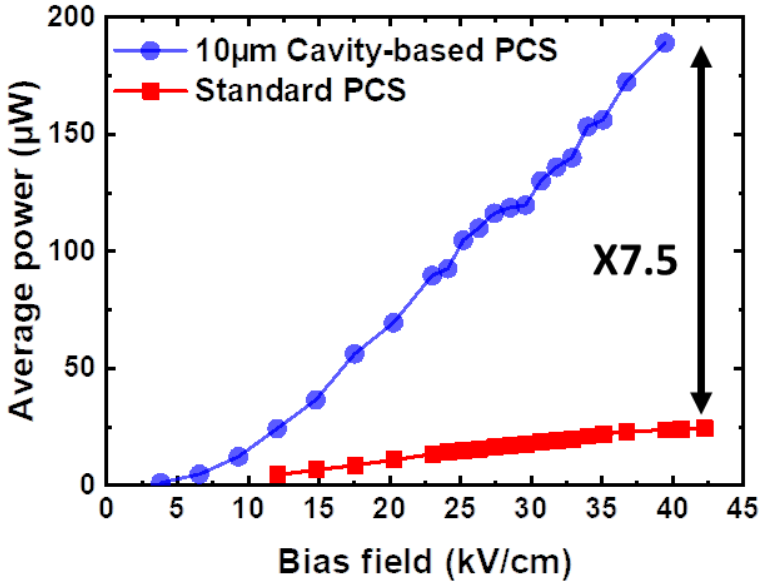

Figure II-10 . Average power as a function of applied field for standard (red) and cavity-based (blue) PCS.

II.7 Further parameter optimization

In this section, we will discuss the effect of bias voltage and modulation frequency over the THz pulse for the $10\mu m$ cavity-based PCS. This aspect is particularly relevant for chapter V related to the study of polaritons where the highest THz power is beneficial to this complex investigation. Typically, PCS are biased with a square signal modulated in the kHz range with an amplitude of few Vs. To maximize the power even further, we performed THz absolute power and electric fields measurements for modulation frequencies ranging from 10 kHz to 200 kHz along the same ranging bias as above. Results are shown in Figure II-11 where panel a and b display respectively the THz absolute power and the normalized THz electric field. One can clearly see that higher power can be reached for frequency modulations around 125-150 kHz giving a maximum power of $\sim 240\mu W$. Above these values, the THz power drops, which might be related to the added capacitance from the buried Au plane. The electric field shows the same trend. Note that THz higher power might be reached for even higher bias fields but may also result in permanent damage of the device.

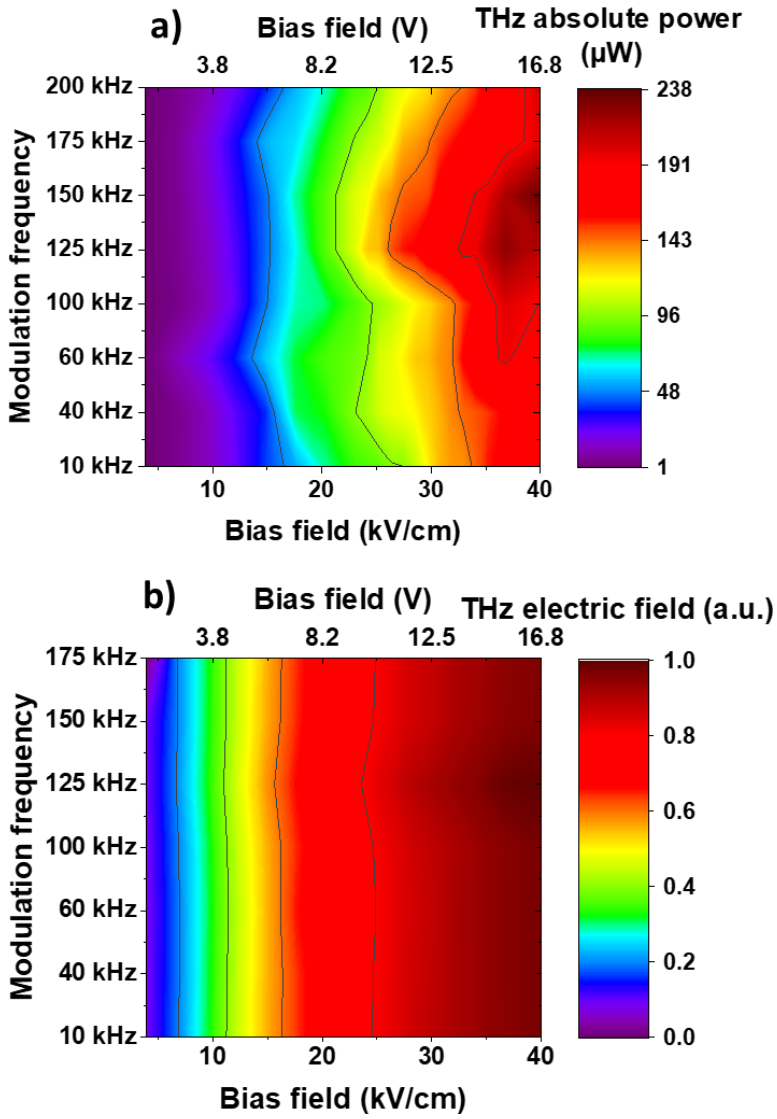

Figure II-11 : a) 2D colormap of the THz power vs bias fields for different modulation frequencies. We can clearly see a modulation frequency sweet spot in the range of $125 - 150\ kHz$ *giving large THz power, with a maximum of* $\sim 240 \mu W$ *. b) shows the THz maximum Electric field, as a function of bias and modulation frequency. The same trend as a) can be seen.*

In the next section, we will use our $10 \mu m$ cavity-based device to show the first demonstration of broadband THz real time imaging from a PCS.

II.8 Towards real time imaging

To illustrate the application of these high THz average powers, real time THz imaging was performed using a recently commercialized THz camera (i2S) based on a micro-bolometer array [19]. Previous work with this type of camera has shown the real time imaging only with a THz QCL [19] and imaging of only the focus spot of a standard THz PCS [33] (FWHM = 320 µm). An optically opaque plastic object is shown in Figure II-12 a) and Figure II-12 b) and is placed in the path of the THz beam just after the focusing parabolic mirror. The illuminated circular area has a diameter of ~ 2 cm. Figure II-12 c) shows the THz image collected by the camera in real-time and clearly revealing the hidden text with a spatial resolution of approximately 400µm. Importantly, unlike THz imaging with monochromatic sources such as QCLs [34] no strong diffraction effects are observed owing to the spectrally broadband nature of the THz switch where the diffraction of each frequency interferes deconstructively. This highlights the advantage of using spectrally broad sources for THz imaging. A real-time video of the object moving in the plane of the THz beam can be found in the supplementary material of our publication (visualisation1)[14]. The bright spot in the centre of the image is a result of a hole in the first parabolic mirror that is used to excite the switch in reflection mode. Although images with greater resolution and quality can be achieved with THz QCLs (owing to a shorter wavelength and higher powers) these operate at cryogenic temperatures. Further QCL operate at higher frequencies (>2 THz) where material losses are greater, reducing the penetration and hence the applicative potential in non-destructive testing. Here further optimization will permit photoconductive switches to reach milliwatt power levels (see below) that will improve the image quality, although resolution will be limited by the inherent emission that is centred around 1.5 THz.

Figure II-12 a) Picture of the object to image b) Hidden text c) Real-time image from the THz camera using the high average power from the cavity PCS showing the hidden text. A real-time video is shown in the supporting content (see visualisation1).

II.9 Conclusions

In this chapter, we introduced the operational principles of PCS and how placing such a device in a cavity can enhance the THz emission. This was done with a buried metal plane below a 10µm thick GaAs layer. From our simulations, we showed a factor 3 increase in THz field between a standard (without the buried Au plane) and a cavity-based device. Furthermore, we showed that the frequency response of the cavity-based devices for different depth of the Au plane remains spectrally broad. This along with the increase in THz emission were confirmed by experiments that compared the THz fields of a standard, 6µm and 10µm thick cavity-based devices. By performing careful absolute power characterization, we highlighted a ~7.5 factor increase in power for 10µm cavity-based structure compared to the standard, close to the expected value of 9. We show a maximum absolute THz power of 240 µW for the 10µm cavity-based device. These high powers were used then to show the first demonstration of broadband real time imaging using a PCS.

We further judge that this average power can be further optimized by at least an order of magnitude and reach the milliwatt range by increasing the pump power, thickness of the cavity (with a small sacrifice in bandwidth), area of the active surface, and engineering the optical beam to excite only the exposed GaAs of the switch. For example, by increasing the thickness of the structure to 15 µm, the power can be enhanced by 36%. Using a spatial light modulator (or simply microlenses), the excitation beam can be designed to excite only the parts of the GaAs that are exposed (currently 25% of total area), resulting in a further increase by 75% if optical saturation is avoided. Further, these structures can be easily scaled: by increasing the active region to 1 mm by 1 mm, the optical excitation power can be increased by a factor of 4 (with a constant power density), bringing the THz power to mW levels. Similar concepts could be transferred to InGaAs based PCS to be compatible with the fast-evolving telecom femtosecond lasers. This, we believe, would be of interest to a wide range of researchers working in fundamental science as well as applications, removing an important bottleneck in the performances of THz sources.

Chapter

III

III Heavy metal based spintronic THz emitters

Terahertz spintronic based devices represent a novel and fast-growing topic among both the spintronic and THz communities. As for PCS, they are optically driven with femtosecond lasers but offer the advantage of ultra-broadband operation owing to their phonon-less spectrum [35], and their nanometric layer thicknesses that can be grown on virtually any substrate. However, these THz processes of these promising sources are not fully understood and have lower performances compared to established THz technologies (e.g. PCS). In this chapter we will introduce key concepts of ultrafast spintronics, spin-to-charge conversion for THz pulse generation and detail our work towards the understanding of the underlying physics and the optimization of such devices. Specifically, ferromagnetic/heavy metal (FM/HM) based heterostructures, which currently displays the best performances, will be presented. (Other technologies based on quantum materials such as Rashba interfaces, topological insulators, and Weyls semi-metals will be detailed in chapter IV).

From the spintronic point of view, we will show that THz TDS can be used as a non-destructive, fast, and reliable method to probe the physics of these devices. In detail, we will compare the THz emission and transport parameters extracted by ferromagnetic resonance spin-pumping (FMR-SP) of several structures relying on different FM and HM materials. Modelling of a FM/HM structure carried out by CNRS-Thales with support from the University of Nebraska will also be presented to analyse the differences between THz emission and FMR-SP and highlighting the relevant metrics to optimize the THz emission. The framework of this study is based on a strong collaboration between the CNRS-Thales and the LPENS. My implication was focused onto THz investigations of materials, benchmarking and understanding the generated THz electric fields with femtosecond optical pumps. The theoretical expertise, fabrication and spin pumping experiments were performed at CNRS-Thales

Chapter III

III.1 THz spintronics - Introduction

Historically, charge and spin have been considered separately, for instance in logical circuits where the flow of carriers is the main metric for the bits of information, or in hard drive technology that relies on magnetic moments to store data. Spintronics is a relatively new field of research that links these two parameters with the aim of building new devices to take advantage and manipulate simultaneously spin and charge. Spintronics can unlock novel and more efficient devices for data storage by magnetic memories [36], in computing by the implementation of spin logic and in THz generation which is the focus of two chapters of this manuscript [37].

In 1985 Mark Johnson and collaborators published the first demonstration of spin-polarized interfacial current [38]. Later, in 1988, giant magnetoresistance was independently discovered by Albert Fert and Binasch [39], [40], a discovery that lead to a joint Noble prize in 2007. At this point spintronics attracted significant attention from the scientific community and is developing into a mature technology. For the THz community, the first demonstration of THz radiation from ultrafast spin-to-charge conversion by Beaurepaire et al. [41] in 2004, opened the gate to new optically driven THz emitters. Importantly, these structures are able to generate ultra-broadband absorption-free spectra, unlike PCS, as metal based spintronic based emitters do not possess phonon absorption in the 0-30 THz range [35]. Ultra-broadband spectra of bandwidth ~ 30 THz have been experimentally demonstrated by Seifert and collaborator in 2016 [24]. THz spintronics is a very fast growing and hot topic in modern physics, which can be used as a probe of spintronic phenomena and could eventually impact industrial applications of THz waves. Figure III-1 shows a comparison of the spectral bandwidth of metallic spintronic emitters with established broadband THz technologies (a GaAs based PCS, and ZnTe and GaP nonlinear crystals). These are all excited with an infrared (IR) femtosecond laser, generating a THz pulse. The spintronic structure is based on an optimized nanometric trilayer structure of tungsten – ferromagnetic – Pt (W/FM/Pt) and clearly highlighting the potential of ultra-fast spintronics in there ultra-wide, phonon-free, spectrum.

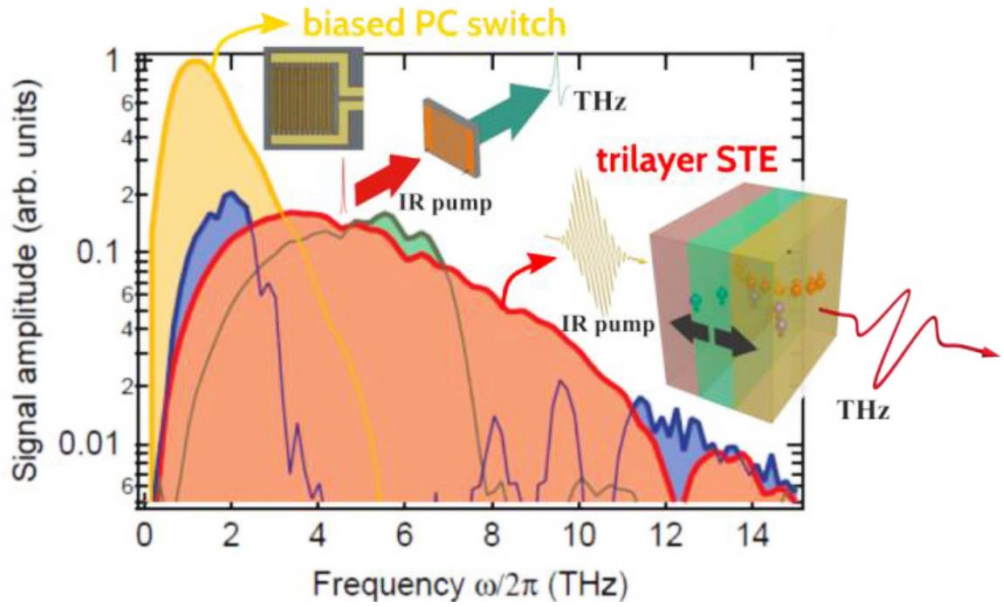

Figure III-1: Spectrum summarizing optically driven broadband THz sources: Ultra-fast spintronics emitter (STE) - red, PCS - yellow, ZnTe – blue and GaP green plots. Adapted from [35]. Note that the spectrum of the spintronic emitters shown in this figure is bandwidth-limited by the detector used and the absorption at 12 THz is from the detector.

III.2 Important concepts in THz spintronics

As the THz community and the spintronic community may not be familiar with the same notions, this section presents some key concepts of spintronics that are required to understand the fundamental processes and optimization of ultrafast THz spintronic emitters.

III.2.1 What is a spin current?

Spin is the intrinsic angular momentum of a carrier rotating on his own axis and two possible states exist called “spin up” (↑) and “spin down” (↓).

At the electronic scale, a charge current is a flux of carriers regardless of their spin. Spin-currents, however, can consist of either i) a spin polarized current where the carrier flux is polarized in spin, or ii) a pure spin current where spin polarized carriers are moving in an opposite direction, resulting in total spin displacement that is twice as large as i) (see Figure III-2). Another case exists; the spin wave or magnon oscillation that is the result of collective interaction of spins precessions, able to transport spin-currents in insulator ferromagnets (for example, Yttrium iron garnet). However, as this case falls out of the scope of this manuscript,

the interested reader could refer to [42], [43] for more details on the underlying physics and applications of such phenomenon.

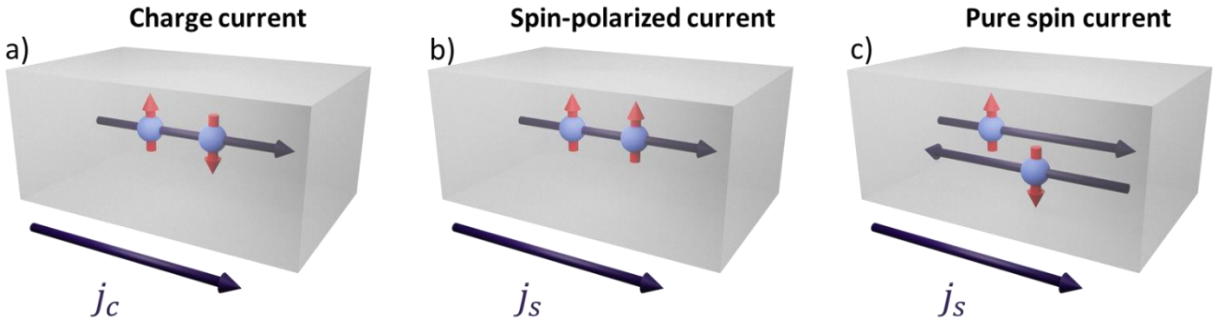

Figure III-2: Descriptions of charge and spin current: a) Charge current: carriers flowing regardless of their spin b) Spin-polarized current arising from the motion of carriers. c) Pure spin current flux of two spin polarized current opposite in direction $J_s = J_\uparrow - J_\downarrow$.

A vast array of physical processes can be used to generate spin polarized currents (see Figure III-3). The most widespread include spin-orbit effects stimulated by magnetic fields or by a magnetization precession, an electric field, the application of an electromagnetic wave, Zeeman splitting, thermal gradients such as Seebeck or Nernst effects. In this work the generation of spin-polarized current relies on the application of an ultrashort NIR pulse onto a magnetic material for the THz pulse generation. However, the magnetization precession method will also be discussed in the section III.2.8 as it is used to understand spin transport in FMR-SP.

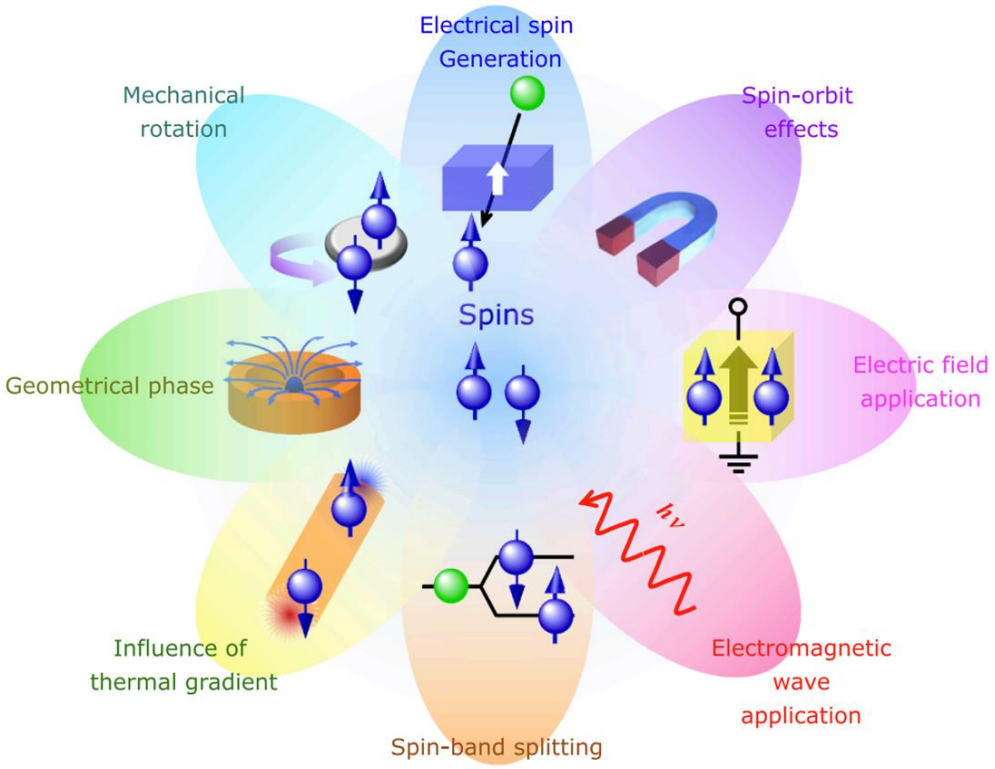

Figure III-3: Diagram of main techniques used to generate spin-polarized currents. From [36]

III.2.2 Ferromagnetic materials

Here we will introduce notions of FM materials and discuss why they are relevant for THz generation. For spin injection, FM materials are of particular interest as their magnetic moments tends to align themselves to form domains. Under an external magnetic field, all the moments of these domains align. This peculiar trait makes them suitable for polarized spin current injection. Magnetism in FM is caused by an imbalanced density of states between spin up and spin down. The conduction band electrons (at the fermi level) are then spin-polarized owing to the energy splitting of the d bands in two subbands. A simplified picture of their spin dependent density of state is shown in Figure III-4 a), where the majority and minority d subbands are separated by their exchange splitting, resulting in spin polarized electronic states at the fermi level. It is then possible to define the spin polarization *P* in % as equation (III-1)[44], [45] with $N_F^{\uparrow(\downarrow)}$, being the spin ↑ or (↓) density of states at the Fermi level. Typical values of P (sensitive to the fabrication) from the literature are displayed in Figure III-4 b) for Co, Ni, Fe, NiFe and half FM materials (such as Co_2MnSn Heusler alloy).

$$P = \frac{N_F^{\uparrow} - N_F^{\downarrow}}{N_F^{\uparrow} + N_F^{\downarrow}} \qquad (III\text{-}1)$$

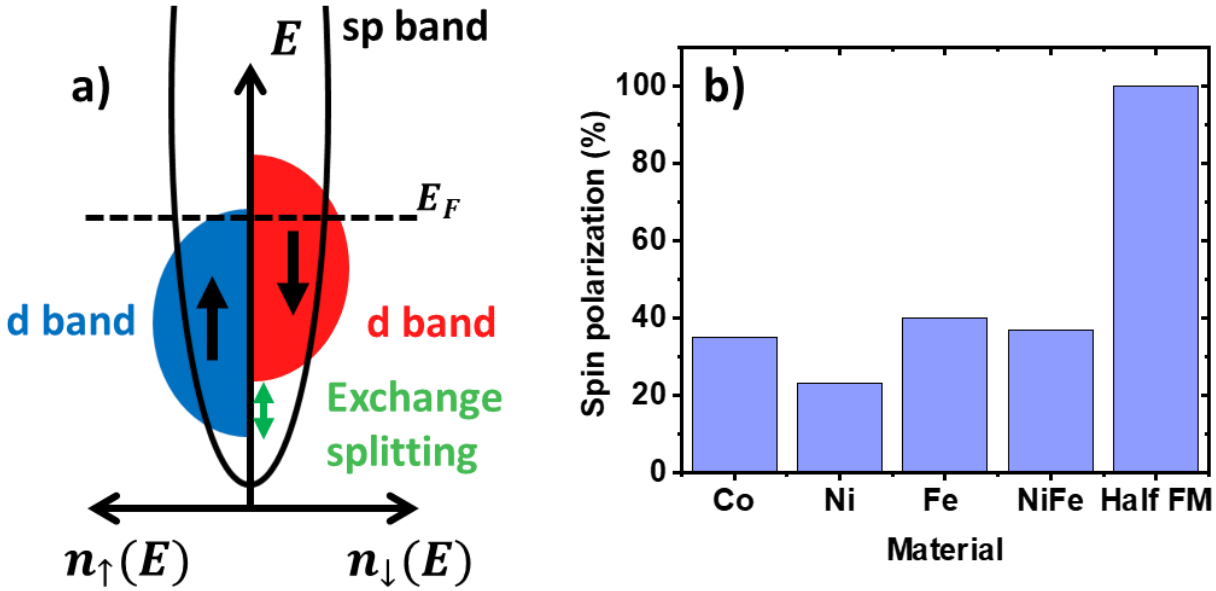

Figure III-4 : Schematic density of state of FM materials. The blue and red area represents respectively majority spin down and minority spin up carriers. FM are characterized by the exchange splitting separating the spin up and spin down density of states. b) typical spin polarization value for Co, Ni, Fe, Ni0.8Fe0.2 and half ferromagnetic materials (such as Co2MnSn Heusler alloy) reported in [44], [45]

Since the pioneering demagnetization experiments of Beaurepaire et al. in 1996 [46] followed by complementary investigations, [26],[30] it is now believed that the excitation of a ferromagnetic material by an ultrafast laser pulse leads to a picosecond demagnetization of the ferromagnetic films within the 3d band. Such a demagnetization process is accompanied by ultrafast hot carrier spin currents in the 4sp band, as proposed in [48]. This therefore can be used to generate an ultrafast spin polarized current.

III.2.3 From spin currents to THz – spin-to-charge conversion

The current (2021) state-of-the-art in THz spintronic emitters are ferromagnetic/Heavy metal (FM/HM, also referred to FM/NM for normal metal or non-magnetic metals) based heterostructures [1], [35]. They rely on nanometer scale junctions of FM and HM materials. For the spintronics chapters (III, IV) of this manuscript, we will compare different emitters to our FM/HM reference consisting of Co(2)/Pt(4), on a glass substrate with the number between parenthesis corresponding to the thickness of the material in nm.

If we consider the case of the FM/HM junction as pictured in Figure III-5, the THz generation arises from the excitation of the magnetic material (FM) by an ultrafast laser pulse leading to a picosecond demagnetization of the FM film. Such demagnetization process is accompanied by an ultrafast hot carrier spin current. Follows a diffusion of spin-current through the interface of the structure into the HM where an ultrafast **spin-charge conversion** (SCC) phenomenon converts the ultrafast spin current into an ultrafast charge current. This is through the inverse Spin Hall effect, described in section III.2.5. Similarly to the PCs described in Chapter I, the transient charge current generates the THz linearly polarized electromagnetic dipolar radiation. This emission can be described in the far field by equation (III-2) where the THz electric field is proportional to the time derivative of the charge current, j_c.

$$E_{THz} \propto \frac{\delta j_c}{\delta t} \qquad \textit{(III-2)}$$

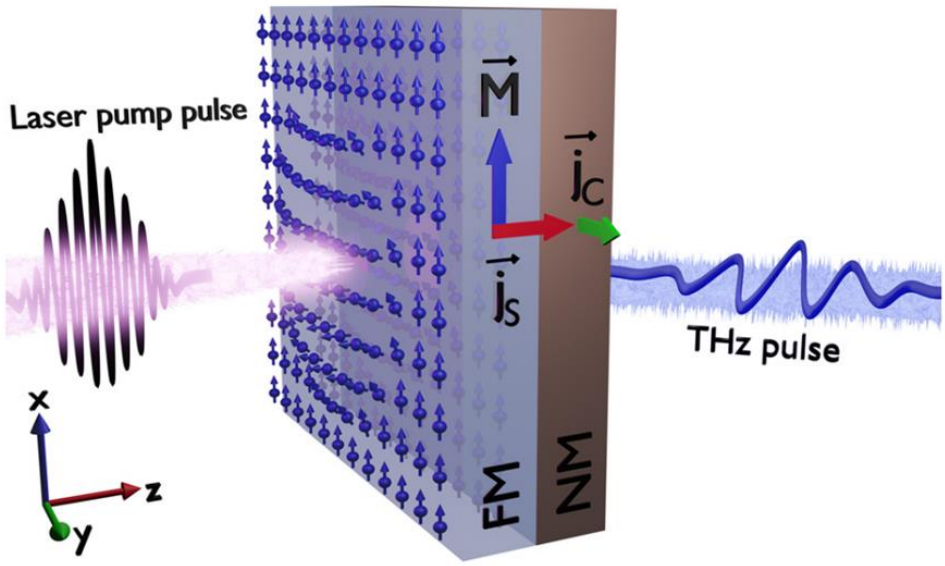

Figure III-5 :Representation of THz generation from a spin-current in FM/HM system. From [1]. A polarized spin-current is injected into the FM by ultra-fast demagnetization induced by the fs pulse, SCC occurs in the HM, the relaxation of transient charge current leads to a THz dipolar emission.

The electric field emission of our reference Co(2)/Pt(4) is benchmarked in Figure III-6 to other technologies of THz emitters. We can clearly see that the emission of Co(2)/Pt(4) is comparable with ZnTe optical rectification, although considerably less than a technologically mature and intensively investigated PCS, as also reported in [35]. Note that in this picture, the THz signal of PCS are scaled by a factor 0.01. Also, due to the nanometric thicknesses of

FM/HM structures, their infrared absorption is reduced to about few tens % [49] of the beam, compared to PCS where GaAs fully absorbs the infrared excitation beam. The spectrum of each emitter shows comparable spectral bandwidths, limited by our detection scheme (500µm ZnTe detection crystal).

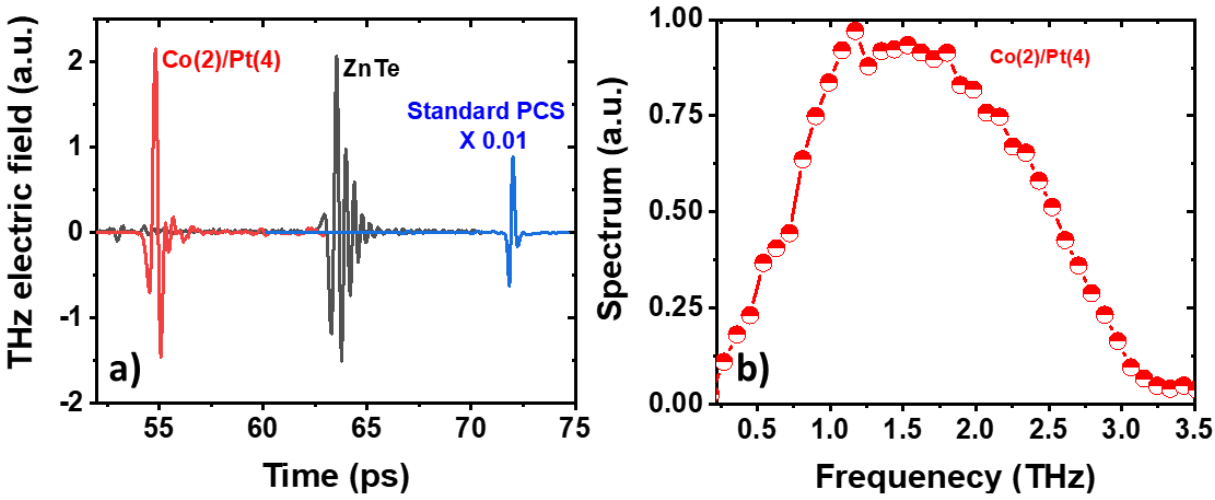

Figure III-6 : THz emission of Co(2)/Pt(4) FM/HM junction. a) Comparison of spintronic emitters with ZnTe, standard PCS (see II.3). b) Spectrum of the Co(2)/Pt(4) emission.

The thicknesses of our structure have been chosen accordingly to studies comparing THz emission for different HM and FM layer thicknesses [50], [51]. The optimal thickness for the FM and the HM layer were studied for different materials with a THz emission maximum in the range of few nm [1] for both materials. The thickness of these layers impacts several intricated metrics such as resistivity, THz and infrared absorption, and will be discussed in section III.4.1.

We will now discuss the physical processes that gives rise to THz emission from spintronic emitters.

III.2.4 Physical ingredients

III.2.4.1 Spin-orbit coupling

SCC is made possible by spin-orbit coupling (SOC) or spin-orbit interaction (SOI), which is an important concept in spintronics as it leads to its exotic properties. SOC arises from the interactions of an electron`s spin with its motion inside a potential. From the classical picture, electrons with a charge $-e$ orbit around their nuclei charged by $+Ze$ with Z the atomic number. From the frame of reference of the electron, the nucleus is orbiting around the fixed electron with an orbital angular momentum L, generating a current that translates to an electric field E. This electric field gives by induction a magnetic field B that will interact with the spin magnetic momentum (μ_s) as depicted in Figure III-7. The SOC describes this interaction between the angular momentum L and the spin S, and can be derived from the Dirac equation with an added term to account for this interaction [52] (see equation (III-3)).

$$H_{SOC} = \frac{e\hbar}{4m_e^2c^2} E.(k \times \sigma) = \lambda S\,.\,L \qquad (\text{III-3})$$

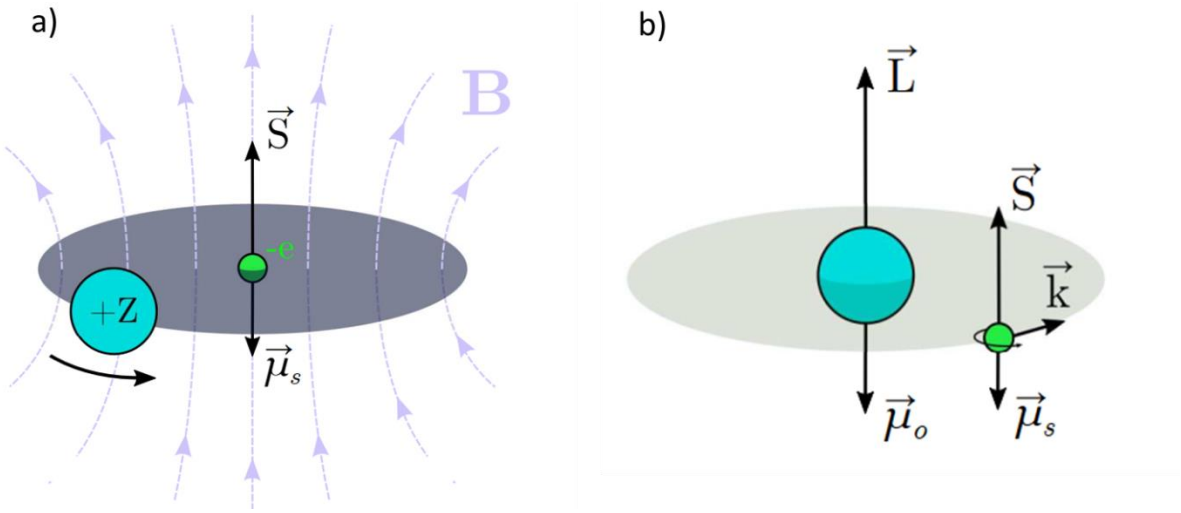

Figure III-7: Spin orbit coupling a) a fixed nucleus and an orbiting electron b) electron orbiting around a nucleus S and L can be parallel or anti parallel according to the orbiting direction of the electron. Adapted from [53]

With λ giving the strength of this coupling as described in (III-4), the orbital angular momentum L corresponding to $L = r \times k$ and the spin angular momentum as $S = \frac{\hbar}{2}\sigma$. σ and k are respectively the Pauli matrices and the electron crystal momentum.

$$\lambda(r) = \frac{er^{-1}}{2m_e^2c^2}\frac{\delta V(r)}{\delta r} \qquad (III\text{-}4)$$

With r representing the distance between the electron and the nucleus. Evaluating the value of λ with the Coulomb potential $V(r) = -Ze^2/r$ shows that λ is proportional to Z^4, which indicates that the spin-orbit coupling is much stronger for heavy materials and especially for electrons of inners shells. This is a well know result in the simple atomic case of hydrogen-like atoms. In solids, however, with more complex band filling, λ scales with a Z^2dependence [52]. This explains the reason why heavy metals are essentials ingredients in spintronics, as they possess a strong SOC. Typical material commonly used and characterized by a large atomic number Z with strong SOI are 4d (Pd) or 5d (Pt, W, Ta, Au:Pt, Au:W, Au:Ta) transition metals. Figure III-8 gives the spin-orbit coupling for increasing Z number atomic species. The shaded area corresponds to the outer shell electrons that scales with Z^2.

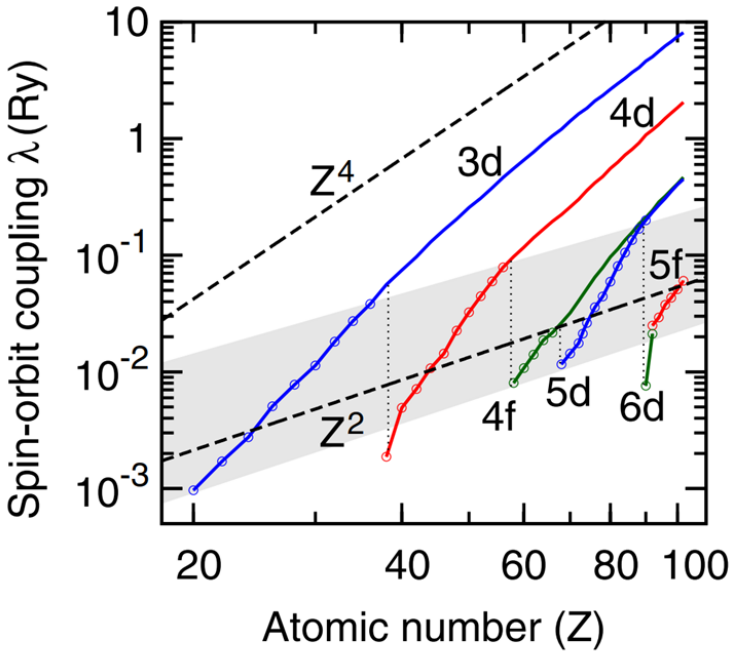

Figure III-8 : Spin orbit coupling strength λ in Rydberg unit for an increase of the atomic number, As the electronic shells fil the SOC increase with a Z^2dependence. The shaded area corresponds to outer shells, from [52]

Several mechanisms exist for a SCC; the Inverse Spin-Hall Effect (ISHE), which is a bulk effect, and the Inverse- Rashba-Edelstein- Effect (IEE), which is an interface effect. In this chapter we will discuss the spin-Hall effect, as the IEE is mostly related to quantum materials, details will be given in chapter V. Note however that in equation (III-4) the term $\frac{\delta V(r)}{\delta r}$ can be decomposed as bulk (atomic) and surface (Rashba) contributions, this will be introduced in section III.4.5.

III.2.5 The Spin-Hall effect

The spin-Hall effect (SHE) is a variation of the more "conventional" Hall effect discovered in 1879 [54] where the generation of a transverse Hall voltage across a conductor arises from an electric current and a magnetic field. It was then pointed out that ferromagnetic materials behaved differently than non-magnetic conductors [55]. The Hall effect on ferromagnetic materials was found sensitively stronger. This behaviour was classified as the anomalous Hall effect and was explained by an intrinsic and extrinsic contributions (see Figure III-9) on the Hall conductivity. Historically, the correlation between these different contributions to the anomalous Hall effect were the centre of controversies, and the interested reader can find further details on the development of the current model in reviews [56]–[58].

The intrinsic effect addresses the case of pure materials. It is caused by the effect of SOC on the band structure that can gives an anomalous velocity to electrons, owing to the Berry`s curvature (which can be seen as a strong magnetic field in k-space) [59] that is caused by the spontaneous time reversal symmetry breaking from ferromagnetism. The extrinsic mechanism relies on spin-dependent impurities scattering and is constituted of two contributions: i) Skew or Mott scattering that arises from the spin orbit interaction of the impurity with incoming electrons. Electrons flowing are symmetrically deflected by an angle θ according to their spin; ii) Side-jump scattering where electrons are symmetrically deflected in opposite directions according to their spin by the SOC of impurities but with an angle θ and a lateral displacement δ. It is important to note that all these mechanisms rely on SOC, with the intrinsic contribution being dominant in HMs [60].

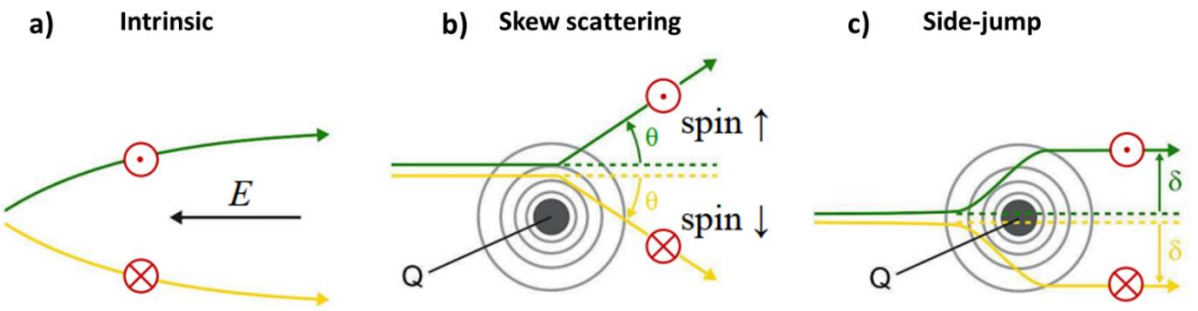

Figure III-9 : Representation of intrinsic and extrinsic mechanisms responsible for the anomalous Hall effect. a) intrinsic contribution b) Skew or Mott scattering c) Side jump scattering. From [53].

Based on these scattering mechanisms, the SHE was predicted by Dyakanov and Perel in 1971 [61], observed experimentally later in semiconductors by Kato and co-worker in 2004 [62] and in an aluminium system in 2006 [63] by Valenzuela *et al*. The SHE is a SCC process where a spin polarized accumulation (pure spin current) can be observed on the boundaries of a material when a charge current is present. The resulting spin current is perpendicular to the charge current applied (see Figure III-10 a)). As the origin of this effect are similar to the anomalous Hall effect [59], SHE is strongly dependent of the material SOC and does not require an external magnetic field.

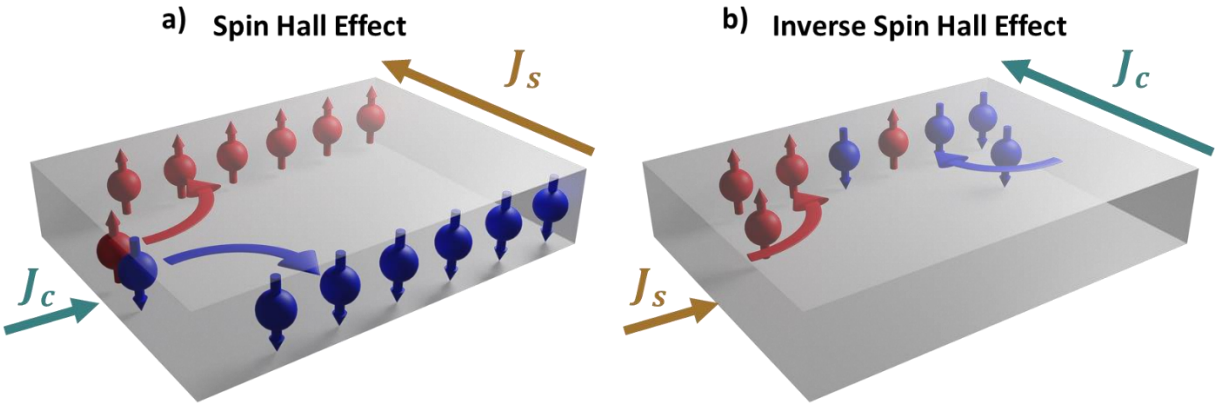

Figure III-10 Representation of a) the spin-Hall effect and b) the inverse-spin-Hall effect. j_c and j_s represents respectively charge and spin current (teal and yellow arrows).

The inverse process is the ISHE (Figure III-10 b)) where a charge current arises from a spin current. This mechanism is used in FM/HM heterostructures to convert ultrafast hot carrier spin-currents induced by our fs laser to a transient current for the generation of a THz pulse. A figure of merit to quantify the conversion efficiency between spin and charge is the so-called spin Hall angle (SHA), $\theta_{SHE} = j_c/j_s$ ratio between the transverse charge current generated over the spin current. The spin Hall angle can also be defined from the off-diagonal

terms of the conductivity tensor σ_{xy} as described in equation (III-5) corresponding to the transverse spin Hall conductivity with σ_{xx} the longitudinal conductivity.

$$\theta_{SHE} = \frac{\sigma_{xy}}{\sigma_{xx}} \qquad (III\text{-}5)$$

The transverse spin Hall conductivity is composed of contributions arising from the intrinsic σ_{xy}^{int}, side-jump σ_{xy}^{s-j}, and skew σ_{xy}^{skew} scattering mechanisms described above (see equation (III-6)). Note that the SHA is proportional to the transverse spin Hall conductivity and can be enhanced by adding impurities to favour intrinsic scatterings, this will be discussed in the case of Au:W and Au:Ta in latter sections.

$$\sigma_{xy} = \sigma_{xy}^{int} + \sigma_{xy}^{s-j} + \sigma_{xy}^{skew} \qquad (III\text{-}6)$$

The charge current that arises from the spin current is defined by equation (III-7) where a the spins contained in the Pauli matrix (σ) must be perpendicular to the propagating spin current. Note that it has been shown by [39] and [40] that the SHA relying on extrinsic spin Hall effects materials (alloys) are larger than their intrinsic (pure materials) counterparts.

To give a magnitude of the SHA to the reader, values for materials considered in this chapter are given for few intrinsic (blue) and extrinsic (green) materials in Table III-3. Note that the SHA values in the literature are not homogenous due to the strong dependence of the spin Hall conductivity over disorder and thus, material fabrication. In the case of extrinsic alloys, the SHA shows a strong dependence in the impurity concentration [64], [66]. It is worth mentioning that the SHA can be negative, in such a case, the charge current propagates in the opposite direction. This has been applied by Seifert and co-workers in the optimization of trilayer structures, where the FM material is embedded between two different HMs with opposites SHA. This enhances the THz emission as the resulting radiation from each interface has the same phase [35] for constructive interference.

$$\boldsymbol{J_c} = \frac{\boldsymbol{2e}}{\hbar}\boldsymbol{\theta_{SHE}} \cdot (\boldsymbol{J_s} \times \boldsymbol{\sigma}) \qquad (III\text{-}7)$$

Materials	Pt	W	Au:W	Au:Ta
θ_{SHE}	0.1	-0.07	0.15	0.25

Table III-1 : Reported value of SHA for intrinsic (blue) and extrinsic (green) materials [11].

For laser induced ultrafast spin-current and the ISHE for SCC conversion, we typically use the Co/Pt structure as pictured on Figure III-11. Initially, an ultrashort laser pulse generates hot spin-polarized carriers by absorption from states below to states above the Fermi level of the ferromagnetic layer (Co). These hot spin current diffuses into the Pt (SOC material). The SCC occurs in the Pt at the interface with Co over a typical length scale given by the spin-diffusion length (discussed in section III.2.6) of the material (in the order of few nm). Penetrating the heavy metal, the ultrafast spin-current gives rise to an ultrafast transverse charge current by ISHE. This transient charge current is then responsible for the THz dipolar emission. The SHA that scales the efficiency of the conversion is thus of crucial importance in the choice of material. A benchmark of different materials used for spintronic THz generation are displayed on Figure III-12 where CoFeB (3nm) is used as a FM material along with a HM (3nm) composed of either, Cr, Pd, Ta, W, Ir, Pt:Mn and Pt. It is clear that the THz emission is the strongest in the case of Pt.

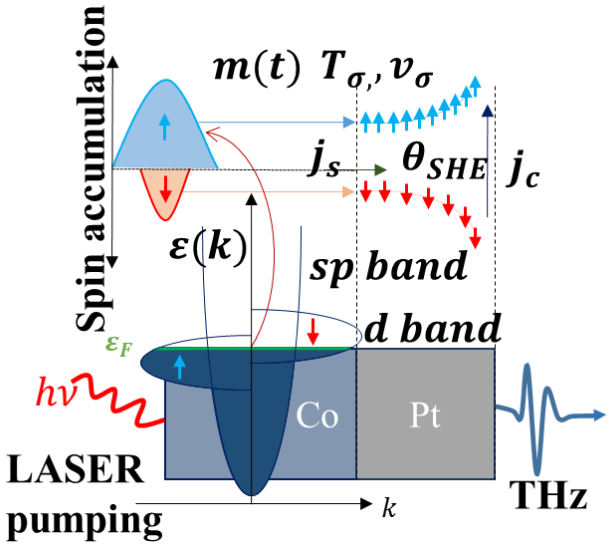

Figure III-11 Laser induced inverse spin Hall effect. A short laser pulse excites hot spin-polarized electrons in the 4-sp conduction band diffusing out after some energy loss into the adjacent layer where SCC occur close to the interface by ISHE process.

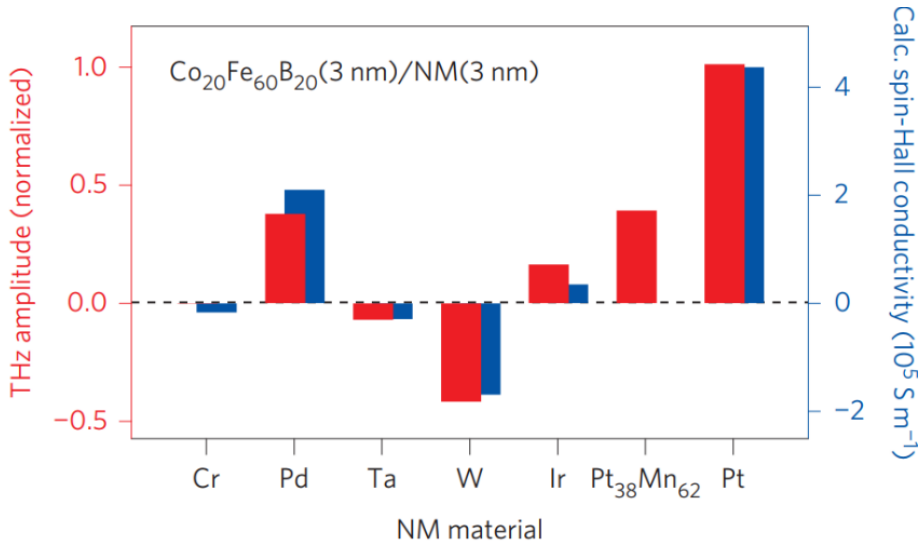

Figure III-12 : THz emission and spin hall conductivity benchmark of Cr, Pd, Ta, W, Ir, Pt/Mn and Pt for 3 nm $Co_{20}Fe_{60}B_{20}$ FM. from [35].

III.2.6 Spin memory loss and spin-diffusion length

Flowing electrons in a material may lose their spin polarization upon reaching impurities or phonons. According to [67], three scattering channels exist, by: i) magnetic impurities; ii) magnons; or iii) impurities with high spin-orbit coupling. This phenomenon is known as spin-flip events and may happened in the bulk of the material. The spin memory loss (SML) is a spin-flip event, however, specifically related to the interface between the FM and the HM [68], [69]. This is when incident electrons encounter interfacial electric fields owing to SOC induced by the inversion symmetry breaking of the interface and can be seen by Rashba fields (see sections III.3, IV.1).

Considering the case of the FM/HM heterostructure, when a polarized spin-current is generated in the FM and diffuses to the HM, a spin accumulation occurs in the HM. Its magnitude is determined by the equilibrium between the rates of spin injection and dissipation, where spin flip scattering represents the main dissipation source. It results a spin accumulation from the interface which decays exponentially across the thickness. The exponential behavior of the decay defines the spin diffusion length (l_{sf}). This length typically ranges from few nm for high SOC materials to few hundred nm for low SOC materials [36]. The spin diffusion length in metals is heavily dependent on impurities since they bring a source of spin flip probability. A mathematical description of the spin diffusion length is shown in equation (III-8) with $\overline{D}$ being the average diffusion constant of spin polarized

electrons given by $\bar{D} = v_f^2 \tau_{sf}$, where v_f is the Fermi velocity of carriers and τ_{sf} the spin relaxation time often noted spin-flip time.

$$l_{sf} = \sqrt{\bar{D}\tau_{sf}} \qquad (III\text{-}8)$$

$$m(x) = me^{-\frac{x}{l_{sf}}} \qquad (III\text{-}9)$$

A picture of the spin accumulation (m) over the thickness (x) of the heterostructure can be made using equation (III-9)[70]. At the interface, the spin accumulation is maximum and then decays exponentially over the spin diffusion length defined by the material. Another consideration is the interfacial SML between the FM and the HM layer as spin orbit and scattering effects may occur. These losses are represented on the Figure III-13 with the spin memory loss at the interface highlighted in purple that represents a real challenge for the optimization of THz sources [11]. Generally, bulk transport can be understood with a magnetoelectronic [71] (spin conductance) picture but when addressing interfacial transport quantum boundary conditions are required. This will be discussed in section III.4.5.

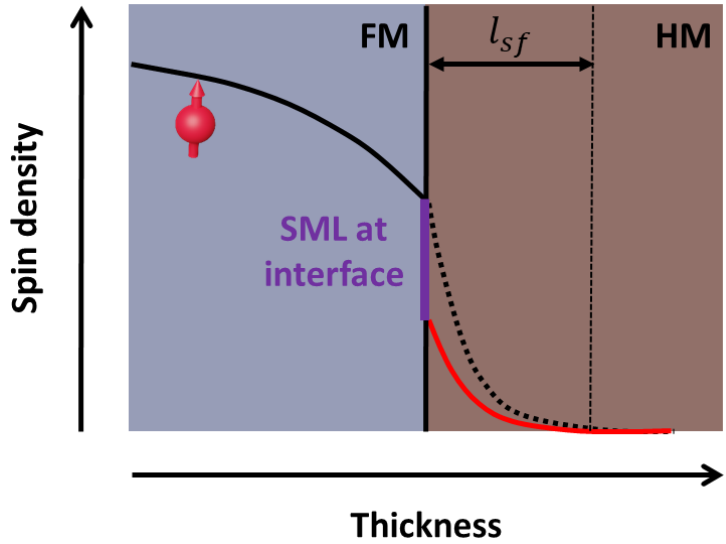

Figure III-13: Representation of typical spin accumulation and spin diffusion length in a FM/NM heterostructure. With the black dashed and red exponential decay being the spin density without and with interfacial spin memory loss.

III.2.7 State-of-the-art

A range of recent THz emission investigations have been demonstrated in FM/HM heterostructures, using engineered spintronic multilayers for optimal energy absorption of the exciting laser pulse [49], constructive interferences of ultrafast spin-currents in FMs with generated photoconductive carriers in a semiconductor switch [72], or stacks of active multilayers [73] to name a few. Currently, to our knowledge, the best performances are obtained by trilayers structures with two opposite SHA material placed on either side of a layer of CoFeB as FM material [74]. Co/Pt and Fe/Pt are also being extensively investigated for their spin-orbit torque (SOT) properties, where a flowing charge current can change the magnetization of the FM (Onsager effect in spin pumping), required for magnetic commutation functionalities. Progress in these materials is particularly focused on interface engineering for the optimization of the spin transmission [75]–[77]. This is to significantly reduce the interfacial spin memory loss (see sections III.2.6 and III.4.5) as shown in recent experiments [65], [78] and more recently via first-principles calculations [68], [79], [80]. The interested reader could find a very recent review detailing the current improvements regarding the THz emission of FM/HM in [1].

III.2.8 Experimental spin transport

In this section other metrics relevant to the THz emission will be discussed, as well as the means to experimentally extract them. This will be particularly relevant for the comparison with THz emission spectroscopy. The typical method to characterize SCC and ISHE is to extract spin transport parameters with ferromagnetic resonance spin-pumping (FMR-SP) (see Figure III-14) [81]. The ferromagnetic resonance is a phenomenon resulting from the resonant coupling of an electromagnetic wave with a magnetic field (FMR frequency). For FM materials resonant absorption of a microwave photon results in the precession of the magnetization (collective localized spins) known as the Larmor precession. This precession of localized spins leads to an out of equilibrium spin current. As the spin polarized electrons diffuse through the interface of the FM/HM heterostructure, ISHE occurs (as described above) in the HM, giving a direct mean to evaluate the conversion by measuring the SCC DC current.

Experimentally it consists in placing the sample into a strip line geometry for microwave injection (h_{rf}) (see Figure III-15) and applying a DC magnetic field (H_{dc}) from an

electromagnet. The resonance conditions are experimentally investigated by changing the DC magnetic field H_{dc} that drives the magnetization precession giving access to a direct measurement of the absorption of the microwave field at the resonance. To establish an analogy with optics, FMR-SP can be seen as a transmission measurement of h_{rf}. Typically, the FMR frequencies lies within the 6-10 GHz range. Figure III-14 gives a schematic representation of the FMR-SP technique and highlights that the out-of-equilibrium spin-polarized carriers remains within an energy range ε at the vicinity of the Fermi levelε_F ($\varepsilon \approx \varepsilon_F \pm \hbar\omega_{rf}$) leading to steady-state spin-current.

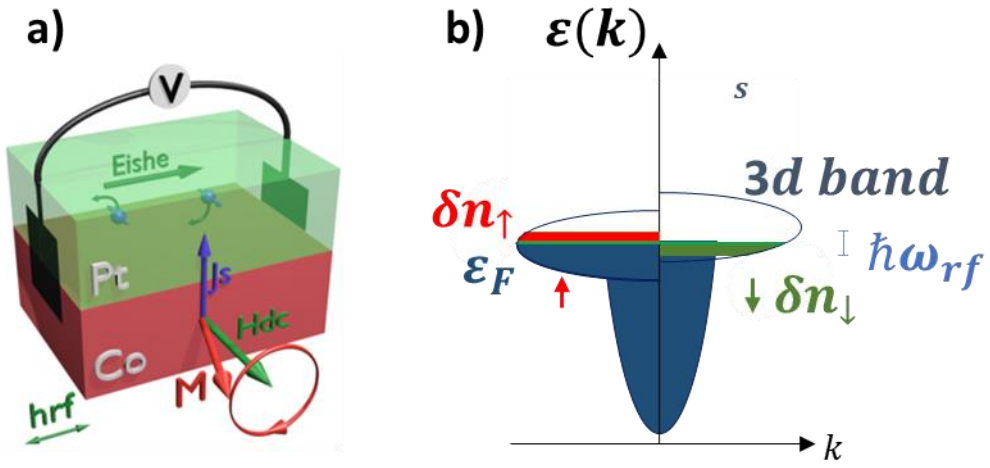

Figure III-14 a) spin-pumping (SP) experiment FMR-SP/ISHE. The radio-frequency magnetic field h_{rf} and the external applied dc magnetic field, H_{DC} are orthogonal in respect of the growth axis. The frequency of h_{rf} is fixed, H_{DC} is swept through the FMR resonance condition. The strength of h_{rf} is determined by measuring his magnitude giving the absorption for different values of H_{DC} . b) The out-of-equilibrium spin-density and spin-current are generated in the GHz regime in an energy range close to the Fermi level.

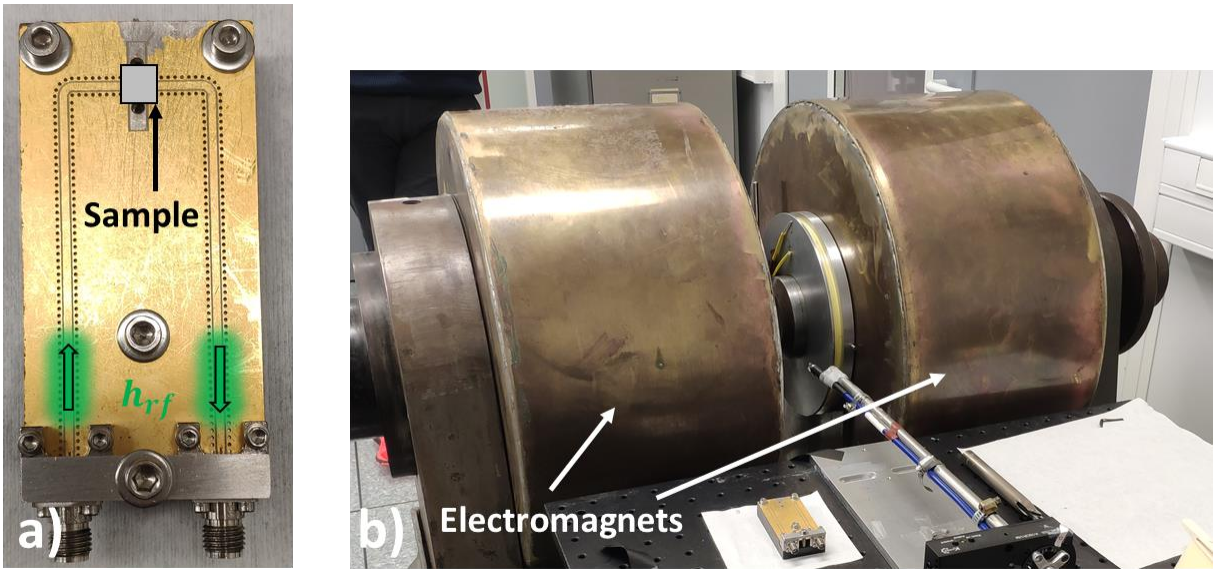

Figure III-15 : Photograph of a) the strip line used by CNRS-Thales to inject h_{rf} and b) the electromagnets used to generate H_{DC}, the strip line with the mounted sample is placed between the coils.

The Landau- Lifschitz-Gilbert equation (III-10) describes the magnetisation precession mechanism.

$$\frac{\delta M}{\delta t} = -\gamma M \times H_{eff} + \frac{\alpha}{M_s} M \times \frac{\delta M}{\delta t} \qquad (III\text{-}10)$$

With M representing the magnetization, γ the gyromagnetic ratio, M_s the saturation magnetization of the FM, H_{eff} the effective magnetic field and $\boldsymbol{\alpha}$ **the Gilbert damping** which describes the spin`s precession dynamic of relaxation (see Figure III-16). This damping is given by the $\frac{\alpha}{M_s} M \times \frac{\delta M}{\delta t}$ term. Physically H_{eff} is the magnetic field "felt" by the magnetization accounts for the DC magnetic field H_{DC}, the microwave magnetic field H_{rf} as well as anisotropic effects (H_{uni}) and demagnetisation. The resonance conditions are obtained by the Kittel formula (equation(III-11)).

$$f_0 = \frac{\gamma}{2\pi} \sqrt{H_{DC}(H_{DC} + \mu_0 M_{eff})} \qquad (III\text{-}11)$$

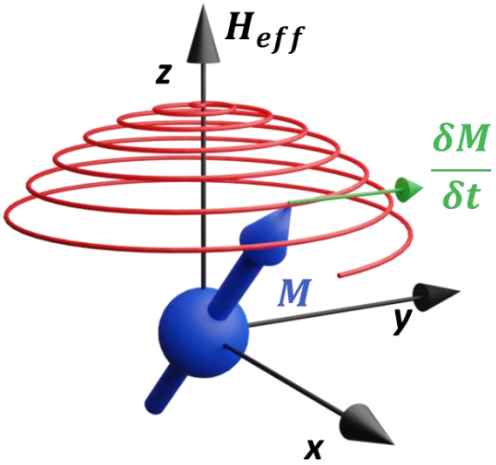

Figure III-16 : Representation of the magnetization dynamic of the precession. $\frac{\delta M}{\delta t}$ *representing the precession, the damping is given by the* $+\frac{\alpha}{M_s} M \times \frac{\delta M}{\delta t}$ *term of the Lifschitz-Gilbert equation.*

With $f_0$being the resonance frequency, and $M_{eff}$the effective saturation magnetization which can be extracted by fitting the FMR data by equation (III-11). The absorption of h_{rf} induced at the FMR is given by the imaginary part of the magnetic susceptibility $\chi``$[82] which is a Lorentzian. The linewidth of the absorption contains information regarding the relaxation of the magnetic system, albeit experimentally the access of the derivative value of $\chi``$ is often easier. The maximum of absorption is then obtained for a value of $\frac{\delta \chi``}{\delta H} = 0$ The linewidth of the derivative of the susceptibility is then defined by equation (III-12) (without accounting for inhomogeneous broadening). This can be seen on a typical FMR spectrum along with the ISHE voltage collected from the conversion of spin current generated by magnetization precession on Figure III-17. A polarity reversal of the voltage upon a flip of the magnetization is shown, which is an important feature of ISHE mechanism, more generally it denotes its magnetic origin.

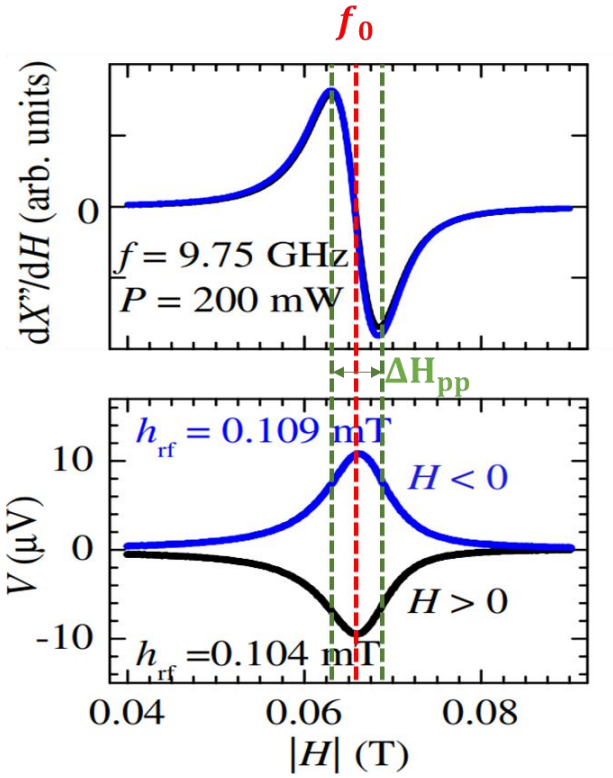

Figure III-17 : Typical FMR spectrum with the resonance frequency, the linewidth and the magnetization are highlighted. Adapted from [65], [83].

$$\Delta H_{pp} = \frac{2\pi f_0 \alpha}{\gamma \mu_0} \qquad (III\text{-}12)$$

By combining a FM with an adjacent layer where spin current can diffuse, one should expect an enhancement of the Gilbert damping from the spin current transfer between layers. This enhancement is seen in experiments by broadening of the linewidth of the FMR spectra, and (when comparing spectra from FM and FM/HM layers) can be determined by extracting the linear dependence and slope of the FMR linewidth vs. the rf-frequency. This linear regression given by equation (III-13) then provides with the Gilbert damping, accounting for the inhomogeneous broadening (H_0) that arises from disorder in samples.

$$\Delta H = \Delta H_0 + \Delta H_{pp} = \Delta H_0 + \frac{2\pi f_0 \alpha}{\gamma \mu_0} \qquad (III\text{-}13)$$

Figure III-18 shows a typical broadband FMR-SP measurement from [84] with the extraction of the effective magnetization saturation M_{eff} and the Gilbert damping fitted with respectively Kittel`s equation (III-11), and the linear regression (III-13).

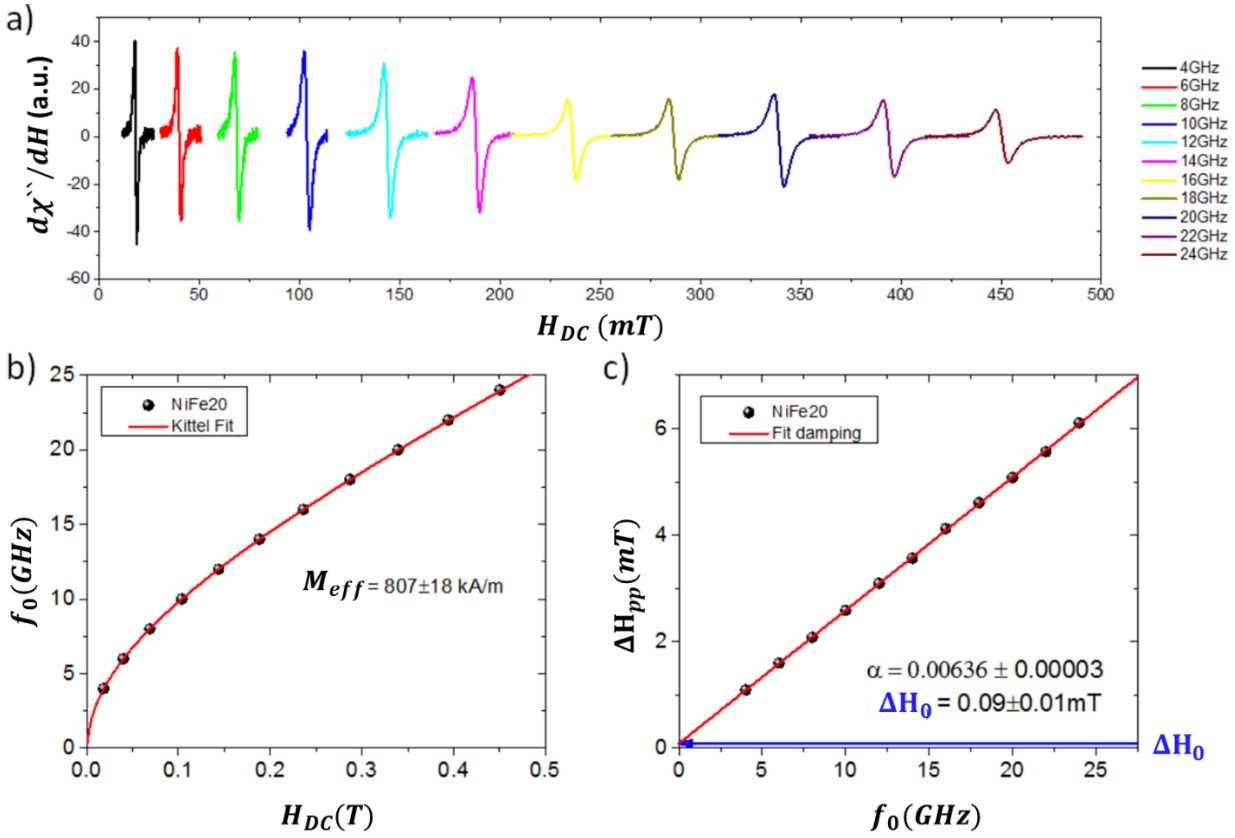

Figure III-18 : Broadband FMR-SP measurement of a NiFe/Pt sample. Adapted from [84] a) FMR-SP spectra for different h_{rf} frequencies and H_{DC} magnetic fields b)Resonance frequencies f_0 for different H_{DC} fitted with Kittel`s equation (III-11) c) Linewidth of the FMR-SP fitted with the linear regression (III-13) giving the Gilbert damping and the inhomogeneous broadening due to material disorder.

In the case of a FM/HM heterostructure the Gilbert damping is higher than for the bare FM, owing to the transfer of spin angular momentum from the FM to the HM [85]. The spin diffusion length in the HM can then be experimentally obtained by performing a thickness dependence on the FM layer and extracting the respective Gilbert damping. In such structures, the Gilbert damping has two components as $\alpha = \alpha_{intrinsic} + \alpha_{SP}$. Here $\alpha_{intrinsic}$ is the intrinsic contribution measured on a reference sample (bare FM) of the same quality (typically with layers of Al(2) and AlOx(3) providing specular reflection of the spin current at the Al(2)/AlOx(3) interface (the spin currents are not escaping the structure)). α_{SP} is the Gilbert damping induced by spin pumping.

From here, the effective spin-mixing conductance $g_{eff}^{\uparrow\downarrow}$ can be extracted, which describes the spin-current dissipation and experimentally the FMR-SP linewidth (α) enhancement (α_{SP}). This quantity is a metric of how much spin current flows towards the HM and includes interfacial losses such as SML or electronic reflections (discussed in section

III.4.5). The parameter α is generally related to $g_{eff}^{\uparrow\downarrow}$ by equation (III-14) with t_{FM} the thickness of the FM layer.

$$\alpha_{SP} = \alpha - \alpha_{intrinsic} = \frac{g\mu_B}{4\pi M_{eff} t_{FM}} g_{eff}^{\uparrow\downarrow} \qquad (III\text{-}14)$$

Further, the FM/HM interfacial electronic transparency can be quantified with the spin mixing conductance $g^{\uparrow\downarrow}$ describing how much of the angular momentum (spin current) is flowing from the FM to the HM [85]. This quantity does not account for interfacial loss or electronic reflections, and so $g^{\uparrow\downarrow} > g_{eff}^{\uparrow\downarrow}$. The spin mixing conductance $g^{\uparrow\downarrow}$ can be extracted with equation (III-15) with r_{sl} being the interfacial spin resistance corresponding to the ratio of the boundaries resistances. This parameter will be discussed in section III.4.5.

$$g_{eff}^{\uparrow\downarrow} = \frac{g^{\uparrow\downarrow}}{1 + g_0^{\uparrow\downarrow} r_{sl}} \qquad (III\text{-}15)$$

At interfaces (including FM/HM or FM/vacuum), electrons may either be transmitted or reflected due to a mismatch of spin subbands at the fermi level between the two materials [71], [86]–[88] (this will be discussed in section III.4.5). To illustrate this, Figure III-19 display the case of an incident spin current flowing from the FM towards the HM where at the interface a portion of the incident electrons can be reflected or transmitted. We also represented this phenomenon for the FM/vacuum interface in green but note that this happens only if the HM thickness is smaller than the spin diffusion length.

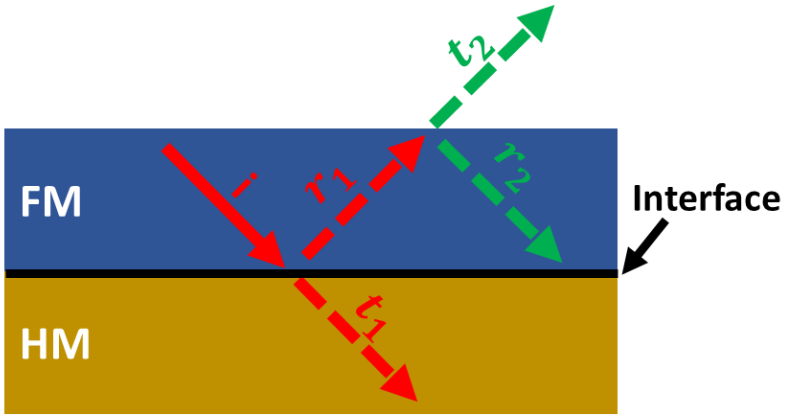

Figure III-19 : At interfaces incident spin currents can be either reflected or transmitted. Note that upon electronic reflection, the spin of reflected electrons is flipped.

The resulting spin current can be written as equation (III-16) [11] where θ_m stands then for the average precessing angle of the magnetization around the local effective static field H_{DC}, with the result that $sin^2(\theta_M)$ is proportional to the rf-power absorbed by the ferromagnetic material. It also shows that the charge current after spin-charge interconversion in the heavy metal is directly proportional to $P_{rf} \propto sin^2(\theta_m)$ [11].

$$j_s = \frac{2e^2}{\hbar} g_{eff}^{\uparrow\downarrow} \frac{\hbar 2\pi f_{rf}}{e} sin^2(\theta_m) \propto P_{rf} \qquad (III\text{-}16)$$

To summarize, FMR-SP for ISHE measurements represent a powerful tool to probe relevant spintronic transports parameters that are important in the optimisation of ultra-fast spintronic THz emitters (see section III.3.3). A disadvantage of FMR-SP measurements is that they are generally slow, as the full characterization of samples generally require a thickness variation on the HM, and contacts must be patterned on the sample. In stark contrast, THz emission TDS represents a fast and non-destructive mean to extract similar parameters.

III.2.9 THz emission TDS

The properties of spintronic heterostructures can also be investigated by THz emission TDS. The use of this method is becoming more common within the spintronic community to characterize such devices. Compared to FMR-SP, this approach requires no patterning of contacts and enables fast, contactless, and non-destructive access of the time dependent dynamics of spin transport under non equilibrium ultrafast spin-currents. It should be also noted the energy of the pump used to generate spin currents - in the case of FMR-SP this energy is in the vicinity of the Fermi level as a microwave wave is responsible for the magnetization precession, whereas for the TDS the fs Ti:Sa oscillator provides an excitation of energy of 1.5eV (~800nm) resulting in an ultrafast demagnetization. Our THz TDS system is based on the reflection geometry (presented in section I.2) to study the different types of materials. The PCS typically used for THz generation used in previous chapters is replaced by a spintronic based emitter (see Figure III-20). The emitters were placed on a mount with small magnetic field parallel (between 10 mT and 0.2 T) to the spin interface to align the magnetic moments of the FM (see Figure III-21). ZnTe or GaP crystals for detection are used, depending on the signal level and the spectrum bandwidth required. The modulation for the lock-in detection is done by mechanically chopping the THz beam at 6 kHz.

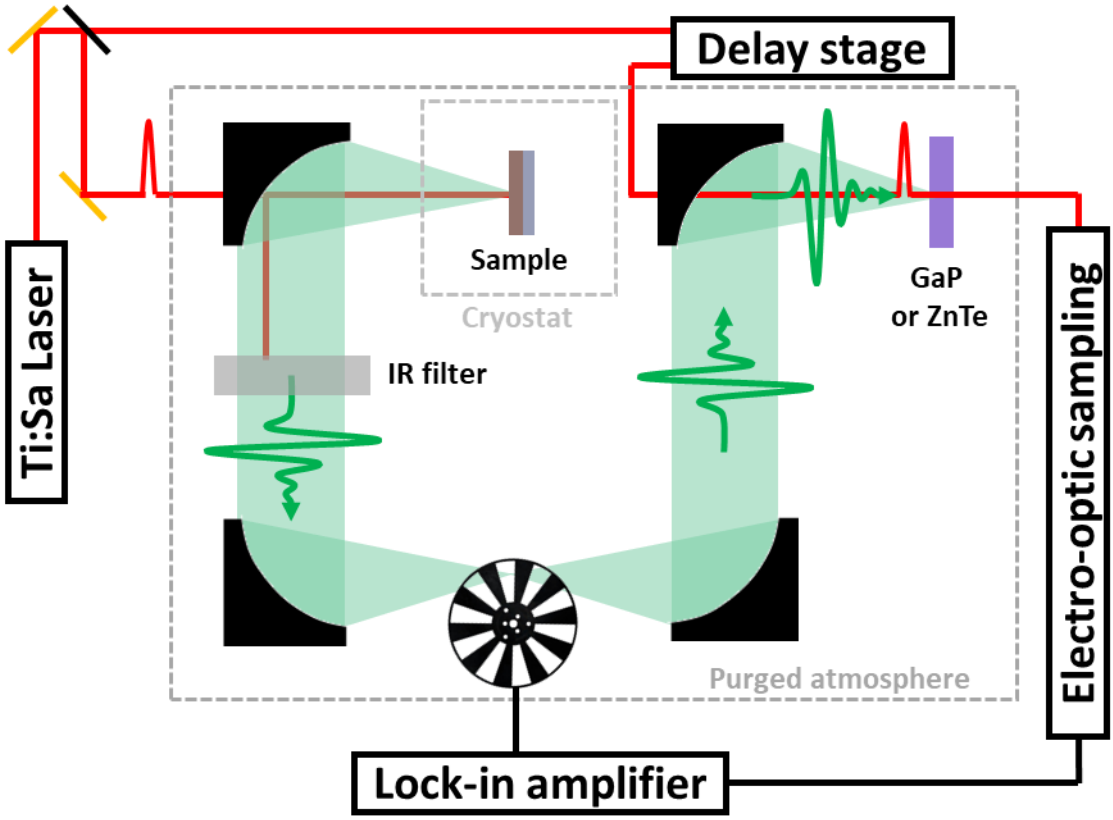

Figure III-20 THz time domain spectroscopy system used to investigate samples. The cryostat is used when low temperature is required. ZnTe and GaP non-linear crystals were used for EO detection.

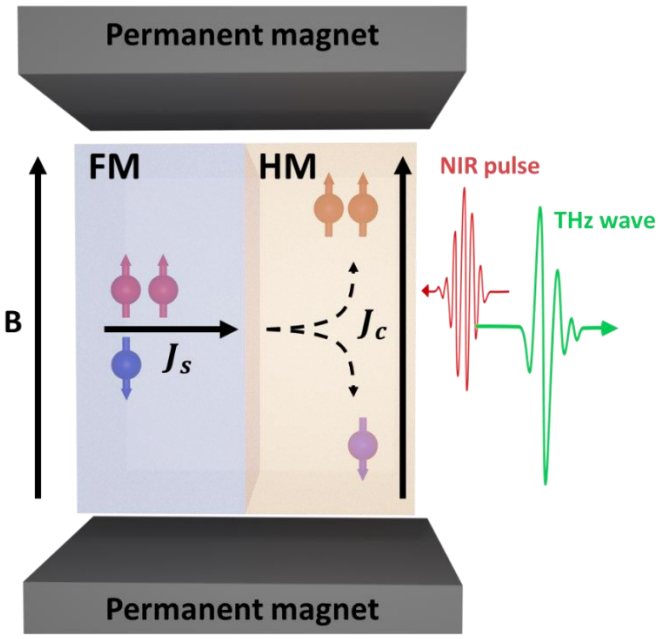

Figure III-21 : Representation of the sample inside the TDS system. The magnetic field comes from a permanent magnet, the NIR excites the FM through the HM, a spin current J_s is induced by the ultra-fast demagnetization of the FM, J_s diffuses into the HM, and, by ISHE, a charge current J_c arises and generates a THz pulse.

In the following sections, we will experimentally study the THz emission and transport properties by THz emission TDS and FMR-SP of several structures: i) glass/Co/Pt, and NiFe/Pt to investigate the effect of a different FM material; ii) NiFe/Au:W and Nife/Au:Ta will be compared to Co/Pt structures to study the effect of extrinsic spin Hall material with higher SHA than Pt for SCC conversion. Theoretical modelling of the Co/Pt structure highlighting the differences between FMR-SP and THz emission results will also be presented; iii) The Co/X/Pt system is investigated with X representing different thicknesses of Au or Ti to degrade the interface. On one hand, this will be analyzed to test the correlation between, interfaces transparency probed by THz TDS and FMR-SP, thus proving the relevance of ultrafast TDS as a powerful characterization tool adapted for spintronics. On another hand, we will assess, the interface of this Co/X/Pt system by modelling the induced SML with a quantum transport model, iv) Finally, we will present early data of optimized novel spintronic heterostructures capable of outperforming the THz emission of our Co/Pt reference.

III.3 Investigation of spintronic THz emitters

The spin transmission efficiency is generally determined by combining spin-pumping and ISHE experiments in the ferromagnetic resonance regime. The SCC efficiency scales with the spin transmission, characterized as the spin-mixing conductance of the considered interface [69], [78], [79]. The combination of FMR-SP and THz techniques thus offers the ability to analyse the anatomy of spin-current injection in HM based multilayers from which the spin transmission appears to be the key physical parameter [65] as discussed very recently in the analysis of THz emission from spintronic emitters [89], [90]. For this work, we chose to study the THz emission of different FM materials by comparing NiFe/Pt against the established Co/Pt as the demagnetization dynamics of their 3d bands are different. Owing to the giant SHA found in extrinsic AuTa [64] and AuW [66], it is expected that structures relying on these materials for SCC would result in enhanced THz emissions. To this end, we investigate the THz emission from NiFe/Au:W and Nife/Au:Ta structures. Note that the SHA considered in this experimental section, refers to published values from CNRS-Thales or their collaborators (precise measurement of the SHA requires complex angular FMR-SP measurements coupled with thickness dependence of the HM [91]).

III.3.1 Sample preparation and properties

For the first part of this study, the samples investigated are made of glass/Co(2)/Pt(4) and glass/NiFe(2)/Pt(4) 3d/5d transition-metal based bilayers where the numbers in parenthesis indicates the thickness in nm. The structures are grown by magnetron sputtering, with Co(2)/Pt(4) considered as our reference sample, as its THz emission is larger than that obtained with ZnTe or GaP crystals. A second series of 3d/5d transition metal samples are made of NiFe(2)/$AuW_{0.13}$ (4) and NiFe(2)/$AuTa_{0.05}$(4) structures deposited by co-sputtering (co-deposition) of the two pure materials. In (Co, or NiFe)/Pt devices, Pt is known to provide an intrinsic SHE mechanism with SHA typically lying in the range [0.05-0.2] [59]. On the other hand, Au:W as well as Au:Ta impurity alloys are known to promote an extrinsic side-jump SHE whose efficiency value may reach $\theta_{Au:W} = 0.15$ for AuW and $\theta_{Au:Ta} = 0.4$ [64] depending on the impurity content. For our sample, $AuW_{0.135}$ and $AuTa_{0.05}$, we obtain respectively $\theta_{Au:W} = 0.15$ and $\theta_{Au:Ta} = 0.25$ [64], [66]. These are larger than that for Pt. However these materials have a larger resistivity, $\rho_{AuW_{0.135}} = 90\ \mu\Omega.cm$ and $\rho_{AuTa_{0.05}} = 50\ \mu\Omega.cm$ compared to Pt ρ_{Pt}=17 μΩ.cm at room temperature (see Table III-2).

	Pt	$AuW_{0.135}$	$AuTa_{0.05}$
Resistivity (μΩ.cm)	17	90	50
Spin-Hall angle	0.1	0.15	0.25
l_{sf}(nm)	3	2[66]	4[64]

Table III-2 :Resistivity and SHA of Pt, AuW and AuTa. The color denotes the origin of the SHE: blue intrinsic and green extrinsic.

III.3.2 THz emission TDS on transition metal based spintronic emitters.

III.3.2.1 Co/Pt and NiFe/Pt

We first describe the THz emission from Co(2)/Pt(4), NiFe(2)/Pt(4) samples. Figure III-22 a) displays the typical THz-TDS signal on the Co(2)/Pt(4) sample at room temperature according to our experimental set-up described above under an excitation power of $200mW$. This signal highlights the relaxation, in the Pt, of the hot electron spin current (spin ↑ and spin

↓ populations) that is converted to a transient charge current by ISHE. This measured THz pulse corresponds to the derivative of the transient ultrafast charge current from SCC with $E_{THz} \propto \frac{\delta j_c(t)}{\delta t} \propto \theta_{Pt} \frac{\delta j_s}{\delta t}$ with θ_{Pt} scaling the SCC conversion.

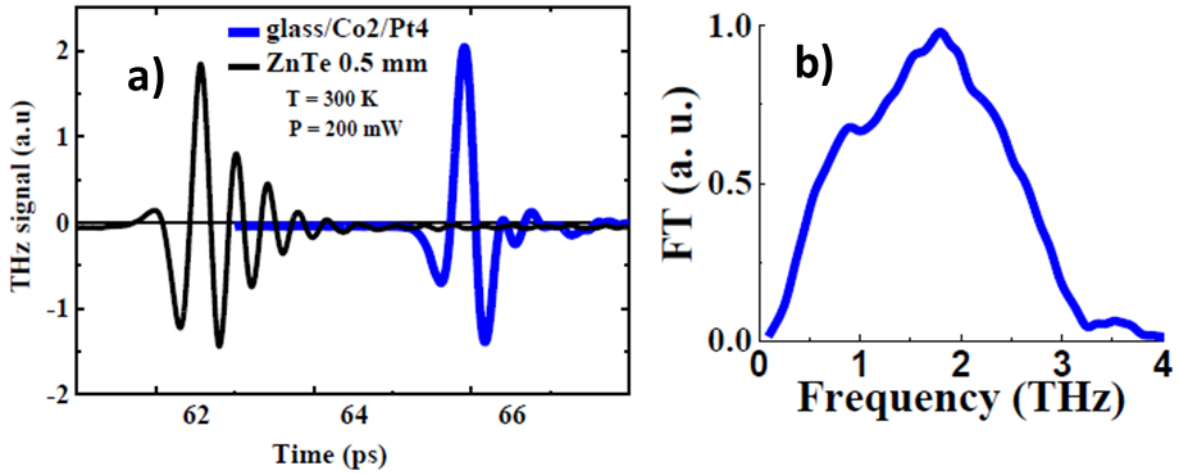

Figure III-22 : a) THz-TDS emission acquired at room temperature from Co(2)/Pt(4) (blue curve) and from a ZnTe crystal via optical rectification under a 100 fs laser pulse and power P = 200 mW excitation. b) Fourier transform (FT) of the Co(2)/Pt(4) signal showing emission up to 3 THz.

This THz emission is comparable to optical rectification in a 0.5 mm thick ZnTe crystal in the same experimental conditions. Figure III-22 b) shows the typical spectrum (Fourier Transform spectrum of the time domain signal) with emission up to ~ 3 THz, limited by the detection set-up and the width of the laser excitation pulses (100fs). Figure III-23 a) shows the typical angular dependence of the THz electric field when the applied magnetization is rotated in the film-plane over the full 0-360 degrees range. We can observe an almost perfect sine angular variation where the angle $\theta_M = 0$ corresponds to the direction of the ZnTe crystal principal axis (direction of the analyser). This exhibits a signal maximum when the magnetization is perpendicular to the detector axis or equivalently, that the electric field is perpendicular to the magnetization direction, according to the SHE/ISHE conversion rules. Figure III-16 b) demonstrates the variation of the peak electric field as a function of power and shows two important features. First, it demonstrates that the amplitude of the THz waveform increases almost linearly with the laser excitation power within the range 0-600 mW. This behaviour is analogue to the output transverse ISHE voltage vs. rf-power in FMR-spin pumping experiments and denotes no saturation effects. Second, the sign (or polarity) of the THz electric field can be reversed upon magnetization reversal. This feature is the signature of the THz magnetic origin and if often used to validate that the THz emission has a

spin origin. This originates from the symmetry rules of the ISHE where the direction of the carrier spin must be perpendicular to the direction of the spin polarized carrier flow to maximise the outgoing charge current (see equation (III-17) for ISHE and (III-18) for SHE by Onsager reciprocal effects).

$$J_c \propto \sigma \times j_s \qquad (III\text{-}17)$$

$$J_s \propto \sigma \times j_c \qquad (III\text{-}18)$$

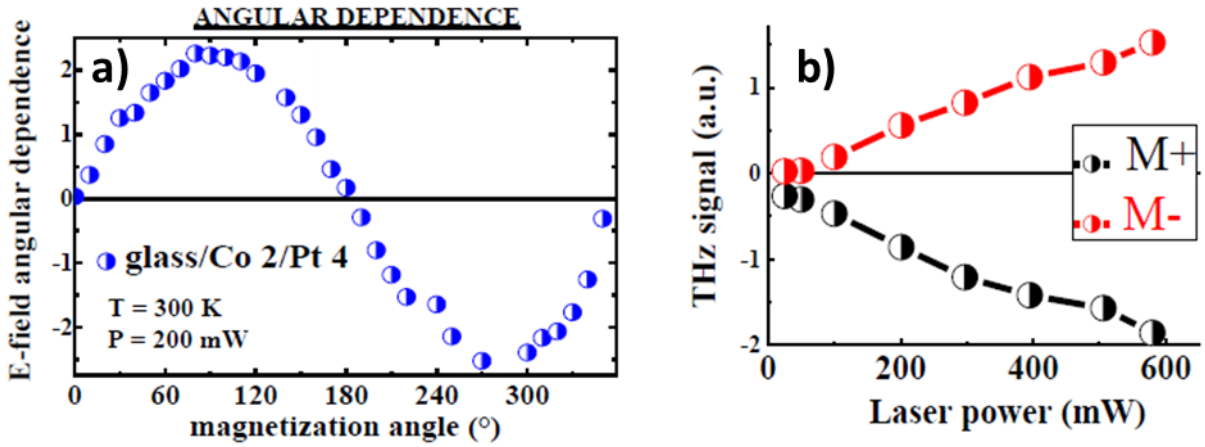

Figure III-23 : a) Characteristic Sine angular dependence of the THz-wave amplitude by varying the in-plane Co magnetization angle b) Amplitude of the maximum THz wave vs. laser power excitation in the 0-600 mW range and under two different opposite magnetic polarity.

The comparison of the THz-TDS time traces acquired between Co/Pt and NiFe/Pt samples at room temperature in the exact same excitation configuration are displayed on Figure III-24. We observe an almost identical response in both cases, in that sense, the HM seems to be the predominant factor. This will be experimentally supported in next section where alloys rules the SCC.

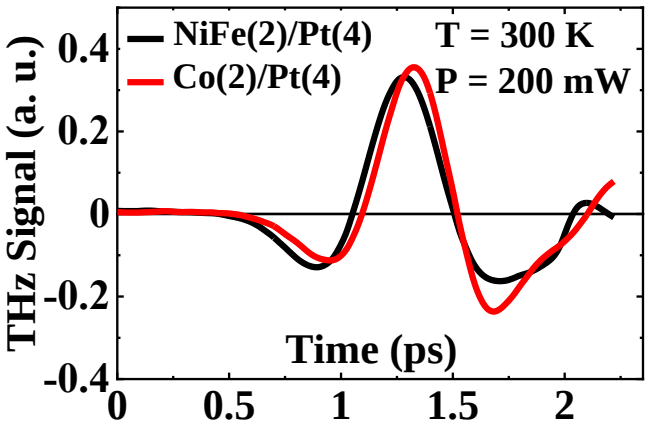

Figure III-24 : Comparison of the THz emission at room temperature (P = 200 mW) acquired on Co(2)/Pt(4) and NiFe(2)/Pt(4) samples showing similar features and equivalent amplitudes.

One can conclude that the optimized performances obtained with 3d/Pt systems clearly identify Co/Pt and NiFe/Pt as the one of the most relevant interfaces owing to their optimized spin-dependent electronic transmission. This will be supported theoretically by advanced ab-initio methods done by the University of Nebraska, and our collaborator CNRS-Thales in Section III.3.4.

III.3.2.2 NiFe/AuW and NiFe/AuTa

We emphasize here the impact of two linked physical parameters for NiFe/AuW and NiFe/AuTa systems on the THz emission, namely a larger spin Hall angle θ_{SHE} compared to our Co/Pt reference (respectively 0.15 for AuW and 0.25 for AuTa) but with also a larger alloying resistivity ρ due to scattering enhancement.

Figure III-25 a) and b) displays the typical THz temporal emission for each case (AuW and AuTa), showing the signature of hot spin current relaxation on the ultrafast time scales, but with a strong reduction in field by a factor 20 compared to Co/Pt or NiFe/Pt. This observation is surprising as an increase by a factor between 2 and 5 would be expected owing to the larger SHA in the Au-based alloy systems (see Table III-2). THz emission results are summarised on Figure III-26 for Co/Pt NiFe/Pt, NiFe/AuW and NiFe/Ta. As demonstrated below, the reasons for such a decrease are potentially twofold: i) the enhancement of the alloy resistivity strongly decreases the THz emission due to spin current relaxation effects and ii) a reduction of the spin-transmission at NiFe/Au interfaces compared to Co/Pt or NiFe/Pt, as revealed by FMR-spin-pumping experiments (see section III.3.3.3).

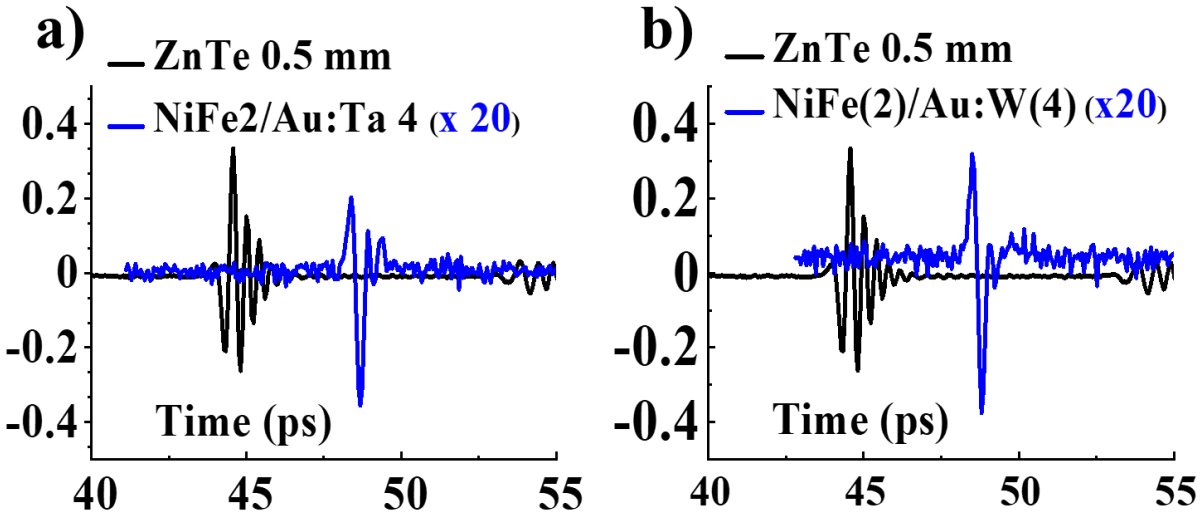

Figure III-25 : a) and b) Emission of NiFe/Au:(W,Ta) systems compared with ZnTe(110) crystal. Measurements taken at room temperature under a laser power P = 200mW.

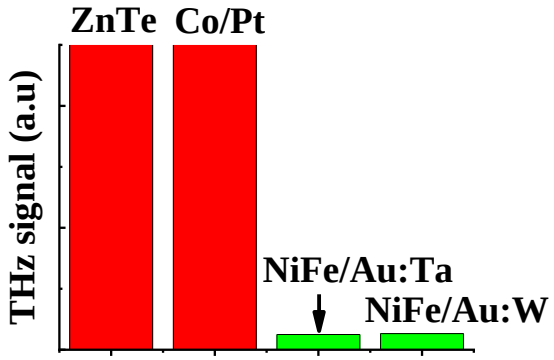

Figure III-26 : d) Peak-to-peak THz amplitude comparison between ZnTe(110) and spintronic-based emitters including the reference Co/Pt and NiFe/Au(W,Ta) systems.

III.3.3 Spin pumping and interface transparencies

The second type of experiment used to characterize this set of samples is the FMR-SP coupled to ISHE. This part has been carried out by our collaborator CNRS-THALES.

III.3.3.1 Sample preparation

For these experiments, a series of thicker ferromagnetic and spin-orbit based material samples has been prepared, respectively Co(15)/Pt(30), NiFe(15)/Pt(30) as well as NiFe(15)/$AuW_{0.135}$(30) and NiFe(15)/$AuTa_{0.05}$(30) grown by magnetron sputtering in a single deposition chamber on SiO_2-terminated Si wafers and in the exact same conditions as the ones prepared on glass for the THz emission experiments. A thicker ferromagnetic layer (15 nm) is

suitable to enhance to the FMR resonance, whereas the thicker SOC material is beneficial to avoid the electrical rectification contribution to the signal. Indeed, in spin-pumping experiments, the generation of a charge current in the Pt needs to avoid as much as possible the lateral expansion in the ferromagnet. Here, anisotropic magnetoresistance (a change of the material resistance with the applied he magnetic field) and the Planar Hall effect may give rise to a spurious electrical signal [83]. For the purpose of FMR-SP, contacts where patterned and samples were then cut in an elongated rectangular shape of typical dimensions $L \times W = 2.5 \times 0.5mm$.

III.3.3.2 The case of Co/Pt and NiFe/Pt

Combined FMR-SP and ISHE measurements were performed as presented above. The radio-frequency magnetic field h_{rf} is set along the long axis and the external applied DC magnetic field, H_{dc} along the width of the rectangle. The frequency of h_{rf} was fixed around 9.6-9.8 GHz whereas H_{DC} has been swept through the FMR resonance condition. At the resonance condition, the derivative of FMR energy loss ($\chi^{``}$) is acquired as the ISHE voltage is recorded across the long extremity of the sample (along the perpendicular direction to the H_{DC} field and magnetization). We have also performed a frequency dependence within the 3-24 GHz range of the FMR spectrum to extract the effective saturation magnetization M_{eff} as well as the Gilbert damping constant α. A refined analysis of the damping constant generally requires a reference sample free of spin-current dissipation at interfaces, (to prevent spin currents from escaping the structure). Ideally one would use a single Co layer capped by an oxidized Al capping layer.

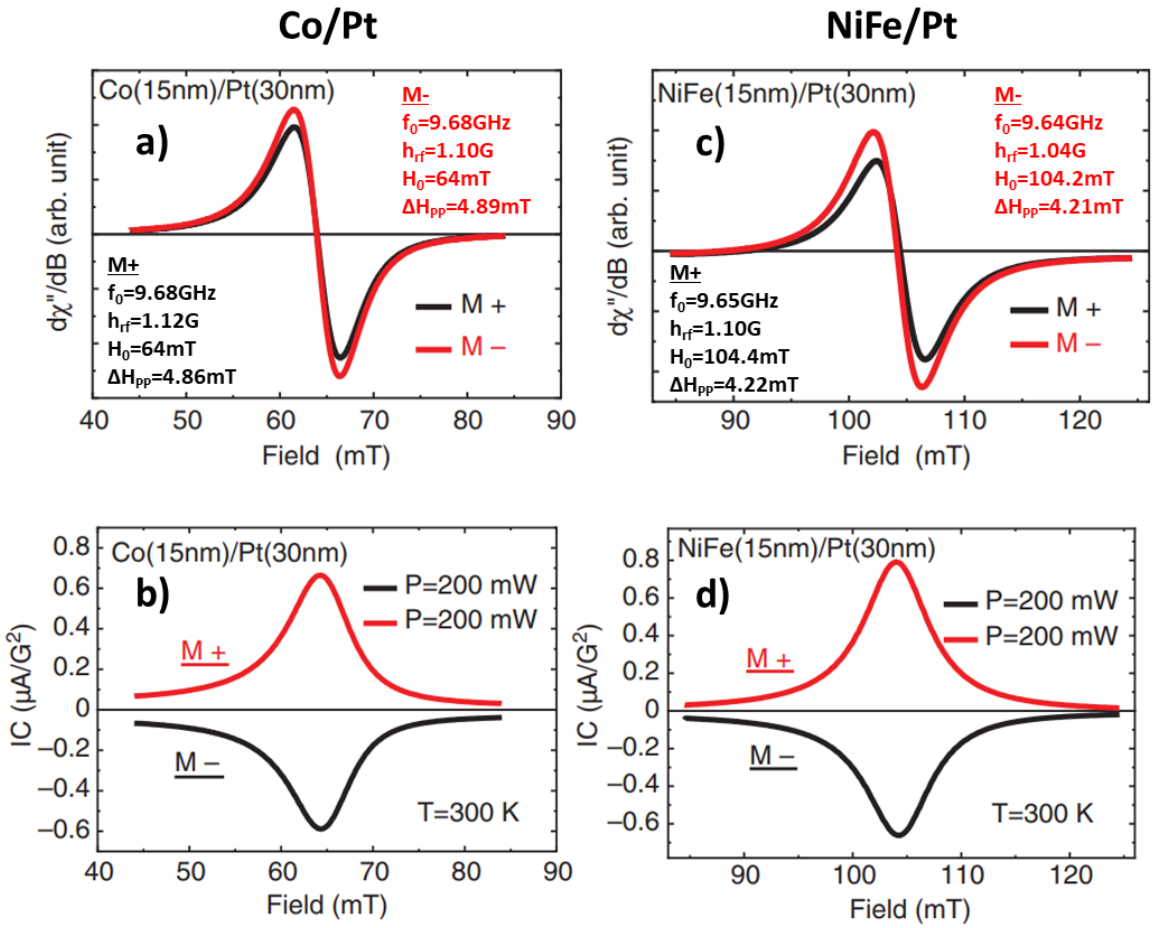

Figure III-27: Ferromagnetic resonance (FMR) acquired by the derivative of the absorption spectra for the respective positive (M+) and negative (M-) magnetization directions for (a) Co(15)/Pt(30) and (c) NiFe(15)/Pt(30) samples. The frequency of h_{rf} is fixed at f=9.68 GHz and the-field is about h_{rf} = 1.1 G. Corresponding DC ISHE current spectra acquired on Co(15)/Pt(30) and NiFe(15)/Pt(30), respectively (b) and (d), in the same experimental conditions and displaying the same quantitative and qualitative output signal.

We first focus on the results obtained on Co/Pt and NiFe/Pt characterized by a high electronic transparency and large THz emission. Figure III-27 a) and c) display the typical FMR spectra obtained by sweeping the dc in-plane magnetic field at the FMR, the frequency of h_{rf} is set at f = 9.68 GHz. These spectra corresponding to the field derivative of the FMR absorption $\frac{d\chi''}{dH_{dc}}$, are almost unchanged when the magnetization is reversed (H_{dc}) +M→-M. This behaviour is almost equivalent for Co or NiFe samples. The corresponding field dependence over the resulting transverse ISHE DC current I_C can be seen on Figure III-27 b) and d). This DC ISHE current level has been extracted by dividing the acquired transverse voltage by the device resistance ranging between 30 and 90 Ω. In both cases of Co and NiFe-based samples, the level of current lies in the range 0.6-0.7 $\mu A.G^{-2}$, which is a signature of a

very high carrier transmission efficiency and an efficient spin-charge interconversion in Pt. Moreover, when H_{DC} and consequently the magnetization is reversed by 180°, the sign of the ISHE current I_C changes polarity, as expected by the SCC rule for the ISHE. The result in the effective spin-mixing conductance at saturation for Co/Pt is estimated $g_{eff}^{\uparrow\downarrow} \approx 22 \times 10^{18} m^{-2}$. A similar value of $g_{eff}^{\uparrow\downarrow}$ for NiFe/Pt is found, in agreement with the work of Berger et al [78].

III.3.3.3 NiFe/AuW and NiFe/AuTa

We now turn to the NiFe/AuW and NiFe/AuTa sample series, displayed on Figure III-28 These samples are characterized by a high spin-conversion efficiency (larger SHA) but modest THz emissivity.

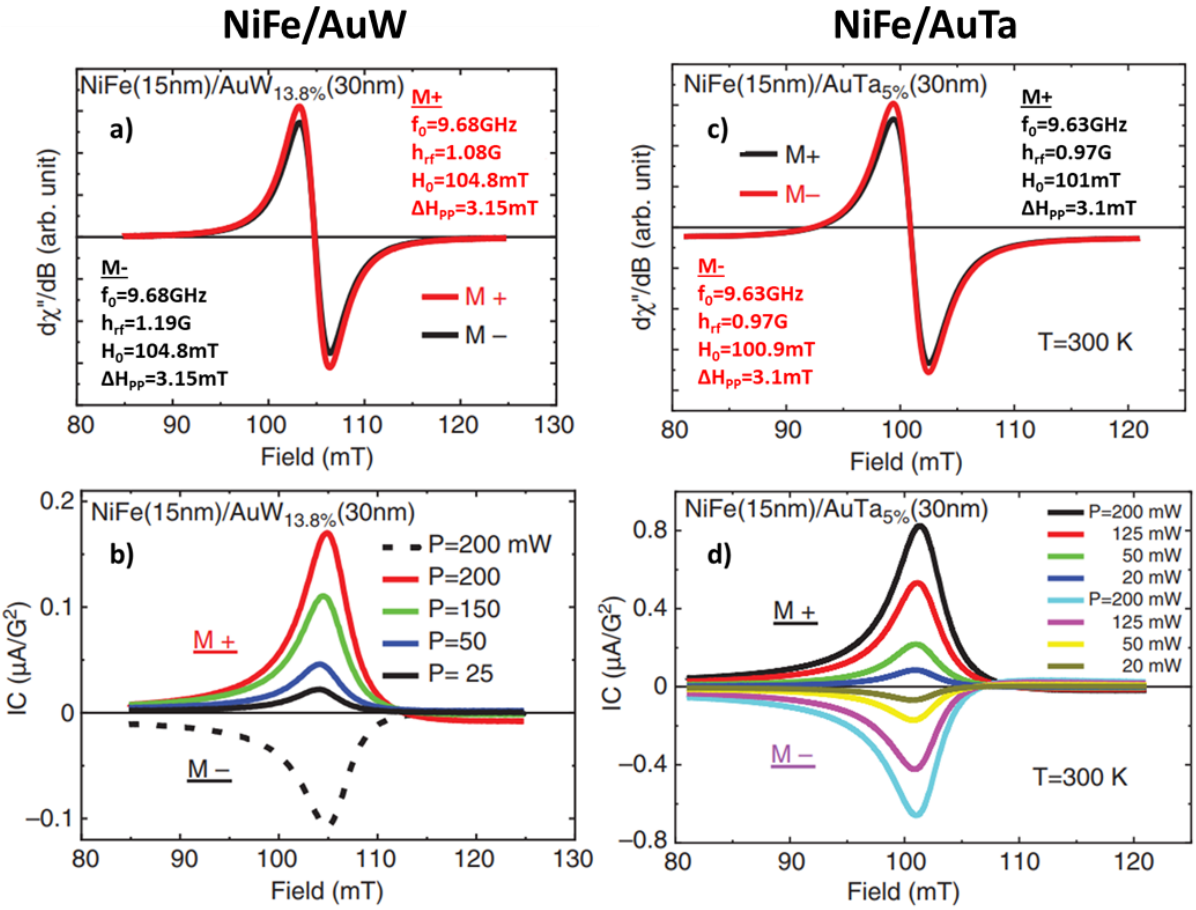

Figure III-28:a) Ferromagnetic resonance (FMR) acquired at room temperature by the derivative of the absorption spectra for positive (M+) and negative (M-) magnetization directions for NiFe(15)/AuW$_{0.135}$(30) a) and for NiFe(15)/AuTa$_{0.05}$(30) c). The frequency h_{rf} is fixed at f_0 = 9:68 GHz and the rf-field h_{rf}= 1.1 Gauss for panel a) and at f_0 = 9:63 GHz and the rf-field h_{rf}= 1 Gauss for panel c). The resonance field was found at 104.8 mT for NiFe/AuW and 101mT for NiFe/AuTa. The same absorption spectra is acquired when switching the

direction of the magnetization in both cases. b) and d) Inverse Spin Hall effect (ISHE) current spectra acquired in the same experimental conditions and for different rf-powers (from 20 mW to 200 mW). The sign inversion of the DC-current signal is representative of the ISHE effect. Note that the ISHE signal increases almost linearly with the rf-power injected.

The bare damping constant for NiFe was found to be $\alpha_{Intrinsic}^{NiFe} = (6.9 \pm 0.1) \times 10^{-3}$ originating from inhomogeneous broadening. This allows us to estimate the effective spin-mixing conductance $g_{eff}^{\uparrow\downarrow}$ for AuW and AuTa, respectively and thus the spin-current density j_s injected by FMR-SP. The effective spin mixing conductance is then extracted $g_{eff}^{\uparrow\downarrow} \approx 6 \times 10^{18} m^{-2}$ for AuW and $g_{eff}^{\uparrow\downarrow} \approx 4 \times 10^{18} m^{-2}$ for AuTa, considerably smaller than the Co/Pt and NiFe/Pt. A typical factor 5 in the electronic transmission differs between Co/Pt or NiFe/Pt and NiFe/Au based alloys in favor of Co/Pt.

However, one must note that in these spin-pumping experiments, a smaller value of $g_{eff}^{\uparrow\downarrow}$ does not necessarily implies a smaller value of the injected spin-current, owing to the larger precession angle of the magnetization ($\propto RF\ power$) for smaller spin-current dissipation in the HM at low electronic transparency. In the present case, a slightly larger spin-Hall charge current I_C extracted at resonance compared to Co/Pt or NiFe/Pt (see Figure III-27 and Figure III-28) systems can be understood as the result of a larger spin-Hall angle and larger precession angle despite an effective spin-mixing conductance reduced by a factor ~5. However, it appears that the THz emission properties are also highly dependent on the local resistivity r of the material, a larger resistivity being detrimental for the observation of an efficient THz signal. This is discussed further below.

	Co/Pt & NiFe/Pt	**NiFe/AuW**	**NiFe/AuTa**
HM ρ_{xx} (μΩ.cm)	17	90	50
$g_{eff}^{\uparrow\uparrow}(m^{-2})$	22×10^{18}	6×10^{18}	4×10^{18}
θ_{SHE} of HM	0.05	0.15	0.25
THz signal	1	1/20	1/20

Table III-3 :Comparison of FMR-SP and THz emissions of Co/Pt NiFe/Pt NiFe/Au:W and NiFe/Au:Ta

III.3.4 Numerical simulations

Theoretically linking spin transport to the THz emission characteristics has been done by CNRS-Thales by FDTD modelling and the University of Nebraska by Ab-inito calculations. This permits to estimate the transparency of the interface and to then model the THz temporal emission from the spin current parameters. This permits to understand the role of spin transmission that governs the physics of THz emission from ISHE based heterostructures.

III.3.4.1 Calculations of transparencies at Co/Pt interfaces

First-principles calculations giving the energy-dependence of the transmission coefficient were performed for a Co/Pt interface within the atomic sphere approximation in the Green's function-based tight-binding linear muffin-tin orbital (GF-LMTO) method [92], [93], treating exchange and correlation within the local-density approximation (LDA)[94]. The average transmission probability based on ballistic conductance of the Co/Pt bilayer calculated using the Landauer-Buttiker technique [86] for electrons incident from the Co side is given by equation (III-19).

$$\bar{T}^{\sigma}_{Co\to Pt} = \frac{1}{N^{\sigma}_{Co}} \sum_{n} T^{n}_{\sigma} = \frac{g_{\sigma}}{g^{Co}_{\sigma}} \qquad (III\text{-}19)$$

Where σ denotes the spin channel, N^{σ}_{Co} is the number of conducting channels in the Co, T^{n}_{σ} the transmission probability for one of these channels n, g_{σ} the conductance of the Co/Pt bilayer, and g^{Co}_{σ} the Sharvin conductance of the Co lead. More detailed information onto the formalism can be found in [11] and in the appendixes. From this formulism it is possible to extract the transmission of the spin channel ($\bar{T}^{Co\to Pt}_{\uparrow}$ majority or $\bar{T}^{Co\to Pt}_{\downarrow}$ minority) as a function of energy about the fermi level (Figure III-29).

The majority-spin transmission $\bar{T}^{Co\to Pt}_{\uparrow}$ is dominated by electrons from Co transmitting into the electron-like sheet in Pt. A high probability of transmission across the interface is shown over the entire energy window and shows little variation with energy. On the other hand, $\bar{T}^{Co\to Pt}_{\downarrow}$ decreases significantly in the 0.5–0.7 eV range and remains suppressed up to about 1.0 eV, where it quickly rises to almost 1, exceeding $\bar{T}^{Co\to Pt}_{\uparrow}$, corresponding to the

excitation range for THz emission. The drop around 0.6 eV is associated with the closure of the hole-like sheet in Pt (see Figure A 2 in appendixes), which decreases the transmission probability of the minority-spin states from Co. The rise at 1.0–1.2 eV is due to the closure of the similar hole-like minority spin sheets in Co, the electrons from which transmit poorly into Pt but contribute significantly to the Sharvin conductance of Co [11].

Figure III-29 a) shows that the Co/Pt (111) interface has this favourable spin filtering property in the energy window from 0 to 1.0 eV above the Fermi level, and especially in the 0.6–1.0 eV range, between the top of the 5d band of Pt and the top of the minority-spin 3d band of Co. Figure III-29 b) also shows the spin-resolved effective interfacial area-resistance product calculated according to Schep et al.[95]. This quantity represents the apparent spin-dependent resistance of the interface in the circuit under diffusive transport conditions. Although these conditions are not satisfied in THz emission devices, and transport of hot electrons brings its own complications, the spin-dependent effective resistance product can serve as an approximate indicator of the interfacial spin asymmetry, or spin filtering (noted as the γ parameter). Here, we also see that the Co/Pt (111) interface has a larger effective resistance in the minority-spin channel for energies in the 0.6–1.1 eV range, which is in the energy region of hot electrons generated by pulsed laser excitation, suggesting an additional "spin-filtering" effect and an enhancement of the spin-current by this interface.

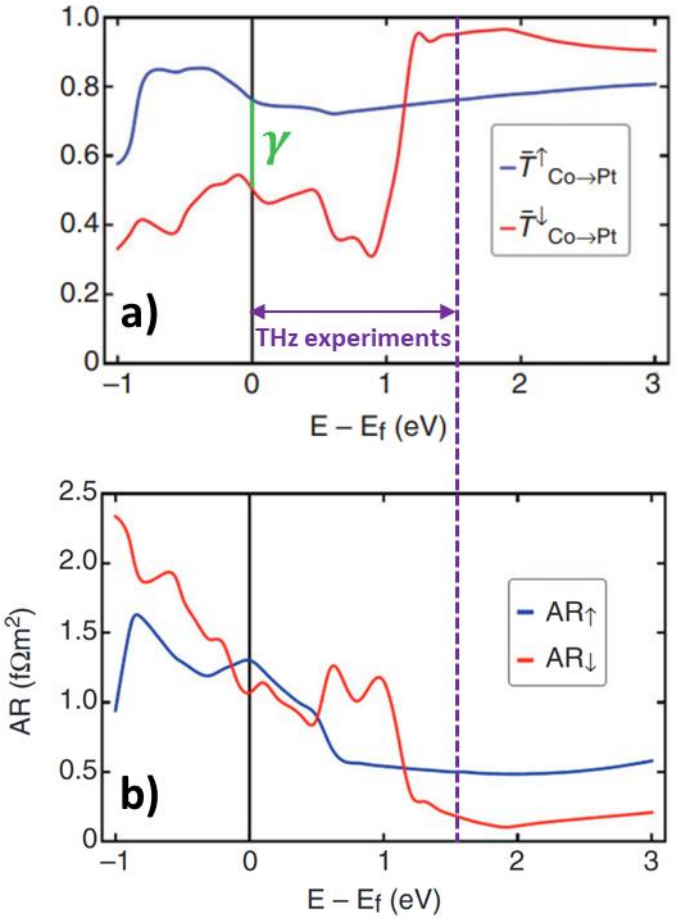

Figure III-29 : (a) Spin and energy-dependent average transmission probability for electrons incident from the Co side on the Co/Pt (111) interface [11]. Blue (red) lines: majority (minority)-spin electrons. (b) Density of states in bulk fcc Co and Pt with the lattice parameter used in the calculations for the interface. Blue (red) solid lines: majority-spin (minority-spin) electrons in fcc Co. Dotted lines: both spins in Pt c) Effective spin- and energy-dependent area-resistance product of the Co/Pt (111) interface. Blue (red) line: minority (majority) spin.

III.3.4.2 FDTD Simulations results

III.3.4.2.1 From spin-transport to THz wave

To further understand our temporal THz emission, finite-difference time-domain (FDTD) simulations were realized. The description of the time-domain dynamics of the hot electrons within spintronic multilayers excited by ultrashort laser pulses is performed in the frame of the Boltzmann transport theory and equations considering the different electronic diffusion and relaxation processes involved in the population evolution [11]. The dynamics of the system is performed using "wave-diffusion modelling", with the far-field THz electric field E_{THz} proportional to the time derivative of the local charge current j_c, and is derived from (III-20).

$$E_{THz} \propto \frac{\delta \int j_c d_z}{\delta t} = -\theta_{SHE} \int (\frac{J_s}{\tau} + \frac{\widetilde{D}}{\tau} \frac{\delta m(z,t)}{\delta z}) dz \qquad (III\text{-}20)$$

with the charge current proportional to the spin current by θ_{SHE} ($j_c \approx \theta_{SHE} \times j_s$). The integral $\int dz$ represents integral over the thickness of the HM layer corresponding to a summation over all the emitting dipole. $\widetilde{D}$ corresponds to the average spin diffusion coefficient and is linked, with the spin lifetime τ_{sf}, to the spin diffusion length by $l_{sf} = \sqrt{\widetilde{D}\tau_{sf}}$. The parameter m defines the spin accumulation as $m = n_\uparrow - n_\downarrow$ where $n_\uparrow$and $n_\downarrow$ refer to the spin up and down populations, and τ the carrier lifetime (10fs). Further details regarding the modelling and simulations can be found in [11]. Figure III-30 displays the simulated time dependence of the out-of-equilibrium spin accumulation or spin-density in the HM of the FM/HM interface (green plot). The corresponding ultrafast charge current J_c in the HM at the FM/HM interface (black plot) and the THz field in the time domain plotted in the far-field region. The shape of the pulse appears to be in close agreement with the experimental results to both Co(2)/Pt(4) and NiFe(2)/Pt(4) (see Figure III-30 b)).

In detail, the out-of-equilibrium spin-density (m(t), green plot on Figure III-30) experiences a maximum around 0.4 ps and a minimum in the vicinity of 0.6 ps, which is converted into an ultrafast charge current (black plot on Figure III-30) by ISHE. E_{THz} (red plot on Figure III-30) is directly considered as the derivative of the surface charge current J_c integrated within the HM volume. This results in two small positive lobes surrounding a large negative one. Regarding the spectral representation of the signal in the frequency domain (see Figure III-30 inset), it covers a wide and continuous band up to 5 THz and fits reasonably well in form with our experimental data on Co/Pt and NiFe/Pt, taking into account the spectral bandwidth limitation of our detector and experimental IR pulse duration.

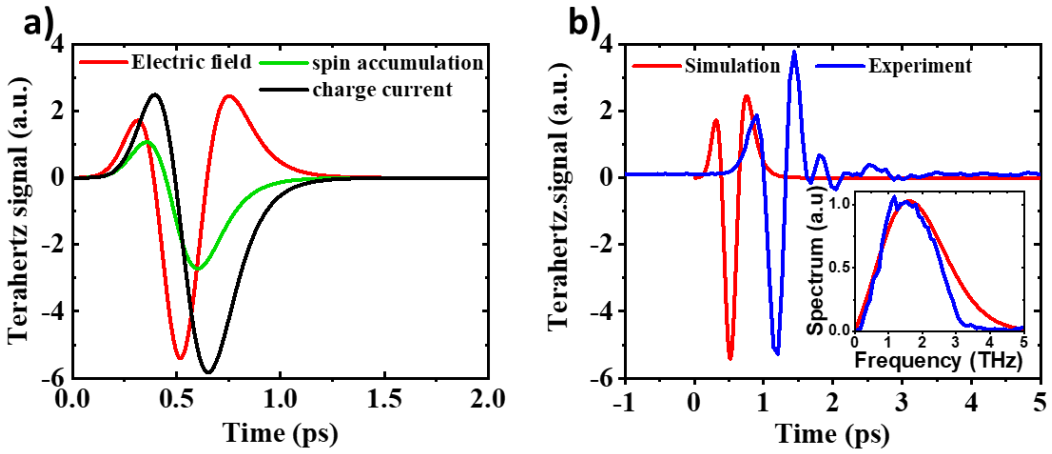

Figure III-30: Simulated time-domain evolution of the emitted electric field terahertz signal (gray) calculated for a Co(2)/Pt(4) structure excited by a 100-fs laser pulse in Co. The generated transient ultrafast surface charge current jc (blue) and out-of-equilibrium spin accumulation (m) (red) are plotted at the interface on the Pt side. The Fourier transform (FT) of the corresponding terahertz signal is given in the inset. The typical slope of the FT signal at low frequency is representative of a derivative signal. In those simulations, inner average transmission coefficient is $T^* = 0.2$.

III.3.4.2.2 Impact of the electronic transmission

In order to first explore the strong impact of the transmission T_σ and the observed differences in the Co/Pt, NiFe/Au:W and NiFe/Au:Ta, we consider the spin average transmission T^* and spin asymmetry γ, as extracted from the ab initio calculations following equation (III-21).

$$T_\sigma = \frac{T^*}{1 \pm \gamma} \Rightarrow T^* = \frac{1-\gamma^2}{2}(T_\uparrow + T_\downarrow) \qquad (III\text{-}21)$$

Figure III-31 displays the results of simulated THz spectrum considering a spin filtering $\gamma = +0.5$. We have investigated the influence of the transmission coefficient T^* at the FM/HM interface for the two different initial spin polarization excited with the optical pump, either (a) minority spin favourably pumped or (b) majority spin favourably pumped. For increasing T^* from 10^{-4} to 0.5, the spectra increase in amplitude by about the same proportion. The THz signal is the largest for $T^* = 0.5$ for both pumped spin polarization. Alongside the difference in their conductivity and in their spin-diffusion length, T^* explains the strong difference in the THz spectra between Co/Pt, NiFe/Pt on one side and NiFe/Au:W, NiFe/Au:Ta on the other side when the transmission for the latter decreases by roughly one

order of magnitude (from the FMR spin-pumping results). Another important feature is the difference in the signal amplitude depending on the spin polarization (majority or minority), showing about an one order of magnitude difference. This feature indicates a preferential spin-selection (filtering) at the interface, allowing a larger THz emission when the preferential pumped spin channel and transmitted spin are permitted.

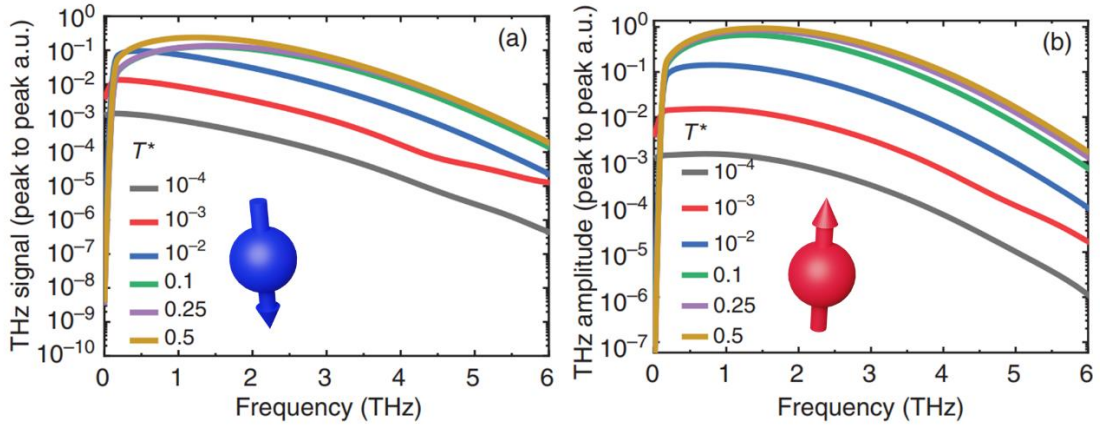

Figure III-31 : Simulation results showing the frequency-domain representation of the emitted THz electric field spectra in the case of Co(2)/Pt(4) excited by a short 100-fs laser pulse and calculated for different average transmission coefficient ranging from. 10^{-4} *to 0.5. The initial spin polarization was reversed from (a)* $S_{\uparrow} = 0.5$ $S_{\downarrow} = 1$ *to (b)* $S_{\uparrow} = 1$ $S_{\downarrow} = 0.5$ *while keeping fixed the interfacial spin-asymmetry coefficient* $\gamma = +0.5$ *through all the simulations. Those simulations emphasize the particular role of the so-called interfacial "spin-filtering" effect played by interfaces on the THz spectra.*

III.3.4.2.3 Effect of conductivity and spin-flip rate

The next step is the study of the impact of materials conductivity and spin flip rates over the THz electric field. The spin-accurate electron motion described by the Elliot-Yafet mechanism [96] links the momentum relaxation with the scattering time such that a probability of spin flip leading to a change in momentum is included in each scattering event. Into the formalism of the simulations, a parameter μ is used as a scaling parameter for momentum relaxation time and spin-flip time in HM and FM (τ_p, τ_{sf} respectively) as equation (III-22).

$$\mu = \frac{\tau_{sf}}{\tau_{sf}^0} = \frac{\tau_p}{\tau_p^0} \qquad (III\text{-}22)$$

With $\tau_{sf}^0$and τ_p^0 corresponding to their normal values. This parameter enables the change of mobility and spin-flip rate of different constituents while keeping the spin-orbit parameter (ϵ) constant as equation (III-23) (here the probability of spin flip is given by ϵ, and is constant).

$$\epsilon = \frac{\tau_p^0}{\tau_{sf}^0} = \frac{\tau_p}{\tau_{sf}} \qquad (III\text{-}23)$$

In Figure III-32, we have explored the effect on the THz spectra of the spin-flip rate in both HM and FM that may be probed in future experiments. One considers here the case of favourably minority spin pumped, $S_\uparrow = 0.5$ $S_\downarrow = 1$, and spin-filtering of majority spins ($\gamma = +0.5$). The typical evolution of THz spectra resulting from a pump pulse of 100 fs on varying $\mu = 0.1, 0.3, 1, 3, 10$ in the FM and HM are shown, respectively, in Figure III-32, for $T^* = 10^{-1}$ ((a) (c)) and $T^* = 10^{-3}$ ((b) (d)).

Two major conclusions can be raised. Concerning the dependence on μ_{FM}, and for $T^* = 10^{-1}$, one notes a significant increase in the THz signal while increasing ,μ_{FM}, from 0.1 to 10. However, this conclusion is exactly opposite in the case of a small transmission $T^* = 10^{-3}$, mainly because the spin-filtering acts in an opposite way to the optical pumping. This yields a reduction of the spin-population in FM and then in the THz spectra (Figure III-32 a) vs Figure III-32 b). Second, a slight increase in the signal due to spin-flip in FM makes the spin-filtering effect more efficient (due to the initial pumping of minority spins). On the other hand, increasing the μ_{HM} ratio increases the amplitude of the THz spectra (Figure III-32 c) and Figure III-32 d) owing to a higher mobility, leading to a larger spin-diffusion length and larger volume of charge relaxation in HM. In this sense, we demonstrate here the relationship by which E_{THz} follows the local HM conductivity (or HM mobility) in being proportional to μ_{HM}. This feature is clearly demonstrated in Figure III-32 c) and Figure III-32 d) for both T^* and also evidenced experimentally when comparing (Co,NiFe)/Pt- and NiFe/Au-based alloys. Note however that in Figure III-32 d), Co(2)/pt(4) and NiFe(2)/Au:W are highlighted by an

arrow that does not take into account their respective interfacial spin transmission but their conductivity (or mobility).

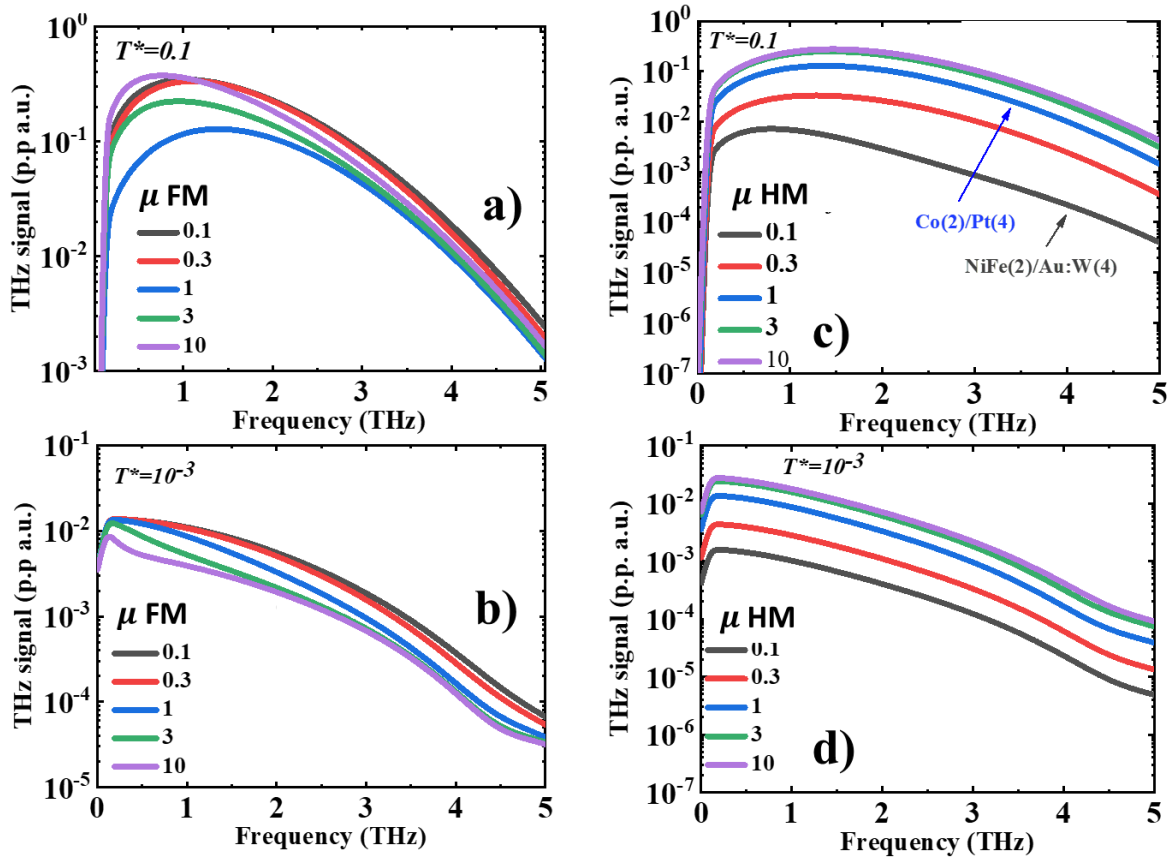

Figure III-32 : Frequency-domain representation of the emitted THz electric field spectra obtained for Co(2)/Pt(4) after a short 100-fs THz laser pulse and considering an initial spin polarization $S_{\uparrow} = 0.5$ $S_{\downarrow} = 1$. *The study focuses on the major role played by the spin dynamics timescale change for a fixed transmission parameter respectively equal to* $T^* = 10^{-1}1$ *[(a) and (c)] and* $T^* = 10^{-3}$ *[(b) and (d)]. Those calculations were performed with a spin scattering time* τ_{sf}^{FM} *[(a) and (b)] and for the heavy metal characterized by a spin scattering time* τ_{sf}^{HM} *[(c) and (d)]. The transformation coefficient a is swept in the [0.1-10] range. A constant* $\gamma = +0.5$ *value was kept for the whole simulations.*

In this section, we showed that the THz emission is larger by more than one order of magnitude in our reference Co/Pt, than provided by NiFe/AuW or NiFe/AuTa alloys that rely on extrinsic ISHE. The difference in the emission efficiency is partly explained from the difference in the resistivity. From our transport simulations, it indeed follows that the optimization of the THz emission requires a maximum spin-Hall angle θ_{SHE}, spin-diffusion length l_{sf}, and electronic transmission T^*, together with a reduced resistivity ρ_{xx}. Most importantly, it seems that the product $\Theta_{SHE}\ \sigma_{xx}\ l_{sf}\ T^*$ constitutes the correct figure of merit for SCC in the time-domain. This explains the difference observed between (Co,NiFe)/Pt- and

NiFe/Au:W- or NiFe/Au:Ta-based alloys with THz TDS acting as a probe of interface transparency. However, the impact of the resistivity is twofold, as it also reduces the THz signal by optical absorption. Thus, future models will take this phenomenon into account to converge towards optimal material parameters.

III.4 Interface transparency probed by THz TDS

Another part of my work onto the optimization of FM/HM based THz devices was the experimental correlation between spin-mixing conductance, spin memory loss and the intensity of the THz electric field. To our knowledge such correlation has never been established and should thus permit the development of more efficient spintronic THz sources. Previously we have seen that the optimal efficiency of such devices requires the engineering of metallic interfaces favouring a higher spin-current generation and interface transparency. In the literature, this point has been addressed by the insertion of transition metals or noble metals between Co and Pt. However, these frameworks do not cover the impact of the electronic transmission at interfaces, neither the discussion of the particular role of the interfacial spin-orbit fields originating from charge transfer and symmetry breaking [97]. Our approach is twofold: i) degrading the optimized Co/Pt interface by inserting another element ii) and comparing the THz emission of such structures with the FMR-SP resonances.

The insertion of an atomically thick interlayer of X=Ti, Au or $Au_{0.85}W_{0.15}$ modifies the ability of the interface to generate spin currents. This property acts, on the same footing, on the emission of electromagnetic radiation as well as the Gilbert damping of the multilayer. Here we define the average spin conductance $(g^{\uparrow} + g^{\downarrow})/2$ that characterizes the ultrafast currents in platinum (equivalent to $g^{\uparrow\downarrow}$ in FMR-SP at $\pm$ 10%, this change in notation accounts for the different spin orientation at the interface of optically excited vs FMR-SP) whereas the effective spin conductance $g_{eff}^{\uparrow\downarrow}$ describes the spin current dissipation (damping torque) in the ferromagnetic material and been addressed above. These two quantities would be proportional to each other if the spin flow was conserved at the interface [71]. In reality, strong spin-orbit assisted scattering processes generate a sink of angular momentum and limit the spin flow that can propagate into platinum [65], [78], [97], [98].To study the impact of those parameters, we choose inter-layer materials with quite different properties - Ti is chemically reactive and has small SOC, whereas Au and $Au_{0.85}W_{0.15}$ are less chemically reactive and host a larger SOC (especially the AuW alloy).

III.4.1 Considerations

First, we must consider few hypotheses to connect the average spin conductance to the emitted THz radiation for the case of a Co/X/Pt structure. In the thin film limit, the THz electric field of a plane wave at the surface of the sample, writes as equation (III-24). This expression links the THz electric field generated to the charge current density via an effective impedance Z given by equation (III-25) [35], [50], [51].

$$\vec{E}_{THz}(\omega) = eZ\int J_c(\omega, z)dz \qquad (III\text{-}24)$$

$$Z = \frac{Z_0}{1 + n + Z_0 \int \sigma(z)dz} \qquad (III\text{-}25)$$

Where n is the refractive index of the substrate, z is the coordinate perpendicular to the interface Z_0 the impedance of vacuum with $Z_0 = 377\Omega$, and $\int \sigma(z)dz$ the local conductivity integrated over the total thickness of the multi-layer. This is important as it enables to deconvolute the impact of the optical absorption (due to the film thickness) on the THz signal from other effects. As explained above for FM/HM systems, the charge current arises from platinum via ISHE, and can be written as equation (III-26) where $\vec{e}_n$ represents a unitary vector normal to the interface (and to the magnetization direction) and $\vec{e}_s$is the polarization direction of the spin current. The interface is set at 0 such that $j_s(0_-)$ represents the magnitude of spin current density generated in the ferromagnet, penetrating into the heavy metal, and thus responsible for the charge current oscillations at the platinum side of the interface.

$$\int_{0_+}^{d} \vec{j}_c(z) = J_s(0_+)(\vec{e}_n \times \vec{e}_s) l_{sf}^{HM} \times tanh\frac{d_{HM}}{2l_{sf}^{HM}} \times \theta_{SHE} \qquad (III\text{-}26)$$

Emission over an ultrabroad spectral range [35], [99], and theoretical modelling [90], [99], [100] show that the spin current evolves on an ultra-short timescale comparable to the energy and momentum relaxation of hot electrons. The ultrafast generation of a spin accumulation on the ferromagnetic side leads to a longitudinal component whereas the spin accumulation on the Pt side induces a transverse component by the ISHE. The resulting spin current corresponds then to (III-27).

$$\vec{J}_s = \frac{\hbar}{4\pi}\left(\frac{g^{\uparrow}+g^{\downarrow}}{2}\langle\frac{\delta_t M}{M}\hat{m}\rangle + g^{\uparrow\downarrow}\ \langle\hat{m}\times\delta_t\hat{m}\rangle\right) \quad (III\text{-}27)$$

In equation (III-27) $\hat{m}$ is the local magnetization, $g^{\uparrow}(g^{\downarrow})$ is the spin conductance parallel (antiparallel) to the magnetization and $g^{\uparrow\downarrow}$ is the spin mixing conductance. The longitudinal component is proportional to $(g^{\uparrow}+g^{\uparrow})/2$ and to the relative demagnetization $(\delta_t M)/M$. This term is driven by the quasi-ballistic transport of highly excited electrons from the Cobalt to Platinum and it represents the dominant contribution in the case of the spin current that is generated by ultrafast laser pulse [90]. Accordingly, the THz emission from Co/Pt is many orders of magnitude more intense [35] than the one observed from an interface where the longitudinal component is inactive [99]. Owing to the quasi-ballistic nature of the injection, the spin current arising from the spin accumulation takes place on a length scale of 1.4 nm[50], [51], [99]. Consequently, the strength of the emitted THz radiation scales with the energy density injected by the pump pulse as equation (III-28).

$$\left|\frac{\delta_t M}{M}\right| \propto \frac{A_B F_I}{d + d_{Pt} + d_{Co}} \quad (III\text{-}28)$$

where A_B is the absorbed fraction of pump pulse in the multilayer, F_I is the incident fluence of the pump pulse, d_{Pt} is the thickness of platinum layer, d_{Co} is the thickness of cobalt layer, d is the thickness of the X = Ti, Au or $Au_{0:85}W_{0:15}$ layer.

III.4.2 Sample preparation

For THz emission experiments we have prepared Co/X(d)/Pt trilayers on glass and highly resistive Si(111) substrates by sputtering deposition at room temperature with standard experimental conditions. The $Au_{0:85}W_{0:15}$ material has been obtained via the evaporation of a rod containing 85% of gold and15% of tungsten. The thickness d of the interlayer is typically varied between 0 and 2 nm. Within this range of d, the absorbed fraction of pump pulse in the multilayer (A_B) coefficient can be considered constant [35]. Moreover, the incident laser fluence F_I has been kept fixed and stable during the experiment.

For FMR-SP Samples made with 5 nm of Pt and thicker Co films (15nm) were deposited on highly resistive Si/SiO2(111) substrates. As explained above, the thicker ferromagnetic layer provides a clearer FMP-SP resonance spectrum than a 2nm layer.

III.4.3 Emission TDS of Co/X/Pt

The TDS setup used for this experiment is the same as described previously. Figure III-33A) displays a set of THz traces emitted from Co/$Au_{0:85}W_{0:15}$(d)/Pt multilayers with different values of the $Au_{0:85}W_{0:15}$ thickness d. The THz traces recorded for different values of d hold nearly identical waveforms. We assume that spin fluctuations, spin mixing conductance and spin-Hall-angle have negligible frequency dependence within the bandwidth of the detected THz. As observed experimentally, the drop of THz signal as a function of d is mainly due to a decreasing spin-mixing-conductance. The latter is related to the detection of the THz field via Equations (III-25)(III-26)(III-27)(III-28). By solving for the spin conductance, we obtain a normalized spin current density in the platinum layer.

$$\eta(d) = \frac{g^{\uparrow}(d) + g^{\downarrow}(d)}{g^{\uparrow}(0) + g^{\downarrow}(0)} = \frac{E_{THz}(d)}{E_{THz}(0)} \frac{Z(0)}{Z(d)} \frac{d + d_{Pt} + d_{Co}}{d_{Pt} + d_{Co}} \qquad (III\text{-}29)$$

Where the impedance $Z(d)$ has been calculated by assuming the THz conductivity in thin films reported in [50], [51], [101], $\sigma_{Co} = 3 \times 10^{6} S/m$, $\sigma_{Pt} = 4 \times 10^{6} S/m$, $\sigma_{Au} = 4 \times 10^{6} S/m$, $\sigma_{AuW} = 1.2 \times 10^{6} S/m$ and $\sigma_{Ti} = 0.5 \times 10^{6} S/m$. Differences of these conductivities with respect to bulk values are due to strong charge scattering at the landscape of the interface and to the formation of small grains [101]. As a matter of fact, the factor $Z(0)/Z(d)$ remains close to unity, owing to the fact that metallic interlayers with nanometric thickness have small parallel conductivity.

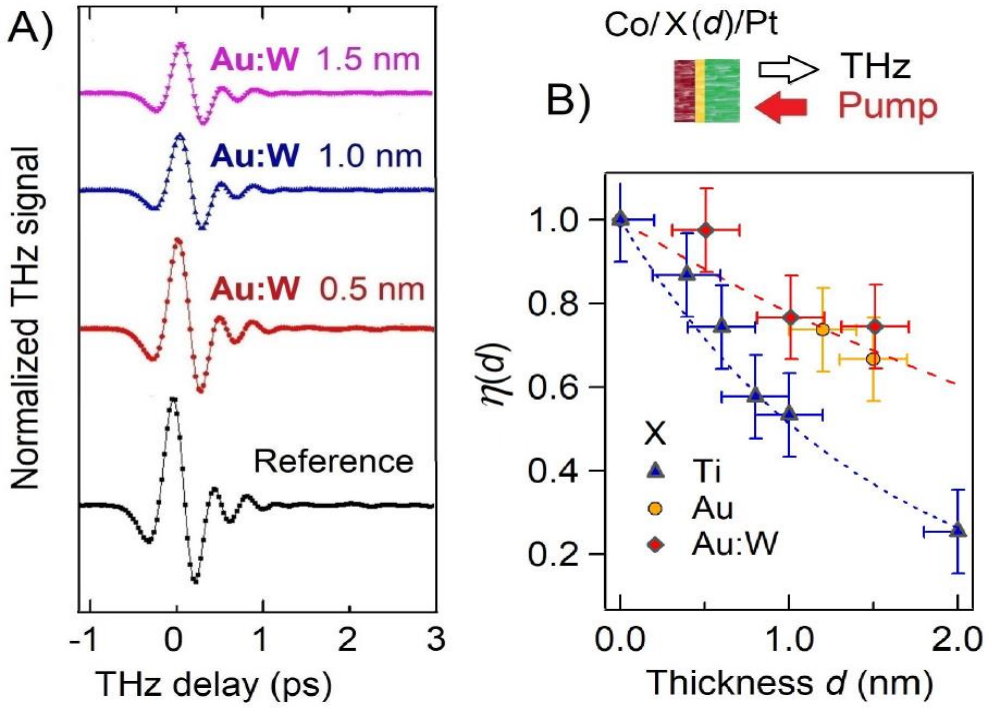

Figure III-33 : A) THz waveforms emitted by a set of different trilayers Co/$Au_{0.85}W_{0.15}$ (d)/Pt. B) Spin current generated in Co/Ti(d)/Pt, Co/Au(d)/Pt and Co/$Au_{0.85}W_{0.15}$(d)/Pt trilayers of different thickness. The Co and Pt layer have fixed thickness of 2 nm and 5 nm, respectively. The thickness d of the X=Ti, Co/$Au_{0.85}W_{0.15}$ layer is instead varied between 0 nm and 2 nm. The parameter η(d) has been extracted from the THz signal via Eqn.(III-29) and can be considered as a normalized spin current density in the platinum layer.

The parameter $\eta(d)$ of equation (III-29) reflects the relative reduction of the spin-injection efficiency in Pt if an interlayer of thickness d is grown between Co and Pt. As shown in Figure III-33 B), $\eta(d)$ follows nearly an exponential decay $exp(-\frac{d}{l_x})$, with characteristic length $l_{Au} = 4\,nm$ for $Au_{0.85}W_{0.15}$ and $l_{Ti} = 1.5\,nm$ for Ti. Apparently, Ti affects the spin conductance much more effectively than Au or $Au_{0.85}W_{0.15}$ do. Recent experiments have shown that a sub-monolayer of Ti can indeed substantially modify the spin-transfer torque of the CoFeB/Pt [102] and Co/Pt [77] interfaces. The insertion of the chemically reactive Ti alters the spin dependent transmission/reflection probabilities that favour the transport of one spin flavour with respect to the other (spin-filtering as discussed earlier). Furthermore, the surface passivation by Ti atoms may modify the spin-flip scattering potential at the interface (electronic interfacial reflections/transmission due to the offset of work functions as introduced in section III.2.8). Although the microscopic mechanisms leading to the large reduction of spin conductance is still debated, a systematic investigation of spin transfer torque with different transition metals concluded that the d-orbital filling has a stronger influence on charge-to-spin conversion than the atomic number [103]. Our measurements

corroborate this finding by showing that the passivation of Co/Pt interface is more effective in the case of a transition metal with incomplete 3*d* shell like titanium than in the case of an alloy with larger atomic number but closed 5*d* shell like Au. Moreover, the larger spin-orbit interaction of W in the $Au_{0:85}W_{0:15}$ does not seem to make any appreciable difference with respect to pure gold.

III.4.4 FMR-SP of Co/X/Pt

Next, we discuss the effective spin mixing conductance measured by FMR-SP. Figure III-34 A) displays the differential susceptibility of the Co/Pt bilayer as a function of the external magnetic field H_{DC}. Curves of different colors stand for increasing frequency of the radiofrequency magnetic field h_{rf}. We show in Fig. Figure III-34 B) the resonance frequency f_0 as a function of H_{DC} for the multilayers Co/$Au_{0:85}W_{0:15}$(*d*)/Pt.

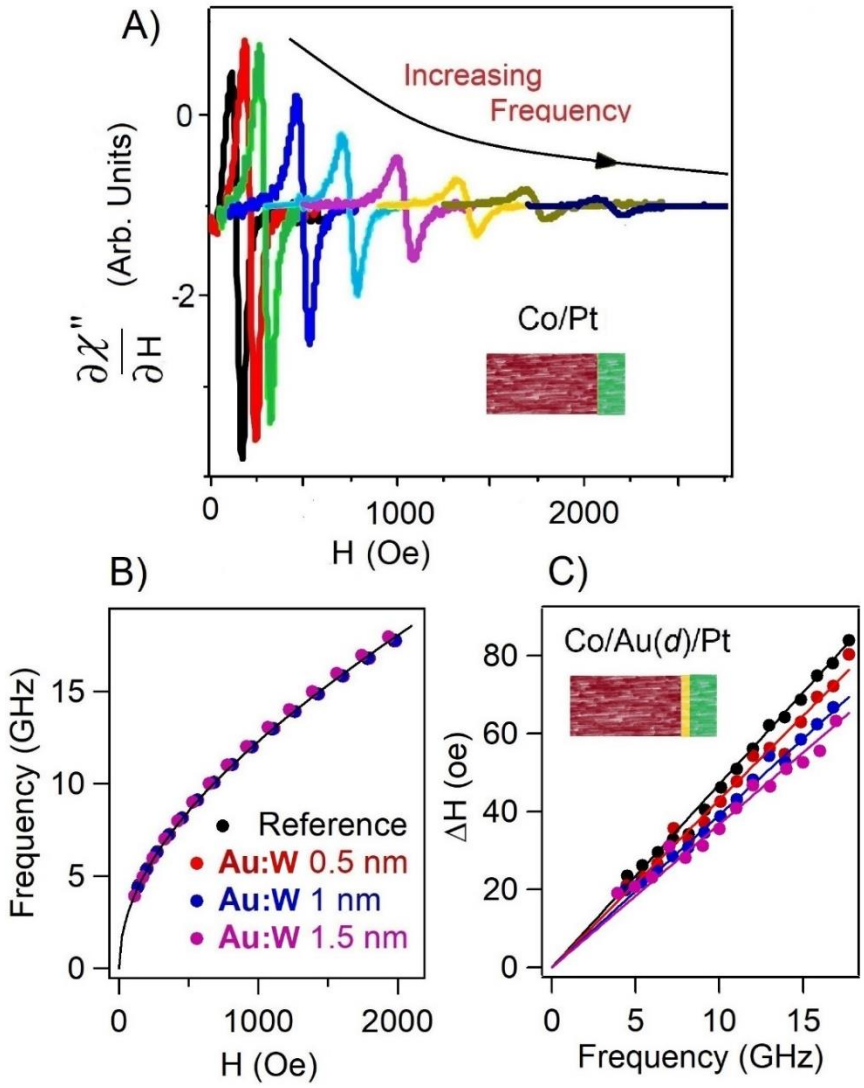

Figure III-34 : A) Derivative of the spin susceptibility vs intensity of the static magnetic field H_{DC} in the reference bilayer Co/Pt. The different curves correspond to hrf frequencies of 4-18 GHz, with step of 2 GHz. B) Variation of resonance frequency as a function the static magnetic field H_{DC} in the Co/$Au_{0.85}W_{0.15}$(d)/Pt trilayers. C) Full width at half maximum of the ferromagnetic resonance in Co/$Au_{0.85}W_{0.15}$(d)/Pt trilayers. The Co layer has thickness of 15 nm, the Pt layer has thickness of 5 nm and the $Au_{0.85}W_{0.15}$ layer has thickness d varying between 0 nm and 1.5 nm.

By fitting the data with the Kittel equation (III-11), it is possible to extract the saturation magnetization M = 1500±50 emu/cm3. The damping term is extracted using the method presented above. As shown by Figure III-34 C), the linear regression given by equation (III-13) quantified by measuring the half width at half maximum ΔHpp of the FMR resonance provides the Gilbert damping $\alpha(d)$ for the Co/$Au_{0.85}W_{0.15}$(d)/Pt series. This procedure is applied here to extract the Gilbert damping of Co/Ti(d)/Pt trilayers. Moreover, the larger thickness of cobalt layer (d_{Co}=15nm for FMR experiments instead of 2nm in the case of THz experiments) . Therefore, α differs from the $\alpha_{intrinsic}$ only by a term arising from the injected spin current into the HM. The effective spin mixing conductance $g_{eff}^{\uparrow\downarrow}$is obtained via equation (III-14). The value $\alpha_0 = 5 \times 10^{-3}$ is obtained for the Gilbert damping of a 15nm cobalt capped by 2nm of Al.

Figure III-35 A) shows α and $g_{eff}^{\uparrow\downarrow}$ for the two trilayer series as a function of interlayer thickness d. Similarly to THz measurements, the drop of spin mixing conductance is faster in Co/Ti(d)/Pt than in Co/$Au_{0.85}W_{0.15}$(d)/Pt samples. This finding highlights an intimate connection between $(g^{\uparrow} + g^{\downarrow})/2$ obtained by ultrafast currents in the THz spectral range, with $g_{eff}^{\uparrow\downarrow}$ extracted from the FMR damping linewidth.

In the following, to quantify the spin-memory loss (SML as introduced in section III.2.6) we assume that $\frac{g^{\uparrow}+g^{\downarrow}}{2} = (1-\xi)g_{eff}^{\uparrow\downarrow}$, where the parameter ξ < 1 arises from SML [65], [69], [98]. Due the spin scattering at the interface, the spin-current leading to THz emission in platinum is 1-ξ times smaller than the spin current affecting the $\vec{M}$ precession. By making use of equation (III-29), we can rewrite the effective spin mixing conductance as described by equation (III-30).

$$g_{eff}^{\uparrow\downarrow} \propto \frac{\eta(d)}{1-\xi(d)} \qquad (III\text{-}30)$$

The solid line of Figure III-35 b) is calculated from equation (III-30) with parameters $g_{eff}^{\uparrow\downarrow}(0) = 75nm^{-2}$ and $\xi(d) = 0.4\eta(d)$. An important result is the relationship between ξ and the spin conductance at the interface. **The more efficient is the generation of spin current, the higher is the spin memory loss.** Further, when expressed in terms of relative variation of the spin conductance, the spin memory loss ξ appears to be insensitive to the compound and thickness that has been employed to perform the passivation of the interface (see Figure III-35 b)).

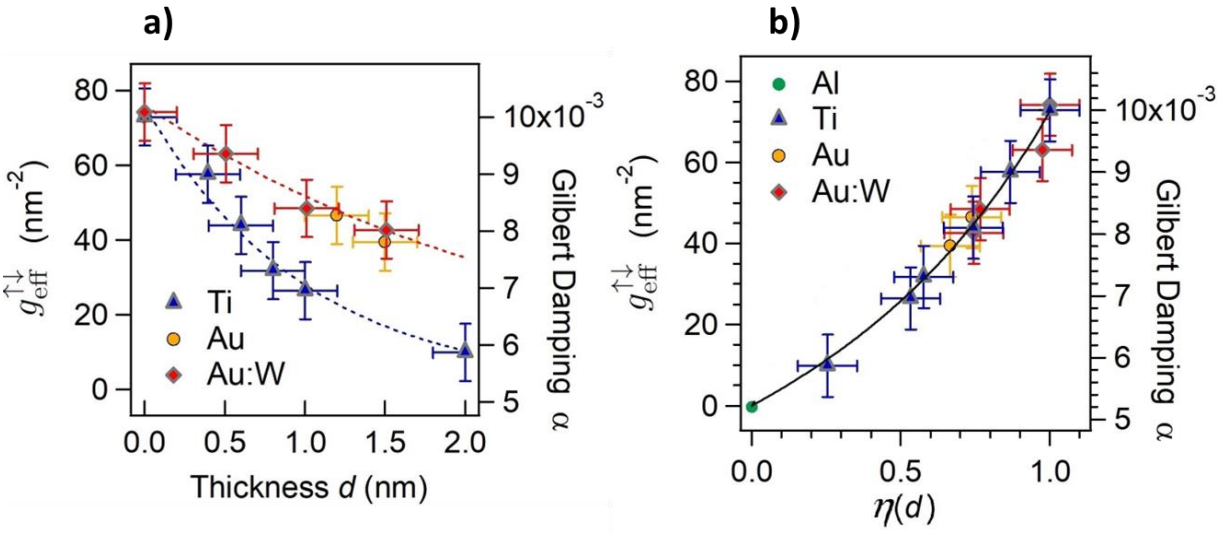

Figure III-35 : A) Gilbert damping and spin conductance in Co/Ti(d)/Pt, Co/Au(d)/Pt and Co/Au$_{0.85}$W$_{0.15}$(d)/Pt trilayers as a function of thickness d. B) Gilbert damping and spin conductance of the two trilayer set plot against the η parameter extracted from the emitted THz. The green dot corresponding to vanishing THz emission is the intrinsic Gilbert damping measured on cobalt capped by 2 nm of alumina. A model that includes the spin memory loss is calculated via Eq. [9] and superimposed (solid line) to the experimental data.

In the following section we will discuss the interfacial effect that drives the spin memory loss by modeling the Co/X/Pt interfaces with Rashba fields (which will be further discussed in Chapter IV.

III.4.5 Modeling of SML

The insertion of an interlayer X at the Co/Pt interface has two main effects: i) the formation of a thin potential barrier is accompanied by a reduction of the spin-transmission in

comparison with Co/Pt. Indeed Co/Pt is known to have an excellent matching for the majority spin channel near the Fermi level whereas a larger chemical mismatch may take place in the case of Co/X/; ii) since Ti or pure Au lack the open 5d shell of Pt, the presence of an interlayer reduces the spin orbit interaction (SOI) at the interface [68]. In the following, we consider a simplified SOI (see appendixes and [104] for details) assisted quantum transmission model that has been recently implemented with success for the description of SOT [105]. This model will first highlight the role of i) and ii) in the description of our data. The interface is treated as an ideal trilayer structure Co/X/Pt with a spin current J_s propagating along the $\vec{e}_n$ direction, normal to the layers (conduction perpendicular to planar geometry). J_s is computed from the propagation of selected plane waves with in-plane conserved wavevector $k_{\parallel}$, and normal wavector kz along $\vec{e}_n$ (see Figure III-36). The quantum transmission is summed hereafter over the Fermi surface, like it is required within an extended Landauer treatment. We obtain the $J_s(z)$ profile across the interface via a refined model involving a Rashba-like term [106], [107].

We restrict the electronic states to two electron bands with spin polarized states. The partitioned Hamiltonian in Co and Pt reads as equation (III-31):

$$\widehat{\mathcal{H}} = \frac{\hat{p}^2}{2m^*} + \Delta_e \hat{m} \,.\, \hat{\sigma} + \hat{V} \qquad (\text{III-31})$$

where $\hat{p} = -i\hbar\nabla_z$ is the impulsion operator, m^* is the effective mass, $\hat{m}$ is the magnetization direction, $\Delta_e \approx 2eV$ is the exchange splitting for Co, and $\hat{V} = \hat{V}_{Co} = 0eV$ represents the energy position of the bottom of the spin-averaged 3d Co bands. Along the same lines, we set for Pt an exchange coupling $\Delta_e \approx 0eV$ and $\hat{V} = \hat{V}_{Pt} \approx -1eV$ The potential difference $\hat{V}_{Co} - \hat{V}_{Pt}$ is representative of the workfunction offset between the two metals. The addition of an interlayer is simulated by an interfacial potential $\hat{\mathcal{V}}_S$ that is expressed by equation (III-32 [105].

$$t_I \hat{\mathcal{V}}_s \delta(z) = t_I \left[\mathcal{V}_X + \frac{\alpha_R}{\hbar} \left(\vec{\hat{p}} \times \vec{e}_n \right) . \hat{\sigma} \right] \delta(z) \qquad (\text{III-32})$$

Where z is the coordinate along the direction $\vec{e}_n$, the function $\delta(z)$ is the Dirac delta function and t_I is the effective interface thickness. The operator $\hat{\mathcal{V}}_s$ is defined via: $\mathcal{V}_X = \frac{\hbar^2 k_X}{t_I m^*}$

is the average interface of an unpolarized potential barrier, and α_R is the strength of the Rashba interaction (interfacial fields due to the inversion symmetry of the metallic interface inducing SOC, see section IV.1). We introduce the two parameters having the dimension of inverse length. The quantity $k_x = \mathcal{V}_X t_I m^*/\hbar^2$ tunes the transmission through the barrier and $k_{SO} = \alpha_R \overline{k_F} t_I m^*/\hbar^2$ determines the strength of the spin-orbit scattering. We then solve the quantum electronic transport problem sketched in Figure III-36 by matching the different electronic wavefunctions $\psi_{k\|}(z)$ in the presence of $\hat{\mathcal{V}}_s$.

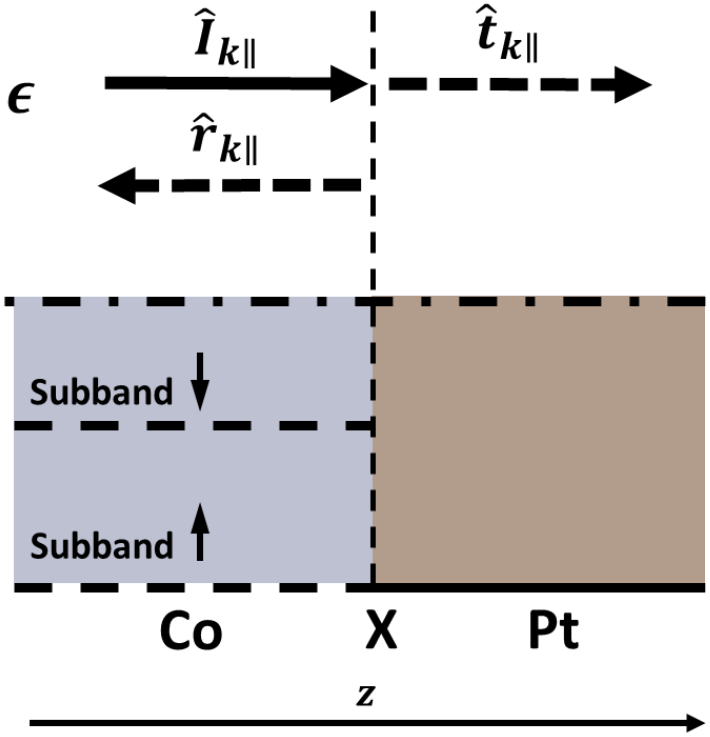

Figure III-36 : Sketch of transmission through an interface with Rashba felds. $\hat{r}_{k\|}$, and $\hat{t}_{k\|}$ are respectively the matrix representing the refection and transmission amplitudes corresponding to electrons of fixed energy ϵ crossing the interface from Co towards the Pt side and including the spin-orbit scattering region. $\hat{I}_{k\|}$ is the incident matrix.

III.4.6 Results of the model

Our model provides the profile of a normalized spin-polarized current originating from Co (where it is normalized to unity) and propagating through a Co/X/Pt trilayer. Figure III-37 A) depicts three specific cases, corresponding to: no interfacial potentials ($k_X = 0$ and $k_{SO} = 0$), a pure Rashba interaction ($k_X = 0$ and $k_{SO} = 2\text{Å}^{-1}$) and, both a potential barrier and a Rashba interaction ($k_X = 3\text{Å}^{-1}$). and $k_{SO} = 2\text{Å}^{-1}$). The spin current is always maximal in the bulk of Co, while it goes towards zero when penetrating in the HM Pt layer and moving away from the interface. In the absence of the scattering potential $\hat{\mathcal{V}}_s$ (black curve in Figure III-37 A)) the $j_s(0)$ value at the Co/Pt interface results from an equilibrium condition between bulk spin-flip rates in the two regions. The spin-current is continuous everywhere (no spin-orbit scattering) and its value $j_s(0) \approx 0.6$ coincides with the prediction of a pure diffusive spin-model. This agreement corroborates the validity of our quantum transmission model in the absence of any $\hat{\mathcal{V}}_s$ scattering.

Adding now a Rashba interaction $k_{SO} = 2\text{Å}^{-1}$ (red curve in Figure III-37 A)) leads to spin-memory loss. Indeed, the Rashba fields are not collinear to the incoming spin and induce a local spin-precession. Only a fraction of spin current coming from the Co reservoir is injected into the Pt layer so that $j_s(z)$ displays a sizable discontinuity at the interface [69]. In order to quantify this effect, we introduce the memory loss parameter $\xi = \frac{j_s(0_-) - j_s(0_+)}{j(0_-)}$, where 0_- and 0_+ are the limiting values reached by approaching the interface from the Co and Pt side, respectively. From the chosen parameters we extract $\xi = 0.6$, which is only 50% higher than our experimental value and in agreement with previous FMR-SP estimates [65]. The presence of an additional unpolarized scattering potential with $k_X = 3\text{Å}^{-1}$ (Blue curve in Figure III-37 A)) has two main effects. On one hand, the larger backflow of j_s in the Co layer leads to a smaller injection of spin-current from the ferromagnet. On the other hand, an unchanged strength of the Rashba field results in a smaller jump of the j_s current at the interface. As shown in Figure III-37 B), the monotonic reduction of spin memory loss as a function of k_X takes place for two representative values of the inverse spin length k_{SO}.

We extract the effective spin conductance from the rescaled ratio between the spin current $j_s(0_-)$ obtained in the presence of an interlayer (i.e. for $k_X > 0$) and the $j_s(0_+)$ obtained for the bare Co/Pt interface (i.e. for $k_X = 0$). Figure III-37 B) shows the calculated

ξ as function of the potential barrier k_X increased linearly to 5Å^{-1} and Figure III-37 C) shows ξ vs $g_{eff}^{\uparrow\downarrow}$ while the value k_{SO} is kept fixed to 2Å^{-1}. Note that the spin memory loss displays the same trend of the curve that is extracted by combining FMR-spin-pumping and THz methods (green dashed line). This shows that an interposition of Ti, Au or $Au_{0:85}W_{0:15}$ introduces a chemical barrier at the interface. The enhanced backward diffusion of electrons has the effect of decreasing both the spin mixing conductance and the spin memory loss. This effect takes place even if the spin dependent scattering k_{SO} remains equal to the pristine value.

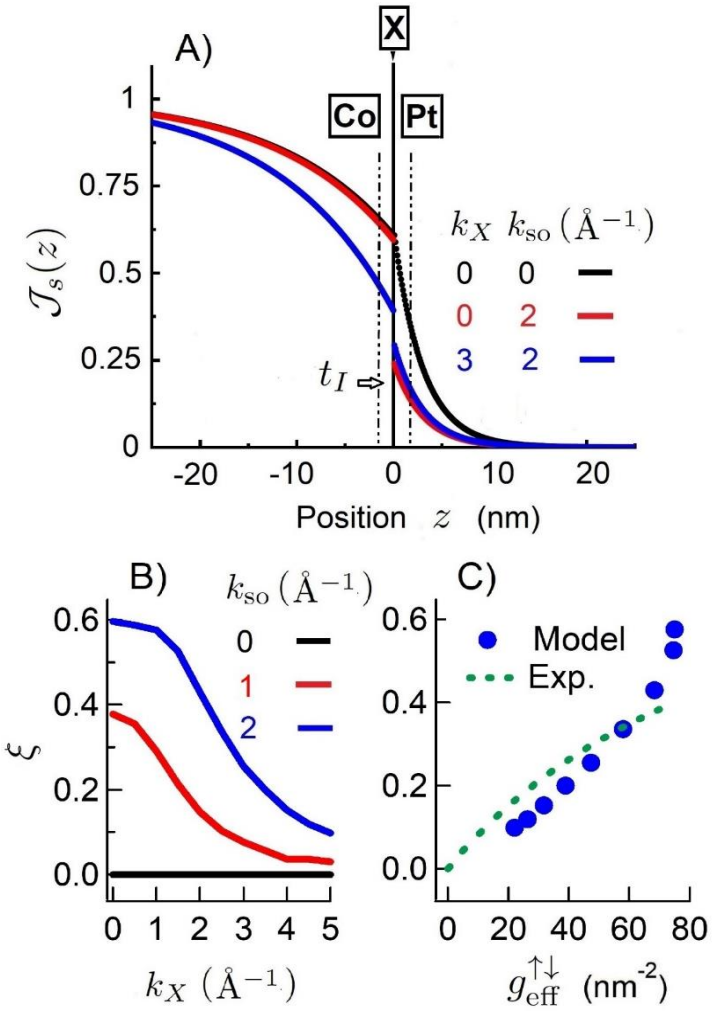

Figure III-37 : A) Profile of spin current J_s in the Co/X/Pt surface at the vicinity of the Co/Pt interface for 3 different cases: no scattering potential (black curve), Rashba scattering only with $k_{so} = 2\ A^{-1}$ (red curve) and Rashba scattering plus a potential barrier ($k_x = 3\ A^{-1}$). The spin memory loss $\xi = (J_s(0_-) - J_s(0_+)) = J_s(0_-)$ is the relative discontinuity of Js at the interface. B) Spin memory loss ξ as a function of potential barrier k_x for three different strengths of the Rashba scattering. C) Spin memory loss ξ as a function of effective spin-mixing conductance $g_{eff}^{\uparrow\downarrow}$ obtained by varying k_x and with spin orbit parameter equal to $k_{so} = 2\ A^{-1}$ (blue circles). As a term of comparison, we also show the relation extracted from the experimental data (green dashed line).

III.5 Implementation of spin-sink

To go beyond Co/Pt, in this section, we will discuss the spin-sink concept that we applied to engineer novel FM/HM THz spintronic emitters with better performances in respect to our Co/Pt reference. This concept is presented along with early experimental results.

In section III.3.3.3, we reported that Au:W could be used as a spin-sink, in other world, the spin diffusion length in this material is small (1.5mn). Note that in Au:W the spin diffusion length is strongly dependent on the alloying that enhances the SOC [64]. This can be used to reduce the heterostructure thickness resulting in less THz absorption and thus stronger emission. To highlight this concept, consider the cases depicted in Figure III-38.For the HM larger than the spin diffusion length, the spin current is fully converted in charge current by ISHE due to the total relaxation, the THz emission is then scaled by the optical absorption induced by the whole structure. The case where the HM thickness is smaller than the spin diffusion length is more complex. The spin current starts to relax, at the HM/vacuum interface, the incoming electrons are reflected, resulting in opposites contribution of the SCC. The electrons may be reflected at each interface according to the work-function mismatch at the Fermi level between the materials. In this case, the THz emission is governed by the competition of i) a smaller THz absorption (due to the thinner structure), ii) the opposite SCC contributions from the directions of the reflected spin current, and ii) the loss of the oscillating dipoles from the thinner HM. The third schematic in the figure corresponds to the spin-sink concept behind the use of Co/Pt/AuW where the thickness of Pt is indeed smaller than the spin diffusion length (see Table III-4 for relevant parameters). Due to a high interfacial electronic transmission between Pt and AuW ($Z_{Pt} = 78,\ Z_{Au} = 79$), no electronic reflection occurs at the Pt/AuW interface, resulting in full relaxation of the spin current distributed in Pt and Au:W. The charge current generated is then constituted by one contribution from the Pt

and one from the AuW layer with their respective SHA scaling the conversion. In addition, the AuW has the advantage to be more resistive than the Pt resulting in less THz absorption. The resulting THz emission then scales with the thicknesses of the HM layers (in the limit of the spin diffusion length) ruling the THz absorption and the quantity of oscillating dipoles ($t^{Pt} \times \theta_{SHE}^{Pt} + t^{AuW} \times \theta_{SHE}^{AuW}$).

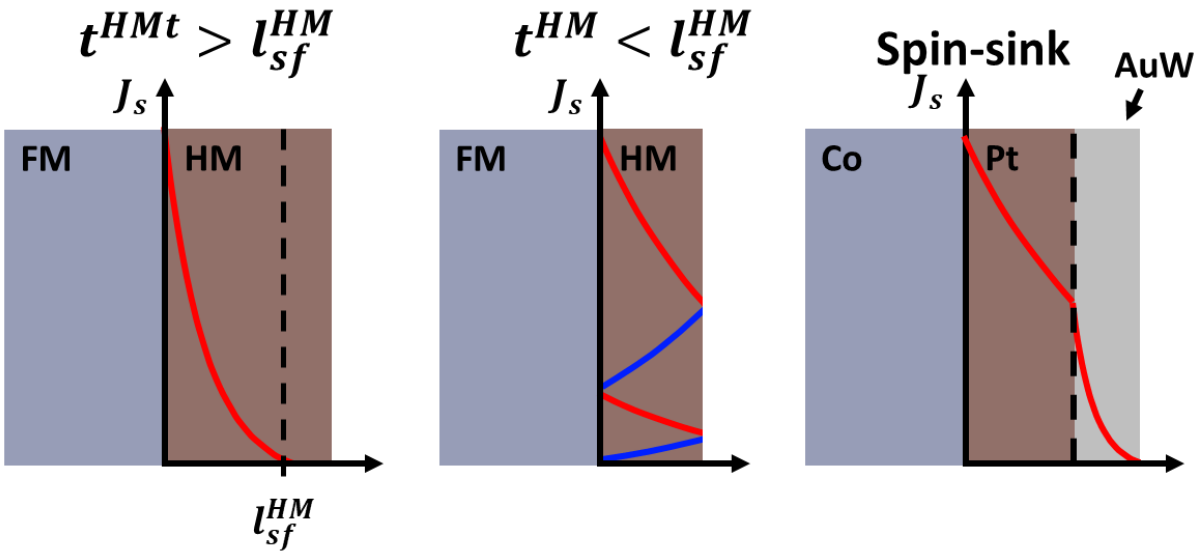

Figure III-38 : Schematic spin current distribution. In the case of the HM thickness larger than the spin diffusion length, the spin current fully relaxes and is converted to charge current via ISHE. When the HM thickness is smaller than the spin diffusion length, the spin current relaxes by reflecting in each interface, resulting in opposites contribution in the SCC. The spin-sink provides full relaxation of the spin current, no spin reflections at interfaces due to the close atomic proximity of Pt and Au. This enables smaller structures resulting in smaller THz absorption.

	θ_{SHE}	Resistivity ($\mu\Omega.cm$)	l_{sf} (nm)
Pt	0.1	*20*	3.4[65]
Au:W	0.15	90	1.5[64]

Table III-4 : Relevant properties in the frame of the spin-sink of Pt and Au:W

To test this spin-sink concept, we realized a series of samples composed of glass/Co(2)/Pt(X)/AuW(2) with X 2nm, 3nm, 4nm, and 5nm. The THz emission of these samples were investigated by our THz TDS system presented in section III.2.9 and compared to our Co(2)/Pt(4) reference. The results are displayed in Figure III-39 where the emissions are normalized in respect to our reference. It is clear that Co(2)/Pt(2)/AuW(2) provides the maximum of THz field with a factor 1.76 of enhancement with the reference. For an increase in thickness, the electric fields scale with the optical absorption and the proportion of

oscillating dipoles ($t_{HM} \times \theta_{SHE}^{HM}$) of each material. The THz emission is also reported higher by a factor 1.44 in the case of Co(2)/Pt(4)/AuW(2) compared to the reference sample, this highlight a significant conversion contribution from Au:W.

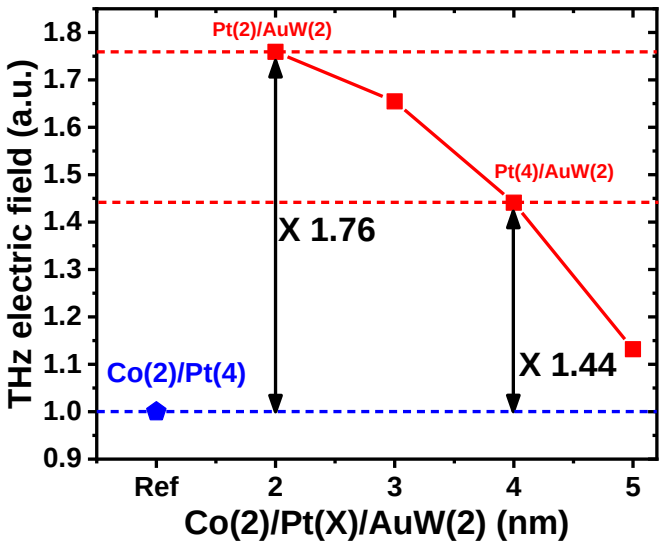

Figure III-39: Amplitude of the THz emission for glass/Co(2)/Pt(X)/AuW(2) with X is 2nm, 3nm, 4nm, 5nm. An enhancement of emission of 1.76 with our reference Co/Pt is found for Co(2)/Pt(2)/Au:W(2). This proves the concepts of spin-sink where the THz emission benefits of the small thicknesses and low optical absorptions.

To go beyond one could fabricate heterostructures with a smaller Pt layer, to benefit fully from the higher SHA of Au:W and lower THz absorption. In that configuration, the Pt layer would be used for its good electronic transparency at the Co/Pt interface, and the resulting THz emission should be stronger.

III.6 Conclusions and perspectives

In this chapter we studied the THz emission of a range of different FM/HM structures. We showed that the THz emission is larger by more than one order of magnitude in our reference Co/Pt, than provided by NiFe/AuW or NiFe/AuTa alloys relying on extrinsic ISHE. This difference was explained by a better electronic transmission at the interface in the case of our Co/Pt reference. Most importantly, the product of the spin Hall angle, the conductivity, the spin diffusion length and the electronic interfacial transmission ($\boldsymbol{\theta_{SHE}\,\sigma_{xx}\,l_{sf}\,T^{*}}$) constitutes the correct figure of merit for SCC conversion in the time-domain. Considering further the intricate weight of the conductivity towards i) larger volumes of charge relaxation in HM and ii) THz optical absorption, this can now be used to predict the THz emission of different structures. We also report that the spin conductance can be extracted from broadband THz spectroscopy. The investigation of Co/X(d)/Pt trilayers with X=Ti, Au and $Au_{0:85}W_{0:15}$ shows that in all cases, an interlayer reduces the spin-to-charge conversion. THz experiments have been bench-marked with the effective spin-mixing conductance extracted by FMR measurements. A model including spin memory loss show that the relative drop of spin current at the interface is proportional to $g^{\uparrow} + g^{\downarrow}/2$ and attains $\xi = 0.4$ at the Co/Pt interface. The simulations indicate that modified spin transmission probabilities at the interface can explain this correlation. Finally, we showed promising early data proving the spin-sink concept where an optimized spintronic heterostructure relying on different HMs outperformed the THz emission of our Co/Pt reference by a factor 1.77. Moreover, through this chapter, we showed that THz emission spectroscopy method applied to spintronics structures is a very efficient, fast, and non-destructive method to determine the spin injection properties at the nanoscale, and can also determine the local spin-conductivity within multilayers as performed in standard non-magnetic layers. Currently (2021) the state of the art of spintronic THz emitter is still dominated by metallic devices, but emerging quantum materials are showing great potential and are the main focus of the next chapter.

Chapter

IV

IV Quantum materials based spintronic emitters

While FM/HM based interfaces still represents the materials of reference for THz ultrafast spintronics, this chapter will present on-going research of THz spintronic emitters using novel materials, as well as other types of SCC conversion mechanisms that can potentially scale the SCC efficiency up to 100% [108]. Beyond ISHE in FM/HM based heterostructures, in this chapter, we will initially introduce Rashba systems along with Topological Insulators in the context of Edelstein effects for SCC. We also present a half-metallic ferromagnet Heusler system (a Weyl semi-metal) that is known to host exotic properties such as a large spin polarization [109], and which is a strong candidate for higher SCC efficiencies. This is followed by the current state-of-the-art of SCC and THz emission from ‘quantum materials.

We will then demonstrate THz emission of spintronic origin from all these material - from Heusler alloy, Rashba interfaces, and Topological Insulators - with their emission compared to our reference FM/HM structure. We will then present our insights into the physics of SCC conversion governing THz emission in these novel materials.

The range of complex materials investigated here show that THz TDS, compared to FMR-SP, is quickly becoming an important tool for the non-destructive and fast characterisation of novel materials. This permits rapid feedback into the growth and optimisation of these materials for their future spintronic devices.

Chapter IV

IV.1 Rashba system

In 1959 Emmanuel Rashba discovered the Rashba effect, which splits the spin energy band in momentum by SOC for materials with a broken inversion symmetry [110]. This discovery highlighted the importance of SOC and paved the way the for famous Datta and Das spin transistor proposal in 1990 [111]. In the bulk of a crystalline solid, a free electron experiences time-reversal and inversion symmetry. The time reversal symmetry represents what is happening to a physical system when the time is going backwards. In the case of a moving electron accelerated by an electric field, the reversion of time makes the electron flowing in the opposite direction until the initial position is reached. The electric field does not break the time reversal symmetry. Magnetic fields however are known to break this symmetry as described from a current loop that reverses under time reversion and thus flips the sign of the magnetic field (ferromagnetism is also known to spontaneously break this symmetry). The inversion symmetry is coming from the crystalline structure of matter where electrons in the bulk will "see" the same 3D potential. These symmetries leads to the degeneracy of the spin in energy with a typical parabolic dispersion given by equation (IV-1). However, in the case of symmetry breaking owing to an interface or a surface, the electric field changes from a 3D gradient of the crystal potential to an electric field perpendicular to the surface. This leads to the Rashba Hamiltonian that describes the Rashba spin-orbit coupling (see equation (IV-2)) which is similar to our definition of SOC in the previous chapter (see section III.2.4.1), adding an SOC term induced by the variance in symmetry.

$$E_{\pm}(k) = \frac{\hbar^2 k^2}{2m^*} \qquad (IV\text{-}1)$$

$$H_R = \frac{\alpha_R}{\hbar}[E_z \times k].\sigma \qquad (IV\text{-}2)$$

with α_R the Rashba parameter giving the strength of the interaction. Therefore, when electrons flow through this symmetry breaking area, they experience an effective magnetic field called the Rashba field. This interaction leads to the Rashba effect that lifts the spin degeneracy of the energy bands in momentum. To maximize this effect, the spin (contained in the Pauli matrix), the k-vector and the electric field E_z must be perpendicular to each other. This gives rise to the peculiar Rashba texture of spins: the helical locking of the spin with momentum often referred as spin-momentum locking. In this case the typical spin dispersion

in energy corresponds to that in equation (IV-3) with the term $\pm$ accounting for the helicity of the spin. The Rashba effect can be seen in Figure IV-1 where a) represents the spin degenerate dispersion of bands, without symmetry breaking, b) corresponds to a breaking of the symmetry that leads to the Rashba effect, while c) and d) are experimental Angle Resolved Photoemission Spectroscopy (ARPES) observations of such behaviour. The signature of this effect has been observed in many systems such as semiconductor interfaces, between HMs, in oxide-based 2D electron gas systems. Rashba systems thus rely on such interfaces to split bands in momentum through SOC. For further details, comprehensive reviews can be found in [112], [113].

$$E_{\pm}(k) = \frac{\hbar^2 k^2}{2m^*} \pm \alpha_R k \qquad (IV\text{-}3)$$

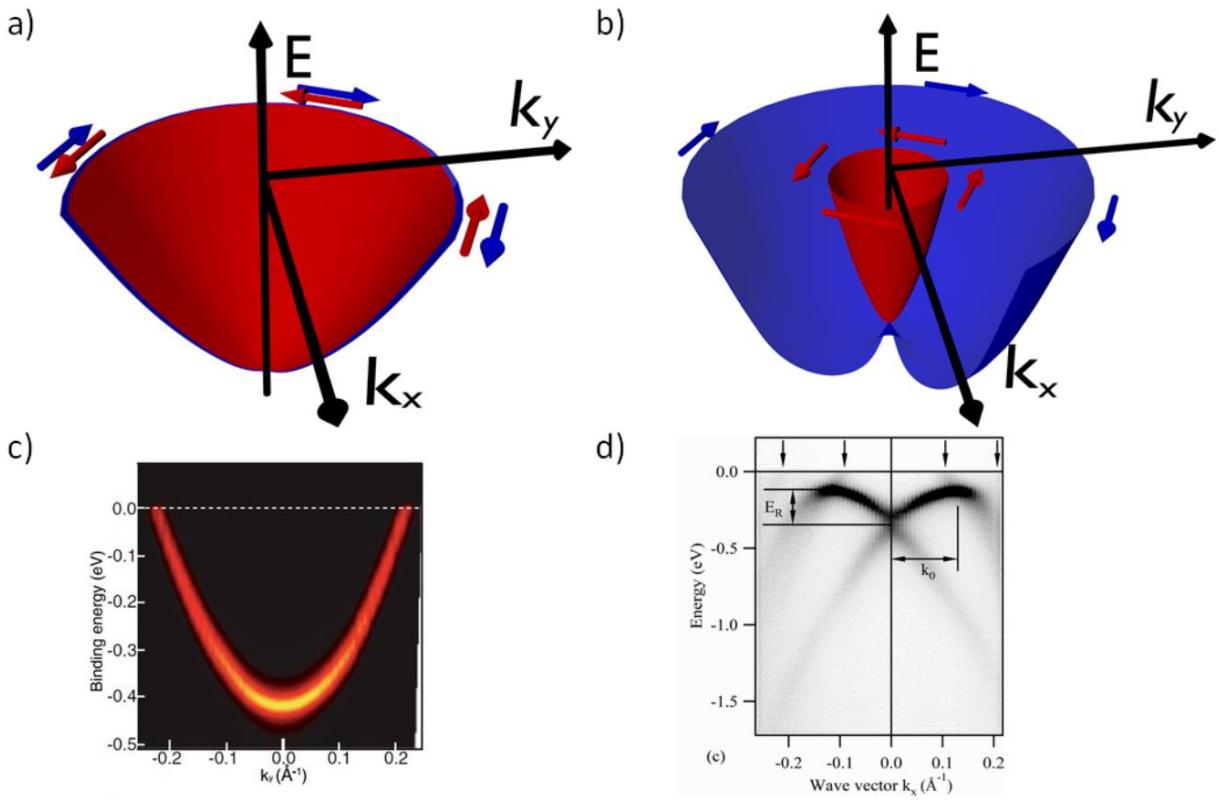

Figure IV-1: Energy dispersion with and without Rashba effect from [84] a) Without symmetry breaking , the system is degenerate in spins b) With symmetry breaking, the Rashba effect occur, the spin degeneracy is lifted with spin locked to the momentum. c) ARPES measurement of free electron dispersion in Cu d) ARPES measurements of the Rashba splitting in Bi.Ag system. Note that the split in momentum and the energy difference between lowest part of the different helicity cones are expressed as k_0 and E_R the energy difference.

In the following, we present our findings regarding a Rashba system and a topological insulator. In both cases the SCC is mostly based on the Inverse Edelstein effect (IEE) (see section IV.3) but with some particularities for each system. For that purpose, before entering in detail on this SCC mechanism, we will give an introduction to topological insulators.

IV.2 3D topological insulators

Topological insulators (TIs) re a novel class of materials described by Kane, Mele and Fu in 2007 [114], [115]. Albeit historically 2D TIs were first discovered through the explanation of the quantum Hall effect [116], 3D Tis has become a very active field of modern Physics. As a complete picture of the field is out of the scope of this manuscript the interested reader will find detailed and comprehensive reviews on the topic in [117], [118]. The particularity of these materials lies in the insulator characteristic of their bulk and a surface conduction carried by edge states. These properties come from an interplay of i) the inversion of the valence and conduction bands induced by SOC (or by strain) and ii) by the invariance of the inversion symmetry of their lattice that opens a gap in the bulk state but giving rise to metallic surface states. Their energy dispersion is typically a Dirac cone owing to their edge states, with spin momentum locking. Figure IV-2 displays the typical energy dispersion of Rashba and topological insulators system along with their Fermi surface. We can clearly see that topological insulators, unlike Rashba systems, have only one Fermi surface. This single Fermi surface is of peculiar importance for the following explanation of the IEE SCC in section IV.3 .The Spin-Orbit Hamiltonian for such systems (equation (IV-4)), albeit similar to the Rashba Hamiltonian, is slightly different. The Rashba parameter is replaced by $\pm\hbar v_f$. With v_f the Fermi velocity while the $\pm$ accounts for the change of chirality around the Dirac point. Note that v_f is often described as the spin-orbit velocity.

$$H_{TI} = \pm \hbar v_f [E_z \times k].\sigma \qquad (IV\text{-}4)$$

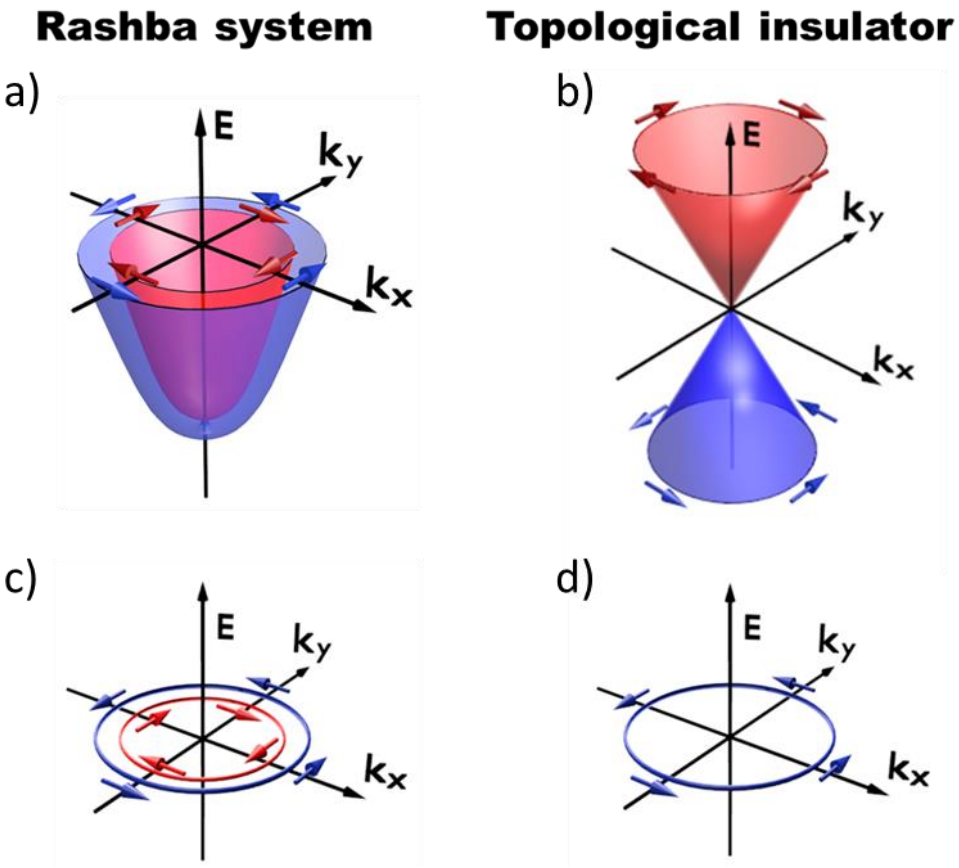

Figure IV-2 : Comparison of Rashba and topological insulator systems. a) Energy dispersion of Rashba states b) Dirac cone of TI surfaces c) Fermi contour of Rashba states d) Fermi surface of Ti surfaces. Adapted from [119]

Figure IV-3 displays the birth of the topological quantum phase by tuning the material composition, which changes the SOC [120]. One can clearly see the typical spin-momentum locking to the topological states and the closing of the gap by the tuning of the SOC. Another attractive property of these materials is the robustness of their edge states as their energy dispersion is defined by the topology and thus protected by the time reversal symmetry. Consequently, their edge states are topologically protected against scattering and thus are very robust regarding fabrication processes.

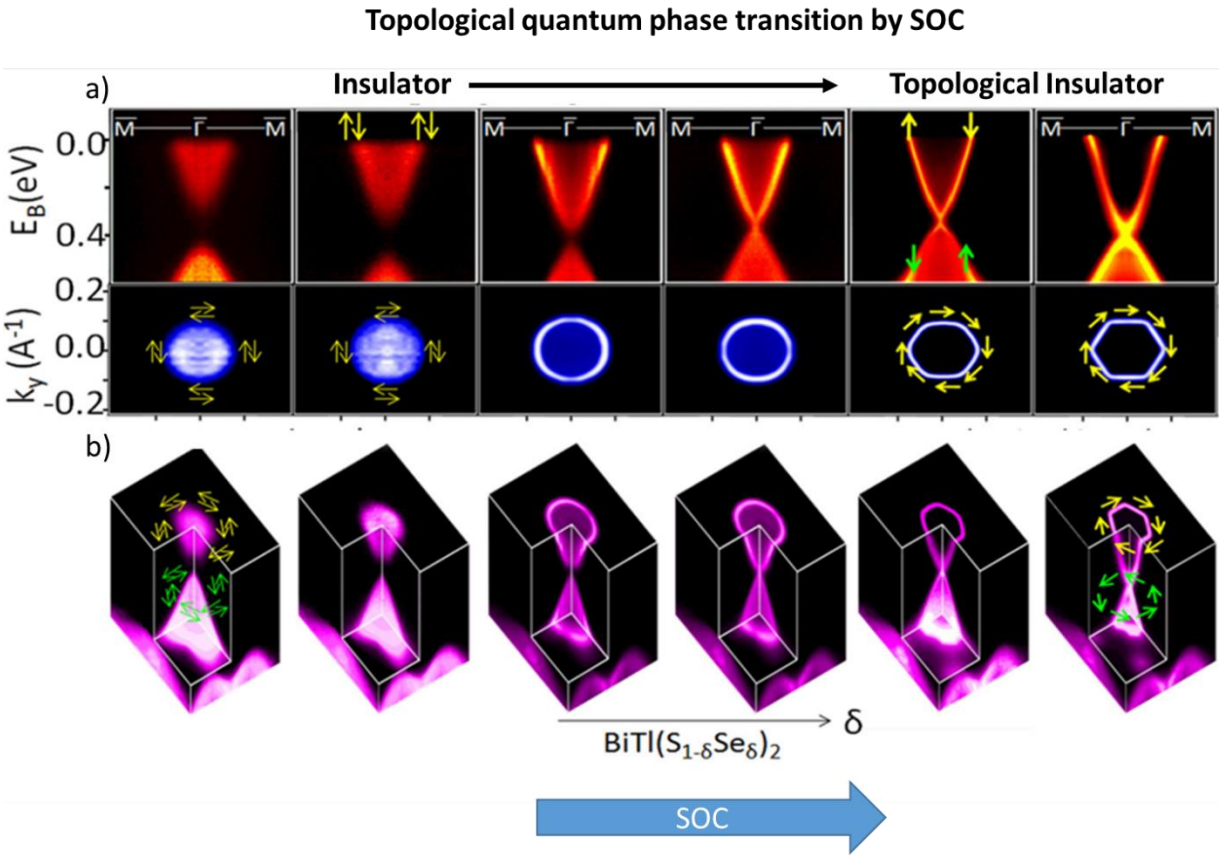

Figure IV-3 : Topological quantum phase transition in a tunable spin-orbit system $BiTl(S_{1-\delta}Se_\delta)_2$ analogue to the Bi2Se3 topological insulator. a) ARPES dispersion measurements from a spin-orbit insulator to a topological insulator by changing the SOC, the bottom panels represent the Fermi surface with spin texture highlighted by arrows. For topological insulators case, notice the spin-momentum locking. b) Map of the energy dispersion over a large energy scale with highlighted spin textures. Adapted from [120].

IV.3 The Edelstein Rashba effects

The Rashba-Edelstein effects ((R)EE), also sometimes referred to as galvanic effects, are SCC mechanisms that relies on spin momentum locking. Figure IV-4 depicts these effects in the case of Rashba systems and TIs. Let us first consider the direct EE in Rashba systems. When a charge current $\vec{j}_c$ is applied on the system, the Fermi contour shifts by $\vec{\Delta}k_x$. This effect leads to spins accumulation ($\delta_\uparrow$ and $\delta_\downarrow$ corresponding to coloured areas in Figure IV-4) along the plane of the charge current. These areas of spin accumulations are proportional to the radius of the Fermi surfaces ($k_F^{in/out}$ for the inner and outer Fermi surface) and the Fermi surfaces shift. As the radii of both Fermi surface are not equivalent, it results in a non-zero

spin accumulation, and thus to a spin current. For the Inverse Rashba Edelstein effect (IEE), a non-zero spin accumulation (spin current) shifts the Fermi surfaces. However, due to their opposite helicity, the Fermi surfaces shift in opposite directions. The resulting charge current (2D) is then described by equation (IV-5) where the term $(\delta_{\uparrow out} - \delta_{\uparrow in})$ accounts for the spin accumulation competition of both Fermi surfaces. Therefore, the total spin accumulation is reduced due to the inverse helicities.

$$J_C = \frac{q\alpha_R}{\hbar} \times (\delta_{\uparrow out} - \delta_{\uparrow in}) \qquad (IV\text{-}5)$$

For TIs, the conversions mechanisms are similar, but due to their single Fermi surface there is no competitions between spin accumulations, potentially resulting in larger SCC, when compared to Rashba systems.

In these systems, the conversion efficiency is defined as the inverse Edelstein length λ_{IEE}, corresponding to the ratio between the 2D charge current induced by IEE and the spin current, as expressed by equation (IV-6). However, the calculation is not the same for Rashba and TI systems due to the additional Fermi surface in the case of Rashba systems [119] The typical formulas for both cases are presented in Table IV-1.

$$\lambda_{IEE} = \frac{J_c^{2D}}{J_s^{3D}} \qquad (IV\text{-}6)$$

Efficiency	Rashba	TI
$\boldsymbol{\lambda_{IEE}}$	$\frac{\alpha_R \tau}{\hbar}$	$v_f \tau$

Table IV-1 :Conversions efficiencies : λ_{IEE}lengths for Rashba and TI systems as obtained by [119]. With τ and v_f being respectively the relaxation time of the Ti states and the Fermi velocity of the Dirac cone.

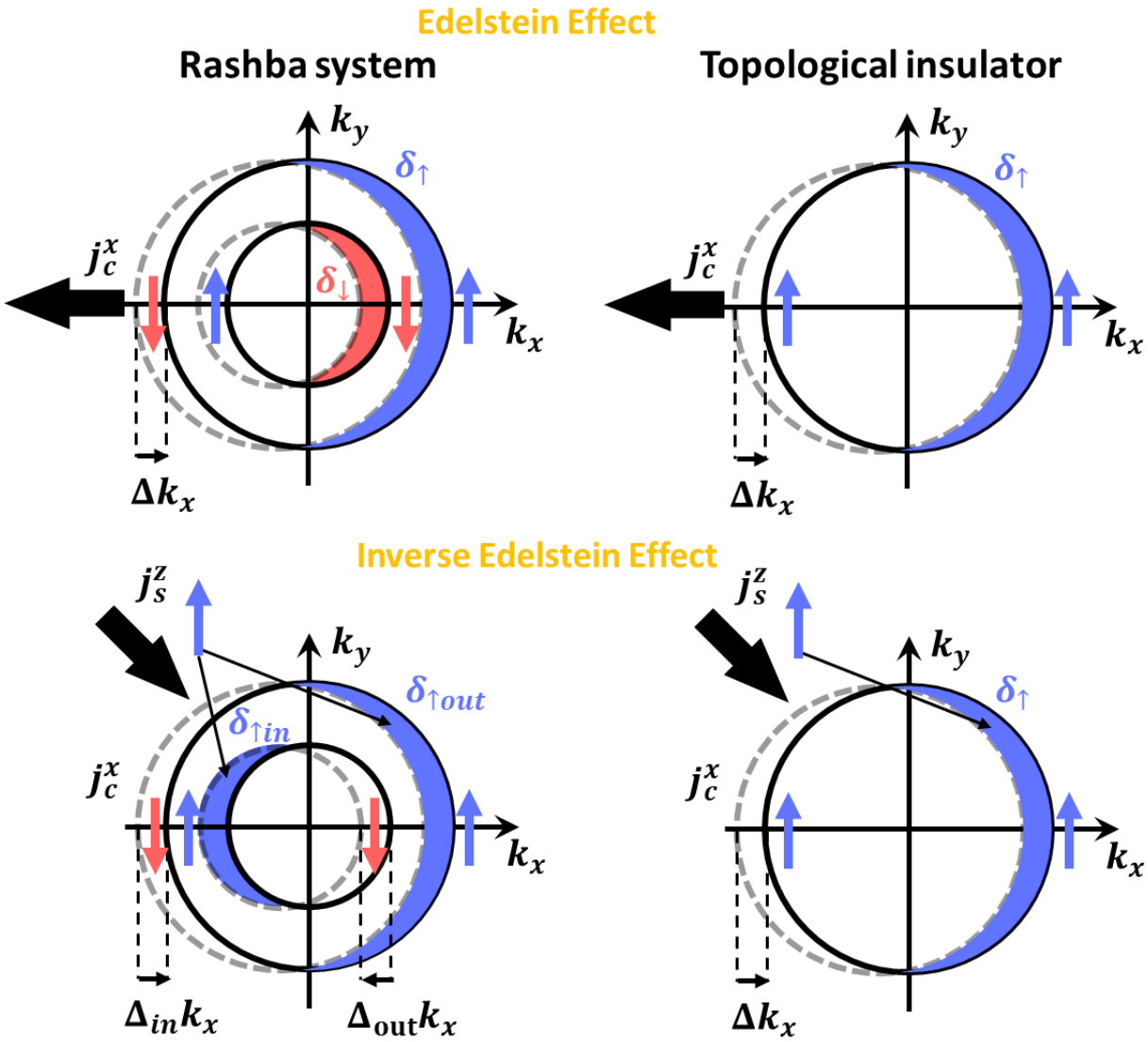

Figure IV-4 : Description of the direct Edelstein and inverse Edelstein effect in Rashba and topological insulators system. The Edelstein effect converts a charge current into spin current, the incoming charge current shifts the Fermi surface leading to a spin accumulation thus to a spin current. The inverse Edelstein effect converts a spin current into a charge current, the incoming spin current unbalances the initial spin population and shifts the Fermi surfaces leading to a charge current, Note the case of Rashba system having two Fermi surfaces shifted in opposite direction, this behaviour is due to inverse spin helicity. Figure inspired from [53], [121].

We will now briefly introduce another family of material that is potentially of great interest for the development of new THz spintronic emitters.

IV.4 Weyls semi-metals

Another type of quantum material similar to TIs are Weyls semi-metals (WSM). In 1929, a solution of the Dirac equation was demonstrated by Hermann Weyl for massless

chiral fermions called Weyl fermions. Although they were not observed at the time, they were discovered recently in the TaAs system [122]. In solid-states band structures, Weyls semi-metals bands originates from the topological phase transition where the bandgap barely closes as a complex interplay between SOC and time or inversion symmetry breaking. With this symmetry breaking, the Dirac point is split into two chiral nodes called Weyl point that displays a linear dispersion in 3D momentum space (see Figure IV-5). Weyls points are linked by a type of 2D non-closed Fermi surface called Fermi arc giving to the surface their exotic properties. Due to their inverse chirality, Weyl points act as monopoles and sinks of Berry curvature. The Berry curvature can be seen as a topological entanglement of valance and conduction band wavefunctions and is equivalent to a very strong magnetic field in momentum space. It has been pointed out that in such materials, owing to this Berry curvature, anomalous and strong Hall effects have been experimentally [123] demonstrated and strong SHE and thus a large SHA have been predicted [124]. In this manuscript the Weyl-semi-metal used for THz generation is a part of the wide family of Heusler compounds.

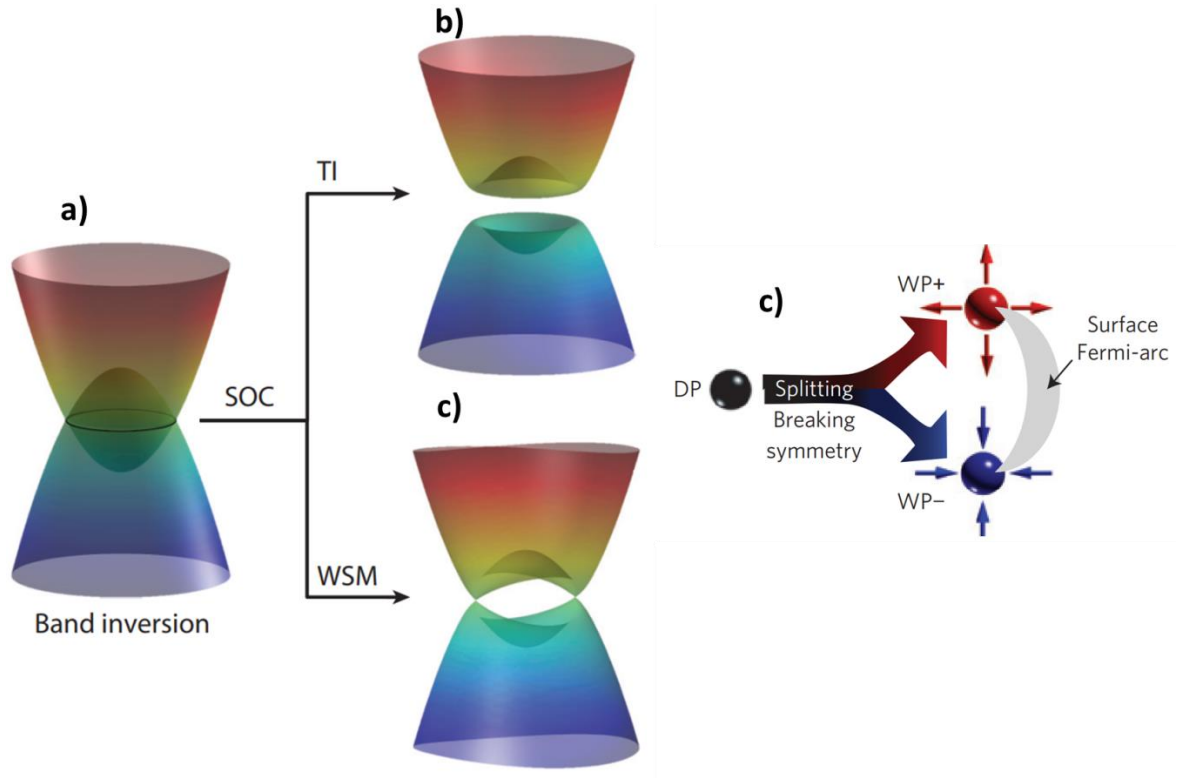

Figure IV-5 : The topology of TI and WSM arise from the same principle, after the band inversion a), the SOC opens a gap in their bulk, c) in the case of a WSM, under a variant in either time or inversion symmetries, the dirac point split into two chiral Weyls points connected by a Fermi arc and acting as monopole and sink of Berry curvature in momentum space. Adapted from [125] and [126].

Heusler compounds were discovered in 1903 by Dr, Fritz Heusler. It was pointed out that the alloy from three non-magnetic metal with different proportion (Cu_2MnAl) exhibits FM properties at room temperature although none of the metals themselves had magnetic properties. Today this class of material have more than 1200 compounds and are classified by their composition denoted as XYZ (half-Heuslers) and X2YZ(full-Heuslers) with XY being transition-metals and Z a main group s-p element. These materials display a wide tunability via their composition and atomic arrangements for exotic properties, as their huge composition space can unlock unusual behaviours such as half metal, spin-gapless semiconductors, superconductors, topological insulators, with more being found constantly [109]. The interested reader could find a detailed review on Heusler alloy based spintronic developments in [127]. The wide diversity of Heuslers gives the possibility to look for strong SOC alloys, although their potential for ultrafast spintronics is still mostly untapped.

Co based full Heuslers alloys have already been pointed as a good candidate for spintronic applications due to their strong anomalous Hall effects that depends on their structural order, resulting in large Berry curvatures and large spin polarization [128]. Indeed, these materials are half-metallic ferromagnets, and thus the large spin polarisation arises directly from their band structure. Their half metallic character opens a gap at the Fermi level for the minority spin band, leading to larger spin polarization than more traditional ferromagnetic materials such as Co, Fe or Ni [129]. By their crystalline symmetries and the breaking of the time reversal symmetry from ferromagnetism, these materials are also known to host strong Hall effects (due to a strong Berry curvature) and may potentially show self SCC. Such phenomena was observed in a Co_2MnSn alloy, where an ultrafast demagnetisation lead to a ISHE self-SCC for THz emission [129]. This is of particular interest, as coupled with our concept of spin-sink (see section III.5), it would be possible to design structures with potentially high THz output. This will be highlighted in our experiments in section IV.6.

IV.5 State-of-the-art

In this section, we will discuss the current state-of-the-art regarding the SCC efficiency and in a second time the THz emission of the different types of materials presented in this chapter.

IV.5.1 SCC efficiency

To compare the efficiency of ISHE and IEE based SCC, one must scale the dimensionless spin-hall angle with the inverse Edelstein length. A common practice for HM is to multiply the spin-Hall angle by the spin-diffusion length to homogenize units between the two metrics (equation (IV-7)). This length matches with the total volume of transient dipole charge oscillations responsible for the THz dipolar emission and enables direct efficiencies comparison between ISHE and IEE SCC processes.

$$\lambda_{IEE} \equiv \theta_{SHE}^{2D} = \theta_{SHE} \times l_{sf} \qquad (IV\text{-}7)$$

Table IV-2 regroups experimental efficiencies (λ_{IEE}) from transport measurements reported in the literature of SCC for Rashba systems, TIs, Weyls semi-metals and HM based spintronic devices for comparison. Rashba systems $LaAlO_3/SrTiO_3$ (LAO/STO) and $AlO_3/SrTiO_3$ (AlO/STO) have a conversion efficiency reported of 32 and 100 times higher than Pt. Moreover, a more recent study on the AlO/STO highlighted a gate tuneable giant SCC efficiency of 20nm [130]. These efficiencies make this system particularly interesting for the development of new spintronic based THz emitters. (However, it should also be noted that there are other factors that affect the THz emission as detailed in chapter III). LAO/STO and AlO/STO structures will be described in detail in the section IV.7. Tis α-Sn, $BiSb_2Te_3$ and Bi_2Se_3 have shown, respectively, a SCC higher by a factor 10.5, 5 and 2 times than Pt, although SCC up to 100% has been predicted [108] in topological insulators. We believe that this system shows strong potential for THz spintronic emitters due to their single Fermi surface and will be investigated in section IV.8. As Heuslers represents a very broad family of materials, we restrict ourselves to Co based half-metallic ferromagnetic compounds where very recent results show a SCC efficiency of -0.6nm in Co_2MnGa, which is 3 times higher than Pt (note the negative value), along with a large spin polarization at the Fermi level of 65% (Co spin polarization at the Fermi level $\sim$0.34%) [131]. This makes Co_2MnGa interesting to combine with either our spin sink concept or trilayers structures for high power THz emitters. This will be discussed in section IV.6. Interestingly, despite the single Fermi surface of TIs, the current largest experimental SCC efficiency is surprisingly found highest in the AlO/STO structure. This may be explained by the relative recent and few experiments carried out on TIs.

Material	Type	Efficiency λ_{IEE} (nm)	Reference
Bi/Ag	Rashba	0.4	[132]
LAO/STO	Rashba	6.4	[94],
AlO/STO	Rashba	20	[95]
α-Sn	TI	2.1	[130]
$BiSb_2Te_3$	TI	1	[134]
Bi_2Se_3	TI	0.4	[135]
Pt	HM	0.2	[65],[130]
Ta	HM	0.3	[130]
W	HM	-0.43	[130]
Co2MnGa	Weyl & FM	-0.6	[131]

Table IV-2 : Comparison of the experimental efficiency of different spintronic systems.

Note that these SCC efficiencies were measured for energy in the range of few tens of μeV (microwave) and might not be similar for higher energy i.e., laser induced spin currents. Nevertheless, we will now turn towards the reported THz emission of these materials.

IV.5.2 THz emission

THz emission from Rashba states with CoFeB/Bi/Ag that scales to a FM/HM reference by a factor 0.2 have been reported [136]. To our knowledge, THz emission has not been demonstrated for LAO/STO or AlO/STO. Recently, successful implementation of TI-based THz emitters have been demonstrated using Co/Bi_2Se_3 [137]. The emission was compared to a FM/HM (Co/Pt) reference with a factor 1.7 in favor to the TI system. Interestingly this 1.7 factor, close to the SCC enhancement from Pt to Bi_2Se_3 suggests a good spin transmission at the interface between Co and Bi_2Se_3. Another demonstration highlighting the potential of TI for the development of spintronic THz sources showed an enhancement of the THz emission by a factor ~ 2 for a FM/HM/TI structure in respect to the same structure without the TI layer [138]. THz emissions from Weyl semimetals has already been successful in several works on TaAs and Mg_3Bi_2 [139], [140] through the circular photo-galvanic effect [141]which rely on the helicity of the incoming laser polarization. However, the complex band structure of Weyl semimetals often shows surface and bulk states, leading to potential SCC based on ISHE and IEE processes. Theoretical predictions within these materials even proposed an IEE efficiency one order of magnitude above the IEE occurring in Rashba

systems and TIs [142]. Another recent work regarding THz emission of Co_2MnSi/Pt revealed to be a better emitter than their CoFe/Pt reference by a factor 1.5-2 and was attributed to a larger THz transmission of the material [143].

Due to the SCC efficiencies of these quantum materials well above the established HMs, in the coming sections we will investigate the THz emission of a Co_2MnGa half ferromagnetic Weyls Heusler compound, along with IEE based SCC of LAO/STO, AlO/STO and Bi_2SnTe_4 Tis, which can potentially exceed HM/FM heterostructure performances. The strength of the THz emission of each investigated structure will be compared to our Co(2)/Pt(4) FM/HM reference.

IV.6 THz emission from Weyl semi-metal

In this section we will study the THz emission of a half-metallic ferromagnet based full Heusler alloy that has been identified as a Weyl semimetal [144]: Co_2MnGa. These samples were provided by Claudia Felser`s group from the Max Plank institute Dresden Germany in the frame of the European project SKYTOP.

The strong Berry curvature of the band structure combined with the half-metallic ferromagnetic character of this material may allow a self SCC conversion. However, the study of self SCC of the ultrafast spin current is not trivial. Consider a bare Co_2MnGa layer as depicted in Figure IV-6 a) where an ultrafast laser induced demagnetization occurs as the laser penetrates the material. This results in a propagating polarized spin current, and when combined with SCC induces THz dipoles over the whole depth of the layer. This statistically results in THz dipoles located in the centre of the layer (black dashes). Internal spin current reflections at the vacuum/Co_2MnGa interfaces during the spin current relaxation (leading to a SCC) would then lead to a compensation of opposite spin currents. In this balanced case, no THz signal would be expected. However, one can use our concept of spin-sink (see section III.5) to study this self SCC by caping the system with a non-active ($\theta_{SHE} = 0$) metallic layer such as AuW (see Figure IV-6 b)) where the SHA can be tuned to 0 with the Au composition [66]. This would enable to supress the spin current reflection at the Co_2MnGa/AuW interface, and thus a non-zero THz emission. This self SCC could be estimated with a thickness dependence of the Co_2MnGa. However, to verify this possibility, one must first investigate such ultrafast spin current injection within this material and SCC with an established HM.

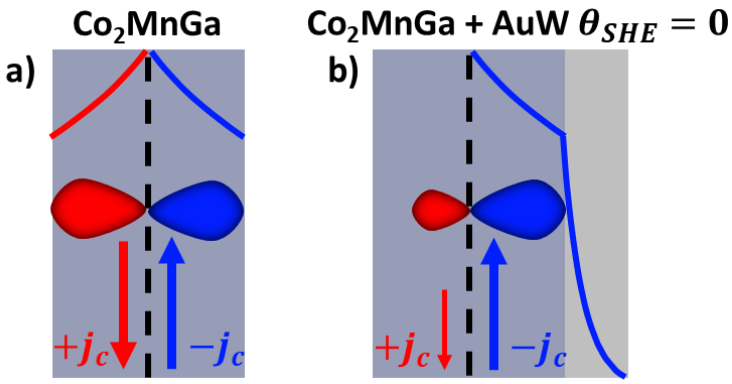

Figure IV-6 : Bare Co_2MnGa, the black dashes represent the statistical center of THz dipoles. This results in balanced opposite contributions of charge currents ($\pm j_c$), and therefore no THz emission. b) proposed structure to study the potential self SCC of Co_2MnGa, a layer of non-active AuW caps the structure forbidding interface reflections, resulting in unbalanced contributions of charge current and thus to a non-zero THz emission.

These samples were grown on MgO substrate by magnetron sputtering at 550°C, the individual sputtering rates of each species were adjusted to obtain the $Co_2Mg_{50}Ga_{50}$ composition. This is followed by the deposition of a 4nm Pt layer and a post-annealing treatment of 20 min to improve crystal quality [145]. The anomalous Hall angles reported for this material were found to increase with the thickness of this material, highlighting a strong bulk contribution. For THz spintronic emitters applications, it is crucial to understand this thin film limit. For that purpose a thickness dependence is performed on MgO/Co_2MnGa(x)/Pt(4) samples with x = (0 ; 8 ; 10 ; 20 ; 30) nm. The samples are placed in our TDS system presented in section III.2.9, inside an in-plane magnetic field to align the ferromagnetic domains of the alloy. Results are available in Figure IV-7. First it is important to note the inversion of the THz electric field polarity for an opposite applied magnetic field giving a THz signature of magnetic origin, with virtually zero emission from the MgO substrate. The THz emission of the Co_2MnGa alloy increases with a decrease of the Co_2MnGa thickness to reach a maximum at 8 nm. This results in an increase by a factor 1.33 of the peak-to-peak value compared to our Co(2)/Pt(4) reference (see Figure IV-7 a)and d)). This increase is still in discussion within our collaborators, but one possible mechanism apart for optical absorption is proposed in Figure IV-8 which show the opposites signs of the SCC efficiencies (λ_{IEE}) between Pt and Co_2MnGa. Indeed, thin Co_2MnGa layers would limit the oscillating dipoles that acts in opposite way to Pt, leading to most of the conversion occurring in Pt. The larger THz signal would then be a result of a better spin injection (higher spin polarization of Co_2MnGa). Interestingly a similar recent study showed a stronger THz emission by a factor 1.5-2 with respect to a FM/HM [143]. The detection limited THz spectrum highlights similar

characteristics to our Co/Pt reference (blue trace) but seems broader possibility highlighting different spin dynamics.

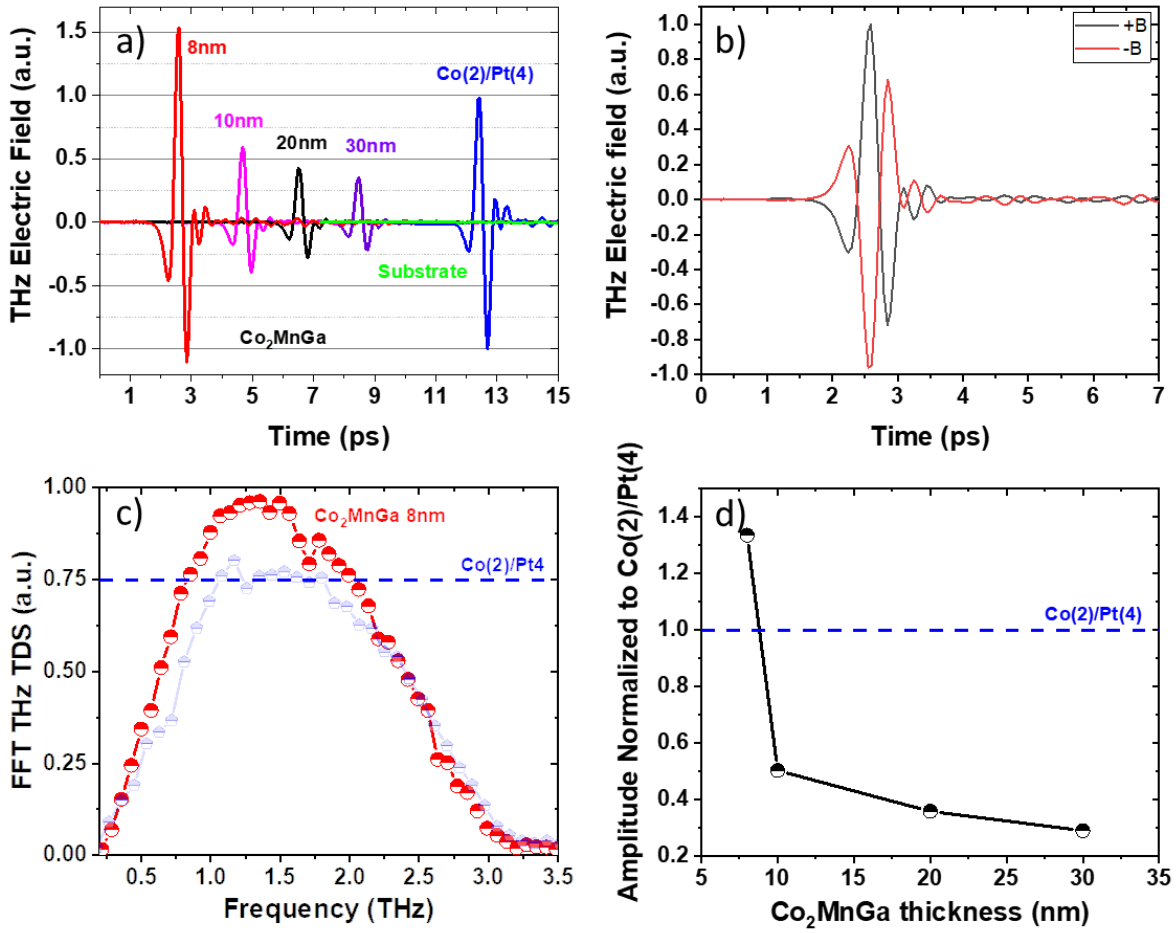

Figure IV-7 : THz emission from MgO/Co₂MnGa(x)/Pt(4) a) Emission TDS of Co₂MnGa of different thicknesses, MgO substrate, and Co(2)/Pt(4) reference, shifted in time for clarity. b) Inversion of the THz Electric field polarity upon reversal of the magnetic field which highlight the magnetic origin of the emission. c) Spectrum of the emission of 8nm of Co₂MnGa normalized over its emission, note the Co(2)/Pt(4) mark and the blue trace d) Amplitude of the THz signal for different thickness of Co₂MnGa normalized over Co(2)/Pt(4) reference. For 8nm thick Co₂MnGa, 133% of Co(2)/Pt(4) is reached. The emission decreases quickly for an increase of Co₂MnGa thickness.

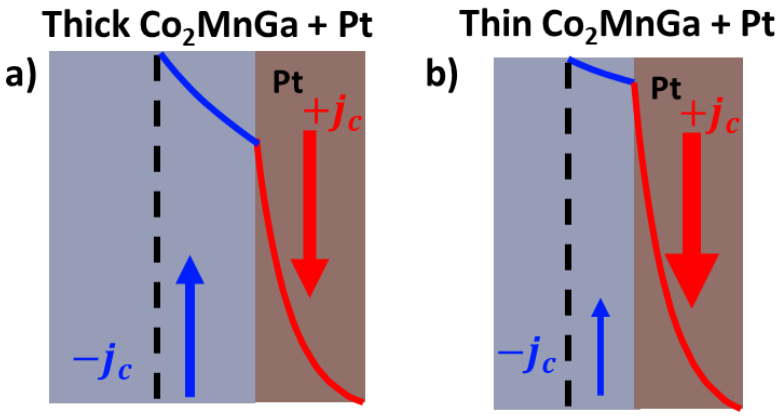

Figure IV-8 : Proposed mechanism explaining higher THz signal for thinner Co_2MnGa layer.

In this section we showed the strong potential of a Co-based Heusler half-metallic ferromagnet for THz spintronics. Futures measurements will consist in replacing the Pt by a non-active AuW layer to study the self-SCC as proposed in Figure IV-6, and performing a thickness dependence on the Co_2MnGa layer to find the optimal dimensions. Further interesting heterostructures could be designed by embedding Co2MnGa between two HM with opposite λ_{IEE} to form trilayers capable of enhanced THz emission.

In the next section we will describe the LAO/STO and AlO/STO Rashba system and discuss their THz emission.

IV.7 LAO/STO 2DEG system

In 2004 Ohtomo and coworker discovered a high mobility electron gas at the interface between two insulating oxides $LaAlO_3/SrTiO_3$ [146]. It was pointed out by Thiel *et al* that a transition from an insulator to a conducting state occurs for a LAO critical thickness of 4 unit cells (u.c., $1\text{u.c.} = 0.4nm$) [147]. The origin of the 2DEG was attributed to the polar discontinuity at the LAO and STO interface described in Figure IV-9. The STO unite cell is composed of $Ti^{+4}(O^{-2})_2$ and $Sr^{+2}(O_{-2})$ where charges are balanced. However, the LAO made of $La^{+3}O^{-2}$ and $Al^{+3}(O^{-2})_2$ is unbalanced as they present a charge (Q) of +1 or -1. When put together, this leads to a divergent electrostatic potential field (V) that increase with the LAO thickness: the so-called polar catastrophe. However in reality the material is reconstructing the electrons distribution by transferring half an electron (per unit cell) from the LAO to the STO interface, leading to a finite potential [148], [149]. The band structure of LAO/STO is displayed in Figure IV-9 b) for the polar catastrophe and the electronically reconstructed scenario. For the latter, as the LAO thickness increase, the electric field builds up and thus tilts the LAO bands. At the critical thickness, the valence band (VB) of the LAO reaches the conduction band of STO in energy, which permits to form the 2DEG and enables the conduction state. A bottleneck for spintronic applications, remains however, their relatively low barrier transparency even for very thin oxide barrier. A scientific breakthrough [150] lowered the critical thickness down to 1 uc by metal caping. Similar 2DEGs were also demonstrated for a $AlO_3/SrTiO_3$ (AlO/STO) structure [133] with a striking SCC conversion efficiency reported of λ_{IEE} on the order of 20 nm. In the case of a perfect electronic transmission, one should expect an increase the THz emission by one order of magnitude.

The LAO/STO platform is particularly interesting owing to the very high conversion efficiency and the possibility of tuning the Rashba SOC that arises from the 2DEG by the addition of a electrical gate [130], [151]. This can be used to increase or switch the conversion efficiency of the device. The implementation of a gate to control the THz spintronic emission would be of great interest as it will enable electrically modulated spintronic THz emitters. This would represent a significate advance in the field. Current schemes described in section III are passive and require a chopper to mechanically modulate the THz electric field.

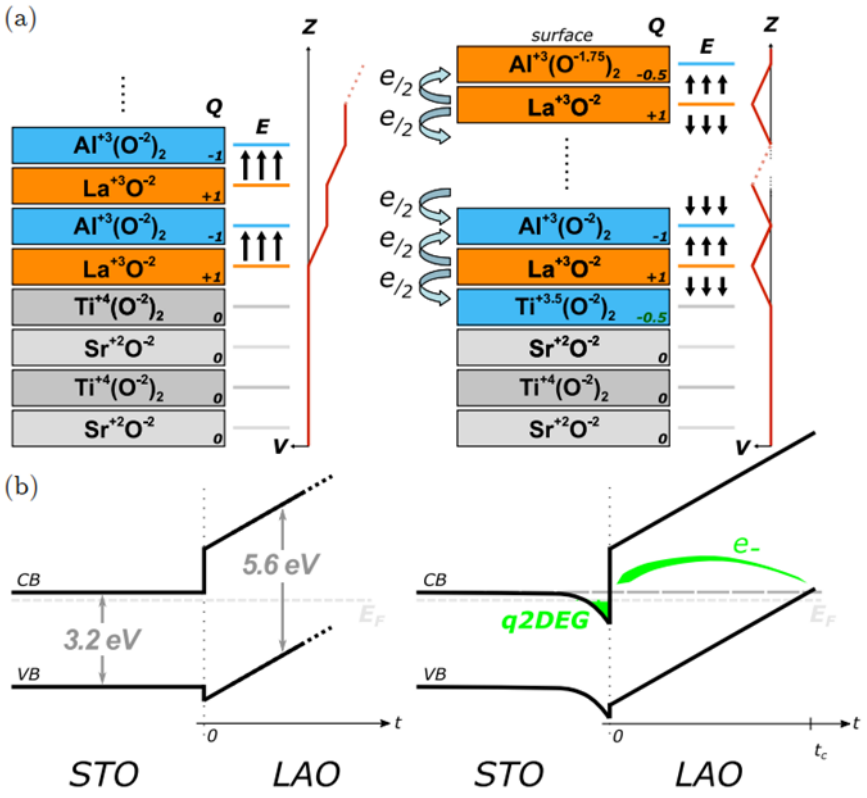

Figure IV-9:a) Representation of the LAO/STO structure. Left panel describes the polar catastrophe where the electrostatic potential V is divergent with the thickness of LAO by unbalance charges in LAO. The right panel describes the electronic reconstruction: each LAO uc shares half of an electron to the interface. This leads to a finite potential. b) band structures of both cases, the tilt of the band is linked to the electric field build up by the increase of the LAO thickness, enabling above the critical thickness an electronic conduction where the valence band (VB)of the LAO reaches the conduction band (CB) of the STO. From [53].

A decrease of the sheet resistance with temperature and a higher SCC at cryogenic temperatures have been reported through FMR-SP [152], [130]. The requirement of cooling is linked to a drastic change of the dielectric constant [153] that i) increases the Rashba fields of the barrier and ii) provides a high mobility of the 2DEG, thus providing an enhancement of the SCC. Although THz emission from Rashba states has been shown in CoFeB/Bi/Ag [136], the LAO/STO and AlO/STO remain unexplored for THz emission. In the coming section we will present THz emission spectroscopy results and perspectives of LAO/STO and AlO/STO based 2DEG devices. Preliminary results over the implementation of a gate will also be presented and perspectives towards optimisation.

IV.7.1 Sample preparation and THz emission

In this work, transition metal oxide-based 2DEG are respectively composed of NiFe(2nm)/LAO/STO and NiFe(2nm)/AlO(x)/STO, with STO the substrate, by combining pulsed laser deposition (PLD) for the LAO/STO part, and by sputtering concerning the Al/STO template that is oxidized to form a thin AlO_3(x) layer of nominal Al thickness of x = (0.25 0.5 0.75) nm. This Al thickness dependence is studied to investigate the possibility of hot electrons tunnelling through the barrier as reported by FMR-SP experiments [150] for electron energies in the vicinity of the Fermi level. In the case of hot electrons tunnelling through the barrier, the expected THz signal should then be maximum for thinner barriers. The schematic band structure of LAO/STO and AlO/STO are displayed in Figure IV-10 along with reported LAO and AlO barrier heights of 2 and $3.8eV$, respectively [154], [155].

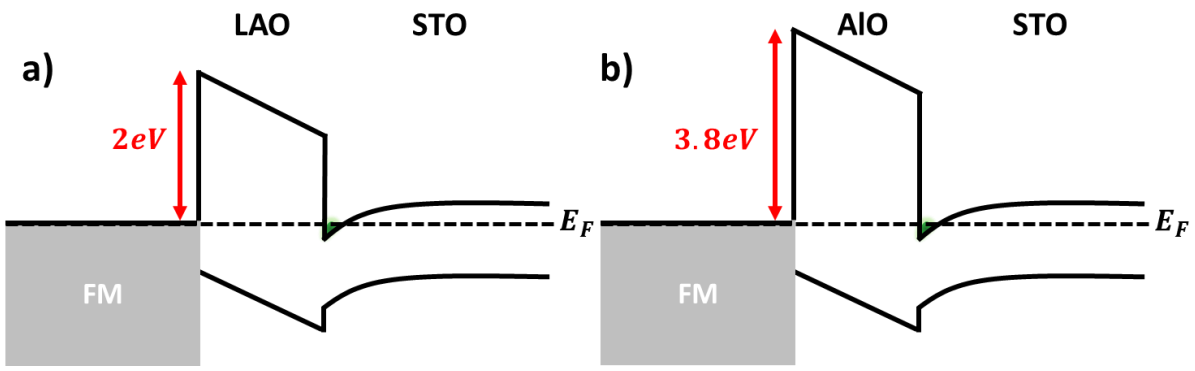

Figure IV-10 : Schematic band structure of the LAO/STO and AlO/STO giving the tunnel barrier height according to [154], [155].

The NiFe (2 nm) layer is deposited by the same sputtering method and protected by a 2 nm Au layer (to avoid oxidation). Figure IV-11 : displays the sheet resistance measured by Van der Pauw characterization of NiFe/LAO/STO, NiFe/AlO/STO with the 2DEG and NiFe/STO as a reference without the 2DEG contribution. The 2DEG contribution is calculate by a simple two conduction channel resistance model [150]. The resistance decreases with temperature to reach respectively $500\Omega_{\square}$ and $300\Omega_{\square}$ for the LAO and AlO systems, indicating the presence of the 2DEG.

The NiFe is used for its ferromagnetic properties to inject the spin-current into the junction under optical ultra-fast excitation. To investigate the high SCC efficiencies reported in these materials with FMR-SP [152], the samples are mounted inside a continuous helium-flow cryostat with an in-plane magnetic field relative to the sample to align the ferromagnetic

domains of the NiFe layer. The resulting THz emitted pulses are then detected using our TDS system presented in section III.2.9

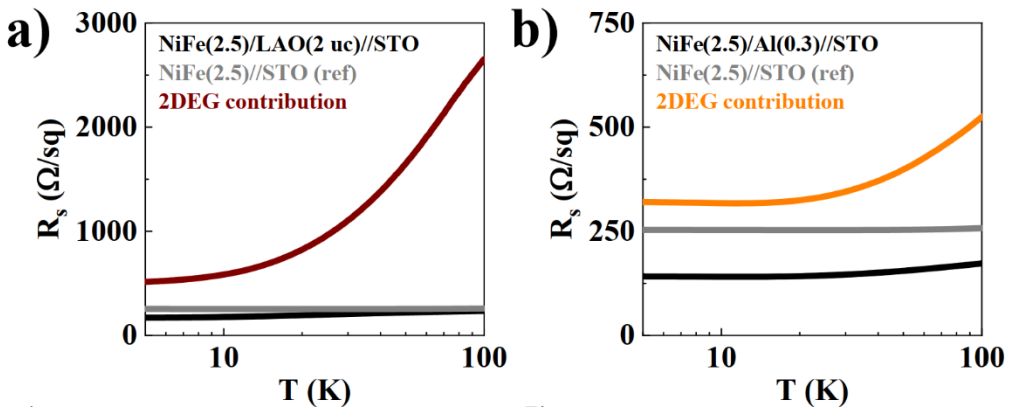

Figure IV-11 : Sheet resistance measured by Van der Pauw methode for NiFe/LAO/STO, NiFe/AlO/STO and NiFe/STO as a reference without the 2DEG contribution. The 2DEG contribution is provided by a simple two parallel conduction resistance.

Figure IV-12 describes the principle of THz generation from Rashba states, where an ultra-short optical pulse injects spin polarized current into the FM layer by ultra-fast demagnetization. The spin current diffuses to the LAO/STO interface where the 2DEG breaks the symmetry of the system by Rashba SOC to enable a IEE SCC, hence leading to THz emission. The NiFe(2)/LAO(1u.c.)/STO ($1\text{u.c.} = 0.4nm$) THz emission for different configurations of pump fluences and orientation of the magnetic field is displayed in Figure IV-13. Panel a) shows the THz electric field with the sample at 10k with a fluence of 200mW, b) the nearly linear electric field dependence over the fluence indicates no saturation effects and c) the rotation of the magnetic field (at room temperature) displays a nearly sin behaviour under the change of the magnetic field, which is a signature of the magnetic origin of the THz emission. This shows, to our knowledge, the first ultrafast IEE based THz emission from LAO/STO heterostructures. In the following section we will compare this emission to our Co/Pt reference.

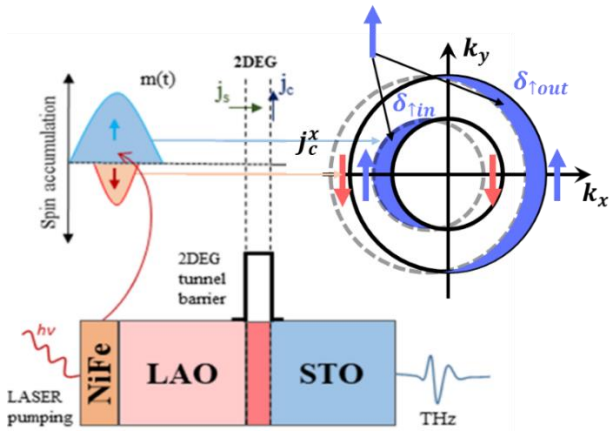

Figure IV-12 :Ultra-fast laser-induced IEE process due to the out-of-equilibrium spin density relaxing on the Rashba split-band.

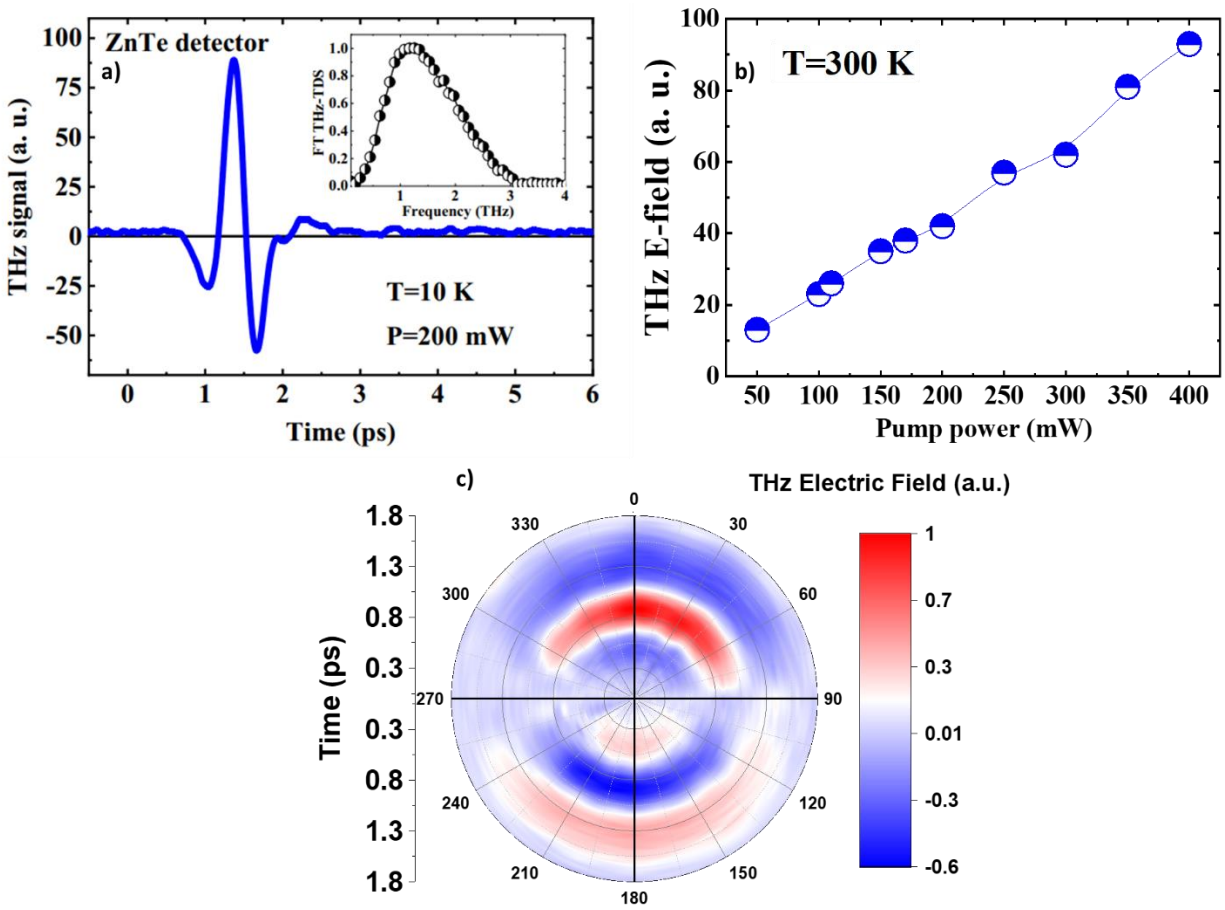

Figure IV-13: THz-TDS electric field acquired at low temperature (10 K) on NiFe(2)/LAO(1u.c.)/STO 2DEG under a 100-fs laser pulse of 200 mW power. insert) Fourier transform of the signal in the [0-4] THz spectral window. b) Amplitude of the maximum THz wave vs. Laser power excitation in the 0-400 mW range. c) Characteristic angular dependence (quasi sinus) of the THz-wave amplitude by varying the in-plane Co magnetization angle acquired at room temperature (300 K). The reversal of the polarity upon the rotation of the magnetization denotes a magnetic origin of the emission.

We now turn on AlO/STO structures where a giant SCC efficiency of 20nm has been reported [133]. The heterostructures studied in this section are made of oxides, consequently, the resistance of the tunnel barrier at the interface is tuneable via the AlO thickness. One should expect higher THz signals for thin layers.

Figure IV-14 compares now the emission of the AlO/STO for a variation of the barrier thickness (Al) along with the LAO/STO system described above for a temperature of 10K. To reference their THz emission to established FM/HM technology, a room temperature Co/Pt structure is used as a reference. The AlO/STO THz signal can be compared with the one obtained with LAO/STO structure in the exact same experimental conditions (10K). We note that the signal obtained for AlO/STO structure are smaller by a factor of 10 compared to LAO/STO and, quite strikingly almost constant for the three different Al thicknesses. These observations seem to discard any effects of carrier transport through the thin tunnel barrier, when compared to spin-pumping experiments, where the electron transmission is exponentially dependent on the thickness [156]. This seems to privilege a hot spin-polarized carrier transport above the AlO and LAO barriers, with a smaller energy barrier height for LAO/STO, before they relax into the STO spin-split Rashba bands on the Fermi surface. We note however that the emission of our Co/Pt is grater by a factor 10 and 100 when compared to LAO/STO and AlO/STO, respectively. Despite the larger SCC efficiency of AlO/STO reported in FMR-SP, this difference in THz emission with LAO/STO could be due to a larger barrier height in the former case (see Figure IV-10) for a hot spin-polarized carrier transport. The time trace of the NiFe/STO substrate without the 2DEG shows that for the NiFe/STO substrate without the 2DEG, an ultra-fast SCC does occur, but weaker by a factor 0.8 in respect to NiFe/LAO/STO with the 2DEG. Although this experiment demonstrates an ultrafast SCC by the generated spin accumulation at the sub-picosecond scale, there is also another type of conversion that occurs in NiFe(2)/LAO. One hypothesis could be the presence of another 2DEG at the NiFe/LAO interface.

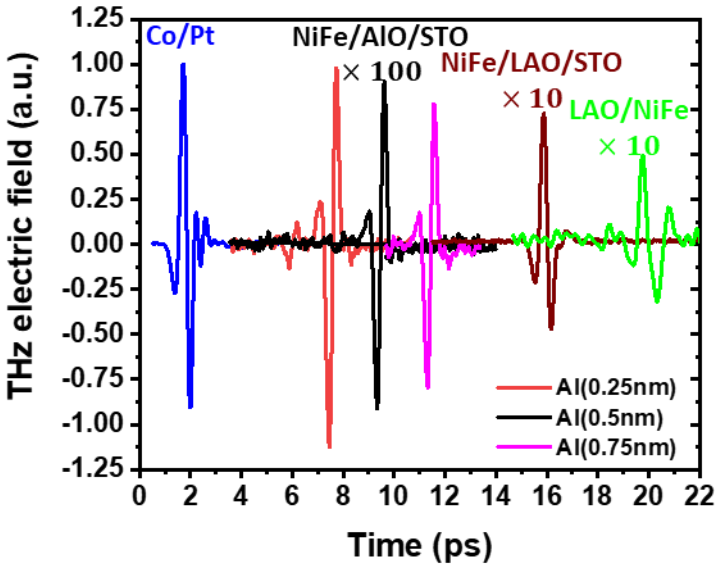

Figure IV-14 : Al dependence of NiFe(2nm)/AlO_3(x)/$SrTiO_3$ (AlO/STO) over the THz electric field compared to the emission of NiFe(2)/LAO/STO at 10K. A Co(2)/Pt(4) reference (room temperature) is shown to scale the emission to established FM/HM technology. This barrier thickness dependence seems to indicate a hot spin-polarized carrier transport above the AlO and LAO barriers. Lastly, the THz emission of the LAO/NiFe without the 2DEG reaches 0.8 of LAO/STO indicates that SCC originate from different contributions. Note the scale of the THz electric Field for the different structures.

IV.7.2 Temperature dependence of the THz emission

As the efficiency of the spin-charge interconversion of the system is reported to change over temperature, the THz emission should scale in the case of an IEE process. Here, we performed a temperature dependence on LAO/STO to investigate the impact on the THz electric field. Figure IV-15 displays the temperature dependence ranging from 4k to 300 K, of the LAO/STO THz emission with panel a) b) and c) being, respectively, the THz electric field time trace, its Fourier transform, and the peak-to-peak value of the THz fields. We denote two main effects. Firstly, the THz-TDS signal, is maximum in amplitude for low temperature, decreases with temperature by a factor ½ over the whole range. Secondly, for the spectrum, one can observe a dip in the frequency domain that shifts with temperature. This behaviour is assigned to the well documented [157] [158] phonon soft mode in $SrTiO_3$ (STO) and has been reported to be dependent on the strain of the STO layer [158]. The larger THz signals obtained for low temperatures could then arise from coupled phenomenon, the shift of the phonon mode and a potential better SCC conversion. This could also explain the minimum at 150K, where the phonon mode is the centre of our THz dynamic range in frequency.

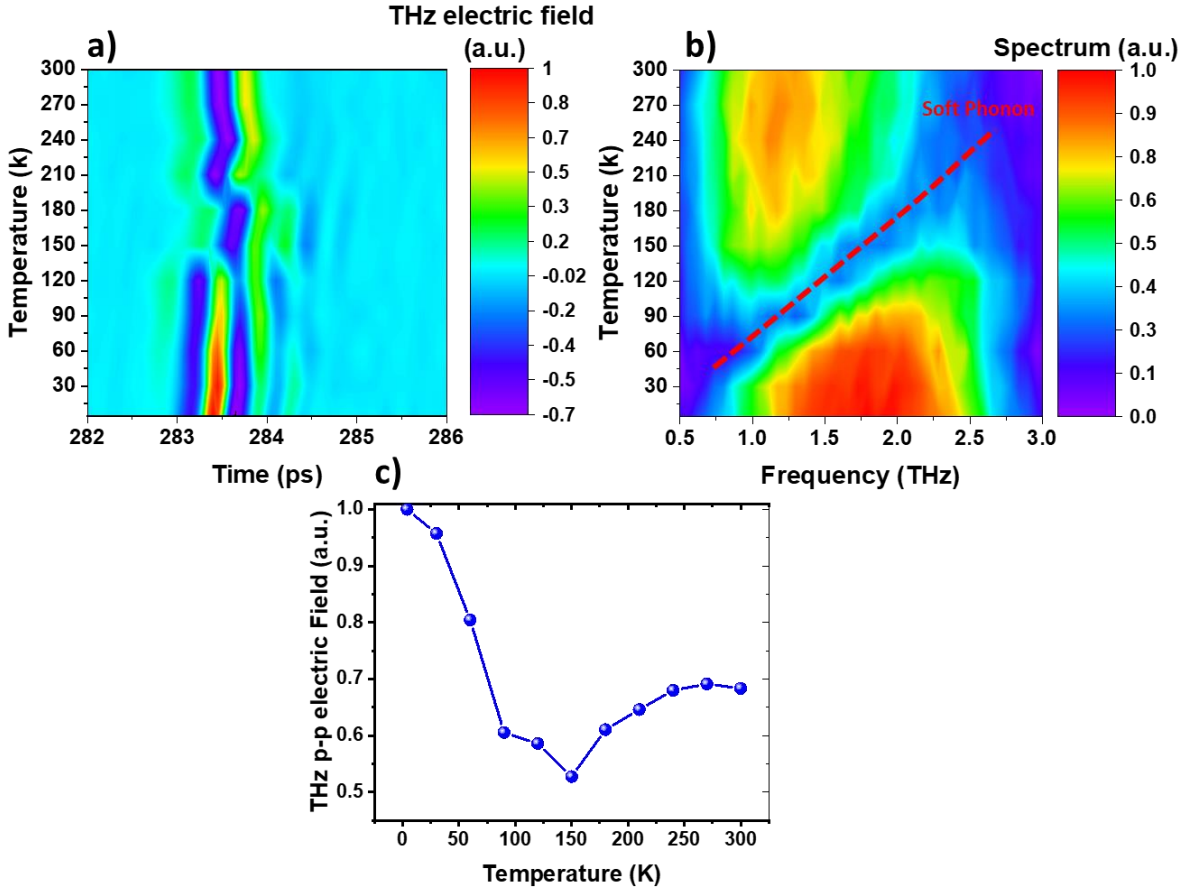

Figure IV-15 : THz Temperature dependence of NiFe(2nm)/LaAlO₃/SrTiO₃ a) in the time domain b) in the frequency domain. The THz electric field is maximum for low temperature. The soft phonon mode of the SrTiO₃ is clearly visible on the spectrum. The positioning of the phonon mode is similar to what has been reported in [157]. c) THz peak-to-peak value of the electric field recorded for the temperature variation.

In the next section, we will discuss the potential gate enhancement of the SCC highlighted in FMR-SP [130].

IV.7.3 Towards gate control of the THz emission

In LAO/STO and AlO/STO, the SOC can be tuned by an electrostatic potential[130], [159]. This is extremely attractive feature that could enable the design of electrically modulated spintronic THz sources. In this context we will discuss the impact of an additional gate to enhance the SCC efficiency, where the electronic 'filling' of the 2DEG can be modulated with the electrostatic potential of the gate. By implementing such a system, efficiencies of $\lambda_{IEE} = 6.4nm$ and $\lambda_{IEE} = 20nm$ were achieved for, respectively, LAO/STO and AlO/STO structures, which represent a conversion efficiency 32 and 100 times higher than Pt [130], [133]. As represented on Figure IV-16 a) by applying a negative or positive gate voltage ($V_g < 0V$ or $V_g < 0V$) it is possible to deplete or fill the 2DEG with electrons

[160]. In the latter case electrons can escape from the 2DEG to be trapped in localized states in the STO substate. Thus, the Fermi level shifts with this electrostatic doping and it is possible to access different Fermi surfaces with different SOC for SCC as, depicted on Figure IV-16 b) and c).

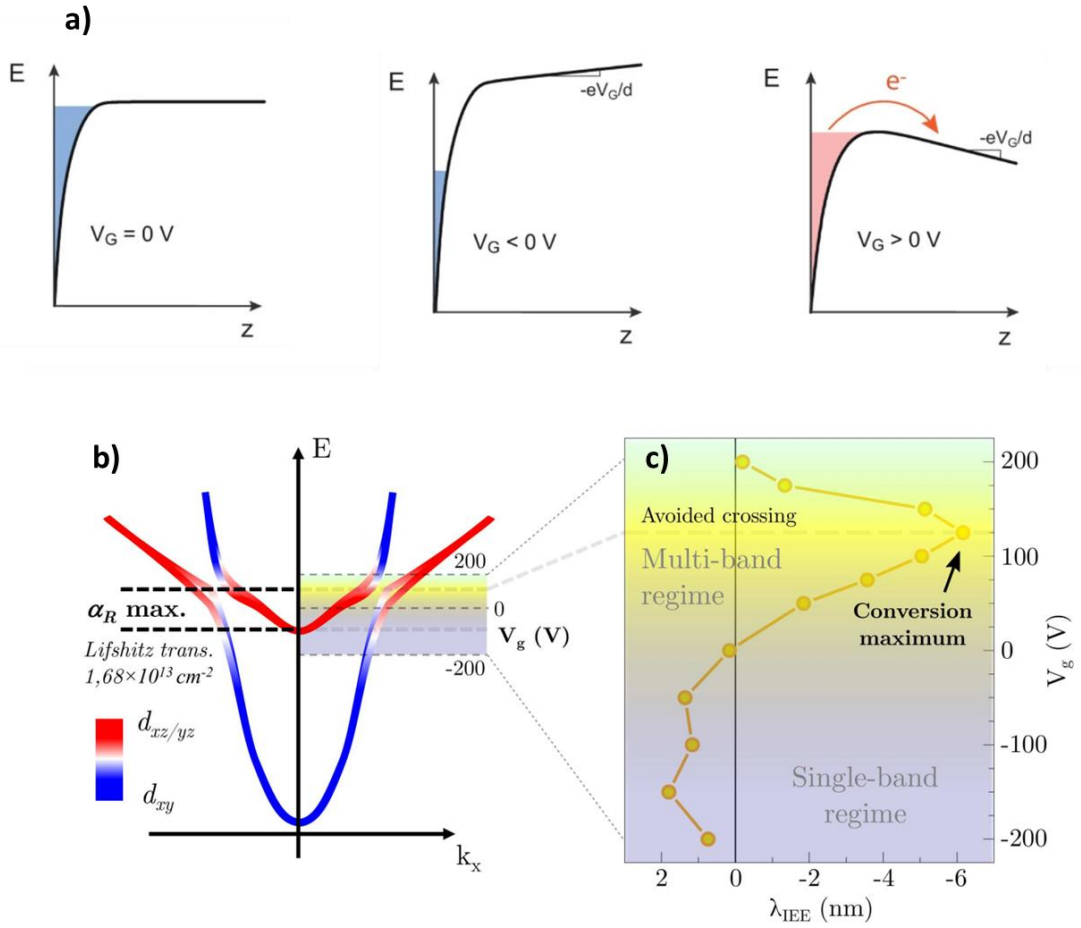

Figure IV-16 : Origin of the SCC gate enhancement demonstrated for FMR-SP (in the vicinity of the Fermi level). a) Representation of the 2DEG, for 0V gate voltage ($V_g = 0V$) the 2DEG is at equilibrium, the application of a gate voltage will fill or deplete the 2DEG for respectively, positive, and negative gate voltage ($V_g < 0V, V_g$ <0V). When the gate voltage is positive, electrons will escape the 2DEG to reach localized states in the STO substrate, resulting in an electrostatic doping. The bands are tilted by $-eV_g/d$ with d being the thickness of the STO substrate. b) c) Represent the bands of the LAO/STO structure and highlights the tunability range of Fermi level and thus the SCC for different biases with the maximum of SOC in the range of the gate voltage. Adapted from [53], [160], [161].

Experimentally a Au gate is sputtered and patterned onto the LAO/STO structure. The sample is then mounted on a copper block for cryostat mounting. The top gate is wire-bonded to a Au contact mounted on an insulating ceramic pad. The bottom contact is connected by direct contact with the copper block (see Figure IV-17). The copper block is electrically

insulated from the cryostat by inserting a 20µm thick film of Teflon between the two. This step ensures that no high voltage bias would be present on the lock-in amplifier ground. The sample is mounted in the cryostat within an in-plane magnetic field relative to the sample provided by a permanent magnet. The cryostat is then mounted in our TDS system to analyse the THz emission and the effect of the gate at 4K.

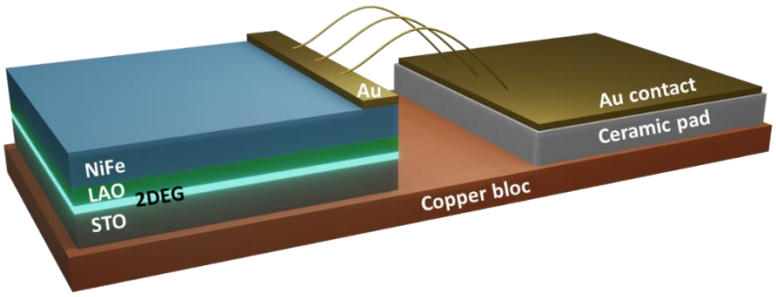

Figure IV-17 Mounting of the LAO/STO sample in the cryostat for gate tuning of the THz emission. The back contact is reported through the copper block in the cryostat.

The results are displayed in Figure IV-18. The panel a) and b) show respectively, the 2D time traces acquired by our TDS system and the peak-to-peak value of the THz field across the range of applied voltages. We can see a small increase of the electric field for high bias in the main THz peak (0.5ps) and a decrease of the peak slightly below 1ps. The 2D spectrum on panel c) highlights the presence of the soft phonon mode reported above which indicates the effective temperature of the sample of 130K (see Figure IV-15 b)). This temperature difference is due to the thin Teflon layer between the cold finger and the copper block to ensure electric insulation of the instrumentation. Therefore, lower SCC conversion efficiency is expected at this temperature. Although we can notice that the soft phonon mode is fixed in frequency over the full range of gate voltage, we can identify 2 contributions to the spectral peaks A (0.5 to 1.5 THz) and B (1.8 to 2.6 THz). For high gate voltage, peak A becomes larger in bandwidth and magnitude whereas peak B gets weaker. This behaviour is clearly visible when one integrates the peaks in panel c). Figure IV-16 showed that the SCC efficiency changes sign between positives and negatives biases with an amplitude of $\sim 8\, nm$. Here for THz emission, although we do not report neither drastic THz enhancement nor polarity reversal, higher (lower) THz fields can be generated for positive (negative) biases. This could be due to the higher excitation energy of spin polarized hot electrons accessing higher energy bands with less SOC. An effect is nevertheless visible with the addition of a gate but the optimisation of the experiment to go towards lower temperature could be

beneficial for more conclusive results. This is because of the efficiency of the SCC should be higher and the soft phonon mode would not blind potential effects.

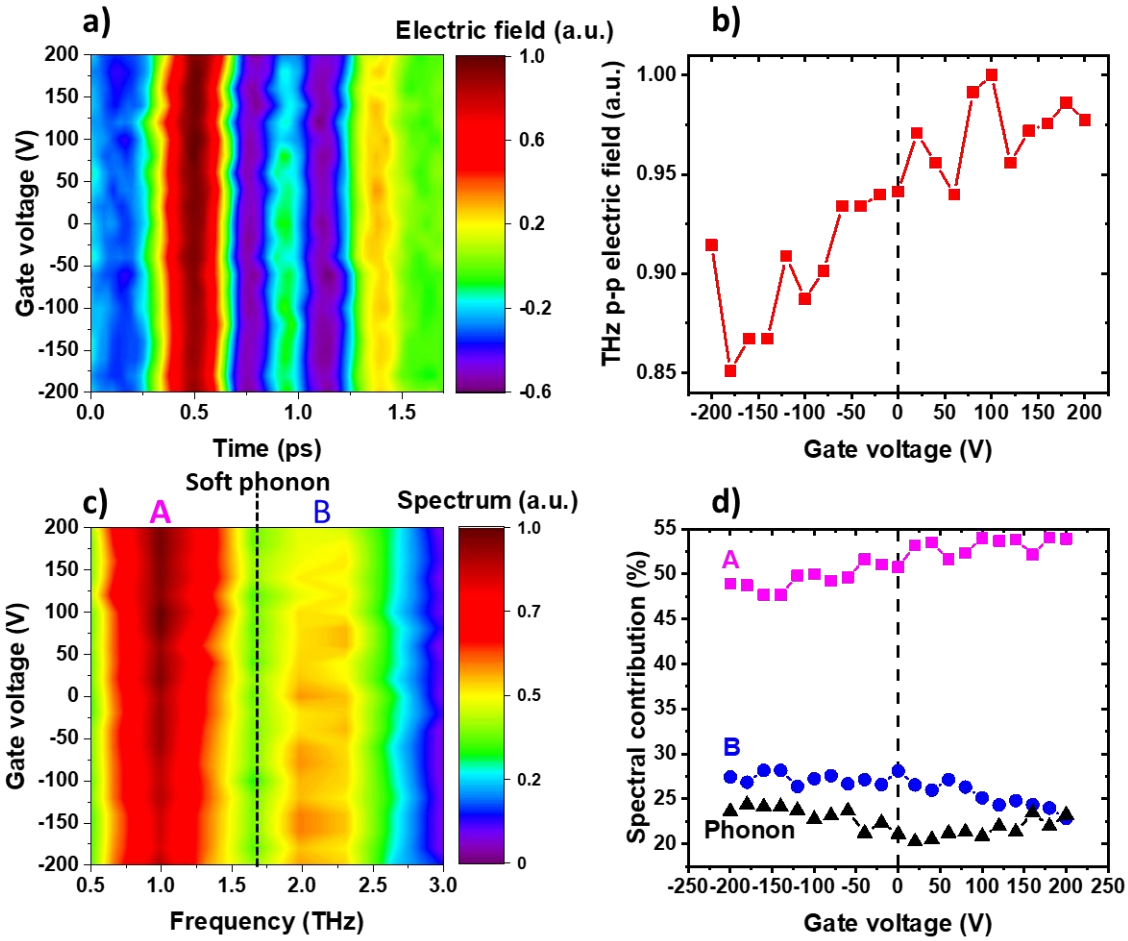

Figure IV-18 a) b) and c) 2D TDS electric fields time traces, THz peak-to-peak electric fields and spectrums for different gate voltages. For high bias the electric field is stronger on the main THz peak (0.5ps), the peak slightly below 1ps is decaying, On the spectrum we note the soft phonon mode of SrTiO3 which indicates an effective temperature of 130K. We can identify two peaks A and B around the soft phonon. A is increasing in bandwidth for high positives biases whereas B shrinks. One must note that the soft phonon mode is fixed in frequency over the range of gate voltage. c) Integrated peaks A, B and the soft phonon mode. The spectral width of the soft phonon is not fixed and reaches a minimum around 0V (the phonon contribution is the smaller than A and B).

Regarding the presented data, we report THz emission resulting of ultrafast SCC from LAO/STO and AlO/STO based structures, as well as identifying a SCC process that contributes to the THz emission at the NiFe/STO interface. By performing the tunnel barrier thickness dependence, we shown that in contrast to FMR-SP experiments, electronic transport seems to privilege a hot spin-polarized carrier transport above the AlO and LAO barriers which can explain the THz emission difference from both structures. The temperature

dependence on the THz electric field showed the temperature tuneable soft phonon mode of STO. For the gate experiment, the recorded THz emission is lower than Co/Pt despite the giant increase in efficiency of SCC reported in FMR-SP experiments. One explanation could be that in the generation of spin polarized current via ultrafast optical pulses possess an energy well above the one used in SP-FRM experiments. The hot spin polarized electrons are then injected higher in energy than the Fermi surface crossing (see Figure IV-15 b)) resulting in lower SOC tuning range than demonstrated for FMR-SP.

Another promising system to overcome these limitations and increase the THz field higher than FM/HM based THz sources are topological insulators (TIs). As mentioned in section IV.3, by their single Fermi contour in TIs, the IEE based SCC efficiency should be higher than Rashba systems to reach in an ideal case of 100% [108].

IV.8 THz emission from topological insulator

Similar to Rashba systems, TIs rely on ultrafast IEE SCC to generate THz waves. Their single Fermi contour of their dispersion potentially makes the IEE process more efficient, and their increased robustness due to the topologically protected energy dispersion make them particularly interesting for the design of high performance spintronic THz sources. In this section we will investigate a Bi_2SnTe_4 based heterostructure (BST). These samples were provided by the group of Athanasios Dimoulas from Greece in the frame of the European project SKYTOP. A recent study from the research group indicates that pure 2D surface state transport can be reached in this material for thin layers. [162]. To investigate the SCC, we analysed the THz emission of this material for a thickness variation of the Bi_2SnTe_4 layer. The complete heterostructure is composed of Si(111)/InAs(35nm)/Bi_2SnTe_4(x)/Co(4)/Al(2nm) with x = (0; 7; 9.8; and 22.4) nm corresponding to respectively 0; 5; 7; and 16 septuplet (SL corresponding to seven atoms rows). The samples were grown by molecular beam epitaxy on a Si(111) substrate. InAs is used as a buffer to tune the lattice parameter of Si to Bi_2SnTe_4. The Al is used as a cap layer to avoid Co oxidation. The detailed fabrication process can be found in [162]. The samples were placed in our TDS as previously within an in-plane magnetic field relative to the sample to align the ferromagnetic domains of the Co layer. We first analysed the THz time traces from the Si/InAs substrate and are shown in Figure IV-19 where the THz electric field polarity is conserved for opposite magnetic field directions. This points to the non-magnetic THz emission origin and could be ascribed to optical rectification in InAs [163].

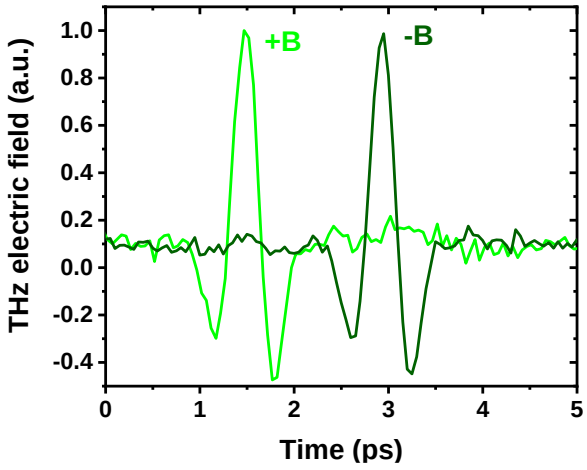

Figure IV-19 : THz emission from Si/InAs substrate for opposites in plane magnetic fields ($\pm B$). The THz pulse conserve the polarity upon switching the magnetic field direction. This points the non-magnetic origin of the emission.

THz time traces from the whole set of heterostructures of BST along with a Co/Pt reference are available in Figure IV-20 a). Note the scale of the Co/Pt reference (divided by 10). We can clearly see that the THz emission is maximum for the thinner 5SL of BST reaching 1/5 of Co/Pt. The THz signal then decreases for an increase of thickness in BST on Figure IV-20 a) and d). This behaviour might be explained by a different contribution of bulk and surface state SCC. Indeed, the growth of such structures is complex, and can results in different Sn/Bi ratio for each sample. Figure IV-21 shows ARPES measurements of Fermi surfaces at the Fermi level indicating noticeably clear surfaces states for all investigated sample, but also nonequivalent bulk states, with 7SL being the most impacted. According to [162], lower Sn/Bi ratios and thinner layer favour material with pure surface state. Thus, the investigation of additional samples with different thicknesses and Sn/Bi ratios could assess the contribution of bulk and surface state in the SCC. Nevertheless, Figure IV-20 b) highlights the flip of the THz electric field (5 SL) polarity upon reversal of the magnetic field pointing the emissions magnetic origin. In the same figure, the InAs contribution to the THz emission is visible as the magnitude of both traces are not equal. The detection limited spectrum shows similar traits to our Co/Pt reference.

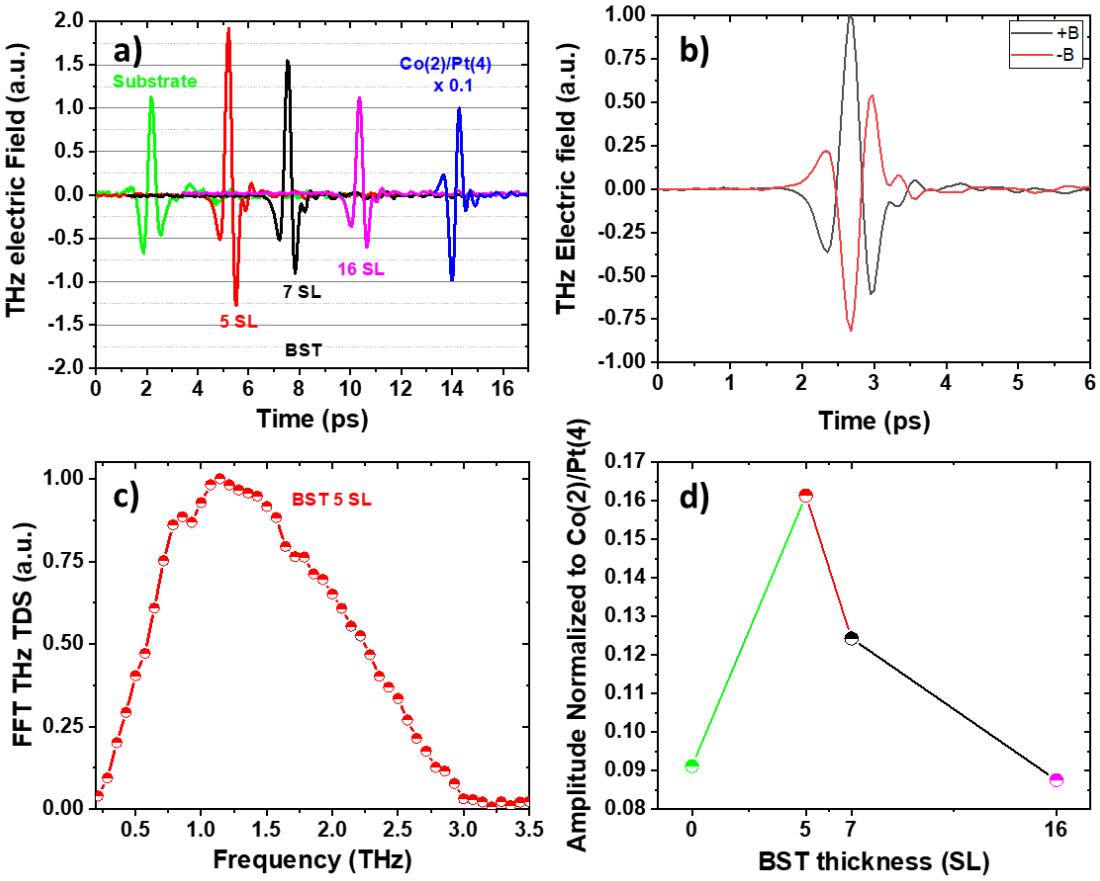

Figure IV-20 : THz emission from Si(111)/InAs(23nm)/Bi_2SnTe_4(x)/Al(2nm) a) TDS time traces of BST thickness dependence, Si/InAs substrate, and Co(2)/Pt(4) reference divided by 10, shifted in time for clarity. b) Inversion of the THz Electric field polarity (5 SL) upon reversal of the magnetic field which highlight the magnetic origin of the emission. c) Spectrum of the emission of 5 SL BST. d) Amplitude of the THz signal for different thickness of BST normalized over Co(2)/Pt(4), for 5 SL of BST, 16% Co(2)/Pt(4) is reached. The emission decreases quickly for an increase of BST thickness which could correspond to a quantum phase transition of the BST.

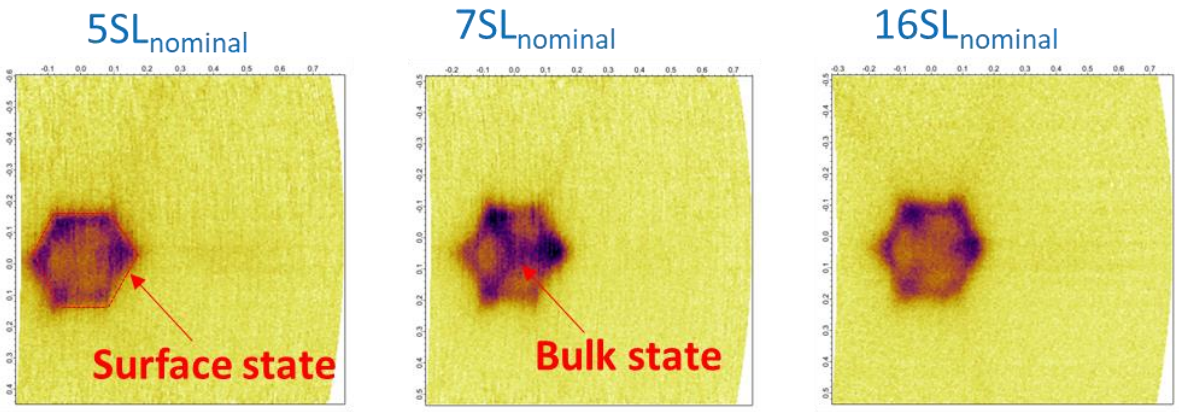

Figure IV-21 : ARPES measurement, Fermi surface at the Fermi level in function of kx ky of Si/InAs/Bi2SnTe4 for the different thicknesses investigated by THz TDS. We can notice a clear surface state, but nonequivalent bulk states (darker areas). Measurements by the authors of [162].

This set of data proves that we observe an ultra-fast SCC in TI materials that leads to THz pulses. The origin of this SCC is still in discussion and to decouple and precisely assess the bulk and surface state contributions, would require further samples.

IV.9 Conclusions and perspectives

In this chapter we have investigated new and promising types of THz spintronic emitters using 'Quantum' materials, beyond established FM/HM heterostructures. Half-metallic ferromagnetic Heusleurs, Rashba interfaces and a topological insulator were investigated as a proof of concept.

1) **Ferromagnetic Heuslers**. Our study on Co_2MnGa shown that thin layer provides a THz enhancement up to a factor 1.33 in respect to our Co/Pt reference. We ascribed this increase to i) a competition of opposite SCC from Co_2MnGa and Pt, and ii) an important spin polarization thus larger polarized spin current. We believe that this platform has a strong potential in the development of strong spintronic THz sources with considerable room for optimization. To this end, we proposed to investigate potential self SCC by coupling this material with a non-active metal such as AuW and optimizing the emission by performing a thickness dependence of the Co_2MnGa layer. Moreover, a trilayer structure can be designed to enhance further the THz emission of Co_2MnGa based devices, where the alloy is embedded between two HMs with opposites SHA.
2) **Rashba interfaces**. We also investigated LAO/STO and AlO/STO 2DEG oxide-based platform, where giant IEE SCC efficiencies have been reported. We indeed showed ultrafast IEE based THz emission for both systems. The AlO/STO barrier thickness study indicated a hot spin-polarized carrier transport above the AlO and LAO barriers, in contrast to FMR-SP that is based on tunnelling. We further note that LAO/STO and AlO/STO showed lower THz emission than the Co/Pt reference by respectively a factor 10 and 100 (explained by a higher barrier height in the latter case). Higher THz signal (50%) was obtained at cryogenic temperatures on LAO/STO, albeit the exact reason is not clear at this time, with STO soft phonon mode seemingly playing an important role in the temperature response. We also performed gate measurements on LAO/STO at cryogenic temperatures, to investigate the gigantic SCC efficiencies reported in FMR-SP techniques. We only showed a slight (15%) increase range of the peak-to-peak THz field with the gate. We highlighted that the STO phonon is active, indicating an effective temperature of 125-130K that most likely limits the SCC. Further optimisation should enable to reach lower temperatures. However, it should be noted that laser induced spin polarized hot electrons results in much higher energy

excitation, unlike FMR-SP where the gate targeted band crossing giving a strong SOC and is easily reachable.

3) **Topological Insulators**. Finally, we analysed the THz emission from a topological insulator. A thickness dependence revealed that strong THz emission can be reached for few layer of TIs, although it a 16% to that of Co/Pt. This correlates well with ARPES measurements that highlighted indeed a clear surface states enabling IEE type SCC for the same sample. However, in the case of other layers there also appears to be contributions from bulk states. The precise conversion mechanism requires further investigations to disentangle the effects of the surface and bulk contributions to the THz emission.

As can be seen above, THz emission TDS provides a relatively simple, non-destructive technique to investigate new spintronic quantum materials that exhibit unique spin-dependent properties and to access their SCC dynamics. As further insights are gathered into these materials, it is expected that they will impact further the generation of broadband THz pulses, as well as a potentially other exotic phenomena at these quantum interfaces.

Chapter

V

V Resonant pumping and broadband probing of THz intersubband polaritons

In this chapter we will discuss the development of THz polaritonic structures to investigate scattering mechanisms, nonlinearities and the possibility of THz gain. This work was carried in the context of a European project "MIR-BOSE" (https://mir-bose.eu/) with the final aim of demonstrating an intersubband polariton laser. This would enable novel THz sources by translating and adapting concepts from traditional excitonic polaritons to intersubband polaritons. My role in this project was to perform resonant optical pumping on a THz polariton system, where a THz cavity is coupled to an intersubband transition, to demonstrate THz gain. To study such a system, we developed a THz time domain spectroscopy setup to probe the time resolved broadband spectrum, while resonantly pumping one of the polariton branches with a monochromatic quasi-CW THz quantum cascade laser. Through careful design of the transitions and the pumping scheme, indications of nonlinearities potentially precursor of uncoherent polariton scattering are highlighted, which is an important milestone towards THz intersubband polariton. In this chapter, we will provide:

- Concepts of ISB polaritons, condensation, coherent emission followed by a brief state-of the art of ISB polaritons.
- An introduction to intersubband polaritons resulting from the strong coupling regime between a THz photonic mode and an electronic transition in a quantum well.
- A theoretical model, developed by the collaborator C2N, capable of gauging the light-matter coupling in these structures, which is extensively applied to the experimental data.

- Details of the pump-probe system. Introduction to quantum cascade lasers that are used as a resonant pump and most importantly their integration in our TDS system. We detail the THz TDS setup developed for optical coherent pumping of polaritonic samples with an emphasis on the geometry of the pump beam.

- Properties of investigated THz cavities, along with experimental reflectivities that are used as an important metric.

- Reflectivity spectrum with resonant pumping of THz intersubband polaritons by varying a range of parameters (pumping power density, temperature and pump angle).

- Details on a possible scattering mechanism assisted by a Brillouin folded mode.

- Finally, preliminary data of nonlinear reflectivities of polaritonic sample with only a narrowband pump beam (no probe). This is coupled with preliminary simulations from the INO-CNR BEC centre in Trento will be presented to assess the origin of the frequency shifts and reflectivity changes under resonant pumping.

We will end this chapter by presenting the conclusions and perspectives of this ongoing work.

Chapter V

V.1 Contributions

As stated in the introduction, this research has been carried in the context of the European project MIR-BOSE. This work is the result of close collaborations between the C2N in Paris providing their expertise on polariton modeling and sample fabrication, the University of Leeds in the United Kingdom for the development of high power quantum cascades lasers and samples growth, and the INO-CNR BEC center in Trento Italy providing a theoretical framework. My contribution was to design, build and optimize the THz TDS capable of probing polaritonic systems with a flexible geometry and experimentally investigate resonant pumping of the polaritonic system. I also continuously coordinated all our partners in a discussion loop to further optimize the experiments and seek the ultimate proof of THz gain in intersubband polaritons.

V.2 Intersubband polaritons

Polaritons are bosonic quasi-particles resulting from a superposition of a photonic mode and a matter transition. Numerous matter systems can be strongly coupled with photons resulting in different polaritons types e.g. Magnon-Polaritons, Exciton-Polaritons, vibro-polaritons… In semiconductors, exciton polaritons, which rely on electron-hole pairs from interband transitions coupled to a cavity, are one of the most widely studied since their discovery in 1992 [164]. Another more recent type is the intersubband (ISB)[1] polariton, experimentally demonstrated in 2003 [165] by investigating the angle resolved reflectivity of a resonator coupled with ISB transitions in series of GaAs/AlGaAs quantum wells (QWs) (see Figure V-1). As these polaritons rely on ISB transitions, the matter transition energy can be widely engineered by changing the dimensions of the QWs and the alloy concentration (see section V.4.1). In addition ISB polaritons have the advantage of maintaining a high carrier density as they are not restricted by the Mott transition limit [166]. When compared to exciton polaritons, this could permit potentially a lower lasing threshold and higher output power [166]. ISB Polaritons (and polaritons in general) originate from reaching the so-called strong coupling regime where a trapped photon inside a cavity needs to be coherently absorbed and reemitted several times by an ISB transition of a QW before escaping the cavity. In other

[1] ISB transitions are transitions between confined electronic states in one band (typically the conduction band) of a quantum wells, details are given in section V.4.1

words, to reach this strong coupling the energy exchange rate between light and matter should be stronger than their decay rates. If this is achieved, the eigenstates are now mixed states of electronic and photonic excitations split into two new states called the upper and lower polaritons (UP and LP), with a splitting in energy proportional to the strength of the light-matter interaction given by the Rabi frequency Ω_R. Figure V-2 depicts the formation of ISB polaritons by combining a matter part originating from an ISB transition between two confined states in a QW and a photonic component defined by the cavity with both transitions at the same frequency. This light and matter coupling gives rise to the UP and LP states separated by $2\Omega_R$.

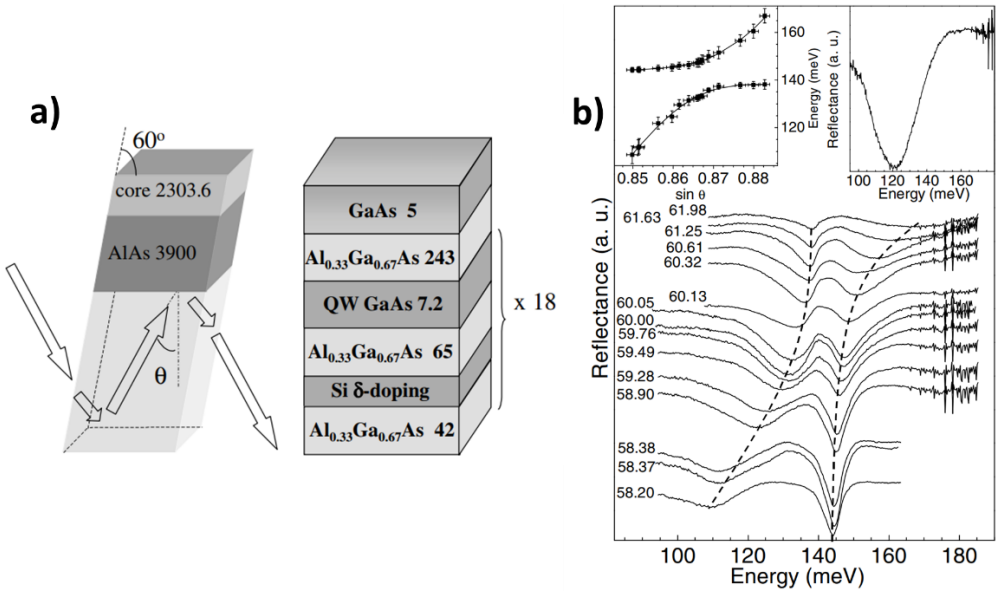

Figure V-1 : First demonstration of ISB polaritons in 2003. a) Total internal reflection waveguide and QW structure. b) top left insert: polariton dispersion, top right insert: Spectra recorded under TE polarization (only cavity observer, no polariton signatures), main panel: Angle resolved reflectivity of microcavity (at 10K and TM polarized). The anticrossing at 60° is the signature of strong coupling.

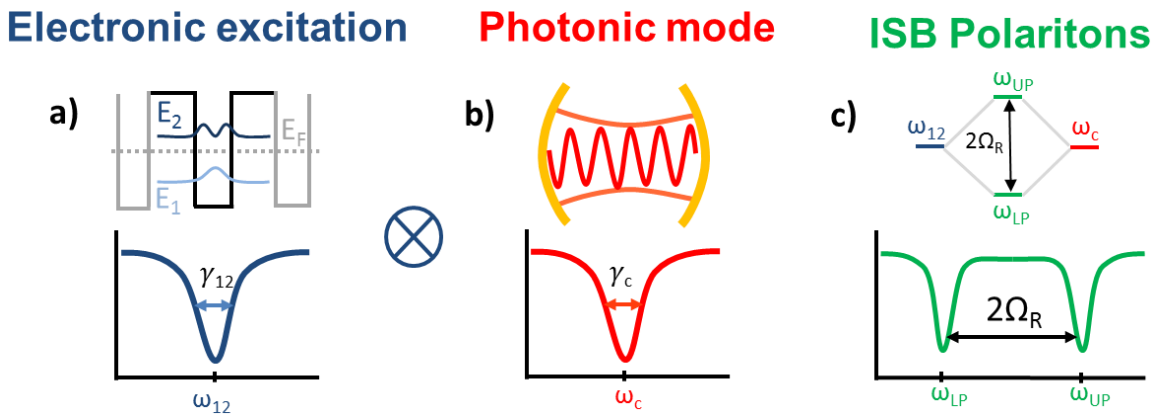

Figure V-2 : ISB polaritons formations. a) Transition between confined electronic state in a quantum well, b) Photonic dispersion of a cavity, c) Interaction of light and-matter leads to a superposition of states called ISB Polaritons with $2\Omega_R$, the Rabi splitting giving the strength of coupling.

A ISB transition coherently coupled with a cavity mode can be describe by the Jaynes-Cumming Hamiltonian [167]. Our ISB system, corresponding to a matter transition, is described here by a fundamental and an excited state written respectively $|\psi_{1,k}\rangle$ and $|\psi_{2,k}\rangle$ of energy E_1 and E_2. The material Hamiltonian of this two-level system is described by equation (V-1). Considering the photon energy $\hbar\omega$ in the cavity, the photonic Hamiltonian can be written as equation (V-2) where $a^\dagger$ and a are the creation and annihilation operators[168], [169].

$$H_{mat} = E_1|\psi_{1,k}\rangle\langle\psi_{1,k}| + E_2|\psi_{2,k}\rangle\langle\psi_{2,k}| \qquad (V\text{-}1)$$

$$H_{photon} = \hbar\omega(a^\dagger a + \frac{1}{2}) \qquad (V\text{-}2)$$

The Hamiltonian, describing the interaction between the ISB electrical dipole and the electric field E, is written as equation (V-3) where $\hbar\Omega_{\mathrm{R}} = \sqrt{\left(\frac{e^2 f_{12}}{4\epsilon_0\epsilon_\infty m^* V}\right)}$ is the coupling strength with V the volume of the cavity mode, f_{12} the oscillator strength, a quantity which denotes the probability of ISB absorption, ϵ_0 and ϵ_∞ are the dielectric function of the QW for respectively low and high frequencies and V the volume. The complete Jaynes-Cumming Hamiltonian describing the photonic and electronic oscillators of energies $\hbar\omega$ and E_{12} (Energy of the ISB transition) coupled by $\hbar\Omega_{\mathrm{R}}$ is then written as equation (V-4).

$$H_{int} = -i\hbar\Omega_R(|\psi_{1,k}\rangle\langle\psi_{1,k}|a + |\psi_{1,k}\rangle\langle\psi_{1,k}|a^\dagger) \qquad (V\text{-}3)$$

$$H_{JC} = H_{mat} + H_{photon} + H_{int} = \begin{vmatrix} \hbar\omega_c & i\hbar\Omega_R \\ -i\hbar\Omega_R & E_{12} \end{vmatrix} \qquad (V\text{-}4)$$

The eigenstates are the intersubband polaritons (LP and UP) described above as mixed states of electronic and photonic excitations and can be written by equation (V-5) [170] with $\alpha_{LP/UP}$ and $\beta_{LP/UP}$ being respectively the light and matter contribution of the polariton called Hopfield coefficients. The energy dispersion of the LP and UP can be expressed as function of the detuning $\Delta E = E_c - E_{12}$ with E_c corresponding to the cavity mode energy and to the

eigenvalues described in equation (V-6), plotted in Figure V-3 along Hopfield coefficients. In this energy dispersion, $2\Omega_R$ accounts for the anti-crossing where the ISB transition and the cavity mode are resonant and the polaritons are equivalently dressed between matter and light, giving the maximum interaction between the two states. The bare cavity and the ISB transition energies (E_{12} and E_c) are also represented. Note that when the Hopfield coefficients are either 0 or 1 the polariton are respectively dressed fully matter or light. This can be seen in the energy dispersion, where the polariton branches asymptotically follows either the ISB transition or the bare cavity dispersion thus inheriting the corresponding character.

$$\begin{cases} |LP\rangle = \alpha_{LP}|\psi_{1,k,}1\rangle + \beta_{LP}|\psi_{2,k,}0\rangle \\ |UP\rangle = \alpha_{UP}|\psi_{1,k,}1\rangle + \beta_{UP}|\psi_{2,k,}0\rangle \end{cases} \quad (V\text{-}5)$$

$$E_{LP/UP} = \frac{1}{2}(E_{12} + E_c) \pm \sqrt{\Delta E^2 + (2\hbar\Omega)^2} \quad (V\text{-}6)$$

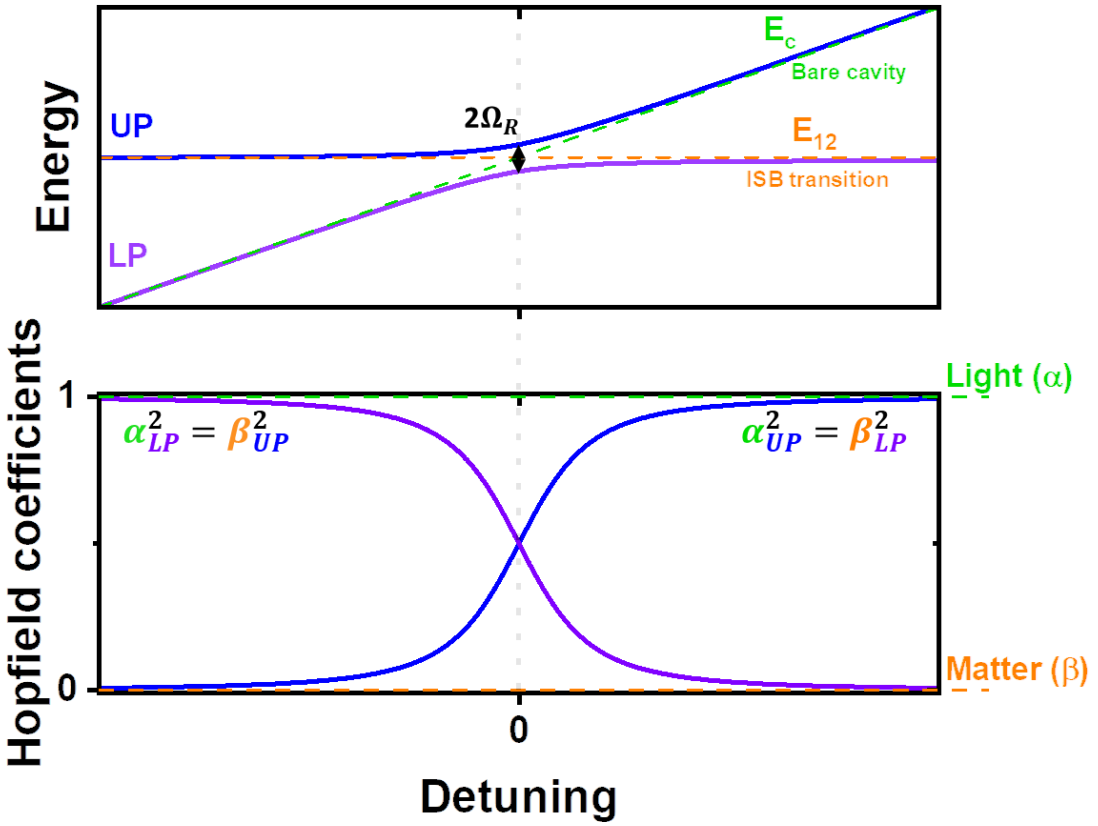

Figure V-3 :Energy dispersion of LP and UP in function of the detuning energy (ΔE), Ω_R accounts accounts for the anti-crossing where the ISB transition and the cavity mode are resonant and the polaritons are equivalent mixed between matter and light giving the maximum of interaction between the two states. The bare cavity and the ISB transition are also represented in respectively green and blue dashes ($E_{12}$and E_c). The bottom panel describes Hopfield coefficients of the LP and UP with 0 and 1 corresponding to respectively polaritons that are fully matter and light. Adapted from [168].

The Jaynes-Cumming Hamiltonian depicts the case of a single ISB transition coupled to a cavity mode. However, reaching the strong coupling with one single emitter is difficult. An alternative approach is to design structures with multiples (identical) emitters that act as a collective excitation.

In the case of multiple quantum well structures, the number of quantum emitters (N) is the number of electrons from doped donors ($N_{2D}N_{QW}$). It is then possible to enhance the Rabi splitting by a factor $\sqrt{N}$ as described by equation (V-7) with N_{2D} and N_{QW} being respectively the electronic density and the number of QWs [169]. This is an important concept to reach the strong coupling regime and is further discussed in section V.4.1.1 in the concept of the depolarization shift.

$$2\Omega_R = \sqrt{\left(\frac{N_{2D}N_{QW}e^2 f_{12}}{4\epsilon_0\epsilon_\infty m^* L_{cav}}\right)} \qquad (V\text{-}7)$$

V.2.1 State of the art

In this section, we will address the current state-of-the-art of polaritons with a focus on ISB polaritons.

The first demonstration of strong light-matter interaction in microcavity in the THz range using ISB transitions has been demonstrated by Todorov and co-worker in 2011 [171] at cryogenic temperature (see Figure V-4 a)). In this study, the authors designed a new type of cavity based on a metal dielectric metal structure providing a subwavelength confinement of the electromagnetic field, thus enhancing the light-matter coupling. Using LC resonators coupled with intersubband transitions from parabolic QWs (where energy level are equally spaced in energy) the research group of Jérôme Faist even showed room temperature THz strong coupling [172] (see Figure V-4 b)). These achievements opened the way towards another type of coupling discussed in next section.

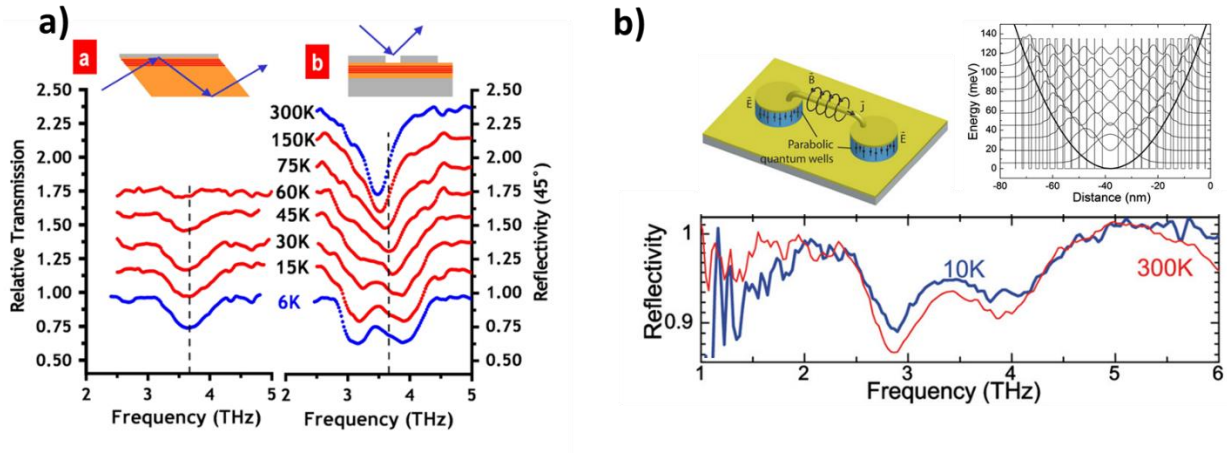

Figure V-4 : a) First demonstration showing THz strong coupling based on ISB transitions of QWs. The left and right spectrum show respectively the ISB transition obtained from multi-pass transmission measurements in function of temperature and the reflectivity of their metal dielectric metal structure [171]. b) LC resonators strongly coupled with ISB transition from parabolic QW at cryogenic and room temperature [172].

V.2.1.1 Beyond the strong coupling regime

As well that enhancing the Rabi splitting with large number of QWs and increasing the doping, another method is to engineer the mode volume of the optical resonator as $2\Omega_R = \omega_p \times \sqrt{fw}$ with ω_p and fw being respectively the plasma frequency of the many body electrons (see section V.4.1.1) and an overlap factor between the optical mode and the QWs. These two degrees of freedom enabled the scientific community to target the ultra-strong coupling regime for ISB polaritons. Here, the Rabi splitting becomes a significative fraction ($\eta = \Omega_R/\omega_c > 10\%$) of the bare transition (ω_c). In this case, processes do not conserve excitations in the system, leading to a ground state containing virtual excitations where the generation of quantum vacuum fluctuations is possible (Casimir radiation). This has many applications, from nonlinear optics to protected quantum information processing. Such a prediction for ISB polaritons was published in 2005 by Ciuti and co-workers [173]. Historically, the firsts demonstrations of this ultra-strong coupling was achieved in the late 2000s by coupling ISB transitions with plasmon waveguides in the Mid-IR[174]–[176]. Shortly after, metal-insulator-metal cavities coupled with ISB transitions also showed signatures of the strong-coupling regime[171], [177] in the Mid-IR and THz domain [178]. The possibility to non-adiabatically modulate the light-matter interactions at a sub-cycle time scale was also demonstrated in [174], [179] (Figure V-5 a)) providing a promising platform for Casimir radiation [173]. The ultra-strong coupling has also be achieved with Landau

polaritons [180], [181] relying on doped QWs embedded in microcavities with the addition of transverse magnetic field. This approach permits to reach very large light-matter interactions with [182] (Figure V-5 b)) holding the record of the largest observed light-matter coupling strength ($\eta = \Omega_R/\omega_c = 143\%$). To get a broader picture on the ultra-strong coupling development and applications, the interested reader will find useful reviews in [183], [184].

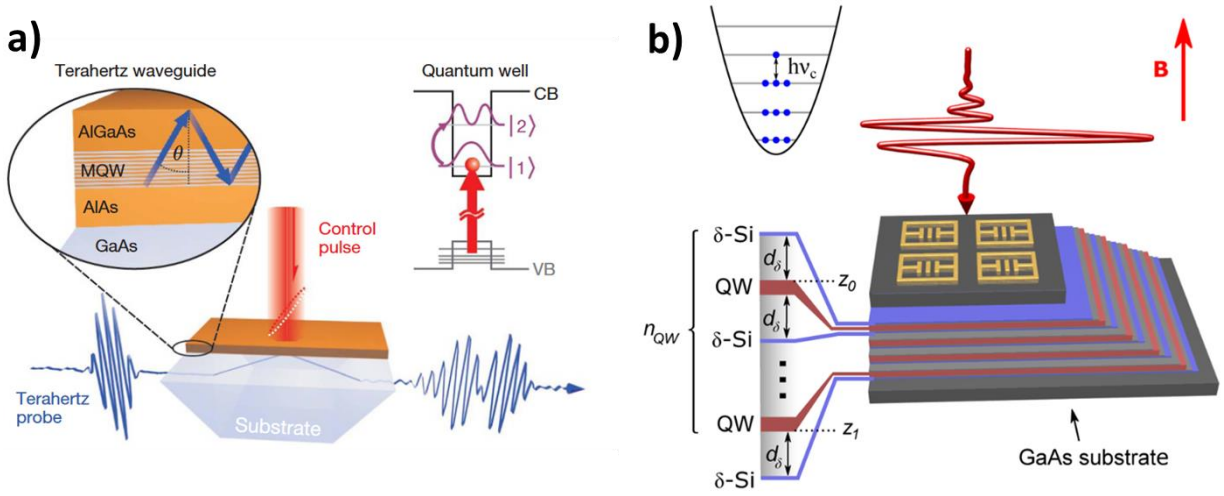

Figure V-5 : Few experimental platforms demonstrating the ultra-strong coupling regime a) ISB transitions coupled to a plasmon waveguide. A pump-probe scheme can non-adiabatically modulate the light-matter interactions at a sub-cycle time scale, from [174]. b) Landau polariton emerging from the coupling between QWs cyclotrons resonance and THz metamaterial, this structure currently holds the record of the largest light-matter coupling strength ($\eta = \Omega_R/\omega_c = 143\%$), from [182].

V.2.1.2 Electrically injected emitters

Pioneering work on ISB polariton electrical injection has also carried in quantum cascade structures relying on injection and extraction minibands (Figure V-6 a)) to investigate their electroluminescent properties [185]–[188]. In such structures the electroluminescent signal of weakly coupled (without top mirror) and strongly coupled (visible in respectively Figure V-6 b) and c)) highlight respectively, the ISB transition and the lower polaritonic branch contribution. Most importantly, the first experimental evidence of scattering (relevant in the frame of bosonic final state stimulated scattering) between ISB polaritons and longitudinal optical phonons had been highlighted [189] (Figure V-6 d)). However, it was found that the electrical injection efficiency is limited by the presence of dark states (between the bright polaritons) that does not couple with light but contribute to electrical transport [190].

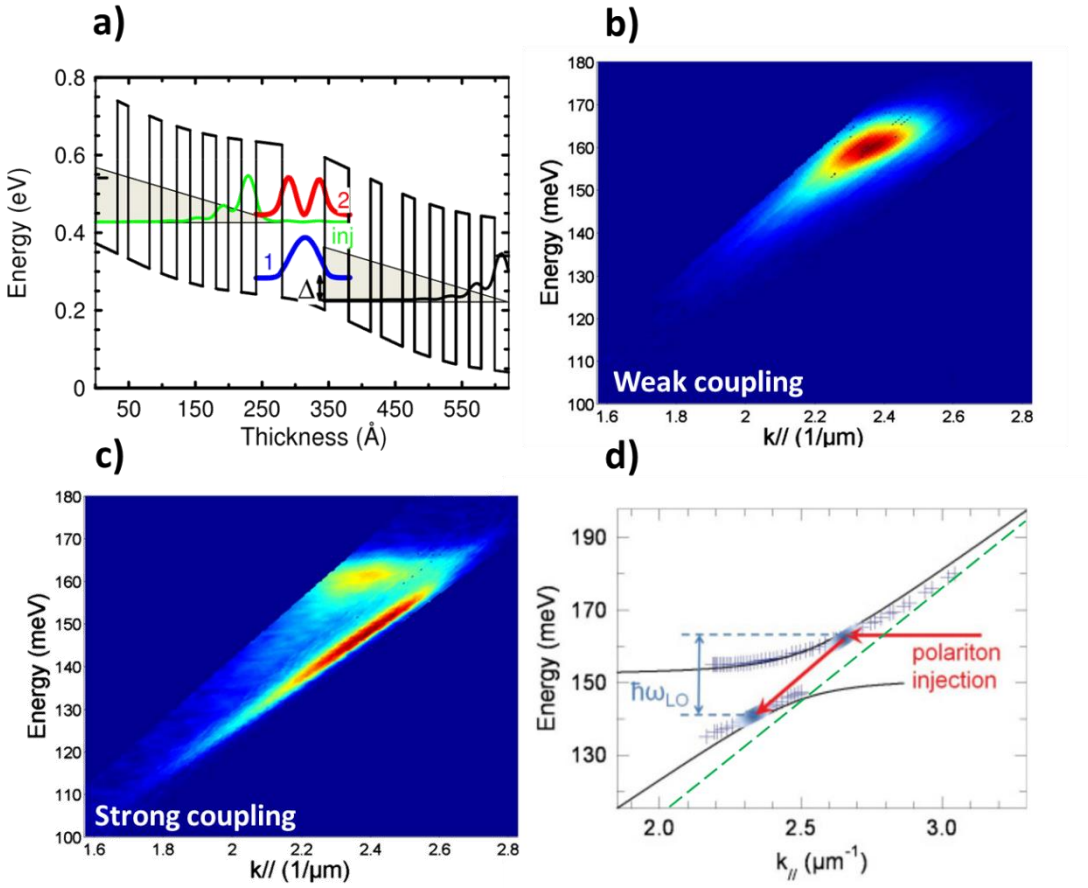

Figure V-6 : Few realizations polaritonic electroluminescence, a) Active region of b) and c) consisting of injection, extraction minibands. b) Electroluminescence in the weak coupling regime, the emission is centered around the ISB transition, c) in the strong coupling regime, the emission is mostly coming from the lower polariton branch. a) b) and c) adapted from [185]. d) First experimental evidence of scattering between polaritons and LO-phonon upon electrical injection, from [189].

Another important work showed the electrical control of the light-matter coupling strength of an ISB polaritonic system [191], [192]. The concept is to electrically switch and modulate the light-coupling strength as shown in Figure V-7 a) that shows an asymmetric QW structure, where the ISB transition of the thinner well is coupled to the cavity. Under electrical bias, electrons can tunnel from the lowest subband of the larger well to the lowest subband of the thinner well, thus modulating the light-matter coupling strength as displayed in Figure V-7 b). More recently, this concept has been implemented to modulate the emission of a Mid-IR laser [193].

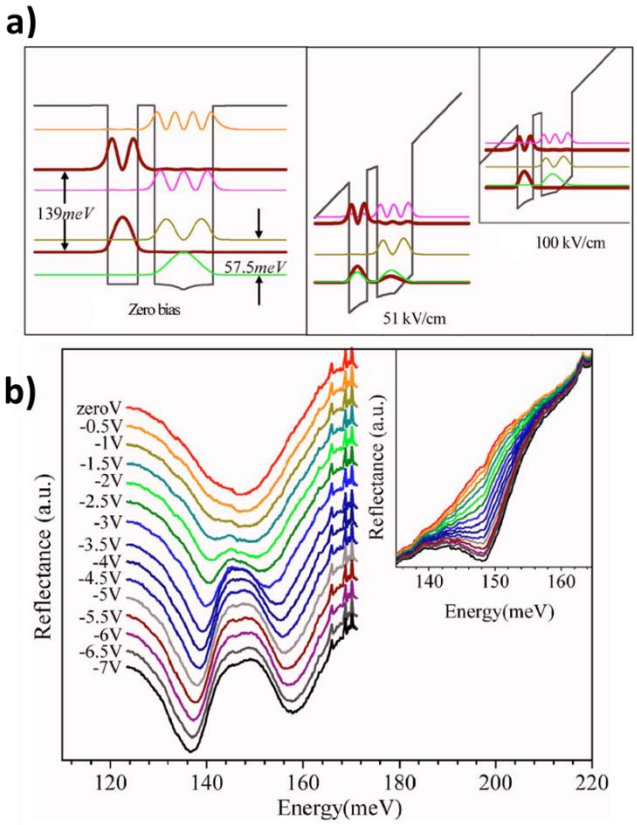

Figure V-7 : Electrical control of light-matter coupling strength, a) asymmetric QW structures, the ISB transition of the thinner well is coupled to the cavity, upon electrical injection, electrons from the larger well lowest subbands tunnel to the thinner well lower subbands providing a modulation of the coupling strength. b) Reflectance spectra, where no bias is applied, the structure operates in the weak coupling regime, upon bias, the device gradually switches towards strong coupling regime. From [192].

V.2.1.3 Few electrons polaritonic platforms

Other research directions are focused towards reaching the strong or even ultra-strong coupling with *few* electrons. This provides a method to reduce the numbers of dark states ($N_{emitters} - 1$) and thus are interesting platforms to develop more efficient electrical ISB polariton injection, along with other functionalities such as photon-blockade or optical bistability. This is possible for structures that target an extremely small modal volume and thus providing strong overlap between the cavities electric field and the QWs. Experimental realizations of strong/ultra-strong coupling with few electrons include, ISB transitions coupled to nanocavities-based metamaterials [194] (Figure V-8 a)) , Mid-IR nano antennas [195] (Figure V-8 c)), 3D THz meta-atoms [196] (Figure V-8 b)), THz LC resonators [197] (Figure V-8 d)) and cyclotron transitions in nanogap hybrid LC Microcavities[198] (Figure V-8 e)).

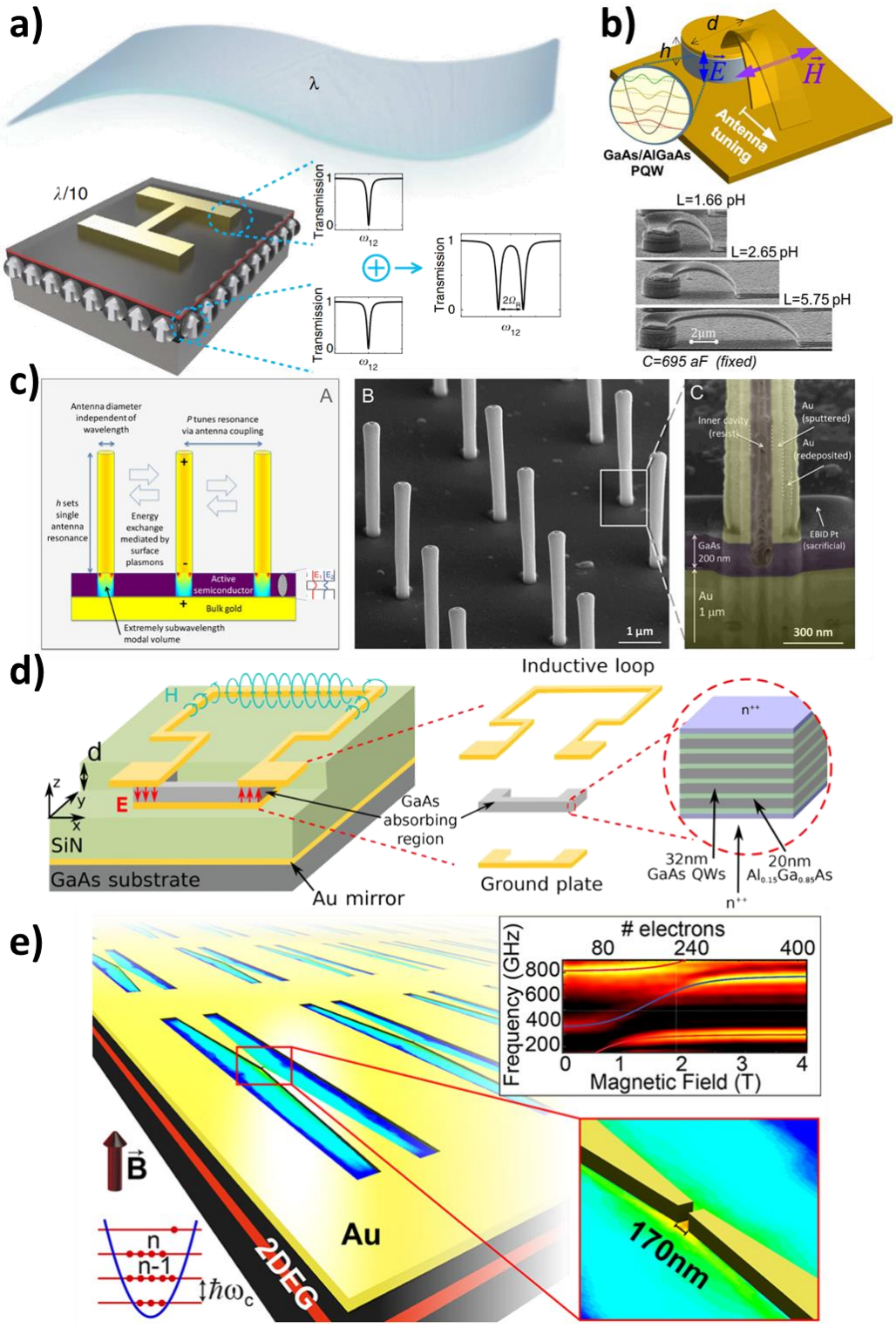

Figure V-8 : Experimental realization of strong and ultra-strong coupling with few electrons. a) ISB transitions coupled to metamaterials nanocavities, from [194], b) 3D THz meta-atoms, from [196] c) Mid-IR nano antennas, from [195], d) THz LC resonators, from [197], e) Cyclotron transitions in nanogap Hybrid LC Microcavities, from [198].

In this brief state-of-the-art of ISB polaritons, we have addressed a snapshot of current research. However, due to their bosonicity, ISB polaritons also show potential as a platform to

develop novel sources of light based on final state stimulation, as achieved in their excitonic counterparts. This will be discussed in detail in next section.

V.3 Polaritonic coherent emission

In this section we will introduce the mechanisms leading to coherent emission in polaritonic systems. We will review the principle successfully applied in excitonic polaritons to achieve laser action and discuss the concepts that can be applied to THz ISB polaritons. Challenges of stimulated ISB-polariton emission linked to the THz domain are also outlined.

V.3.1 Bose-Einstein condensation of polaritons

Bose-Einstein condensate (BEC) is an effect common to all bosons that describe their occupation of a single quantum state, leading to coherent ground state emission [199]. This behaviour was predicted in 1925 by Einstein`s work based on Bose calculations [200], [201], with experimental observation of such condensate reported in 1995 in ultra-cold (nano Kelvin range) gas vapor [202]. From Bose-Einstein statistics, all bosons can undergo a phase transition towards such a quantum fluid, given the condition described by equation (V-8) for a 2D polariton system [203] where n is the 2D polariton density, k_B the Boltzmann constant, $T_{critical}$ the critical temperature and m the polariton effective mass. As the mass of the polaritons are dominated by their photon component, it is orders of magnitude lighter than that of the uncoupled matter component [166]. This implies that BEC condensation of polaritons is possible for relatively high temperatures (few hundreds of Kelvin).

$$\frac{n}{k_B T_{critical}} \geq \frac{2m}{\hbar^2} \qquad (V\text{-}8)$$

V.3.2 Coherent emission from a polariton BEC

Historically, exciton polariton coherent emission was predicted by Imamoglu and co-workers in 1996 [204] and demonstrated in early 2000s [205]–[207] for optically pumped systems (in the near-infrared/visible range). In 2013, even electrically pumped excitonic polariton laser operation was demonstrated [208], opening the gate towards low laser threshold devices. In contrast to atoms in atomic BEC maintained in magnetic trap, these polaritons are coupled to a cavity with a finite reflectivity. Therefore, these cavity polaritons

possess a limited lifetime (in the range of 10ps for excitonic polaritons [209]) and thus cannot achieve thermodynamic equilibrium. For that reason cavity polaritons BEC are classified as non-equilibrium BEC and require either optical or electrical pumping to maintain their polariton density [209]. (Only optical pumping scheme are considered in the scope of this manuscript).

In stark contrast to "classical" lasers relying on inversion of population, polaritons laser are based on bosonic final state stimulation, where polaritons are created in a reservoir and scatter towards a final state. In cavity polaritons, this final state where polaritons can condensate is typically accessible at $k_{\parallel} = 0$. According to Bose-Einstein statistics, in bosonic system the probability of transition to a final-state is proportional to the population of this final-state [210]. In other words, one can seed the polariton population of the final state from a reservoir via a scattering (Γ) mechanism. Once the final state population (n) reaches a critical density, the scattering becomes stimulated as $\Gamma_{stimulated} = \Gamma(n+1)$ leading to faster scattering events and thus an abrupt polariton population build up. This forms a non-equilibrium-BEC in the final state, and hence radiating coherent photon emission from the polaritonic decay in the final-state [209]. These mechanisms are summarized in Figure V-9 where a resonant pump creates polaritons inside the reservoir. An experimental non-equilibrium-BEC of excitonic polaritons is visible in Figure V-10, where a clear condensation appears at $k = 0$ with an increase of the non-resonant[2] pump fluence [206].

[2] In the case of exciton polariton, a non-resonant pump can be used to stimulate polariton-polariton scattering, albeit, early demonstrations used a resonant pump [209].

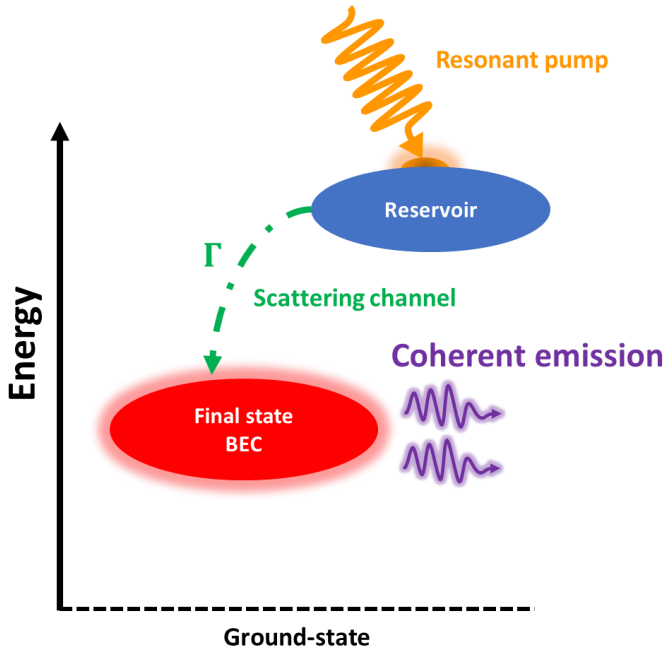

Figure V-9 : Concept of polariton lasing under optical pumping. A pump creates polaritons in the reservoir, scattering mechanism seeds the final-state population leading to Non-equilibrium-BEC, coherent emission occurs by polaritonic decays in the final-state.

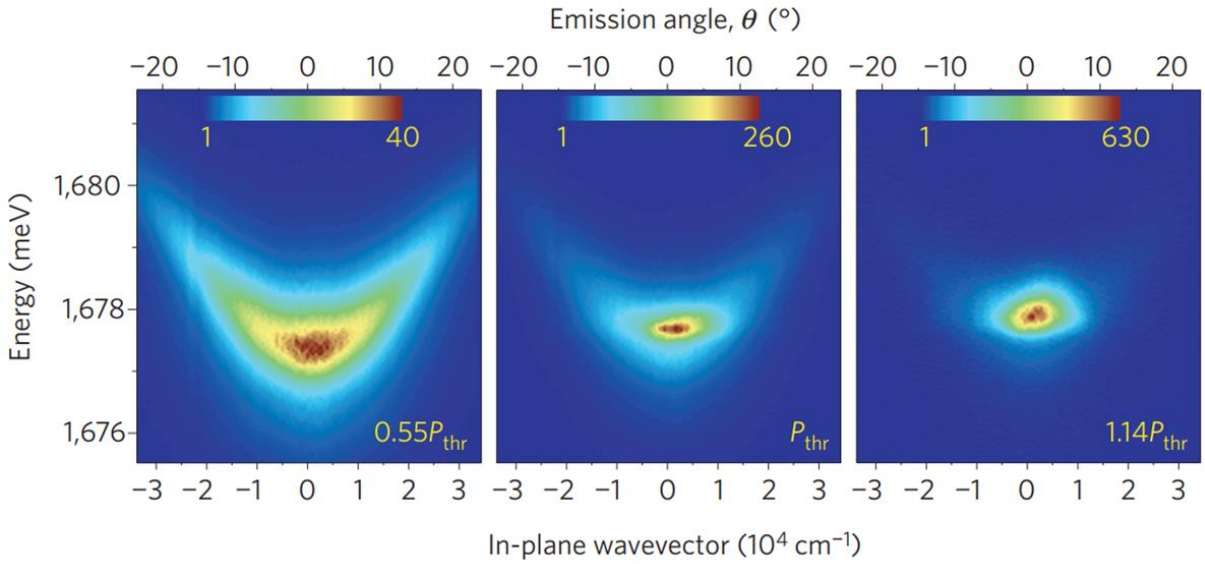

Figure V-10 : Experimental dispersion of excitonic polaritons Non-equilibrium-BEC with an increase of the pump fluence. Note that this excitonic non-equilibrium-BEC was achieved with an out of resonance pump in respect to the reservoir. From [206].

However, the exciton polariton density is limited by the Mott density, corresponding to Coulomb screening. Beyond this, the bosonicity of polaritons is broken and their photonic behaviour dominates [209]. Note that according to [166] ISB polaritons have the advantage

that they are not limited by this Mott transition and can be engineered with high doping, potentially resulting in even higher critical temperatures.

V.3.3 Stimulated scattering in ISB polaritons

In this section we will describe the relevant ISB polariton scattering mechanisms. We highlighted the prime importance of scattering channels when considering light emission from ISB polaritons non-equilibrium-BEC. In the Mid-IR, a mechanism involving LO-phonon scattering was proposed in 2009 [210], depicted in Figure V-11 along a typical ISB polariton dispersion. For a pump beam injecting polaritons at n_2 corresponding to an energy $\hbar\omega_{in}$ and a k vector k_{in}, polaritons can scatter via the GaAs LO-phonon (phonon energy ~ 36meV) to reach the point n_1 where accumulation of polaritons is possible. The scattering process was experimentally demonstrated by C2N in 2018 under optical pumping [211] and in 2011 by University Paris 7 using an electrical injection scheme [189]. However, in the THz range, the energy of the LO-phonon is much larger than the Rabi-splitting ($E_{LOphonon}^{GaAs} \approx 36meV > E_{Rabi} \approx 3meV$) and thus LO-phonon-THz polariton scattering mechanisms are unlikely.

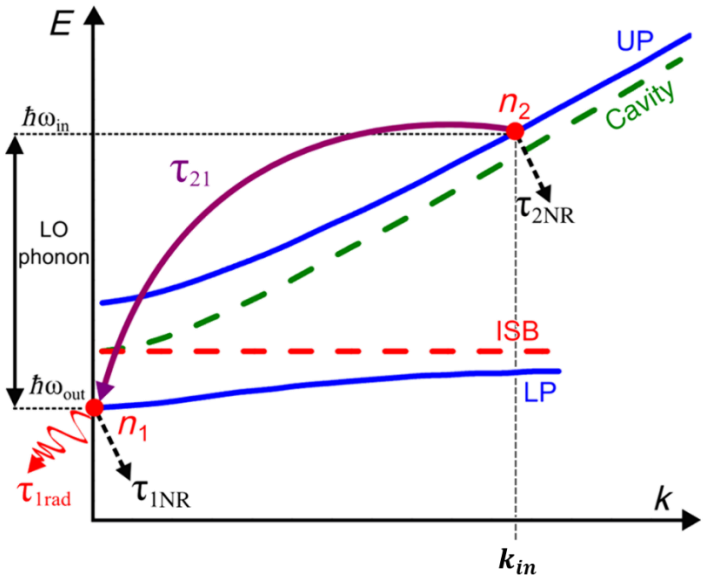

Figure V-11 : Energy dispersion of ISB polaritons. A polaritons pumped with an energy $\hbar\omega_{in}$ and a k vector k_{in} can be scattered by the LO-phonon of GaAs.The scattering process with losses are denoted by arrows. Adapted from [166]

Historically, laser action in exciton polaritons was achieved by resonantly pumping the LP branch at a precise angle to stimulate an efficient nonlinear parametric scattering process: polariton-polariton scattering [212]–[214]. Here the term resonant denotes the matching of the

pump energy with either the LP or UP energy at a finite $k_{\parallel}$ (angle). This polariton-polariton scattering was first highlighted in [215] where an angle resolved resonant pump-probe scheme is used to optically pump the LP while seeding the final state population with the probe. It was found that when the system is pumped at a precise angle, where energy and momentum is conserved on the polariton dispersion (triple resonant scheme or the so called "magic angle"), polariton-polariton scattering is possible and gives rise to an amplification of the probe beam (see Figure V-12). In this early demonstration, although the pumped system was below the threshold of polaritonic coherent emission (stimulated scattering), nevertheless a coherent amplification of the probe beam in two new states (the signal and idler) was observed (similar to a four-wave-mixing process), corresponding to polariton gain. This scattering mechanism could be adapted to THz ISB polaritons and, in fact, has been theoretically predicted [216]. In this work we are applying a similar approach in order to demonstrate the existence of such scattering mechanisms in a THz polaritonic system. I will investigate the polaritonic branches reflectivity to quantify the possibility of the scattering mechanisms and its relevance to gain in THz ISB polaritons.

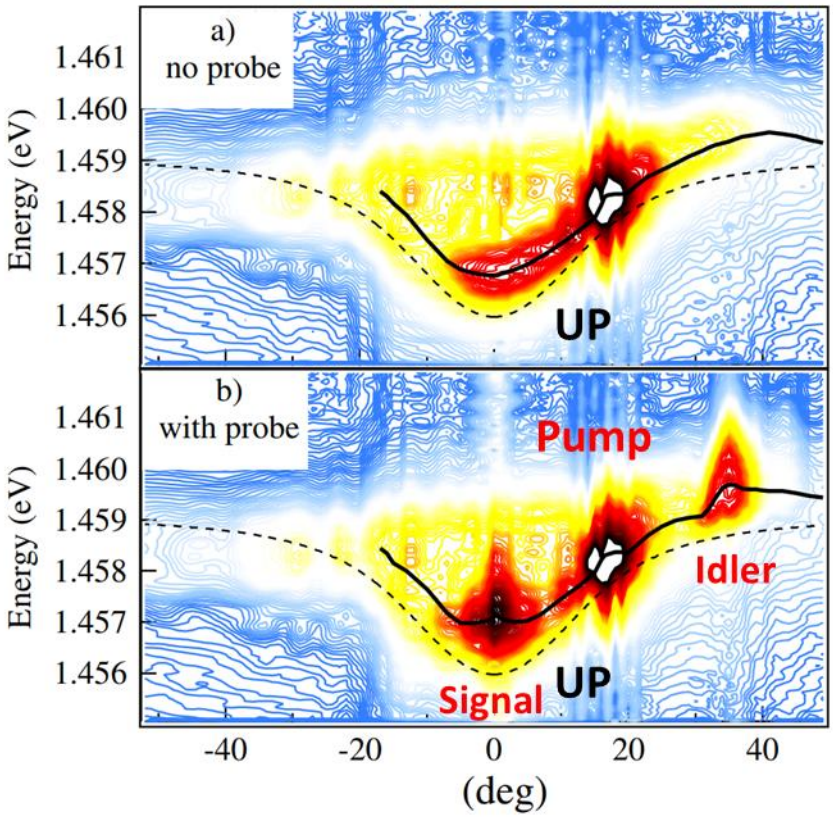

Figure V-12 : Early demonstration of polariton-polariton scattering in excitonic polaritons by [215] Angle resolved photoluminescence spectra of UP branch where a narrow pump and broadband probe excite the sample below lasing action threshold at precises angles. a): No probe excites the LP branch, spontaneous

scattering characterized by incoherent luminescence b) the probe seeds a coherent amplification of the signal and the idler.

Quantitatively, THz ISB polariton-polariton scattering can be described by equation (V-9) involving two polaritons (1 and 2) created in the same state by a THz pump with energy and momentum as $E_{pump}^{(1)}, E_{pump}^{(2)}, k_{pump}^{(1)}, k_{pump}^{(2)}$. The first polariton then transfers part of his energy and momentum to the second and both scatter into two states, the idler and the signal, separated by the same energy and momentum. This energy and momentum conservation is only allowed by pumping at a precise angle the so called "magic angle". Note that in Figure V-13 the polariton-polariton scattering processes highlighted for the LP and UP branches are note unique, with other angles allowing such triply resonant scheme might exist. If the system is pumped "strong enough", ISB polariton accumulation leading to BEC is possible.

$$\begin{cases} k_{pump}^{(1)} + k_{pump}^{(2)} = k_{signal}^{(1)} + k_{idler}^{(2)} \\ E_{pump}^{(1)} + E_{pump}^{(2)} = E_{signal}^{(1)} + E_{idler}^{(2)} \end{cases} \qquad (V\text{-}9)$$

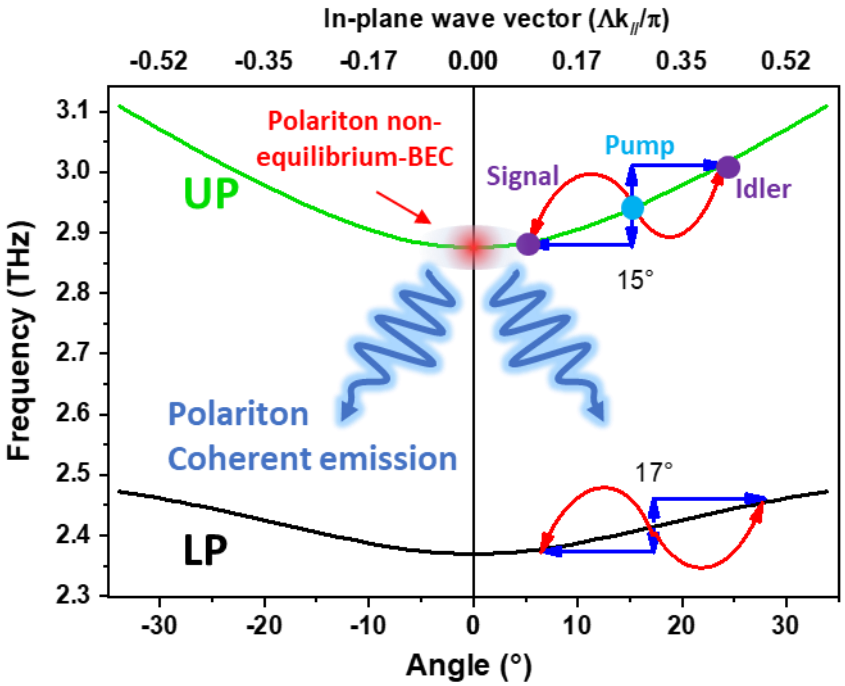

Figure V-13 : RCWA ISB polariton dispersion of our polaritonic sample. Polariton-polariton scattering is available in LP and UP for respective magic angle and frequencies of 17 and 15 degrees and 2.42 and 2,94THz. The stimulated scattering leading to Non-equilibrium-BEC lasing is highlighted in UP branch.

The theoretical study of this mechanism for ISB polaritons, involving an estimation of the threshold and signature of this effect, has been carried by the INO-CNR BEC center in Trento [217]. The dynamics of this process was modelled by Gross-Pitaveskii equations (GPE) which are a type of nonlinear Schrödinger equations suited to bosons [218]. The reflectivity of the signal and the intensity spectrum of the idler is investigated under monochromatic coherent pumping with a continuous wave (CW) beam. The polariton dispersion along with the reflectivity of the signal and the intensity of the idler from this study are displayed in Figure V-14 where a 150 fs Gaussian probe beam of weak intensity (10^{-5} of these units) excite the sample at $k_{\parallel} = 0$ (normal incidence) while the pump is set at the angle that allows the triple resonant scheme.

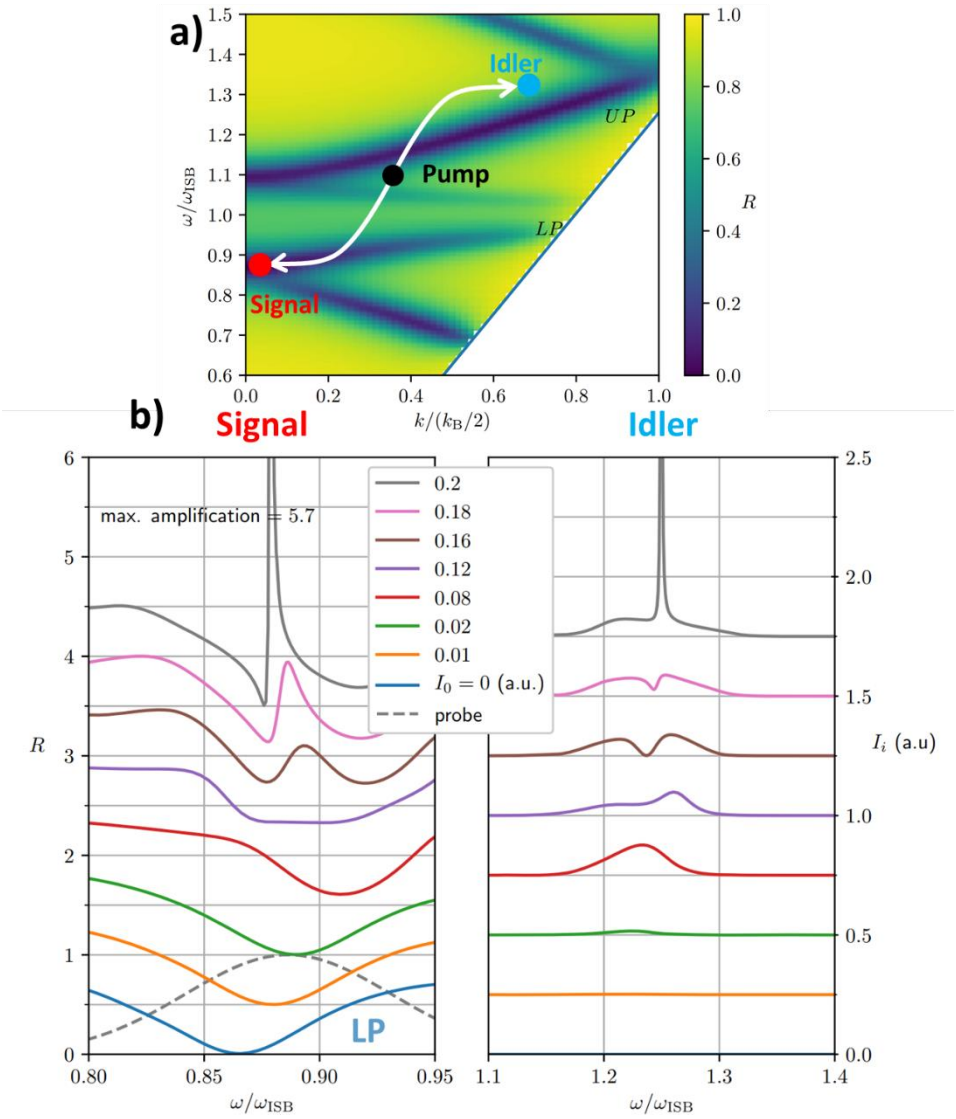

Figure V-14 : a) Polaritonic dispersion of the system investigated in this study. The pump and probe excite the sample at respectively the angle allowing the energy momentum conservation and normal incidence ($k_{\parallel} = 0$). b) Reflectivity of the signal ($k_{\parallel} = 0$) and idler intensity spectrum under resonant pumping. The lasing threshold is $I \approx 0.22$, a clear frequency shift and a sharp optical amplification are visible. Note that the idler vanishes for weak pump intensities. Adapted from [217].

The outcome of this study reveals some typical signatures of polariton-polariton scattering that we aim for in our experiments, namely spectral shifts, the presence of the idler (at a specific k vector) and eventually a sharp change of the signal reflectivity at $k_{\parallel} = 0$. This corresponds to a change of population on the polariton branch leading to an optical amplification of the signal. Note that the full picture of this interaction is still at this time under investigation [217]. It is worth noting that in excitonic polaritons, under optical pumping, blue shifts of the signal are reported [209], but for ISB polaritons other phenomena might arise due to the strong electronic many-body interactions. The ideal pumping scheme to

highlight this ISB polariton-polaritons scattering is a monomode CW resonant pump where the polariton populations can build up constantly. In my work I will use high-power THz QCLs operating in quasi-CW, typically with pulses in the range of few µs which is larger than the buildup time of the polaritons (of few ps), and are thus suitable to stimulate polariton-polariton scattering mechanisms.

The estimation of the pump threshold to enable a THz amplification by polariton-polariton scattering is difficult and currently relies on the rescaling of mid-infrared data obtained in the similar systems. Estimations from INO-CNR BEC centre predict a THz pump of a few $100s\ W/cm^2$ for the system presented in this manuscript. (This value could be decreased for a cavity with less QWs).

Although our approach to show gain is based on taking inspiration from exciton polaritons to ISB polaritons, we have to consider the existence of hurdles inherent to the ISB nature of polaritons and the THz domain. In excitonic polaritons, typically the strong coupling regime is reached with the implementation of high reflectivity Distributed Bragg Reflectors (DBR) resulting in quality factors of a few thousands [219]. This extends the lifetime and narrows the linewidth of the polaritons, as photons are trapped longer and have more time to interact with the matter transition. This approach is difficult to scale to ISB polaritons due to the TM selection rules of ISB transitions (see section V.4.1). The typical quality factor for our cavities are in the range of 30 [166]. Combined with the ultrashort ISB transition lifetimes [4] (in the range of 1ps), this results in broader polariton linewidths and shorter lifetimes. Another consideration for THz frequencies are the less technologically mature pump sources that often involve cryogenic environment with no or little frequency tunability, compared to the near infrared/visible. Further, for excitonic polaritons, optical pump beam diameters down to the micron level can be easily obtained, whereas in the THz a few hundred µm waist is considered tightly focused, owing to the diffraction limit. This represents a considerable challenge in engineering sources capable of reaching high power densities to stimulate polariton scattering for laser action. These limitations are highlighted in Table V-1 along with typical values of Q factors, linewidth etc.

	Excitonic polaritons	**THz ISB polaritons**
Cavity Q factors	Few 1000s	30
Transition Linewidth	Sharp 24GHz	Broad 200GHz

Photon energy	0.3 to 7 eV	12meV
Pump source temperature	Room temperature	Cryogenic temperature
Pump frequency	Tunable	Fixed
Pump waist	Micron level	Few 100µm
Narrow band Pump	Ti:Sapp, laser diodes etc	QCLs

Table V-1 : Typical values of metrics impacting the possibility of polariton condensate comparing excitonic to ISB polaritons.

Experimental observation of THz ISB polariton-polariton scattering thus requires:

1. Optimized light-matter coupling from the cavity and the ISB transitions.
2. Pump source capable of generating high CW monomode THz power densities.
3. Specific pumping geometry enabling resonant polaritonic excitation at an angle allowing energy and momentum conservation between the injected polaritons.
4. Broadband probing at k vectors permitting a polariton accumulation (minimum in energy on the dispersion, typically at $k_{\parallel} = 0$

In the coming sections we will now describe the physical ingredients and the geometries required to reach the strong coupling regime for intersubband polaritons.

V.4 Physical ingredients

V.4.1 Quantum wells and intersubband transitions

Epitaxially grown quantum well (QW) structures emerged in the 1970s [220] using a GaAs/AlGaAs structure. By stacking nanometres thin layers of different bandgap semiconductor, it was found that electrons/holes could be confined through a discontinuity of potential energy in the conduction and valence bands of the materials. (AlGaAs has a large bandgap than GaAs). Photon absorption can then be described by an electron of the valence band (VB) interacting with an incoming photon of energy equal to the interband transition of the well. From this interaction, the electron gains the energy of the photon and is promoted to the higher energy conduction band (see Figure V-15 a)). Depending on the materials used for the QW, the energy of the transition can be engineered from 0.3 to 7 eV [221]. One can then design devices based on QWs interband transitions operating from the mid-infrared to the ultraviolet. The THz range of few meV, however, is difficult to access with this concept owing to the lack of naturally adapted materials. As interband transitions are limited by the material system used for the QW, the expression bandgap slavery is often employed to point out this limitation. ISB transitions which consist of confined states within one band of the QW (typically the CB), however, can be tuned easily to few meV by changing the well thickness, permitting access to THz transitions (Figure V-15 b)). Note that, owing to ISB selection rules, only photons with electric field parallel to the direction of growth of the QW (TM polarized) can couple to confined ISB transitions [222].

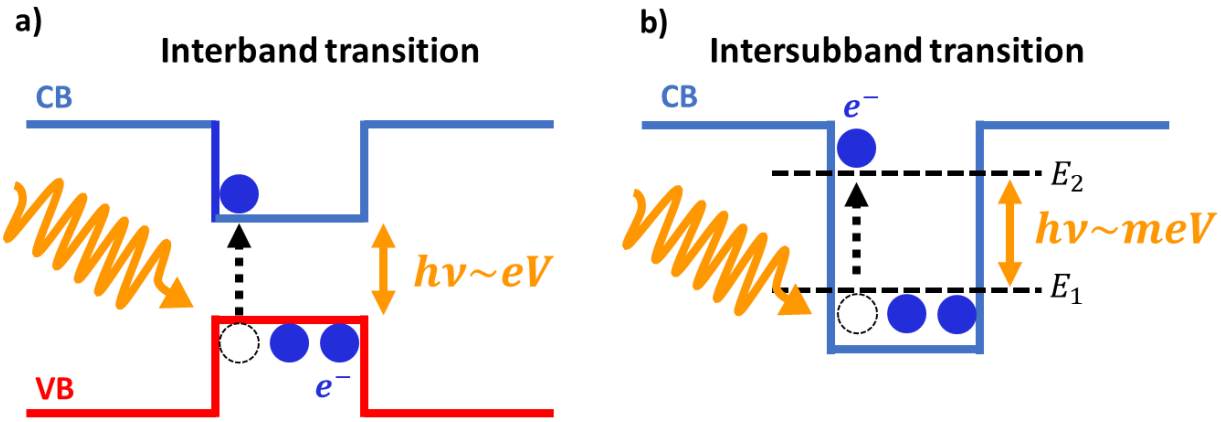

Figure V-15 : Representation of transitions in QWs: a) Interband transition, the wavelength is given by the material system used b) Intersubband transition is tuneable to THz frequencies.

Quantitatively the energy dispersion of the ISBs in the CB for a QW of thickness L along the growth direction z can be described by the envelope function formalism [223] where the contribution of the crystalline potential is defined within the effective mass (m^*) [168]. Wave functions $\psi_i(r)$ are then written as the product of Bloch functions ($u(r)$) (see equation (V-10)) defined by the periodicity of the crystal lattice (r) and a slowly varying envelope function ($f_i(r)$) over the lattice period. The confinement is then accessible by solving the Scrödinger equation ((V-11)).

$$\psi_i(r) = f_i(r)u(r) \qquad (V\text{-}10)$$

$$\frac{\hbar^2}{2m^*}\nabla^2 f_i(r) + V(z)f_i(r) = E_i f_i(r) \qquad (V\text{-}11)$$

Due to the confinement of the system, the artificial potential is created only along z and thus permit to separate the free motion of carriers in the x y directions (see equation(V-12)) With V the volume of the unit cell and $k_\parallel$ the in-plane wavevector.

$$f_{i,k_\parallel}(r) = \frac{1}{\sqrt{V}} e^{ik_\parallel r}\psi_i(z) \qquad (V\text{-}12)$$

By solving this equation in the case of infinite barriers, the eigenenergies $E_n(k_\parallel)$ of subbands can be calculated with n being a positive integer (see equation (V-13)). The significative result is that the ISB eigenenergies can be tuned with the thickness of the well.

$$E_n(k_\parallel) = \frac{\hbar^2}{2m^2}\left(\frac{\pi^2 n}{L^2} + k_\parallel^2\right) \qquad (V\text{-}13)$$

In the next section we will discuss the many-body interactions inherent from the doping required to design ISB optical transitions. This many-body interaction results in an energy-shift of the transition (a blue shift) called the depolarization shift.

V.4.1.1 Depolarization shift

Typically, optical ISB transitions requires a large number of electrons to place the Fermi level between the first and second subband. In this picture, the ISB transition of a multiple quantum well structure is a collective effect from the many electrons behaving as

plasmons. Consequently, a plasma oscillation (ω_p) defined as equation (V-14) can describe the optical response of the structure with N_{2D} the sheet doping density of the QWs, ϵ_0 , $\epsilon_\infty$and L_{QW} being respectively the low and high frequency limit of the dielectric function and L_{QW} the thickness of the QWs.

$$\omega_p = \sqrt{\frac{N_{2D} e^2 f_{12}}{\epsilon_0 \epsilon_\infty m^*(L_{QW})}} \qquad (V\text{-}14)$$

Under an electromagnetic field, the electrons can undergo an optical transition but also experience an induced field resulting from the collective electronic oscillations (the depolarization field). This phenomenon is known to blue shift the optical ISB transition frequency and is called the depolarization shift [224], [225]. Accounting for this shift, the ISB transition frequency is now defined as equation (V-15). It is important to note that the depolarization shift increases with the doping and is larger for THz transitions due to the small photon energy. In this work, THz ISB transitions are reached for a typical electronic density of $10^{11} cm^{-2}$ resulting in a depolarization shift of $\sim 0.4\ THz$ [168].

$$\omega_{ISB} = \sqrt{\omega_{12}^2 + \omega_p^2} \qquad (V\text{-}15)$$

In this work the structure designed by the C2N include 53 GaAs/AlGaAs QWs. The GaAs QWs are 36nm wide separated by 20nm AlGaAs barriers, with doping inserted 5nm before the QW[168]. The Schrodinger-Poisson calculated electronic states are displayed in Figure V-16 along with the QW dimensions where the ISB transition of interest is between $|1\rangle$ and $|2\rangle$ corresponding to $\approx 11.2\ meV$ ($\sim 2.7\ THz$). Multi-pass transmittance measurement carried by the C2N in Figure V-17 shows the optical absorption of the 53 QWs for decreasing temperatures corresponding to a lowering of the Fermi level (see Figure V-17 b)). At 300K, no absorption is visible, for 78K however, the Fermi level is above E_{23}, yielding two absorption peaks at 2.57 and $4.05\ THz$ corresponding to $E_{12}$and E_{23} transitions. At 4K, the Fermi level is between $E_1$and E_2 resulting in a single absorption at $2.75\ THz$. The frequency difference between E_{12} at 78 and 4K corresponds to a depolarization shift due to the reduced oscillator strength in the former case.

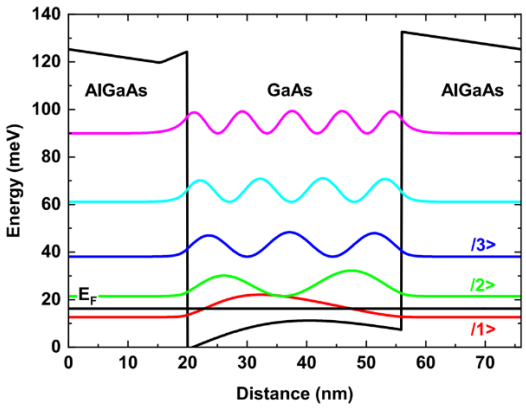

Figure V-16 :) Schrödinger -Poisson simulation of the GaAs/AlGaAs based QW used in this work, the ISB transition correspond to the energy transition between $|1\rangle$ *and* $|2\rangle$*. Simulation from [168]*

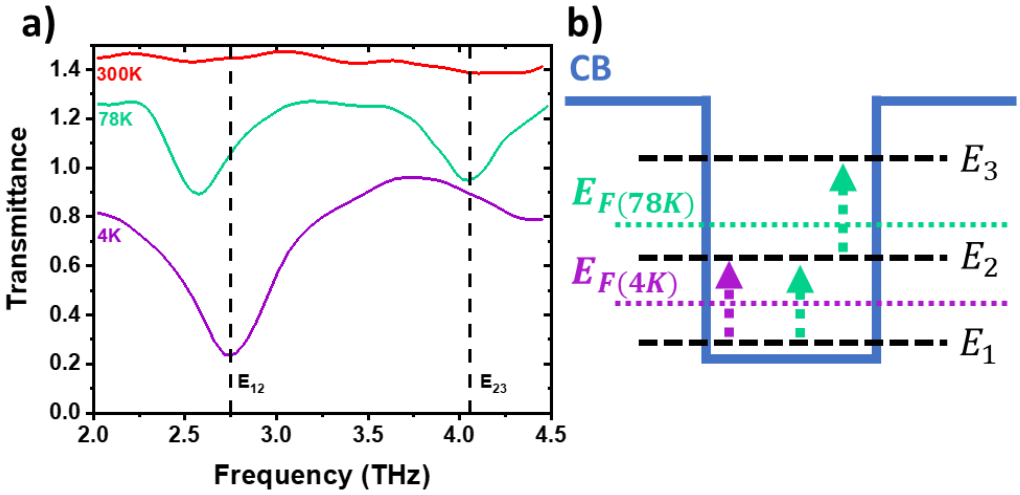

Figure V-17 : Multi-pass transmittance of the 53 QWs used in this work, showing the ISB transitions for different sample temperatures. a) Principle of the experiment, a Globar (broadband) is coupled to the sample by a multi-pass waveguide, the transmitted radiation is analyzed by a Bolometer. b) Transmittance spectra showing no absorption at 300K, at 78K, two peaks corresponding to the transitions E_{12} *and* E_{23} *and at 78K, one peak at* $2.75\ THz$ *corresponding to* E_{12}

In the next section, we will detail the cavity properties to reach the strong coupling regime.

V.4.2 Metal-insulator-metal cavitiy

The metal-insulator-metal (MIM) cavity used in this work is based on the seminal work of a 1D photonic crystal demonstrated in 2010 [32]. The cavity consists of a GaAs layer sandwiched between two Au planes. Openings in the top Au layer are etched to form a grating with a period Λ. These periodic openings enable a top surface coupling of incoming THz waves to be TM polarized, requirement for ISB transitions [133], [135]. Further, it folds the dispersion in the Brillouin zone of this 1D photonic crystal [226] while modulating the effective optical index. Figure V-18 gives a schematic description of our MIM cavity along with the electric field confinement E_z. Panel b) displays the TM_0 polarized photonic dispersion in the Brillouin zone where the 2nd and the 3rd photonic branches can propagate. The energy dispersion relation for TM polarized modes in this cavity is defined by equation (V-16) where c is the velocity, n_{eff} the effective refractive index of the cavity. k_x, k_y, k_z respectively correspond to $k_x = \sqrt{\omega^2 \mu_0 \epsilon - \left(\frac{m\pi}{t}\right)^2}$ (where μ_0 is the permeability,ϵ the dielectric function of the cavity, m defines the order of the mode (0 for TM_0) and t the thickness between the bottom and top Au plates) $k_y = 0$, and $k_z = \frac{m\pi}{t}$ [169]. Dispersive branches can be tuned with the angle of incidence of the incoming wave (θ) as expressed by equation (V-17) [32]. These cavities provide flexibility over the targeted wavelength of operation as their modes can be tuned by changing the thickness and the grating period.

$$E = \frac{\hbar c}{n_{eff}} \sqrt{k_x^2 + k_y^2 + k_z^2} \qquad (V\text{-}16)$$

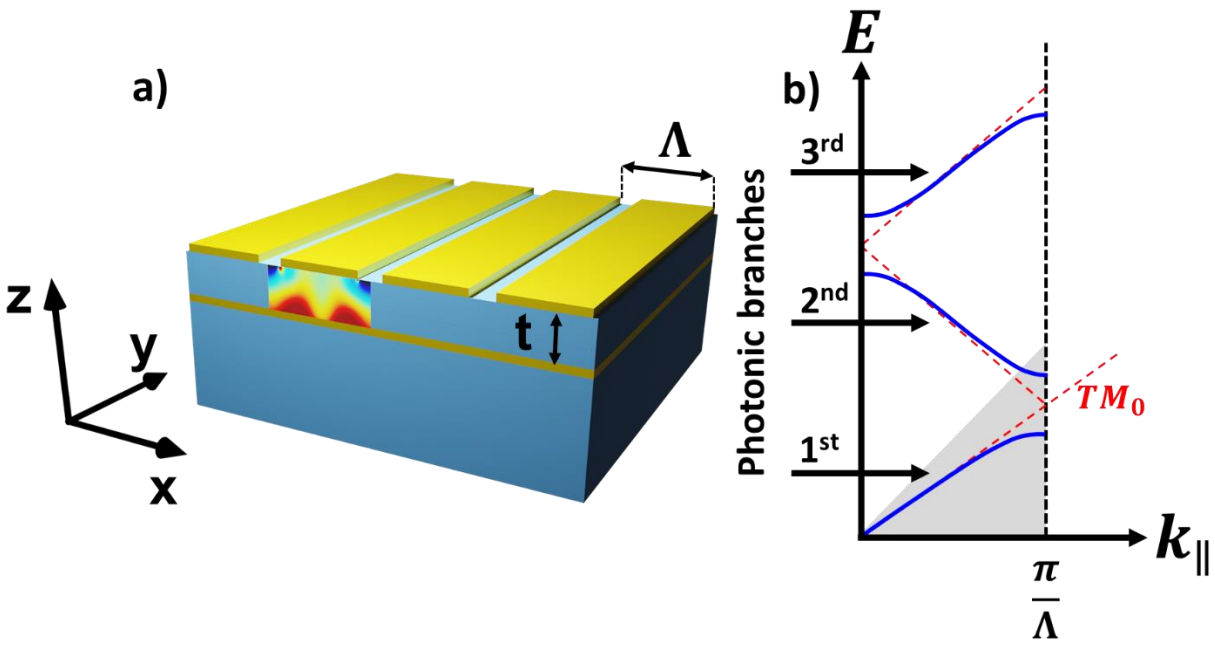

Figure V-18 : a) Schematic representation of the MIM cavity with the electric field confinement below the metal ridge highlighted (E_z), b) photonic dispersion of TM_0 modes folded by the Brillouin zone of the cavity. The grey cone highlights modes below the cone of light. Inspired from [168], [169]

$$k_{\parallel} = \frac{\omega}{c} sin(\theta) \frac{\Lambda}{\pi} \qquad (V\text{-}17)$$

Cavities investigated in this manuscript were designed to have a flat dispersion for the 3rd photonic branch at $k_{\parallel} \approx 0$, to enable a polariton accumulation, at a frequency of $\sim 2.7THz$ (see Figure V-19) (The detection limit of our TDS system is ~ 3.5THz). To give the reader a scale of the typical dimensions, the cavities considered in this work covered a sample area of $\sim 0.2cm^2$, thicknesses t ranging from 11 μm to $\sim 8\mu m$, period Λ of the grating 40 µm and a duty cycle (ratio between top area covered by Au and the period Λ) between 65% and 80%. Dispersion of such structures are experimentally discussed in section V.6 and can be simulated using rigorous coupled wave analysis (RCWA) presented in the next section.

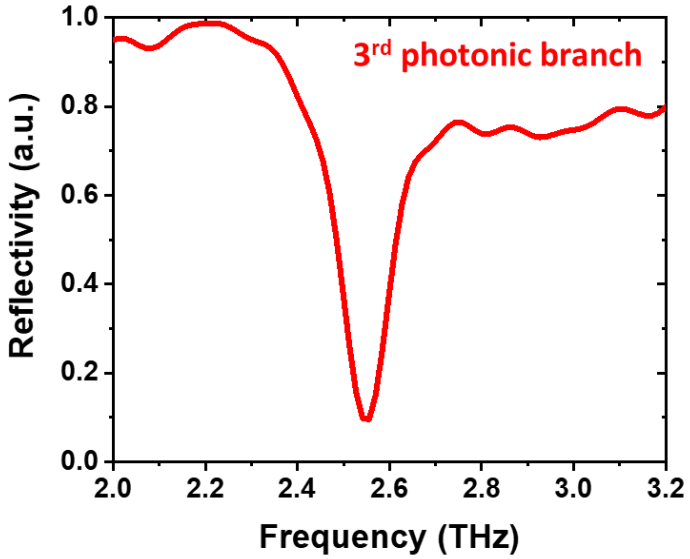

Figure V-19 : TDS reflectivity of a typical MIM cavity at $k_{\parallel} = 0$ (normal incidence) at $300K$ showing the central frequency of the 3rd photonic branch (TM_0 Brillouin folded) at $2.57\ THz$

We will now describe the full THz ISB polaritonic system composed of the MIM cavity with the embedded QWs, permitting ISB polaritons as a result of strong coupling.

V.4.3 MIM cavity and QWs

Considering now, the MIM cavity embedding the multiples quantum wells structure as described schematically in figure Figure V-20. The strong coupling regime in a dispersive regime is reached by engineering cavities to i) ensure a strong overlap between the electromagnetic field and the active area of QWs and ii) by matching the frequency of the ISB transition with the 3rd photonic branch.

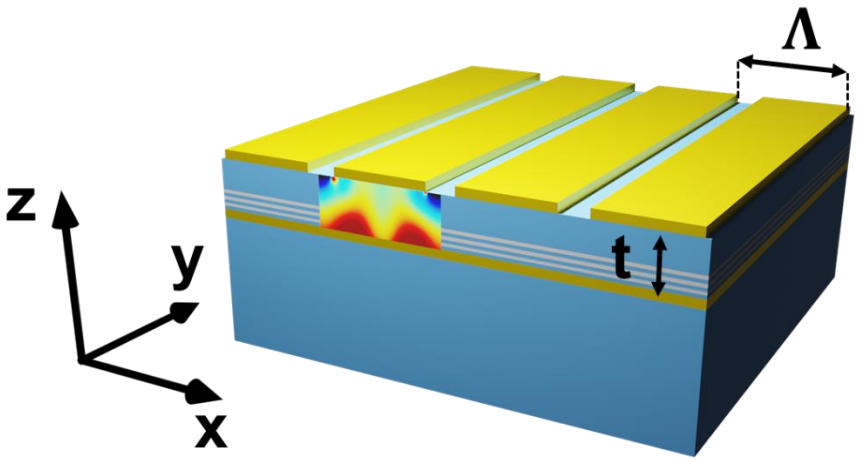

Figure V-20 : Schematic representation of the QWs embedded with the MIM cavity.

Energy dispersion of such structures can be approached using the Rigorous Coupled Wave Analysis (RCWA) approach [227], [228]. For the active region, the Zaluzny-Nalewajko model [229] is used to extract the z component (corresponding to TM cavity modes) of the dielectric tensor as described in equation (V-18). This considers the ISB transition frequency ($\widetilde{\omega}_{12}$) (including the depolarization shifts induced by the heavy doping), the plasma frequency (ω_p), the FWHM of the ISB transition (Γ_{12}), and the dielectric constant of the well (ϵ_ω). Once the structure modelled, the band diagram for different $k_\parallel$ or angles can be displayed along with the reflectivity corresponding to the ratio between incident and reflected electric fields.

$$\epsilon_z(\omega) = \epsilon_\infty \left(1 - f_{12}\frac{\epsilon_\infty^2}{\epsilon_\omega^2}\frac{\omega_p^2}{\widetilde{\omega}_{12}^2 - \omega^2 - i\omega\Gamma_{12}}\right)^{-1} \qquad (V\text{-}18)$$

This method has been successfully applied to describe the energy dispersion of Mid-IR and THz ISB polaritons in MIM cavities by the collaborator C2N in [168], [170].

Considering the detection limit of our TDS system (3.5 THz), the initial optimal parameters of the cavity were investigated to i) place the LP and UP branches in the detection range, ii) allow a flat dispersion of the UP branch around $k_\parallel = 0$ with a good reflectivity contrast of the LP and UP, with an ISB transition coupled with the 3rd photonic branch of the cavity. This optimal results in a cavity with a grating periodic of $\Lambda\, 40\mu m(\approx \lambda/2n)$, a duty cycle (ratio between top area covered by Au and the period Λ) of around 80%, 53 QWs with 8µm of buffer for a total thickness of 11µm.

RCWA simulations for a typical cavity displayed in Figure V-21 along experimental angle resolved reflectivity at 10K obtained by the C2N using FTIR spectroscopy shows a good agreement. The reflectivity of the cavities is investigated and discussed in section V.6.

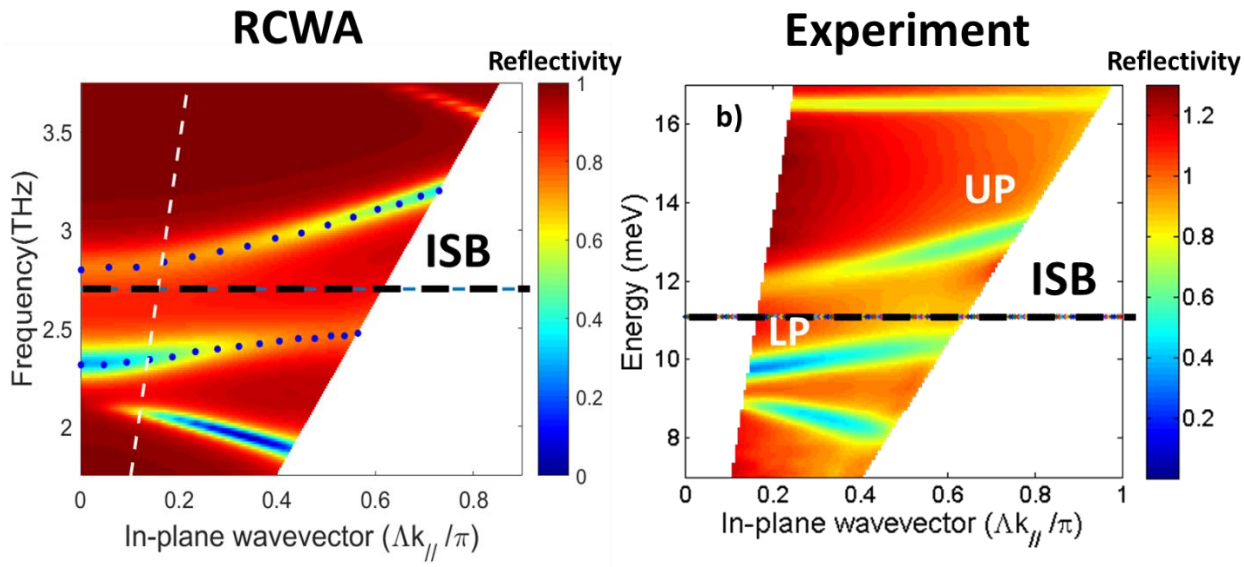

Figure V-21 : RCWA simulated and experimental angle resolved reflectivity of sample 1 with a period $\Lambda = 40um$*, a duty cycle of 80% and a total cavity thickness of 11µm shows a good agreement.*

In the next section we will introduce THz quantum cascade lasers, how they are adapted to be used as a pump for our polaritonic system and their constraints.

V.5 Quantum cascade lasers

In this work quantum cascade lasers (QCLs) are used as a resonant polariton THz pump, exciting the polariton system at the specific angle that permits polariton-polariton scattering as described above. Initially developed in the mid-IR (4µm) by J. Faist and co-workers in 1994 [230] QCLs are electrically injected semiconductor lasers that rely on ISB transitions in stacked QWs. To get a rudimentary picture of the operational mechanism, consider a simplified two-level system of two QWs with CB states $|1\rangle, |2\rangle$ and $|1'\rangle, |2'\rangle$ with an applied electric field as depicted in Figure V-22. Carriers are injected into the state $|2\rangle$ by resonant tunneling and laser action takes place between $|2\rangle$ and $|1\rangle$. Through the applied field, the fundamental level of the first QW $|1\rangle$ is aligned in energy to the second level of the second QW $|2'\rangle$. This process is repeated many times, allowing for the cascade scheme where electrons can tunnel between *N* QWs emitting *N* photons with *N* the number of periods (In typical THz QCLs *N* is 100-200). Note that due to the ISB selection rules, the laser emission is TM polarized.

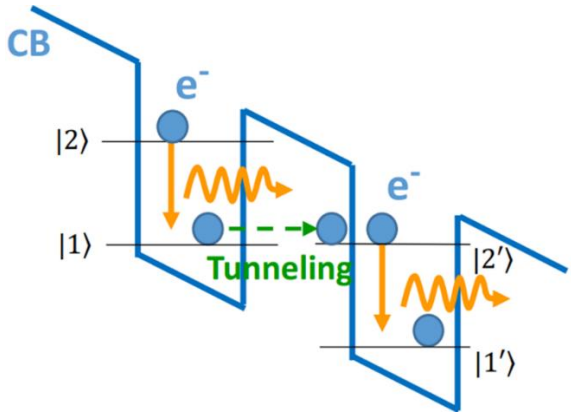

Figure V-22 : Principle of QCLs in a two QW system, Under injection of carriers, bands are tilted in energy by the Stark effect, leading to an alignment of the fundamental level of the first QW $|1\rangle$ to the second level of the second QW $|2'\rangle$, illustrating the cascade scheme where electrons can tunnel between QWs and emit several photons. Illustration from [4].

The ISB nature of the electronic transition gives a large flexibility over the emission wavelength, where the transition energy can be easily engineered with the dimensions of the QWs. This is in contrast to conventional interband semiconductor lasers where the wavelength is roughly fixed by the materials of the active region. Following the first THz QCL demonstrated in 2002 [231], powerful devices able to generate more than 1W of peak power (at liquid helium temperatures) were achieved in 2014 by the implementation of large

active areas and by deposition on one of the facet with a high reflective coating [232], even though obtaining such high power for frequencies below 3THz still represents a challenge. As discussed above, the requirements to stimulate polariton-polariton scattering is in the range of few $100s\ W/cm^2$. Pumping with a QCL capable of providing 1W peak power with a beam waist of $500\mu m$ would reaches power densities of $510W/cm^2$, well above the estimated threshold. Note that this is with QCLs at a fixed emission frequency and at cryogenic temperatures. (Thermoelectric cooled THz QCLs were demonstrated very recently [233], [234]. However, the output power at these temperatures still remains in the mW range). The interested reader could find more information regarding the development of THz QCLs in [235], [236].

THz QCLs used in this work were designed, grown, and processed by the University of Leeds. The active regions are based on a hybrid phonon bound-to-continuum scheme [232] centered at $2.9THz$. The waveguide is based on a single plasmon mode where the active region is sandwiched between two doped layers with a metallic layer on the top surface, providing a low confinement of the THz mode in the laser cavity (see Figure V-23). This permits high output power QCLs and a low diverging mode but at the cost of high threshold currents [237]. Figure V-23 shows the dimensions of our QCLs where a $415\mu m$ wide ridge of length and height of $4mm$ and $20\mu m$, respectively. As detailed in section, V.3.3, monochromatic operation is required for selectively pumping the targeted ISB polariton branch, for QCLs. This can be realized by patterning Distributed Bragg Reflectors (DBRs) on top of the waveguide, covering a length of $2mm$ on one end of the waveguide (see Figure V-23).

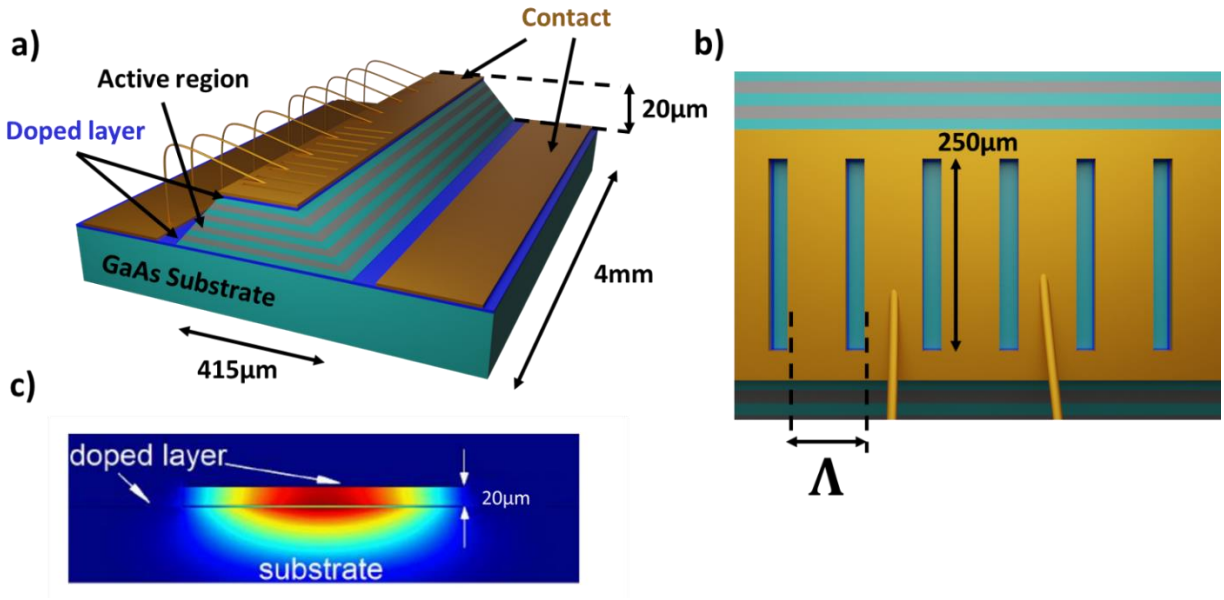

Figure V-23 : Geometry of the QCLs used in this work. a) General structures and dimensions: the active region is $415\mu m$ *wide for length and height of respectively,* $4mm$ *and* $20\mu m$*. The active region is sandwiched between two doped layers providing with a loos confinement visible in panel c). b) Top view of the waveguide, single mode operation is achieved by implementing a distributed feedback reflector periodic by* $\boldsymbol{\Lambda}$ *on top. c) THz electric field intensity distribution inside the waveguide. Adapted from [4].*

DBRs have been widely used to realize robust single-mode emission in THz QCLs [238] The wavelength selection mechanism of DBR is based on the phase matching condition given by equation (V-19).

$$k_i - mk_g = -k_i \qquad (V\text{-}19)$$

Where $k_i = 2\pi n_{eff}/\lambda$ is the wavevector of the incident beam, n_{eff} is the effective refractive index of the structure and λ is the wavelength of the incident beam in free space, m is an integer representing the diffraction order, and $k_g = 2\pi/\Lambda$ is the grating wave vector and Λ is the grating period. For these QCLs, a first order DFB is used for single facet emission. The phase matching condition can then be simplified to equation (V-20).

$$m\lambda = 2n_{eff}\Lambda \qquad (V\text{-}20)$$

Therefore, the desired single wavelength emission can be obtained by the corresponding grating period. For pumping efficiently the UP branch of our samples, we fixed a target frequency of $2.94THz$ (see Figure V-13), the effective refractive index $n_{eff}$is

estimated to be 3.58 [238] around 3 THz. The corresponding grating period is then: $\Lambda = 14.3\mu m$ (measured to be $14.15\mu m$ on the actual device). The DBR is implemented by opening periodic air slits on the top metallization of our THz QCL and consisted of 56 periodic air slits. The width of each air slit takes up 15% of the grating period, i.e. $2.145\mu m$, and the length of each air slit is $250\mu m$. $30\mu m$-wide side-absorbers were implemented on both sides of the QCL waveguide to suppress high-order mode emission [239]. The doping layer under the air slits was removed to ensure that the surface plasmon cannot be supported. A picture of the final device ready to mount in our continuous helium flux cryostat is displayed in Figure V-24.

In the context of the MIR-BOSE project, we were always in a discussion loop with the University of Leeds to develop THz QCLs suited to the ISB polaritons pumping experiments requirements. In the next section we will discuss the implementation of THz QCLs in our TDS system, and give the spectral and power characterizations.

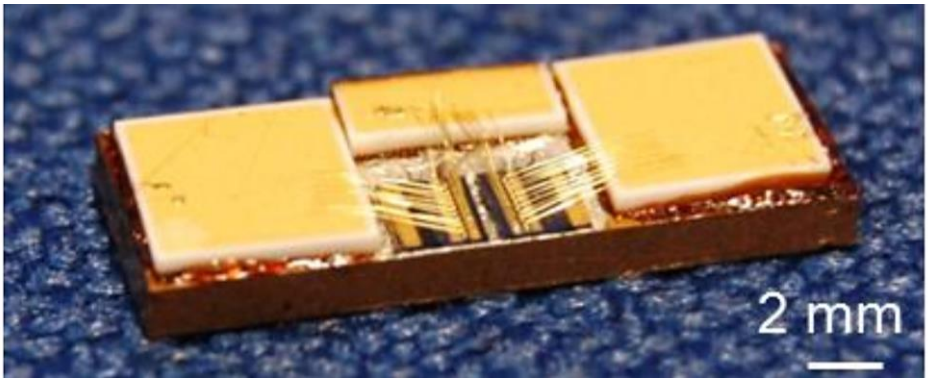

Figure V-24 : Photograph of the finished device, ready to mount in our continuous helium flux cryostat for characterization. Image from [240]

V.5.1 QCL characterizations

QCLs emissions were investigated by extracting their LIV (Light, current, voltage) characteristics with at 50kHz modulation with a low (2%) duty cycle (see Figure V-25 and Figure A 4 in appendix for QCL1). A second low frequency modulation of 20Hz is used to gate the QCL bias for detection of the output THz power using a pyroelectric detector. This LIV is required to quantify the lasing threshold and current operating range.

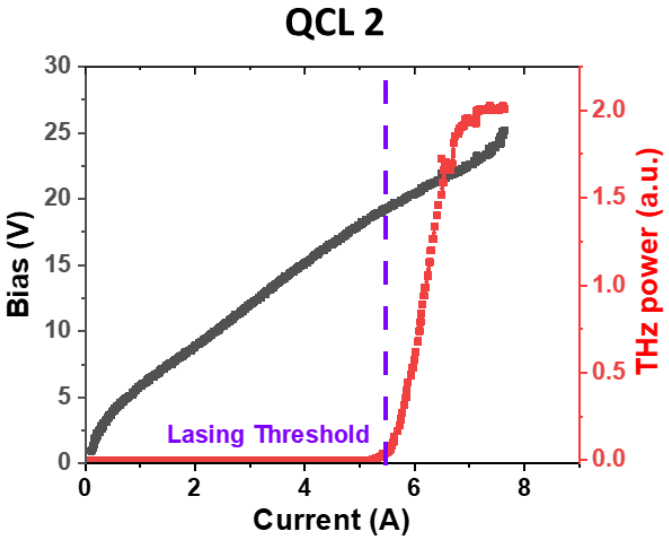

Figure V-25: LIV of QCL2 for a 50kHz 2% duty cycle modulation gated with a 20Hz modulation for pyroelectric detection. The QCL threshold is ~5.3A. Owing to the high power of these devices, the pyroelectric detector/lock-in amplifier saturates for high currents (> 6.5A).

The output power is then characterised with a Thomas Keating absolute power meter for different duty cycles of the QCL bias. (A higher duty cycle will result in a higher signal-to-noise in the TDS measurements). The QCLs spectrum were characterised using a Fourier transform infrared spectrometer (FTIR) to verify monomode operation for the duty cycle selected for polaritonic pumping experiments. Characteristics of the devices are available in Figure V-26 for QCL 1, Figure V-27 for QCL 2. From these characterizations it is clear that both QCLs are mostly monomode and operate at the same frequency of $2.94THz$. QCL1 is emitting a maximum power of $458mW$ for a duty cycle of 5% whereas a maximum of $389mW$ is reached at 17% duty cycle for QCL 2. Interestingly it seems that the maximum duty cycle permitted is related by the number of wire-bounding along the waveguide and might explain the difference between both QCLs. It is worth noting that an increase of the current translates into a linear increase of the output power and thus the power density.

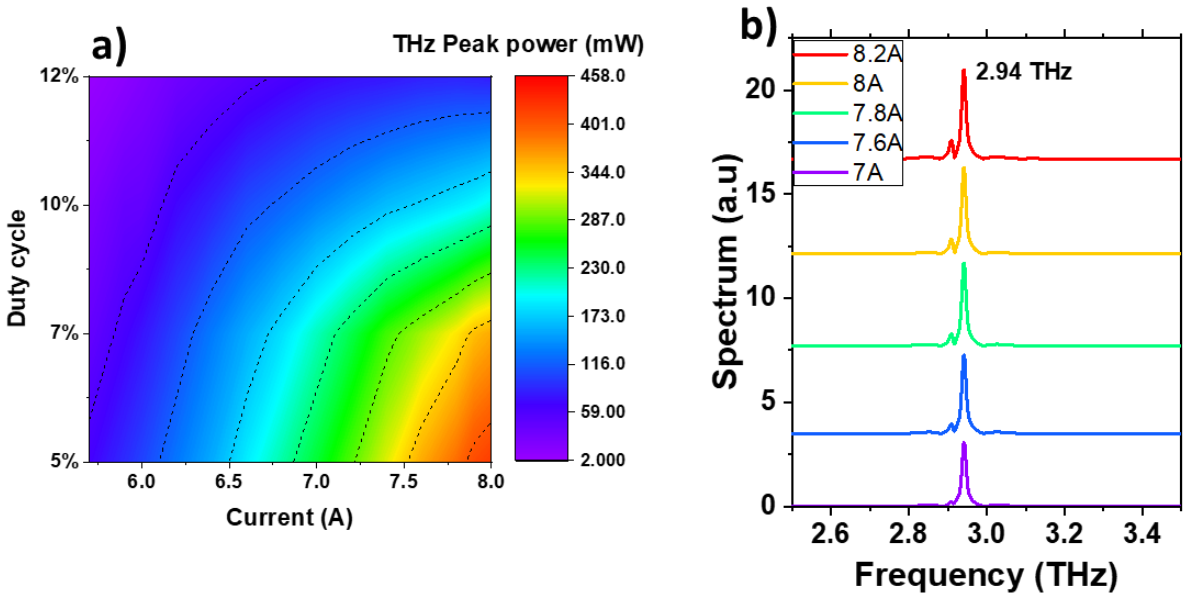

Figure V-26 : Characterization of QCL 1. a) 2D colormap of THz peak power for different current and duty cycles. A maximum power of 458mW is reached for a current of 8A for a duty cycle of 5%. b) FTIR spectrum of QCL 1 for a duty cycle of 7% which corresponds to a good compromise between THz power and TDS signal.

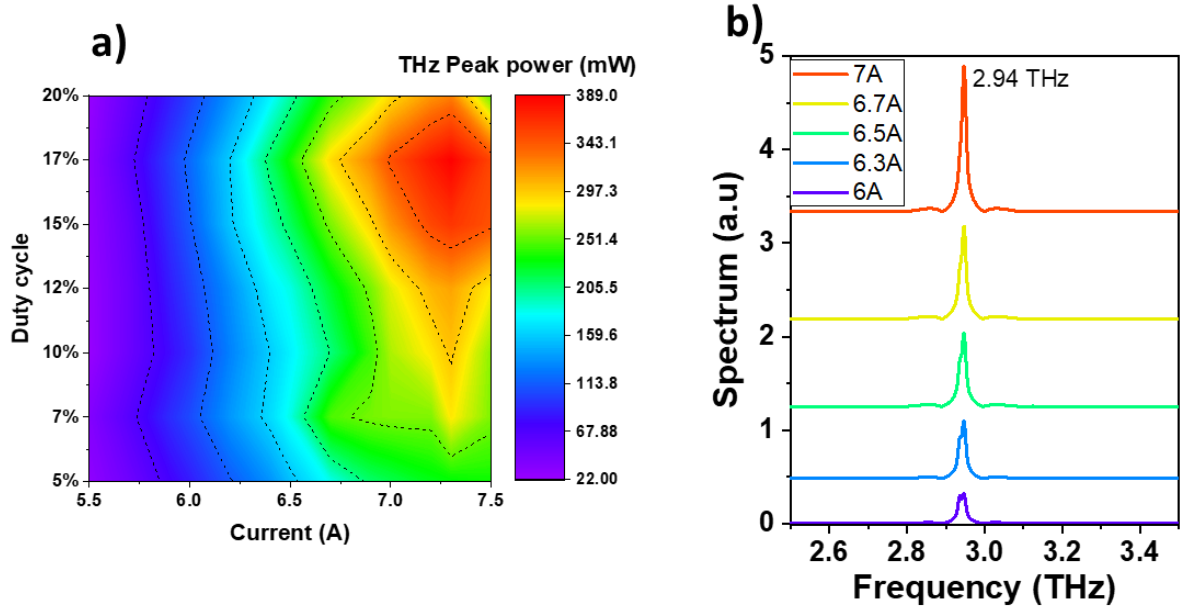

Figure V-27 : Characterization of QCL 2. a) 2D colormap of THz peak power for different current and duty cycles. A maximum power of 389mW is reached for a current of 7.3A for a duty cycle of 17%. b) FTIR spectrum of QCL 2 for a duty cycle of 15% which corresponds to a good compromise between THz power and TDS signal.

Note that the large driving currents require an optimized cooling of the device to be thermally stable. To give an estimation of the dissipated power in the case of QCL 2, considering a 17% duty cycle pulse combined with a $27V$, $7.5A$ bias results in $35W$ of heat that needs to be dissipated. This requires a considerable liquid helium flow to keep the temperature stable during measurements.

We will now discuss the implementation of our QCL pump in the TDS system.

V.5.1.1 QCL implementation in time domain spectroscopy

The aim is to resonantly pump the upper branch at the specific angle (θ) allowing energy and momentum conservation stimulating the polariton-polariton scattering while probing at normal incidence ($k_{\parallel} = 0$) with spectrally broad THz pulses (see Figure V-28) to observe potential gain at $k_{\parallel} = 0$.

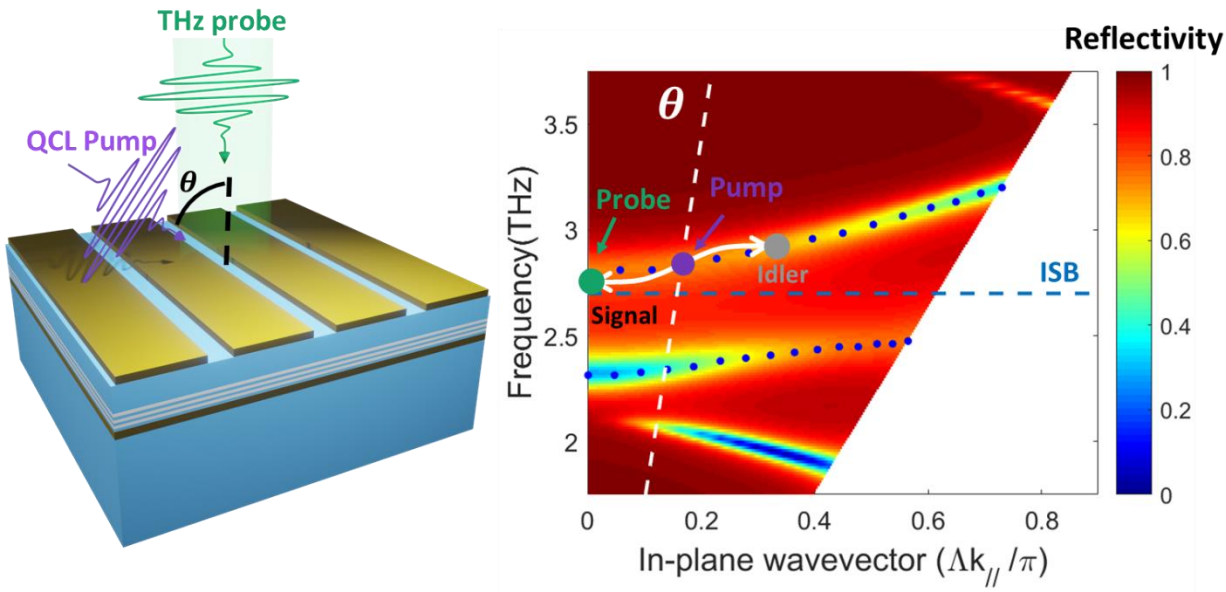

Figure V-28 : Experimental principle of resonant pumping and probing. The resonant pump excites the Up polaritonic branch with an incidence of θ while the broadband THz probe investigate the reflectivity at normal incidence.

TDS is a particularly adapted for such pump-probe setups, owing to its phase sensitive detection. This makes the system "blind" to the strong QCL pump that is not locked in phase to the TDS system. This represents a major advantage compared to more classical spectroscopy methods where small changes in the UP branch reflectivity can be difficult to detect due to an intense pump. In addition, due to the moderate dispersion of the UP branch, the frequencies of the QCL pump and the signal probed at $k_{\parallel} = 0$ are only spaced by $\sim 100GHz$. To investigate changes of reflectivity at normal incidence ($k_{\parallel} = 0$) under resonant pumping of the UP branch, we built a TDS setup (see Figure V-29) based on our high-power and high signal-to-noise ratio photoconductive switches described in section II.3. The normal incidence reflectivity is accessible with the addition of a Si beam splitter (50:50 ratio) placed to direct the reflected probe onto the electro-optic sampling detection scheme. Focusing of the

THz QCL pump is realized by the addition of a TPX lens that allows a beam waist as small as $500\mu m$. Smaller beam waist could be reached for lenses with shorter focal distances, but at the cost of cutting a significant ($> 10\%$) part of the THz probe beam that would result in poorer TDS signals. The angle of the pump can be controlled by moving the additional Au mirror closer or further to the QCL while rotating the mirror on his own axis. For experimental flexibility, all samples considered have been engineered to exhibit such triple resonant scheme with a pump at either 15° or 20°.

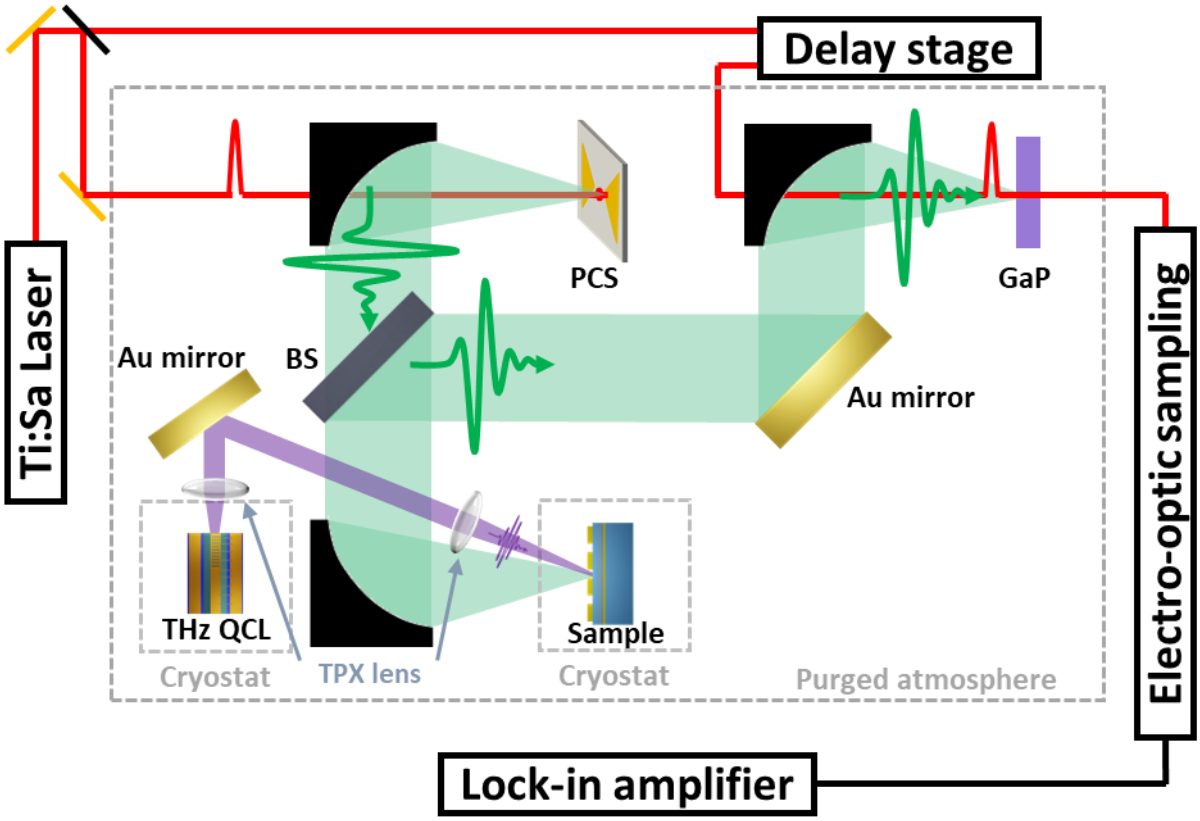

Figure V-29 : THz Time domain spectroscopy probe and QCL THz pump. The beam splitter (BS) directs the light reflected from the sample to the electro-optic sampling detection. The QCL pump beam is focused by a TPX lens, and injected at the required pumping angle by carefully moving the Au mirror.

Lock-in detection is used with the QCL pump and the probe beam from the PC switch synchronised to probe the reflectivity only when the UP branch is pumped by the QCL pump (see Figure V-30). As the output signal of our TDS system is strongly dependent on the duty cycle of the cavity-based PC switch bias, careful characterisations were carried on each QCLs (see sectionV.5.1) to find the best compromise between high QCL THz output power, QCL pulse widths and QCL temperature, for higher TDS reflectivity signal (see Table V-2).

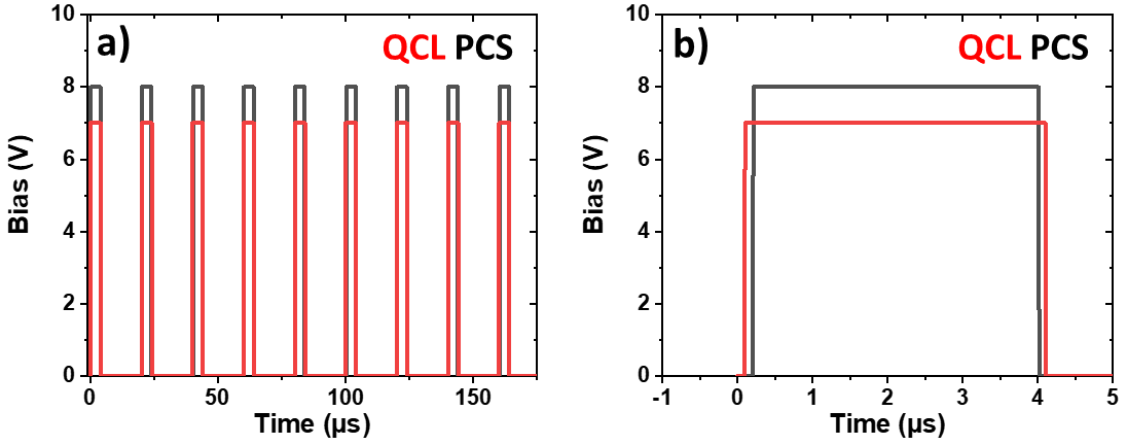

Figure V-30 : a) Electrical synchronization scheme used for locking detection. b) close up of a) The PCs is modulated with a slightly lower (1%) duty cycle than the QCL to ensure the probing of pumped states in the UP branch.

For polaritonic pumping experiments, the duty cycle selected is then a compromise between THz output power (pumping power density), high duty cycle (so the synchronous THz probe will show higher TDS signal) and temperature stability.

.	Frequency	Max power	Max power density	duty cycle for TDS
QCL1	2.94THz	458mW	80W/cm²	7%
QCL2	2.94THz	389mW	184W/cm²	15%

Table V-2 : Summary of the characteristics of the QCLs used in this work. QCL1 beam diameter is 800µm, QCL2 is 500µm this difference is due to an optimized focalization in the case of QCL2.

Regarding the THz probe, the addition of the beam splitter decreases the TDS signal by a factor 4 as the probe beam interacts twice with the beam splitter. This is coupled with the decrease of TDS signal by the low PC switch duty cycle (TDS signal lowered by a factor ~4 for a duty cycle of 15%). Due to the losses highlighted above on the THz probe, the use of our high-power cavity-based device presented in section II.3 represents here a real asset to investigate THz ISB polaritons. In addition, the echoless character of this device permits to records longs scan in the range of 50ps, limited only by the electro-optic crystal thickness, enabling a frequency resolution of $\sim 30GHz$, capable of resolving fine spectral features as highlighted in Figure V-31 for a typical LP and UP polaritons TDS reflectivity.

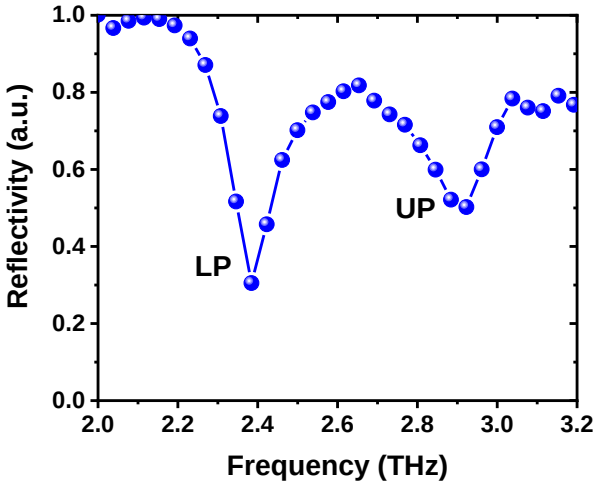

Figure V-31 : Typical TDS reflectivity (at 10K) of the lower and upper polariton branch at normal incidence with data points separated by $\sim 30GHz$.

The full alignment of this experiment is a complex task as it involves, first the alignment of the TDS system, and then in a second step the alignment of the pump with the precisely aligned TDS system. The full procedure is as follows:

- First a THz camera is used to optimize the beam shape at the THz focal points of the setup, i.e. where the polariton sample will be placed and at the position of the electro-optic crystal to optimize the overlap of the THz probe with the infrared pulse.
- This is followed by a precise alignment of the normal incidence TDS reflectivity on the polariton sample and a Au reference (at room temperature).
- The cryostat containing the polariton sample is replaced with the THz camera. The positioning of the camera is then carefully set at the same focal point as the sample by taking the time domain reflectivity of the camera and matching the time of the reflected THz pulse by moving the camera along the focal axis (see appendix Figure A 5 for detailed procedure).
- The probe spot is then recorded, and the QCL beam is aligned to overlap the probe beam with particular care, reducing the diameter of the beam to increase the pumping power density while keeping the QCL pump beam larger than the probe beam to only probe the pumped area (see Figure V-32).

To ensure an optimal power transfer of the pump beam, typical procedure implies swapping back and forth between the camera and the pyroelectric detector. The power density of the QCL pump is then calculated with the diameter recorded at the focal point of the set up by the THz camera (see Table V-2). The power density difference between the QCL1 and

QCL2 is due to a smaller spot size in the latter case from an optimized pumping scheme (shorter focal length of the pump lens).

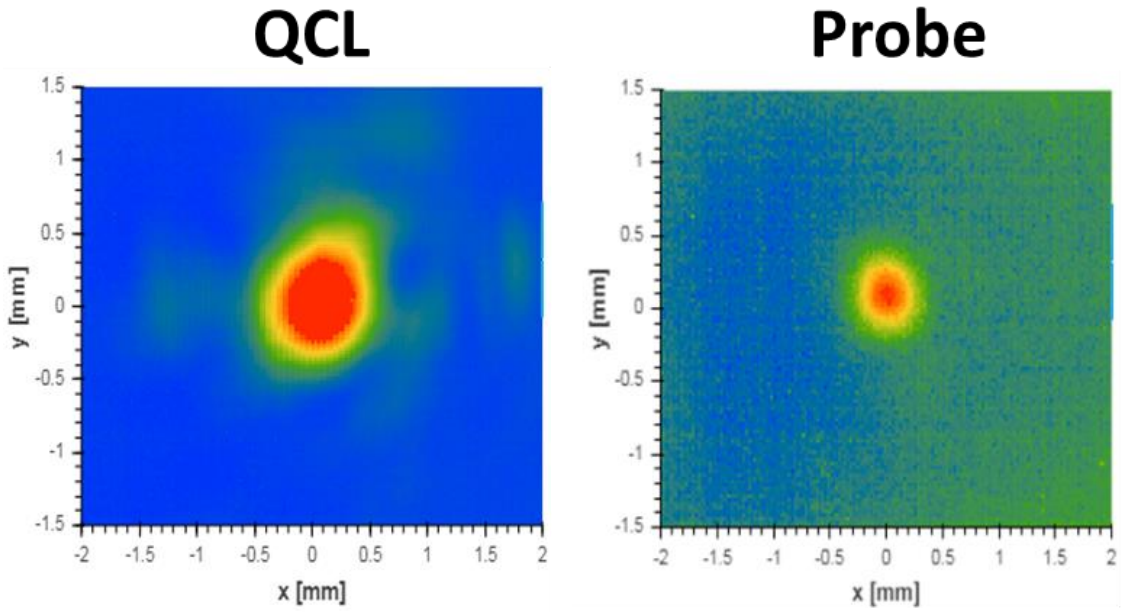

Figure V-32 : Experimental spot of QCL 1 and probe (PCs) beam at the focal point of the TDS system. This was obtained for a fixed camera. Once the TDS setup is aligned with the polaritonic sample, the cryostat containing the polaritonic sample is swapped with the THz camera (SwissTHz) to precisely overlap the QCL and the probe beam. Note that the QCL beam is larger than the probe beam ensuring the probing of pumped regions.

Note that the full alignment of such a setup can take up to several weeks and requires both the QCL pump and the polaritonic sample to be cooled to around liquid helium temperatures ($4K$). This implies that where helium vessels are empty, one must realign the precise overlap of the QCL pump with the TDS probe for the next vessels. To fully appreciate the scale of this pumping experiments, a photograph depicting the TDS with the additional QCL pump during a measurement is available in Figure V-33.

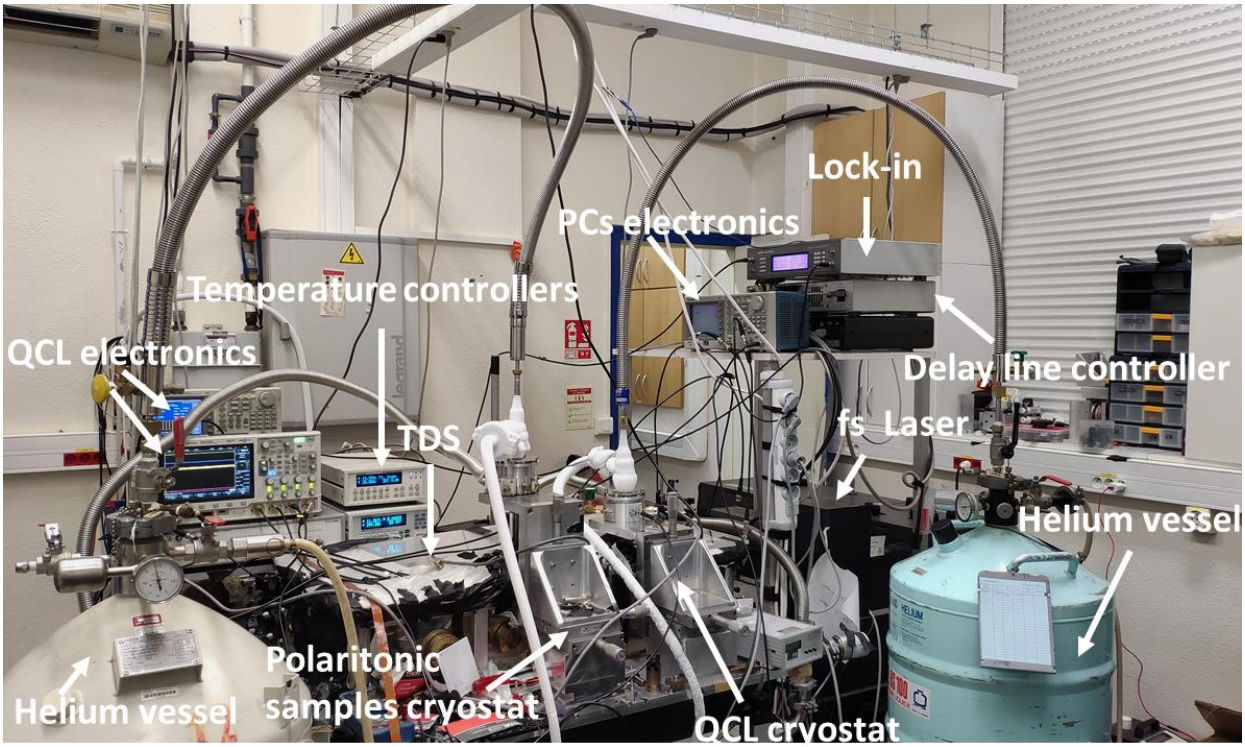

Figure V-33 : Photograph of the TDS with the additional pump QCL during a measurement (Aug 2020).

In the next section we will discuss the reflectivity of our polariton samples as it is a crucial parameter for pumping experiments.

.

V.6 Polariton reflectivity

In this work, two generations of polariton cavities were designed with a cavity thicknesses (t) of, respectively, 11µm and 8.47µm for the 1st and 2nd generation. The latter provides a stronger light-matter coupling (from the better overlap between QWs and cavity electric field) leading to a better UP reflectivity contrast at $k_{\parallel} = 0$ (see section V.7.1). It was realized by thinning down the original 11µm thick sample. Experimentally, the reflectivity is calculated by the ratio between the spectral electric fields reflected by the polaritonic sample and by a reference Au mirror (mounted next to the sample). Normal incidence reflectivities were investigated for all samples, over a polaritonic sample temperature ranging from 4K to 70K, as well as 300K (room temperature) for the 2nd generation of samples. All the results are available in appendix (Figure A 7) but are shown for sample 5 (2nd generation of samples with 65% duty cycle) in Figure V-34 to highlight the LP and UP branches tunability over the temperature variation. For all 8.47µm thick samples, the predicted (RCWA) and experimental normal incidence reflectivities recorded by our TDS setup are compared, with good agreement, in Figure V-35 a) at 10K. The experimental reflectivity is fitted with a fine tuning of the QWs doping density, the cavity thickness along with the duty cycle and the period of the Au grating as parameters with RCWA to fine-tune the model and access accurately the full angular dispersion of the samples. The dotted orange line corresponds to the ISB transitions of QWs.

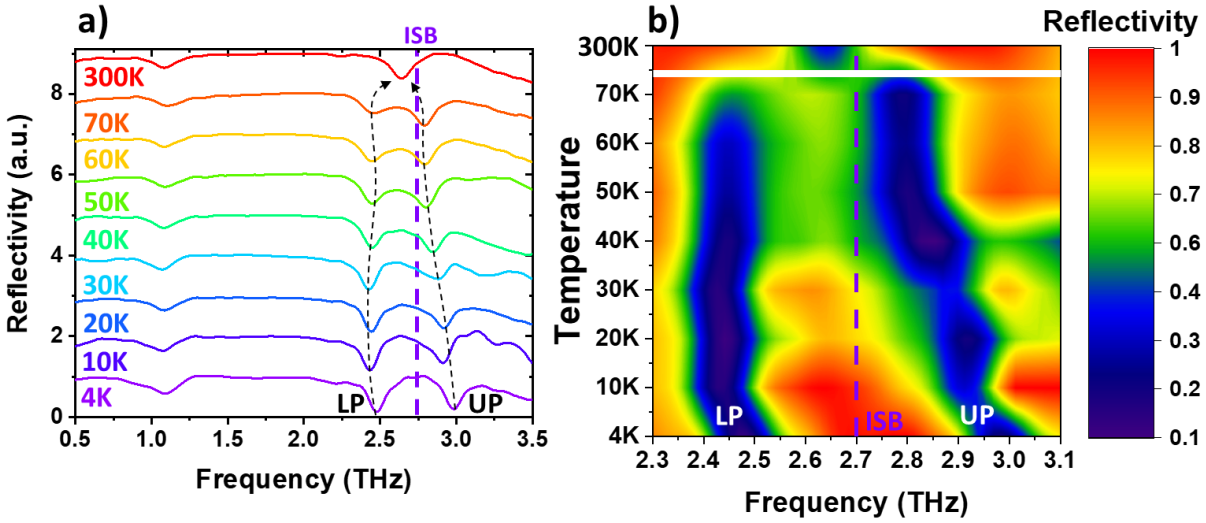

Figure V-34 : a) Temperature dependence (300k-4k) of reflectivity of sample 5 (65% duty cycle). The ISB transition of our QWs is highlighted by purple dashes. We can clearly see the LP and UP branch shifting with the

temperature, the dashed arrows are guide to the eyes. b) 2D colormap closeup of the LP and UP branches reflectivity (note the non-linear scale of temperatures represented by the white line).

As discussed in section V.4.3, the differences in the duty cycles of the samples impacts drastically the reflectivity, the frequency position, the Rabi splitting and the FWHM of the polariton branches. This is clearly visible in Figure V-35 b) where the RCWA extracted reflectivities at $k_{\parallel} = 0$ are plotted for different duty cycles. The important change in reflectivity of the UP branch can be explained by the UP being more matter-like for large duty cycles (the UP gets closer to the ISB transition matter part of the system). Changes induced by the different duty cycles were fitted by a Voigt function (convolution between a Gaussian and a Lorentzian, relevant for spectroscopy [241]) and summarised in Figure V-36, where the central frequency, reflectivity, FWHM and Rabi splitting of the LP and UP ($UP_{k=0}$) at $k_{\parallel} = 0$ are quantified for the 2nd generation of samples. We have highlighted the QCL pump (dashed black line) along with the central frequency of the UP polariton at the pumping angle ($UP_{k_p}, red\ curve$) that allows the triple resonant scheme for the different duty cycles. This metric represents the energy resonance condition between the QCL and the UP branch. From this data we can see that our QCLs can pump resonantly samples 2 and 3 (respectively 80% and 75% duty cycle) and thus can potentially stimulate polariton-polariton scattering. (see appendix Figure A 6 and Figure A 7 for RCWA and experimental TDS reflectivity of 2nd generation samples)

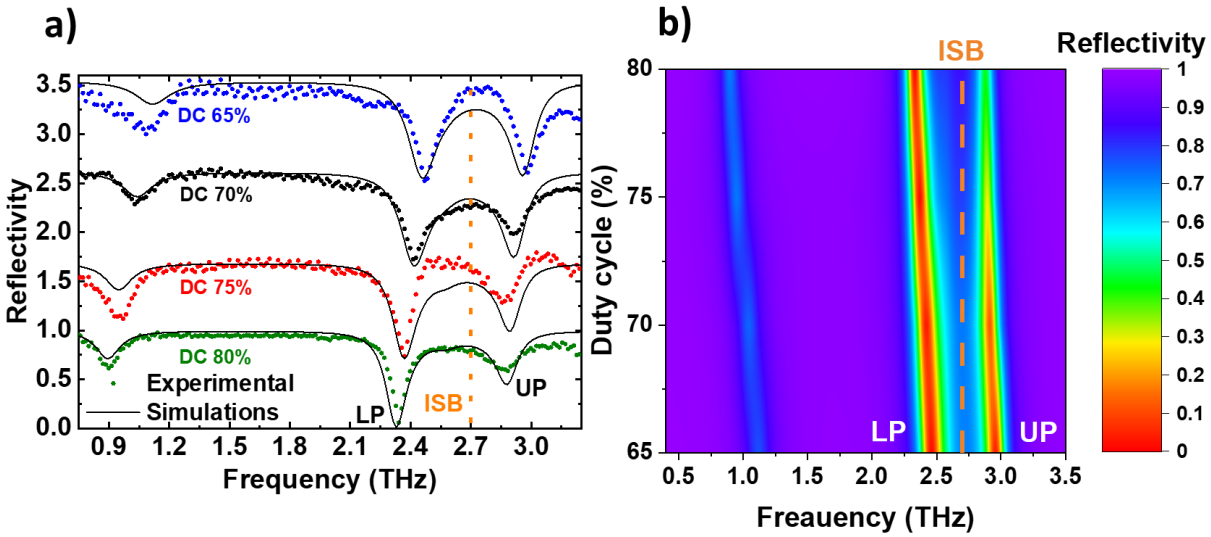

Figure V-35 : a) Experimental TDS reflectivity (in dots) spectrum of samples 2-5 (see Table V-3) at 10K shows a good agreement with RCWA values in plain lines. b) 2D colormap of RCWA reflectivity at $k_{\parallel} = 0$ of the polaritonic samples for different duty cycles

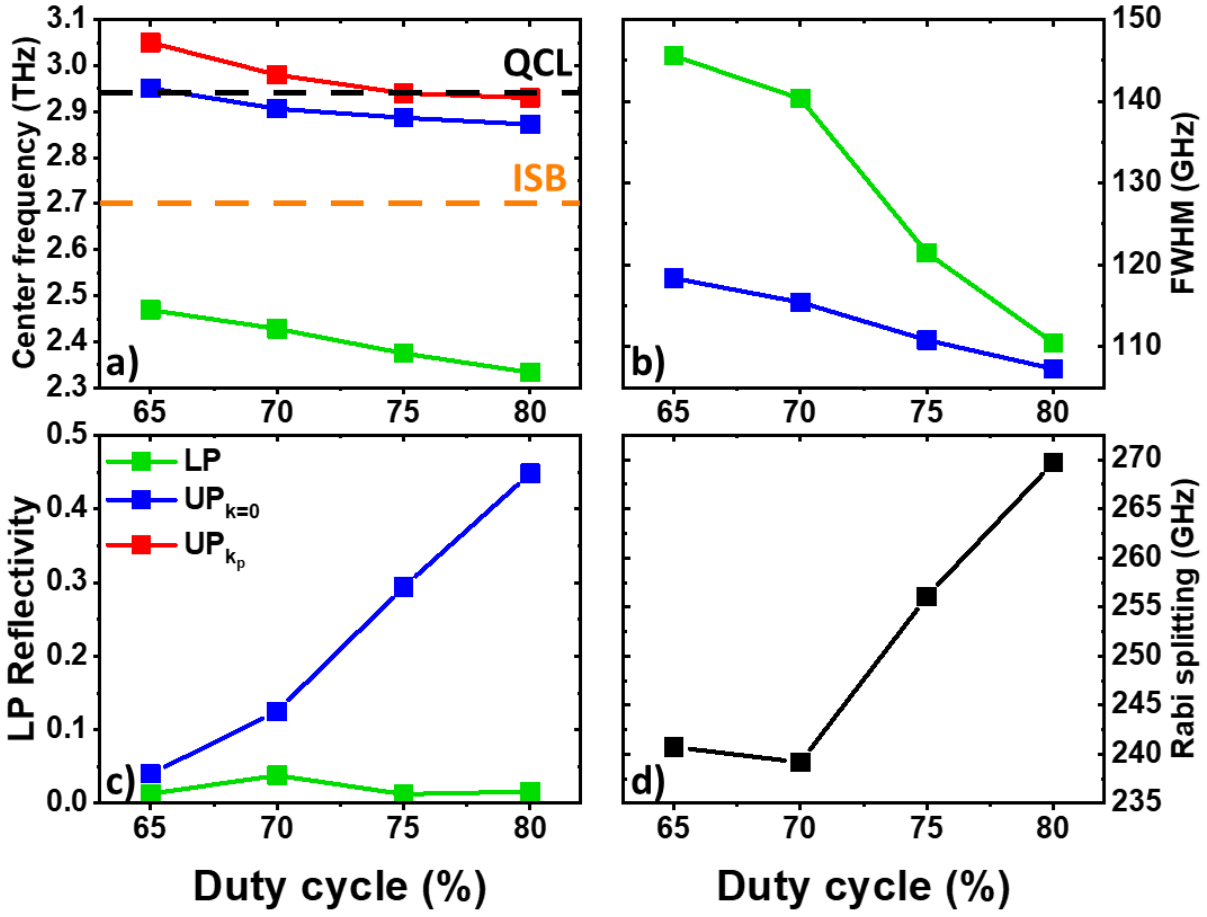

Figure V-36 :RCWA Voigt fitted a) Centre frequency, b) FWHM, c) Reflectivity and d) Rabi splitting evolution of LP and UP branches for the change of duty cycle of samples 2-5 at $k_{\parallel} = 0$. The ISB transition corresponds to the orange dashes, and the QCL pump is highlighted by black dashes. The central frequency of the UP polariton at the pumping angle (UP_{k_p}) highlights the resonance conditions between the QCL pump and the UP branch. The change in reflectivity is explained by a shift of the UP towards the ISB transition resulting in a more matter like character.

Table V-3 Summarize now all the samples considered in this manuscript with all their relevant parameters for resonant pumping of UP branch at the pumping angle and broadband probing at normal incidence, as discussed in the next section.

Samples	**1**	**2**	**3**	**4**	**5**
Duty cycle	80%	80%	75%	70%	65%
Buffer (µm)	8	5.47	5.47	5.47	5.47
N_{QW}	53	53	53	53	53
Total thickness(µm)	11	8.47	8.47	8.47	8.47
UP resonant angle k_p (°)	15	20	20	20	20
Centre frequency $UP_{k=0}$ (THz)	2.90	2.87	2.88	2.92	2.98
UP Reflectivity $UP_{k=0}$	0.83	0.45	0.3	0.13	0.05
UP frequency UP_{k_p} (THz)	**2.95**	**2.93**	**2.94**	2.98	3.05

Table V-3 : Cavities considered in this manuscript, the green and blue colors accounts respectively, for the 1st and 2nd generation of cavities. UP_{k_p} and $UP_{k=0}$ accounts for the UP polariton branch respectively at the predicted resonant angle allowing polariton-polariton scattering, and the signal angle (normal incidence). Note that the UP frequencies at the predicted resonant angle (UP_{k_p}) were extracted from refined RCWA simulations, energy matching with our QCLs pump is highlighted by bold values.

Before presenting our results, it should be mentioned that for intense excitations, it is possible to reduce the oscillator strength of the ISB transition, which in the case of a strongly coupled system could leads to a complete collapse of the light-matter interaction strength [242]. Interestingly, this phenomenon called bleaching has been reported by the research group of Miriam Vitiello in the THz range for similar MIM cavities [243]. The cavity included 35 GaAs/AlGaAs QWs doped at a density of $5 \times 10^{10} cm^{-2}$. Using this structure, THz pumping experiments involving a CW QCL pump of frequency $2.75 THz$ impinging the cavity at normal incidence showed polaritonic bleaching at relatively low power ($10.7\ \mathrm{W/cm^2}$).

In next section we will show the resonant pumping of UP, and even though the QCLs used in this manuscript reached larger power densities, no polaritonic bleaching has been characterized. One explanation could be the larger number of QWs and doping used in our structure, and the use of a resonant excitation.

V.7 Resonant THz pumping of the upper polariton branch

Our ultimate aim is to demonstrate THz gain in the UP branch. For that purpose, we investigated the normal incidence reflectivity while resonantly pumping the UP branch at the specific angle. Pumping at this angle will allow a potential stimulation of the polariton-polariton scattering as the power density is increased, leading to laser action via non-equilibrium-BEC of ISB polaritons. From the samples presented in Table V-3 we chose to investigate the samples 1,3,5 and this section is structured as follows.

1) Historically, the first investigated was sample 1(1st generation) that shows strong coupling but poor reflectance contrast at $k_{\parallel} = 0$ for the UP. While developing improvements for the light-matter coupling with the C2N, we performed resonant pumping on this sample with QCL1 due to the good energy matching with the UP branch.
2) Due to an enhanced reflectivity contrast of the UP, the 2nd generation of samples represents a better platform to observe polariton-polariton scattering and potential gain. In this section, we investigate the resonant nature of the triple resonant scheme on sample 3 by performing:
    a. A temperature dependence of the polaritonic sample to characterize the energy resonant nature of the observed changes in reflectivity.
    b. A pumping power dependence
    c. An angle variation on the pump beam at a fixed temperature to highlight the angle (momentum) resonant change in reflectivity.
3) Then we turned on sample 5, despite the QCL pump being out of resonance with the UP branch. As we will show, the polariton-polariton scattering can potentially be assisted by a Brillouin folding of the cavity.
4) Finally, to further characterise our results, for sample 5 under QCL pumping, we investigate the nonlinear reflectivity of the polaritonic sample by pumping at the resonant angle and collecting the reflected QCL light. Indeed, exciton-polaritonic systems are known for their strong nonlinear behaviour that arise from their matter characteristics [209], but to date no work has been dedicated to the observation of non-linearities in ISB polaritonic system. In fact, the ratio between the incident and the

reflected light shows promising signs to assess nonlinearities from THz polariton-polariton scattering and is supported by preliminary calculations from the INO-CNR BEC centre.

This latter point represents a significant milestone as this nonlinear phenomenon has never been observed for ISB polaritons. In the following sections, we will detail and analyse each investigated scheme.

V.7.1 Coherent pumping on 1st sample generation

The schematic of the pumping scheme of the UP branch and the reflectivity measurements on sample 1, with QCL1 as the pump, are shown Figure V-37. Panel a) is the RCWA dispersion of the sample with the predicted angle allowing the polariton-polariton scattering of 15° highlighted. Note that this RCWA dispersion is accurate as it was fitted to the experimental data of the FTIR reflectivity measurements for angles ranging from 13° to 83° (see ref [168] and Figure V-21). Here, the pump beam is exciting the sample with an angle of 15° and a THz broadband pulse probes the reflectivity at $k_{\parallel} = 0$. Panel b) shows the bare reflectivity of the sample without the QCL pump (black plot) along with relative change in THz TDS reflectivity of the polariton sample, corresponding to $E_{THz(QCL\,pump)}/E_{THz(no\,QCL\,pump)}$ where E_{THz} is the spectral field, for a range of QCL pump powers. Note that if no changes are induced by the QCL pump, we would expect a flat relative reflectivity equal to 1 (but this metric can give artifacts and should be used cautiously). A clear increase in reflectivity is observed at the UP $\sim 2.9\,THz$ with increasing pump power density until $42 W/cm^2$, a possible indication of polariton scattering. The LP is also affected (small frequency shift) and is possibly related to heating of the sample. In the case of a non-resonant pump (using QCLs operating above the UP), no changes in reflectivity could be observed at the UP, suggesting that the process is resonant.

However, the low-light matter coupling at $k_{\parallel} = 0$ of this sample results in a poor UP reflectivity contrast. As we will discuss below, larger effects could be observed on the second generation of samples designed for a stronger light-matter interaction at $k_{\parallel} = 0$.

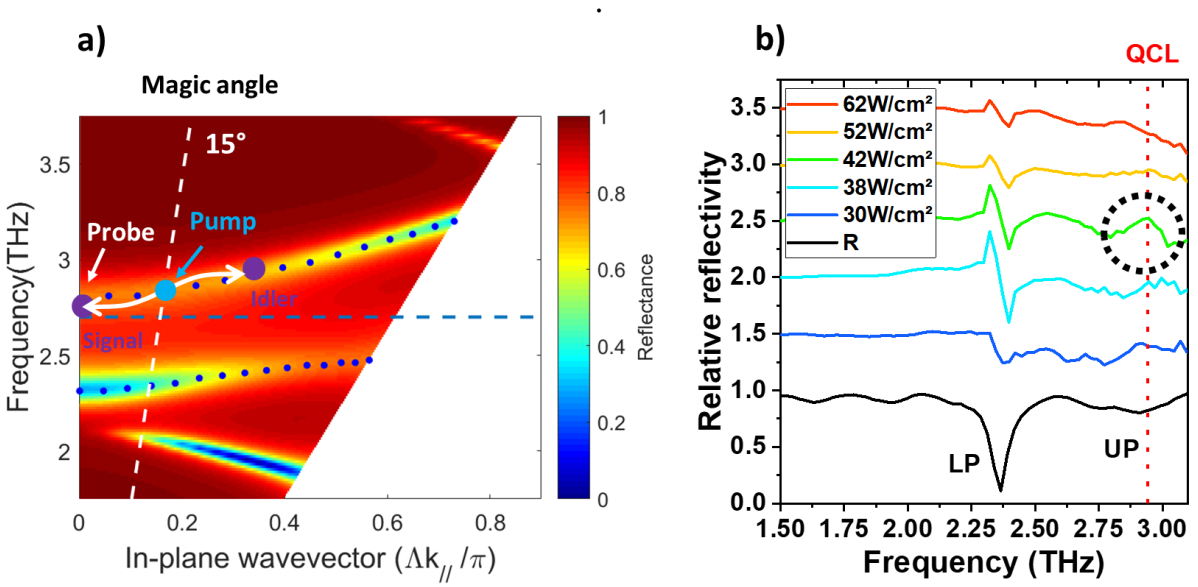

Figure V-37 : a) RCWA simulation showing the Coherent pumping of UP branch of sample 1 with QCL 1. We pump the UP at the resonant angle (highlighted by white dashes corresponding to an angle of 15°) and probe the polariton sample at $k_{\parallel} = 0$ with our THz TDS setup to see a change in reflectivity by increasing the pump power density (the dotted lines show the LP and UP center frequency). b) Bare reflectivity of the polaritonic sample without QCL pump (in black) along with relative change in THz TDS reflectivity of the polariton sample corresponding to $E_{THz(QCL\ pump)}/E_{THz(no\ QCL\ pump)}$.

V.7.2 Coherent pumping of 2nd sample generation and Temperature dependence

The 2nd generation of polaritonic samples was designed to provide stronger light-matter interaction at $k_{\parallel} = 0$ yielding a better reflectivity contrast for the UP. This can be seen in Figure V-38 displaying the RCWA reflectivity resolved polaritonic dispersion of sample 5 where the UP branch reaches a lower reflectivity in respect to the previous sample.

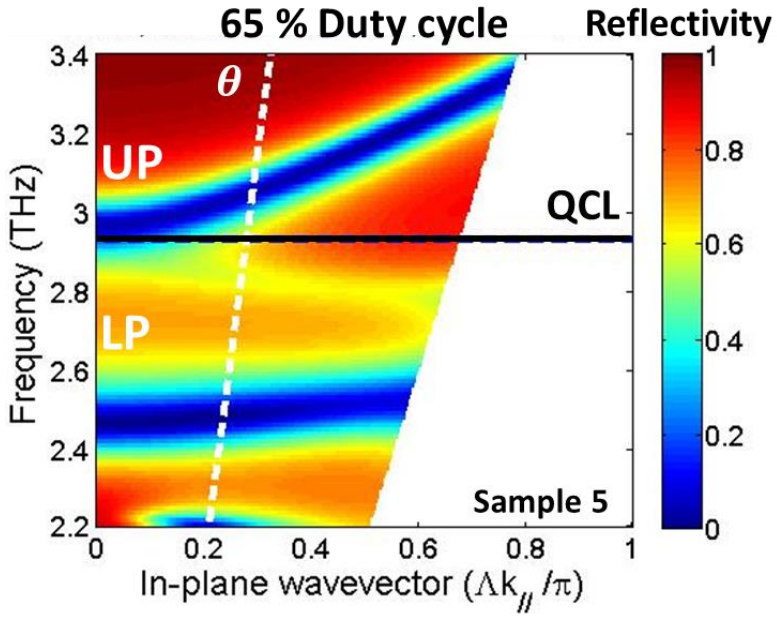

Figure V-38 : RCWA reflectivity resolved polaritonic dispersion of sample 5 from the 2nd generation of samples. The QCL pump frequency along with the resonant angle of the pump (θ) is highlighted.

From Figure V-36, we showed that the energy resonance condition between the UP branch of Sample 3 at the angle allowing the triple resonant scheme (UP_{k_p}) nearly matches the QCL pump energy, with a change of temperature of the polaritonic sample, it is possible to tune the energy dispersion and thus to optimize the triple resonant condition. We will now discuss the changes in reflectivity on the UP branch for sample 3. The polariton sample is pumped by the QCL at 20° for temperatures ranging from 4K to 50K, where the UP shifts towards lower frequencies and a reduced light-matter coupling. As this represents a consequent dataset, detailed results are in appendix (see Figure A 8) but are summarized, firstly by presenting only the most relevant data and secondly, by showing a 2D colormap of the integrated UP reflectivity under resonant pumping for the whole temperature variation.

Results for the temperature dependence are visible in Figure V-39. The top panel represents the relative reflectivities for 10K, 20K and 40K as a function of pumping power density, while the bottom panel is a colormap of the same data centered around the LP and UP branches (note that y-scale of power densities, which reflect experimental values). The energies of the UP branch and the QCL pump are highlighted by, respectively, the blue (UP_{k_p} is the frequency of the UP branch "seen" by the QCL pump at the pump angle) and white dashes, while the black dashes represent the UP_{k_s} frequency at $k_{\parallel} = 0$ (as probed by the THz probe). Note that all colormaps have the same scale for comparison. At 10K, an increase in relative reflectivity is visible in the UP, a maximum of 1.5 is reached for $109 W/cm^2$and decrease with the increasing power density. Reflectivity data for 20K show a stronger change all along the range of power densities, with a maximum of 1.6 reached for a power density of $89 W/cm^2$. When the temperature is set at 40K, nearly no change is visible, a local maximum of 1.15 is reached at $89 W/cm^2$. Comparatively with the reflectivity changes measured for sample 1, we obtained stronger (roughly by$\sim 60\%$) reflectivity changes, but are reached for higher pump power densities. It has to be noted that despite the power density being higher than the previous dataset, no bleaching (saturation leading to collapsing of the polariton states) is observed. To summarize all the data, including those placed in the appendix, one can integrate the reflectivity over the FWHM of the UP for the whole temperature variation. This dataset is shown in Figure V-40 for the integrated reflectivity. The same trend is observed with 20K being a sweet spot, suggesting that this temperature allows an energy resonant condition between the QCL pump and the UP dispersion. For temperatures above this value, nearly no change is measured. These data clearly show that this reflectivity change in the UP branch is resonant at 20K. At 40K the UP is out of resonance with the QCL pump and nearly no reflectivity change is recorded. This reinforces the possibility of being in the presence of a resonant effect and therefore potentially polariton-polariton scattering.

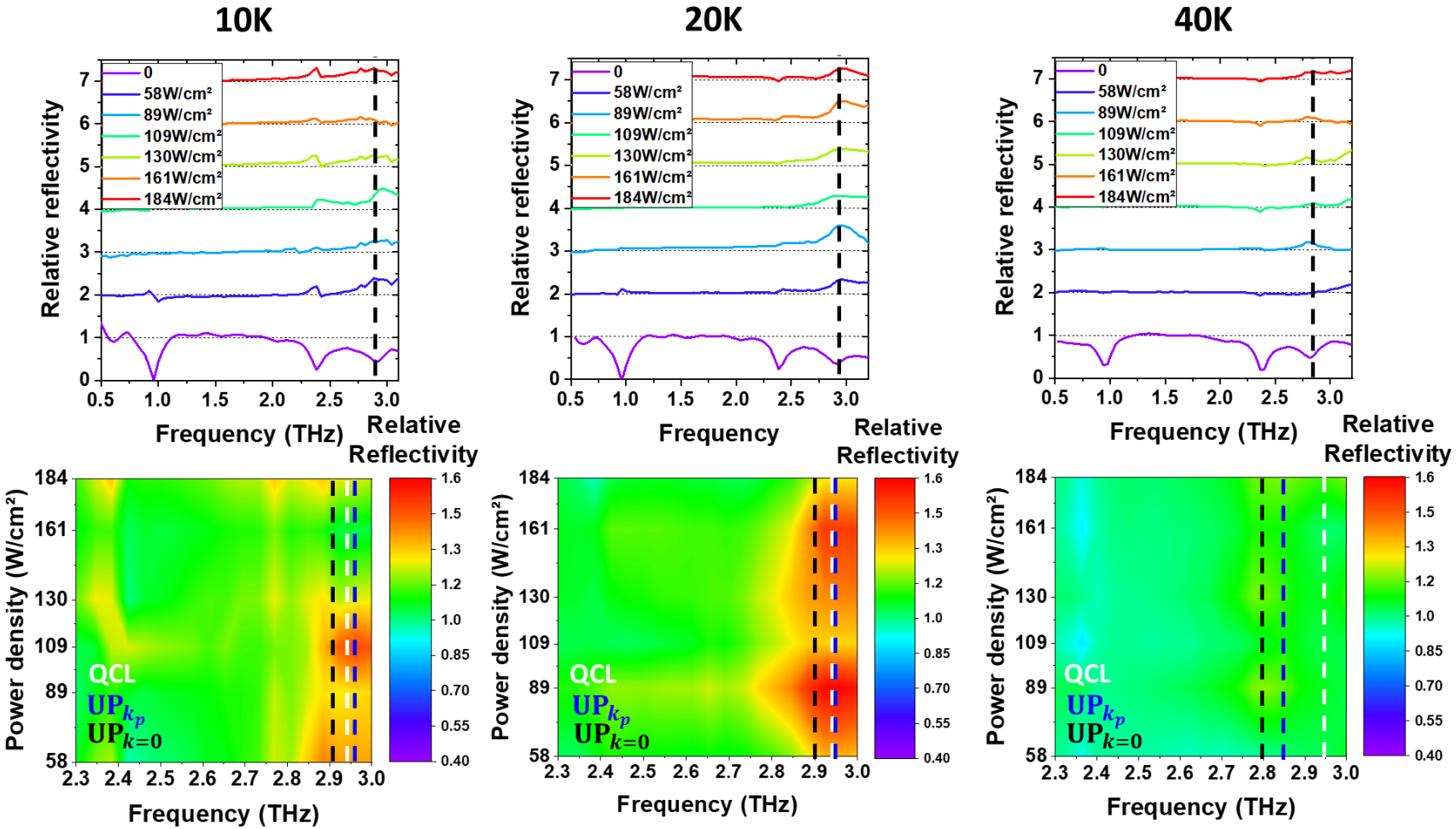

Figure V-39 : Resonant pumping results of sample 3 with QCL2 for a fixed pump beam se at the magic angle (20°) and a temperature of the polariton sample ranging from 20K to 40K. Note that the scale of power densities corresponds to experimental data. The frequency position of the UP branch at normal incidence ($UP_{k=0}$) and at the predicted resonant angle (UP_{k_p}) is highlighted respectively by black and blue dashes while the QCL frequency is marked by white dishes. In these data, it is clear that the change in reflectivity observed is resonant with temperature.

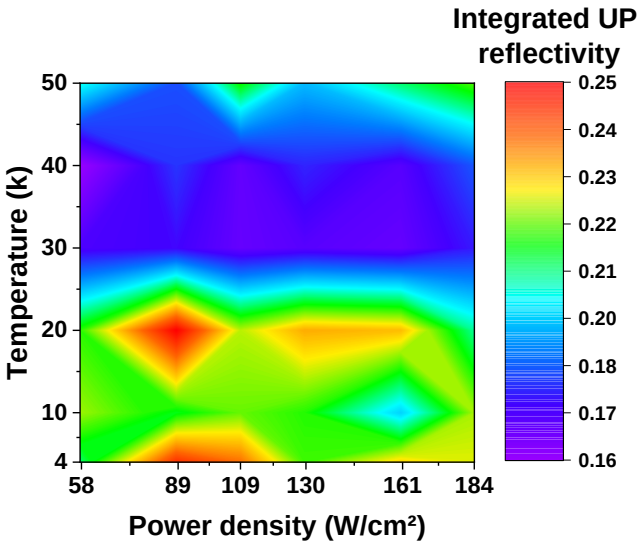

Figure V-40: Integration of the UP FWHM reflectivity on the full variation of temperature. It is clear that these changes in reflectivity are resonant with temperature with 20K being a sweet spot where the QCL is resonant with the UP branch.

V.7.3 Angular dependence of the QCL pump

To further characterize this resonant reflectivity increase, we performed an angular dependence on the QCL pump beam at a fixed temperature (20K) to establish a correlation between the momentum conservation required by the polariton-polariton scattering and the characterized changes in reflectivity. The concept of the angular dependence is schematized in Figure V-41 a) where the UP branch is resonantly pumped at different angles (diagonal dashes on the figures) resulting in a fine-tuning of the pump momentum on the UP branch along the QCL energy and different values of UP absorption (see panel b)).

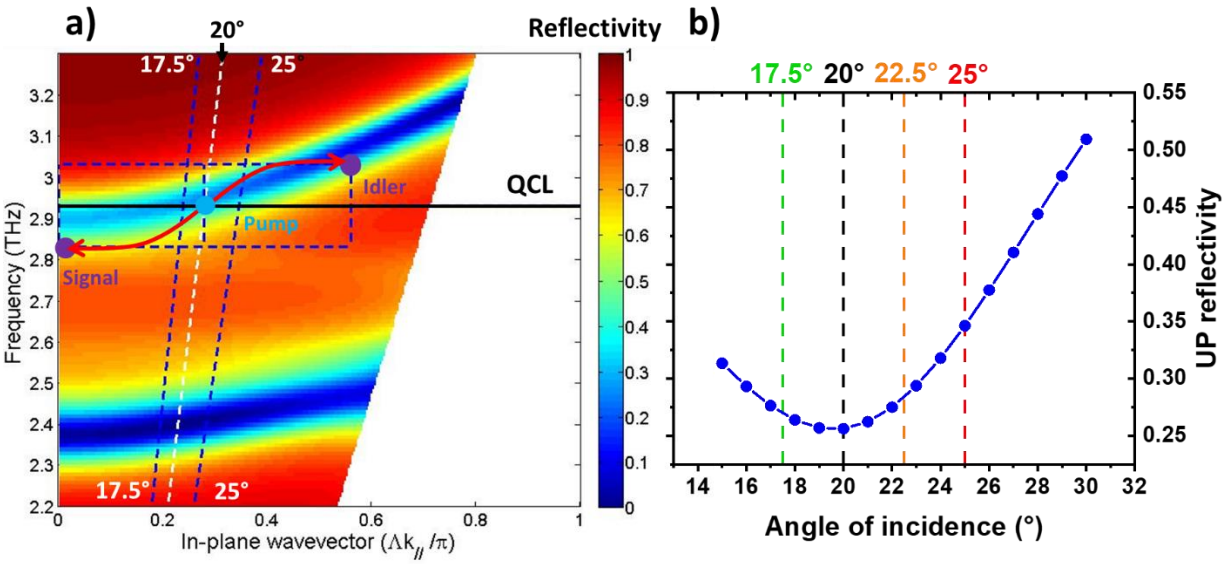

Figure V-41 : a) RCWA dispersion of the sample 3 with the polariton-polariton scattering mechanism highlighted. The diagonal dashes accounts for the variation of angle. For this experiment, the pump excites the sample at fixed temperature, in this figure, the angle variation can be seen as a move of the blue circle (pump) along the QCL axis. b) UP polariton reflectivity in function of the angle of incidence. Different angles of incidence of the QCL pump results in different absorption.

We chose here to investigate the reflectivity for an incident pump beam at an angle of 17.5°, 20°, 22.5° and 25°. For each angle, the QCL pump is resonant in energy with the UP branch. All the datasets are in appendix and will be summarized here. The results for this angle variation are available in Figure V-42 where the top panel represents the relative reflectivities for a QCL pump with an incidence of 17.5°, 20° (predicted angle allowing the triple resonant scheme) and 25°. The bottom panel is a colormap of the same data centered around the LP and UP branches. The resonance condition between the UP branch and the QCL pump is highlighted by, respectively, the blue (UP_{k_p} denotes here the UP frequency at the investigated angle) and white dashes. Note that all colormaps have the same scale for comparison. For this angular variation, the energy resonance condition between the QCL pump and the UP_{k_p} branch at the investigated angle experience a slight change over the variation due to the moderate UP dispersion. At 17.5°, a clear reflectivity change is visible in the UP with a maximum of 1.5 reached for $161 W/cm^2$and decreases with further increasing power density. Reflectivity data for 20° are the same presented in Figure V-40 and show stronger changes all along the range of power densities, with a maximum of 1.6 reached for a power density of $89 W/cm^2$. When the angle of incidence of the QCL pump is set at 25°, nearly no change is visible. In this angular dependence, the reflectivity change is maximum

for a 20° pump, which agrees with the RCWA predicted resonant angle and is further indication of polariton-polariton scattering.

To summarize all the data including those placed in appendix (see Figure A 9), one can, again, integrate the reflectivity over the FWHM of the UP for the whole angle of incidence of the QCL pump variation. These data are shown in Figure V-43 and clearly show that the characterized reflectivity change in the UP branch is resonant with the angle of incidence of the QCL pump. This also excludes heating effects as no changes are recorded for high angles and little change in reflectivity are observed on the lower polariton.

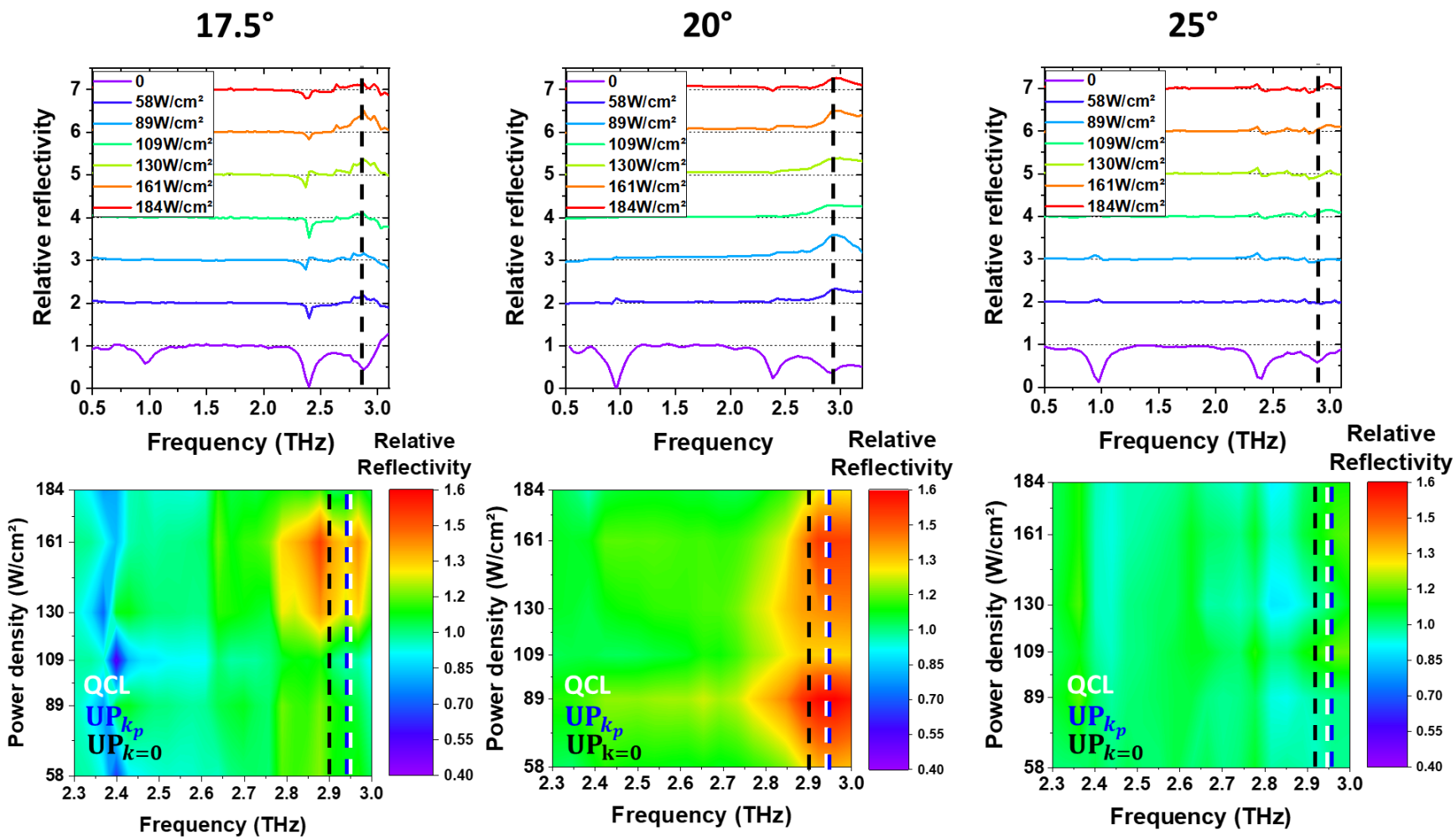

Figure V-42 : Resonant pumping results of sample 3 with QCL2 for a fixed temperature and a variation on the angle of incidence of the QCL pump ranging from 17.5° to 25°. . Note that the scale of power densities corresponds to experimental data. The frequency position of the UP branch at normal incidence ($UP_{k=0}$) and at the investigated angle (UP_{k_p}) is highlighted respectively by black and blue dashes while the QCL frequency is marked by white dishes. In these data, it is also clear that the change in reflectivity observed is resonant with the pump incidence angle.

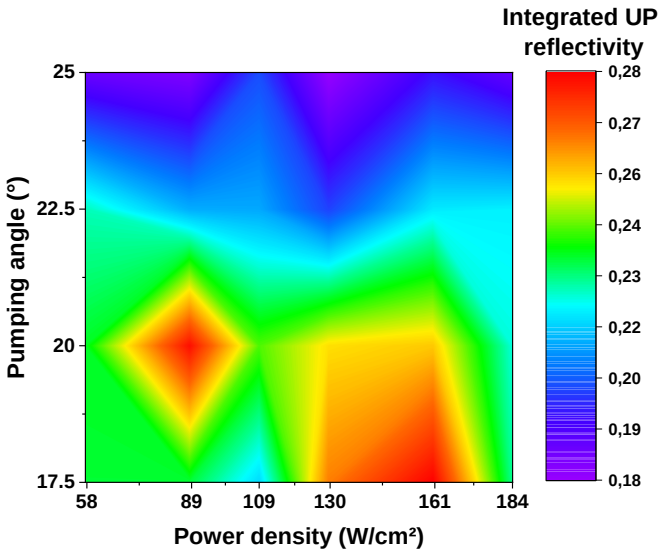

Figure V-43 : Integration of the UP FWHM reflectivity on the full variation of angle. It is clear that 20° is a sweet spot regarding the characterized changes in reflectivity.

Signatures of polariton-polariton scattering would includes a spectral shift of the UP, a decrease of the FWHM denoting the phase transition coherence of polariton condensation [209], a sharp change of reflectivity of the polariton branch from the stimulated scattering process, while maintaining the strong coupling (i.e. no bleaching of polaritons) in the system. To look for these signatures, we fitted the LP and UP reflectivity peaks displayed in Figure V-44 with a Voigt function along the same spectral window for comparison. This enables to extract the polariton branches centre frequency, FWHM, reflectivity minima and Rabi splitting for an increase of the pumping power density, for the case where the polariton sample is at 20K and pumped at 20° (middle plot of Figure V-39 and Figure V-42).

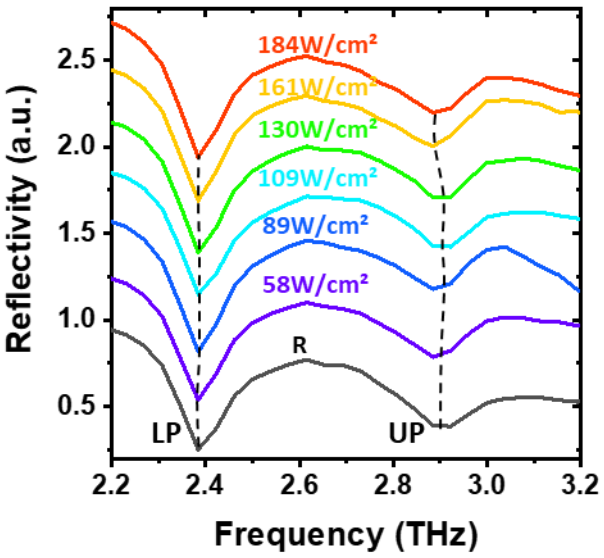

Figure V-44 : Stacked LP and UP branches reflectivity of sample 3 at 20K pumped by the QCL 2 at 20° for increasing power densities. The black trace is the bare reflectivity (no QCL pump), the black dashes are guide to the eyes.

Results are displayed in Figure V-45 as a function of the power density. Note that the R on the x-axis denotes for the bare reflectivity of the sample (no QCL pump), black dashes highlight the bare reflectivity frequency in panel a), and errors bars corresponds to the TDS spectral resolution. The general trend on the UP branch seems to be a slight redshift by $\sim 40 GHz$ with an increase of the pump, whereas the LP roughly stays at his original value. In panel b), the FWHM of the UP branch shows an increase of 143% with the power density, while the recorded LP variation does not exceed the errors bars. In panel c), the reflectivity gradually increases with the pump on the UP to reach a maximum of 160% at $89 W/cm^2$ (as stated in Figure V-39 and Figure V-42), and then decrease. The LP seems less impacted by the QCL pump but follows the same trend regarding reflectivity changes. The Rabi splitting in panel d) seems to slightly ($\sim 5\%$) decrease, although this variation is inside the error bars. Nevertheless, it is clear that for all power densities, the system is still in the strong coupling regime. From this analysis, the characterized frequency shifts, non-trivial reflectivity changes, FWHM increase of the UP, along with the decrease of the Rabi splitting, may suggest that our system is indeed below the threshold of stimulated polariton-polariton scattering.

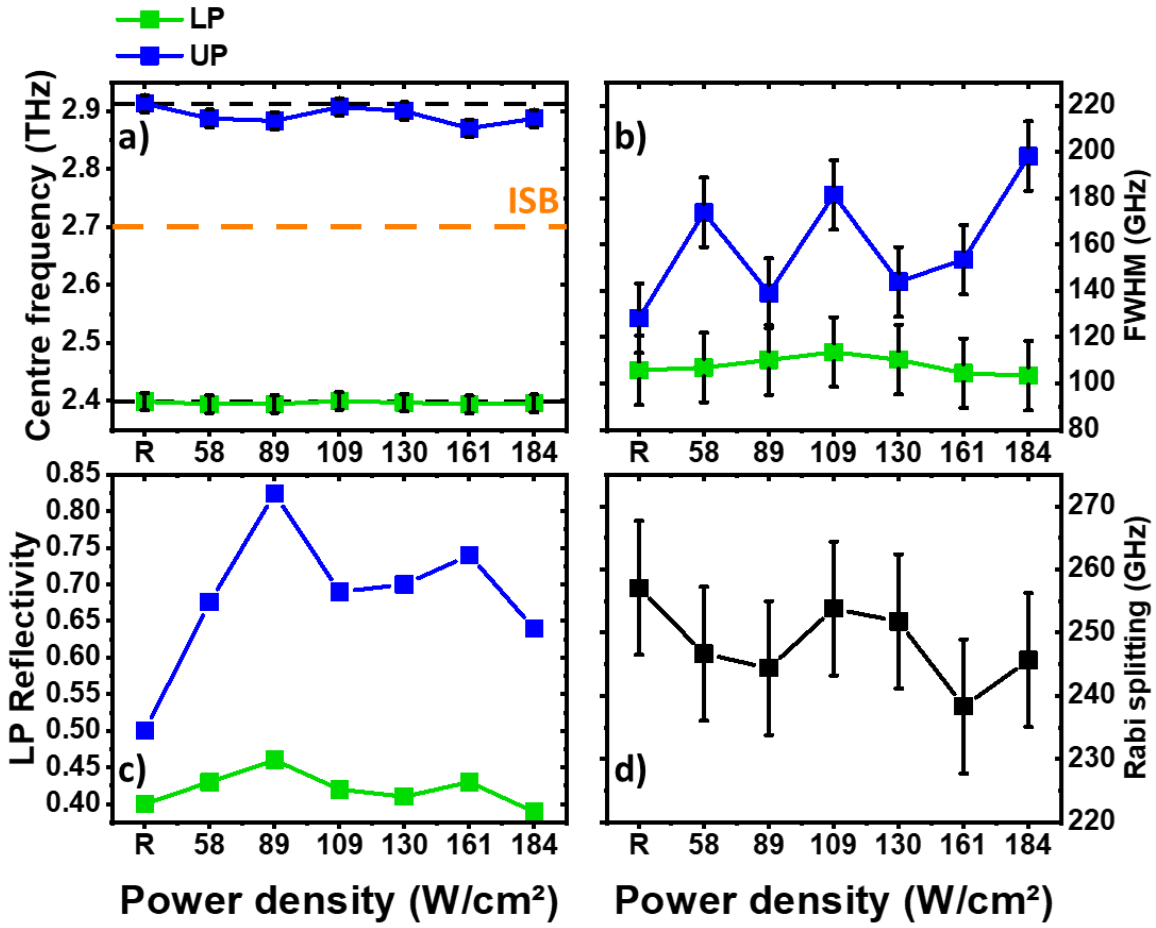

Figure V-45 : Voigt fit of the UP and LP reflectivity yielding a) Centre frequency, b) FWHM, c) reflectivity, of LP and UP branches along with d) Rabi splitting for different pumping power densities of the sample 3 at 20K pumped at the predicted angle allowing the triple resonant scheme (20°). The R on the x-axis stands for the bare reflectivity of the sample 3 without the QCL pump, the initial frequency position of the LP and UP branches are highlighted by black dashed line. a) The UP branch slightly shifts ($\sim 40 GHz$) towards red, whereas the LP seems stable. b) The FWHM shows an increase of 143% for the UP and nearly no changes in the LP. c) the reflectivity of the LP and UP shows the same trend than Figure V-39 and Figure V-42. d) The Rabi splitting seems to slightly ($\sim 5\%$) decrease.

Temperature and angle variations indeed showed resonant behaviour in the observed changes in reflectivity. This agrees with expected signature of a resonant effect and potentially uncoherent (below the threshold) polariton-polariton scattering. To exclude other mechanisms, we take another approach by investigating another sample where the polariton-polariton scattering can be assisted by a Brillouin folded mode from the cavity.

V.7.4 Folded mode assisted-polariton-polariton scattering

Following the concepts of Brillouin folded mode observed by C2N [241], we designed sample 5 where such a mode is available between the LP and UP branches. This is due to the periodic top grating that induces Bragg scattering and thus give rise to a folded mode. This mode is mostly matter as it is located near the ISB transition, and thus faint on the dispersion. Nevertheless, this can be used to assist polariton-polariton scattering mechanism as shown in Figure V-46. Note however that the proposed mechanism might not be unique and thus we are not excluding scatterings between different branches (see below). In this sample our QCL pump is out of resonance with the UP branch but in resonance with the folded mode which can be used to match the energy-momentum conservation requirement of polariton-polariton scattering by pumping in between the UP and the folded mode. By design, the matching of such energy-momentum conservation is respected for QCL pump incident of 20°. To this purpose we pumped this sample with QCL2 at 20° and at 17.5° for a fixed temperature of 20K.

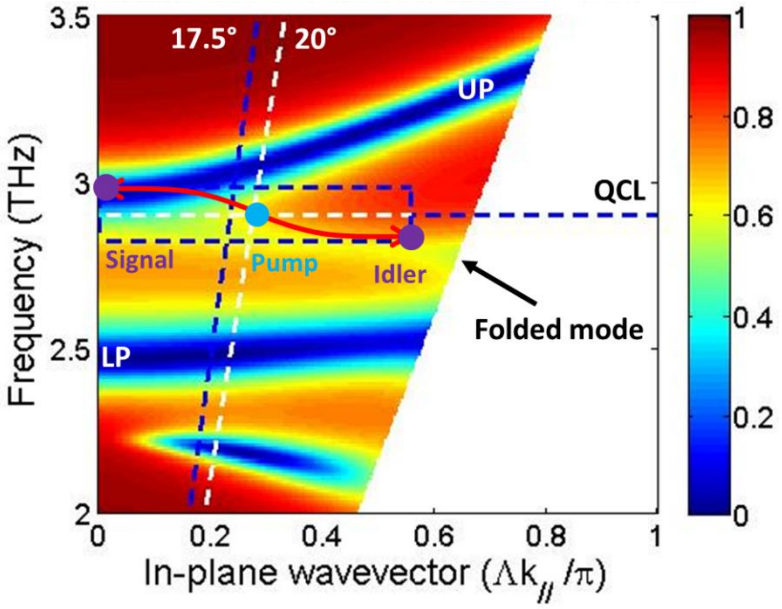

Figure V-46 : RCWA dispersion of sample 5. Notice the Bragg folded mode in between the UP and the LP branches. The idea is to pump between the UP and the folded mode to investigate the presence of a reflectivity change in the UP at $k_{\parallel} = 0$.

Results are shown in Figure V-47 where panel a) and b) are, respectively, the reflectivity and the 2D colormap of the same data zoomed around the UP and LP branches. For both pumping angles, we can see frequency shifts, and changes in reflectivity. Also, on both angles investigated, an interesting feature that changes in reflectivity with the pump

power is present around $2.7THz$ that may coincide with the edge of the folded mode presented in Figure V-46, this suggest the scattering process described in Figure V-48 where the signal is on the edge of the folded mode.

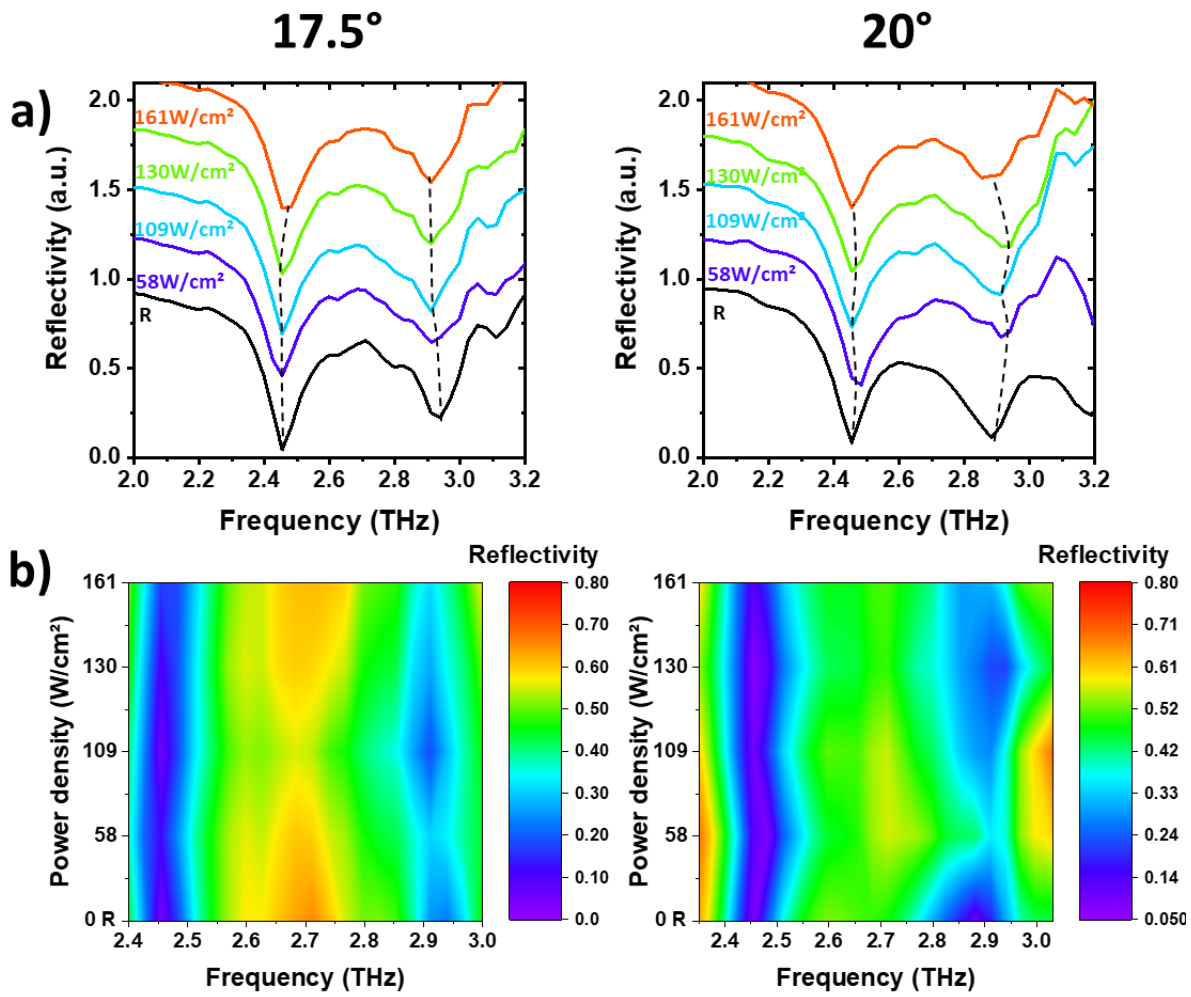

Figure V-47 :a) Stacked reflectivity of the polaritonic for an increase of the power density for sample 5 at 20K pumped by QCL 2 at 17.5 *and* 20°. *We notice frequency shifts and reflectivity changes for both angles, the black dashed are guide to the eyes. b) closeup of the same data centred around LP and UP branches for both angles. We notice an interesting feature that nonlinearly change in reflectivity with the pump power around* $2.7THz$ *which coincide with the edge of the folded mode.*

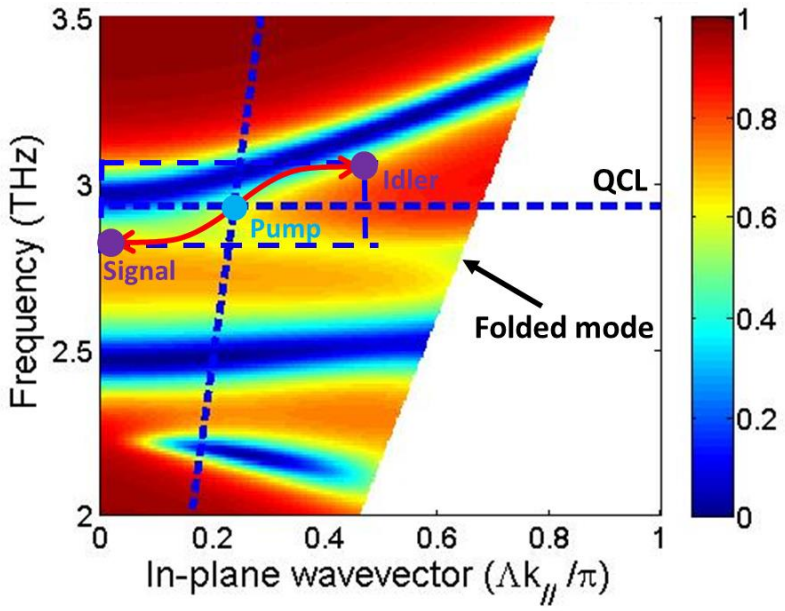

Figure V-48 : LP UP proposed scattering mechanism to explain the feature at 2,7THz

To quantify this behaviour, and look for signature of polariton-polariton scattering, we turn to the analysis of the centre frequency, the changes in reflectivity, the FWHM of the LP and UP branches along with the Rabi splitting as a function of the power density for a 17.5° incident pump. The reflectivity was fitted by a Voigt function. Results are displayed in Figure V-49, where the R in the x-axis denotes values for the bare reflectivity of the sample (no QCL pump), the black dashes highlight the bare reflectivity frequency in panel a), and errors bars corresponds to the TDS spectral resolution. Panel a) shows a clear red shift across the power density of the UP of $\sim 50 GHz$ while the LP slightly ($\sim 20 GHz$) shifts to the blue. The FWHM available in panel b) indicates an increase of the UP FWHM with a maximum of $\sim 215\%$ of its original value reached for $58 W/cm^2$, and a broadening trend on the LP. The reflectivity in panel c) shows increasing values for an increase of the pump power on the LP ($\sim 370\%$) and UP ($\sim 170\%$) branch with, interestingly the LP being the most affected. The Rabi splitting however, is decreasing across the full range of power density, with a variation of $\sim 36 GHz$.

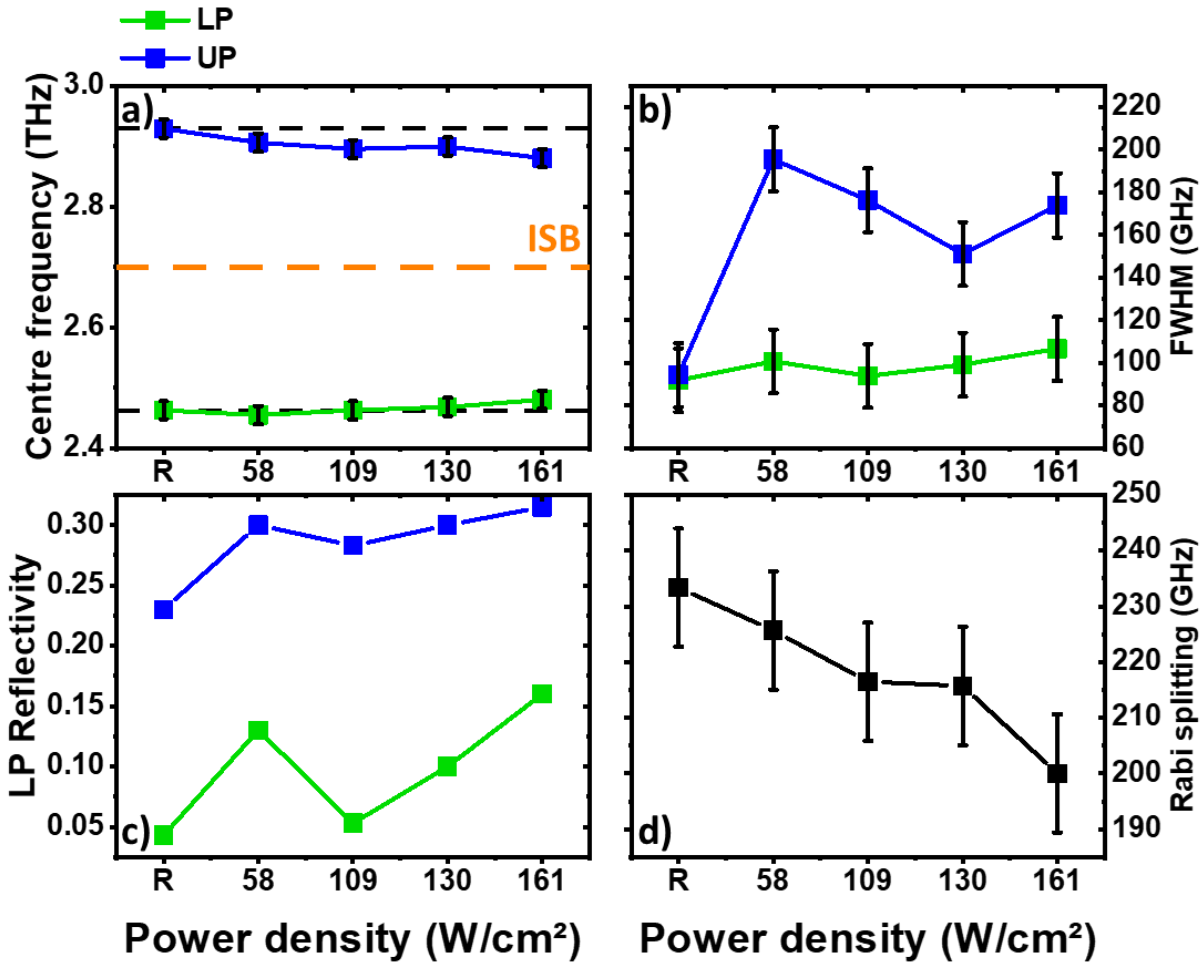

Figure V-49 : Voigt fit of the UP and LP reflectivity yielding a) Centre frequency, b) FWHM, c) reflectivity, of LP and UP branches along with d) Rabi splitting for different pumping power densities of the sample 5 at 20K pumped at the 17.5°. The R stands for the bare reflectivity of the sample 5 without the QCL pump, the initial frequency position of the LP and UP branches are highlighted by black dashed. a) The LP and UP branch shift respectively towards blue by (~20GHz) and red by (~50GHz) The Rabi splitting however, is decreasing across the full range of power density, with a variation of ~36GHz.

Figure V-50 displays the same analysis for a 20° pump. The LP and UP seems to slightly shifts towards the blue (~ 20 GHz) and red (~30 GHz), respectively, with an increase of the pump power. However, owing to the spectral resolution it is difficult to be conclusive. The FWHM of the UP in panel b) shows a small variation, and a slight broadening trend on the LP across the different power densities. The reflectivity displayed in panel c) indicates, however, a visible effect on the UP branch with a maximum of ~350% reached for 58W/cm^2, the LP is mostly stable until a power density of 161W/cm^2 yelding a reflectivity variation of 153% in respect to the original value. The Rabi splitting follows a general

decreasing trend reaching $\sim 20GHz$ but, due to the small LP and UP center frequency variations it is difficult to be conclusive.

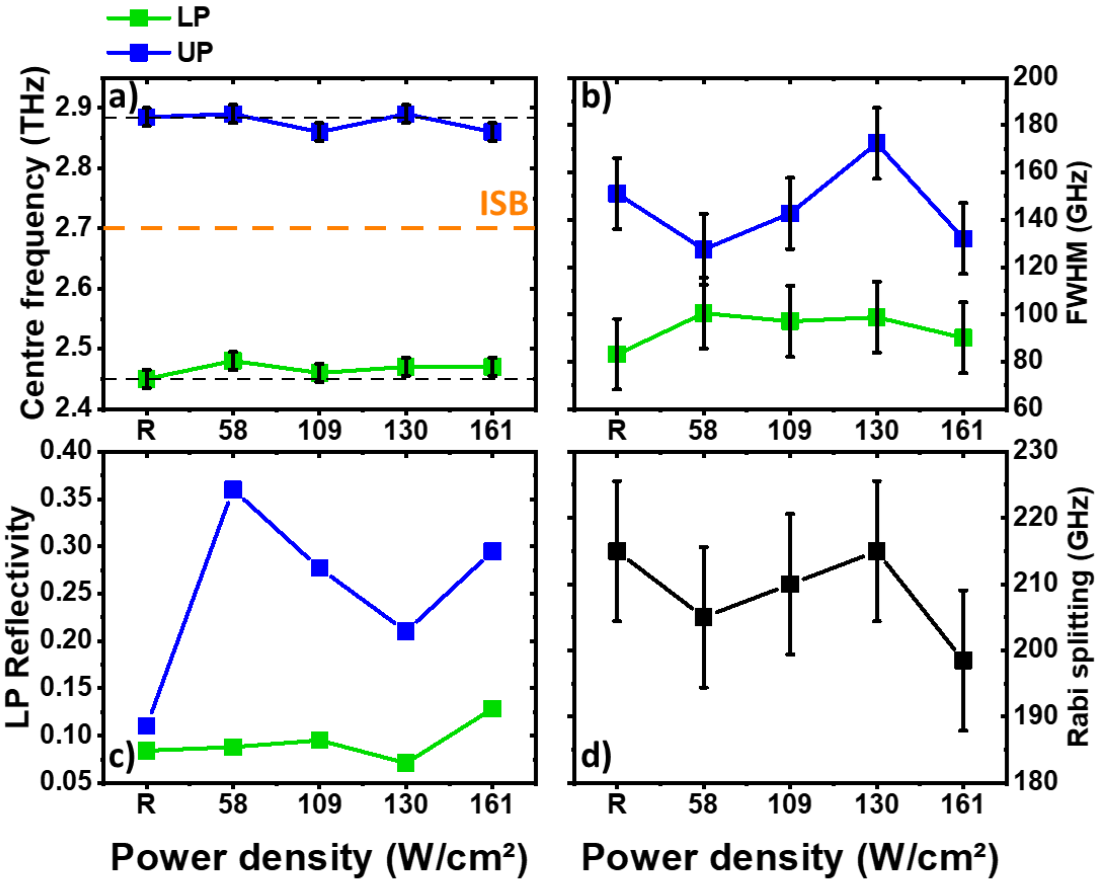

Figure V-50 : Voigt fit of the UP and LP reflectivity yielding a) Centre frequency, b) FWHM, c) reflectivity, of LP and UP branches along with d) Rabi splitting for different pumping power densities of the sample 5 at 20K pumped at the 20°. The R stands for the bare reflectivity of the sample 5 without the QCL pump, the initial frequency position of the LP and UP branches are highlighted by black dashed.

To summarise, larger effects regarding the UP FWHM broadening and the decrease of the Rabi splitting are observed for a pump with a 17.5° incidence. In addition, rather strong frequency shifts of the UP branches seem to agree with the developing theory from the INO-CNR (see below). However, this pumping angle yields also larger reflectivity changes for the LP branch. On the other hand, for a 20° pump, stronger reflectivity changes of the UP are recorded.

By investigating THz ISB polaritons under resonant pumping with an adapted TDS, we showed a non-trivial change of reflectivity with larger effects recorded for a folded mode pumping scheme in sample 5. Moreover, we highlighted the temperature and angle resonant

behaviour of this reflectivity change. Another interesting feature lies in the frequency shifts of LP and UP branches in sample 5 yielding the maximum change in reflectivity. From the Rabi splitting, it is clear that the polaritons are not bleached. However, a common trend recorded for high pump power densities is that the LP and UP branches are blue shifted and red shifted respectively, but with the LP being the less impacted. This suggest that, in addition of characterizing important reflectivity changes we also observe the premises of nonlinear frequency shifts. In fact, the strong pump modulates the carrier density (the electron plasma in the ISB transition) in the QWs inducing two effects: i) a change in the depolarization shift of the ISB transition and ii) a reduction of the Rabi splitting owing to a change in population difference between the fundamental and excited states. This appears to lead then to a virtually fixed LP branch and an UP branch red-shifting at a faster rate with the pump power density. This is illustrated schematically in Figure V-51 considering the LP and UP reflectivity response for a weak and strong pump (black and green traces respectively) in the case of depolarisation effects, a saturation of polaritons splitting (reduction of the Rabi splitting), and both effects together. Indeed, the many body electronic interaction changes for a strong pump, decreasing the electronic density (N_{2D}) of the 1st subband (ground state). This red-shifts the ISB transition by the depolarisation effect (see equations (V-14) and (V-15)), thus red-shifting the LP and UP by the same amount (In this picture, the Rabi splitting is constant). The second effect from the reduction in (N_{2D}) for a strong pump (saturation of polariton splitting) resulting in a decrease of the Rabi splitting, blue- and red-shifting the LP and UP respectively (see equation (V-7)). Both effects combined lead to opposite shifting contributions for the LP, resulting in a small blue shift, whereas the UP largely shifts to the red owing to the constructive contributions of both effects. The demonstration of this mechanism is in fact an important milestone in ISB polaritons as the nonlinearities inherent to strong optical pumping have, to our knowledge, never been addressed before. This is strongly supported by our pumping experiments (see Figure V-49) and could be extended to a full theory of optically pumped ISB polariton-polariton scattering. However, to achieve this, one must decouple and quantify both effect contributions. Nonetheless, these results seem to point towards uncoherent polariton-polariton scattering or, in the less optimistic case, towards scattering effects from optically dark states. A clear distinction between the two process would require a detection of the idler.

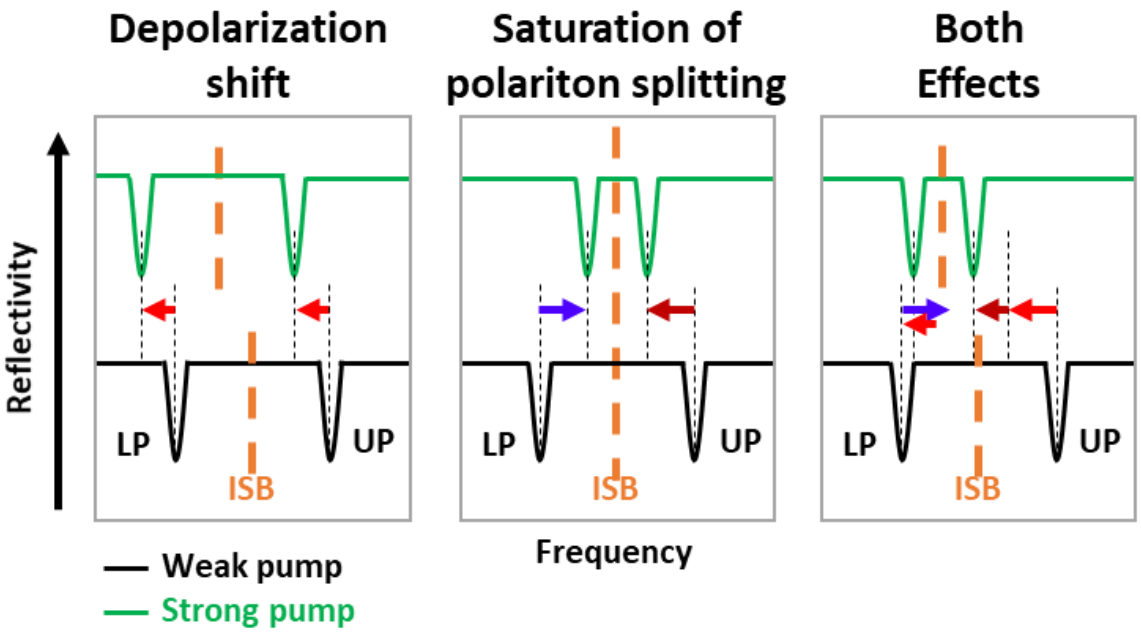

Figure V-51: Impact of the depolarization shift, Saturation of polariton splitting and both effects combined on the LP and UP branch frequency.

To further characterise the changes observed in TDS pumping, our approach is to investigate the reflected pump as a function of the incoming pump power. Indeed, in the case of stimulated polariton-polariton scattering, the phase transition of a low density polariton towards a condensate is coupled with nonlinearities in the ration between the incident and reflected light [209].

V.7.5 Nonlinear Pump reflectivity

Here, we investigate the nonlinear reflectivity of sample 5 by pumping with the QCL at the resonant angle and collecting the reflected light - there is no probe pulse. The ratio between the incident and the reflected light should then highlight nonlinearities in the presence of polariton-polariton scattering, with a linear behaviour expected otherwise. The principle of the experiment is available in Figure V-52 where the sample is pumped at 20° by the focused beam of QCL 2. The reflected beam is then recorded by a pyroelectric detector. Special attention was devoted ensuring that the focused QCL pump waist was identical to that used in the TDS experimental conditions above. Here we present early data where the calibration of the pump power density is performed with our THz camera, while the reflectivities were extracted by calculating the ratio between the reflected beams obtained at 20K and 50K, corresponding to the folded mode in near resonance with the QCL in the former case (reproducing the QCL pump - TDS probe experiment) and mostly out of resonance in the latter temperature.

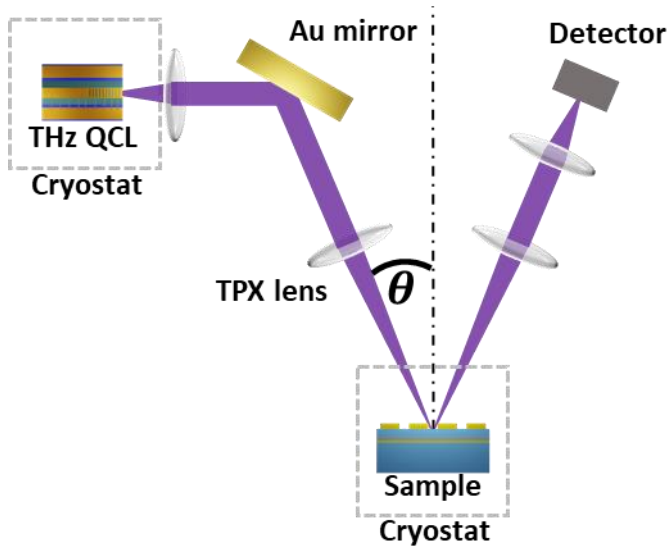

Figure V-52 : Principle of the non-linear reflectivity experiment. The QCL beam pump the polariton sample at the 20° while a pyroelectric detector records the reflected light. The power density was calibrated to be the same as our previous TDS pumping experiments. The reflectivity is then calculated with the ratio of the reflected beams between 20K and 50K which respectively corresponds to the cases of the UP branch close and far to the QCL pump.

The results are displayed in Figure V-53 where the panel a) is the recorded light by the pyroelectric detector for the polariton sample cooled at 20K and 50K. The panel b) is the ratio

between these two traces. At 50K as the folded mode is mostly out of resonance with the QCL pump, the higher reflected power means that mostly no light is coupled to the system. The reflectivity ratio in panel c), however, shows a non-linear behaviour, and we note a drastic change from $100 W/cm^2$ while increasing the QCL pump fluence leading to a saturation of the ratio. This saturation can possibly be related to depolarization effect coupled with a saturation of polariton splitting resulting in a UP shifting towards red (as explained in Figure V-51) and thus less resonant with the QCL pump.

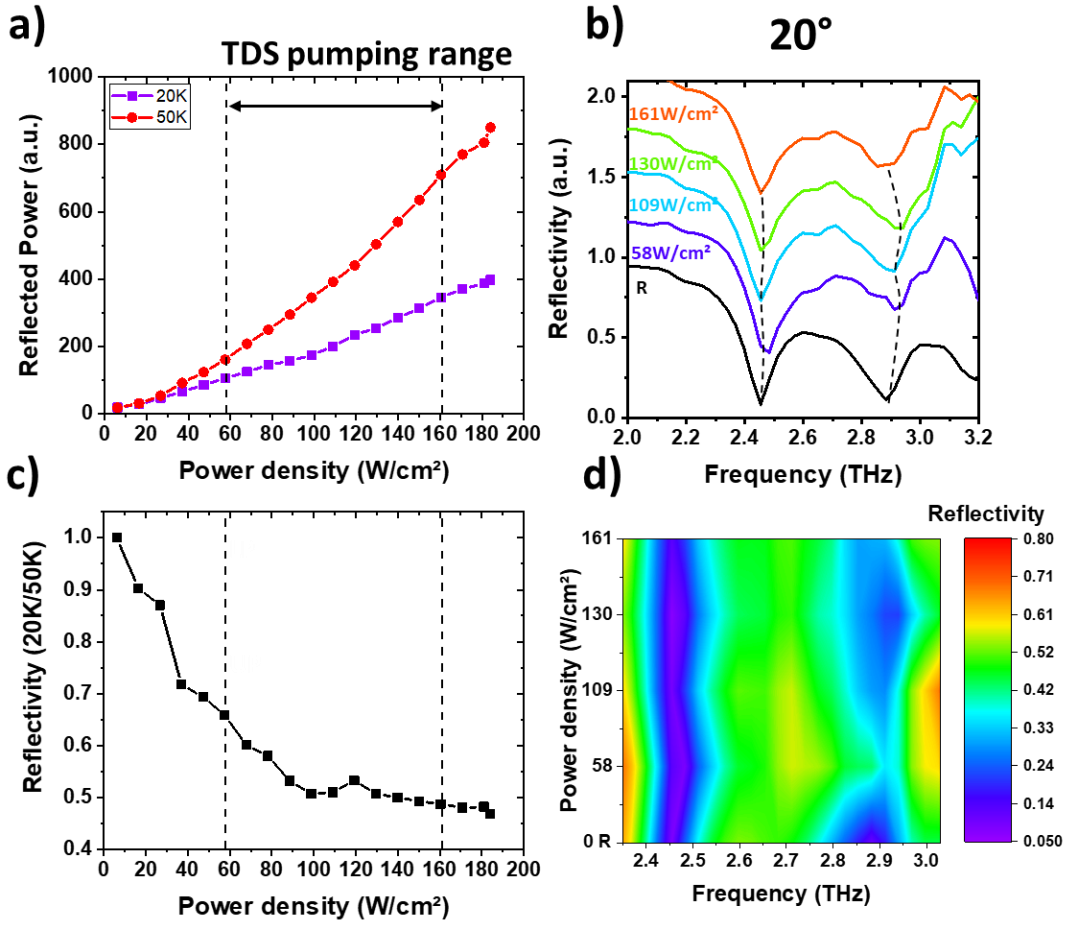

Figure V-53 : a) Reflected QCL beam for polariton sample temperature of 20K and 50K. We highlighted the TDS pumping range where we showed the reflectivity of the system under pumping (panels b and d)). c) Ratio of reflected beams, this non-linear reflectivity shows a saturation behavior around $100 W/cm^2$.

The nonlinear frequency shifts with power density recorded by TDS (panel d)) and the saturation behaviour highlighted in Figure V-53 c) are thus coupled. To link these parameters and support our frequency shifts hypothesis (Figure V-51). Theoretical calculations done by the INO-CNR BEC centre, based on coupled mode theory, were able to reproduce this result by adding a nonlinear term to the Rabi splitting. These coupled equations (V-21) accounts

for the response of the cavity field amplitude a and the ISB coherence field b for an incident electric field E_{pump} with $\omega_c$the cavity frequency, $\gamma_{rad}$and γ_{nr} describing radiative and non-radiative losses. $|a|^2$ and $|b|^2$ respectively represents the electromagnetic energy in the cavity and the energy of the ISB dipole. The term $\Omega(|b|^2)b$ of the first equation is the light-matter coupling whereas the $\Omega(|b|^2)a$ of the second is the matter-light coupling. The nonlinear term that links this interaction is g.

$$\frac{\delta a}{\delta t} = \omega_c a - i\frac{\gamma_{rad} + \gamma_{nr}}{2}a + E_{pump}(t) + \Omega(|b|^2)b$$

$$\frac{\delta b}{\delta t} = \omega_{ISB} b - i\frac{\gamma_{ISB}}{2}b + \Omega(|b|^2)a + g(|b|^2)b \qquad (V\text{-}21)$$

Currently the physics behind this nonlinear term is still under investigation. By solving this system with realistic parameters, INO-CNR were able to calculate the nonlinear transmission of our polaritonic system and the reflectivity ratio of Figure V-53 for an increasing pump power (fixed in frequency). Results of these calculations are displayed in Figure V-54. On panel a) the nonlinear transmission shows the same trend of the LP and UP frequency shift that was characterized with our QCL-pump TDS probe system. The ratio of reflectivity of panel b) is also very similar to our nonlinear reflectivity experiment (see Figure V-53) and shows this saturation effect for a pump power around ~0.1 in this units, thus supporting the shifts induced by a strong QCL pump, up to an UP branch out of resonance with our pump.

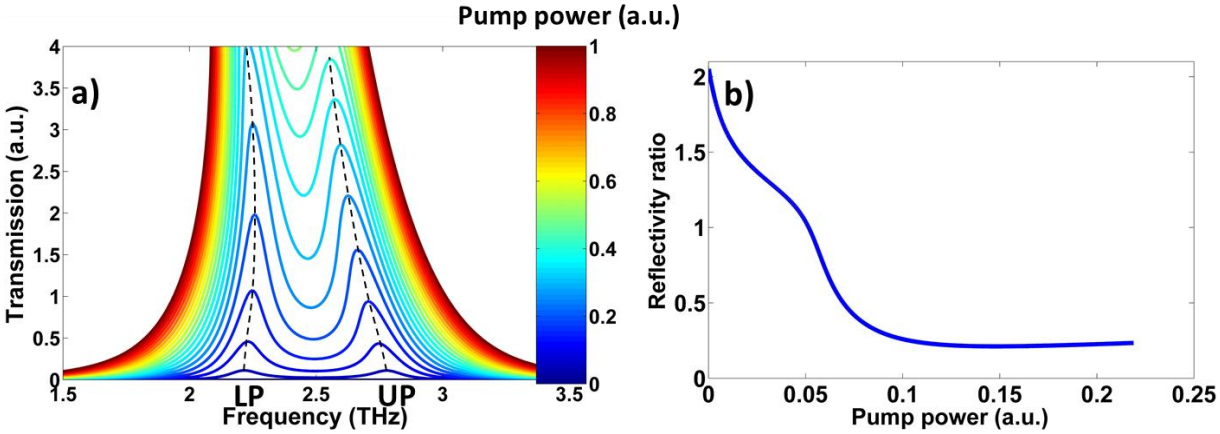

Figure V-54 : Calculations from the University of Trento, a) nonlinear transmission of our polaritonic system as a function of pump power. The LP and UP branches experience a frequency shifts similar to what we characterized with our pump TDS scheme b) nonlinear reflectivity ratio as a function of the pump power, this shows a similar evolution than our measurements reported in Figure V-53.

Further experiment will be conducted to find out the exact nature of the nonlinear g term. We have designed with our collaborators from C2N similar polaritonic devices with 5 times less doping and reduced number of wells. We expect then a strong reduction of the plasma frequency and the depolarization shift, which could show a significant deviation from the present results. Secondly, considering our results, experimental optimisations will include a new higher power monomode QCL with a frequency ideally between the ISB transition and the UP branch to induce red shifts (to the UP) by optical pumping to the point where the QCL is resonant with the shifted UP. This could fully confirm the presence of ISB polariton-polariton scattering.

V.8 Conclusions

In this chapter, we have investigated ISB polaritons to highlight potential polariton-polariton scattering as a steppingstone for the demonstration of THz gain. This would be of prime importance in the realisation of a THz ISB polariton laser [166]. To approach this, we built a TDS setup, coupled with a high-power quasi-CW pump, monomode THz QCL, capable of broadband probing the polaritonic branches under resonant pumping. To this purpose, several samples were designed with different polaritonic dispersions. For the 1st sample generation, we showed a reflectivity increase in the UP branch probed at normal incidence while resonantly pumping the UP branch at the magic angle. Due to the poor reflectivity contrast at normal incidence a second generation of samples were designed with a stronger light-matter interaction at normal incidence, yielding an enhanced reflectivity. These samples represented a better platform to investigate the polariton behaviours under resonant pumping. We showed resonant pumping on this sample generation for i) a variation of the polariton sample temperature and ii) a variation of the incidence angle of the pump QCL, that tuned the UP energy and momentum, respectively These clearly highlighted a resonant behaviour in the reflectivity changes. Another important polariton geometry was investigated where the QCL pump is nearly resonant with a *folded mode* to match the energy-momentum conservation required for polariton-polariton scattering. This revealed much larger changes in reflectivity. Importantly, the analysis of the LP and UP frequency for an increasing pump power reveals opposite frequency shifts that may be attributed to a reduced depolarisation shift, as well as decrease in the Rabi frequency owing to a population difference change. This suggests that our structure might already enable uncoherent polariton-polariton scattering. To further characterize these changes, the final part of our work investigated the nonlinear reflectivity where the sample is excited at the resonant angle and the reflected light is collected by a power meter. This showed a nonlinear behaviour similar to simulations carried by the INO-CNR BEC centre. This work is still in progress, and further experiments are required to fully conclude on the presence of polariton-polariton scattering.

Perspectives

However, the ultimate proof of polariton-polariton scattering, polaritonic gain and coherent emission would be signatures of the idler, which will only exists if this scattering process is dominant. An observation of both idler and signal would require a more complex experimental geometry for the THz range, as the idler is emitted at another (larger) angle than the signal. The most obvious approach would be the extension of our work to look for gain signatures at the idler using TDS but would need to overcome a few technical challenges such as collecting the probe pulses at large angles. An alternative approach would be used to investigate the angle resolved emission with only the QCL pump with a sensitive but compact detector (such as a Golay cell). This would be facilitated with a tuneable THz QCL pump to ensure that we are entirely resonant with the UP branch, and would facilitate other pumping schemes. The current scheme of a single frequency limits the pumping schemes that can be investigated.

As well as idler detection, another approach interesting perspective would be to reduce the expected laser pump threshold. This could be achieved through less QWs and less doping permitting to reach polariton condensation with less pump powers. This would be allow stronger and clearer spectral signatures in reflectivity measurements to assess the polariton scattering mechanisms under intense THz pumping, potentially showing the first demonstration of THz gain with ISB polaritons.

Chapter

VI

VI General conclusion

My thesis research has focused on different aspect of modern condensed matter physics that can used to realise novel THz sources and investigate their fundamental properties. This could in the long term, lead to further in-depth understanding of THz carrier dynamics and more efficient technology for THz industrial take up and applications. In summary, after a short introduction in chapter I on the THz domain:

Chapter II was focused on the optimization of photoconductive switches (PCS) to generate powerful THz pulses, which would be used later in chapter V. To this end, I studied a cavity-based GaAs interdigited PCS. The singularity of this device comes with the addition of a buried Au plane at a subwavelength depth beneath the active surface. Through FDTD modelling, I showed an increase of THz field by a factor 3 in respect to the same structure without the buried Au layer. Moreover, by changing the subwavelength depth of this layer, I showed that the centre frequency of the device can be engineered. The field enhancement and spectral engineering was experimentally confirmed using THz TDS. Very careful THz absolute power measurements were performed with the cavity-based device showing a factor of 7.5 increase when compared to the standard device. Further optimisation in the applied bias yielded an absolute power of 240μW. These demonstrated high powers resulted in the first demonstration of real time imaging using a PCS where a THz camera (i2S) was used to image text through an optically opaque object. The interesting part of this work is that this scheme is easily scalable to reach higher powers and fields. This would include: larger area devices, thicker cavities, and the possibility of engineering the optical beam using a microlens array to excite only the exposed GaAs (75% optical power is reflected of the electrodes). This could lead to high THz fields that can be electrically modulated at high frequencies, in contrast to using nonlinear crystals. Also, the concepts could be easily transferred to InGaAs devices, and

thus compatible with THz generation from rapidly evolving telecom (1.55µm) femtosecond lasers.

In chapter III, I introduced ultrafast spintronics phenomena leading to THz pulse generation from ferromagnetic/heavy metal (FM/HM) heterostructures. This emerging technology is flexible, requires only a few nanometres thick material that can be deposited on almost any surface, cost effective and phonon-less. The generated THz fields are currently smaller than technologically mature PCS but can rival those from nonlinear crystals. The process is based on an ultrafast excitation that generates a spin current in the FM. These carriers migrate to the HM where spin-to-charge conversion (SCC) occurs through the Inverse Spin-Hall Effect (ISHE), resulting in a transient charge that radiates a THz pulse. In detail, different interfaces were investigated here to assess the impact of the fundamental material parameters on the THz emitted field, with the role of the transmission of the HM (Pt or Au-based) being critical. FMR-SP measurements coupled with THz TDS, and modelling done by CNRS-Thales and the University of Nebraska, showed that the product of the spin Hall angle $\boldsymbol{\theta_{SHE}}$, the conductivity $\boldsymbol{\sigma_{xx}}$, the spin diffusion length $\boldsymbol{l_{sf}}$, and the electronic interfacial transmission $\boldsymbol{T^*}$ ($\boldsymbol{\theta_{SHE}\,\sigma_{xx}\,l_{sf}\,T^*}$) constitutes the correct figure of merit for SCC conversion in the time-domain. This product will be of further importance is optimising future THz spintronic emitters.

In a second study, I investigated a Co/X/Pt trilayer structure, where X (either Ti, Au, or AuW) degrades the optimized interfacial electronic transmission of Co/Pt. This permitted the relationship between the spin conductance extracted by emission TDS to be linked to the more traditional spin mixing conductance obtained by FMR-SP through the spin-memory loss (SML). With comparison with the experimental data, a model including interfacial Rashba scattering, built by our collaborator CNRS-Thales, showed that the SML of the Co/Pt structure was evaluated $\xi = 0.4$. This work also showed the advantage of using the fast and non-destructive character of emission TDS to characterise spintronic devices.

Finally, I introduced the concept of a spin-sink where the spin reflexions at the vacuum/HM interface can be supressed by the addition of a layer with a small diffusion length and a SHA of the same sign as the HM. This permits to reduce the thickness of the structure to limit the THz absorption. This was experimentally demonstrated for a Co/Pt/AuW structure,

enhancing the emission of our Co/Pt reference by a factor 1.77. However, this concept can be pushed further by designing trilayers relying in opposites SHA, where even higher THz fields could be obtained.

Chapter IV presents recent and ongoing research based on quantum materials in THz spintronics, potentially dethroning FM/HM heterostructures. In particular the Inverse Edelstein Effect (IEE) was introduced as another SCC mechanism that relies entirely on interfacial effects, along with its implication in Rashba materials and Topological Insulators (TIs) that are promising THz spintronic materials.

1) **Heusler compounds**. Among the many properties of Co based full Heuslers alloys, they are half-metallic ferromagnets [128], and thus a large spin polarisation arises directly from their band structure. This makes them particularly interesting for SCC. Here we investigated the Heusler Co_2MnGa to design efficient spintronic heterostructures. Experimental characterizations revealed that Co_2MnGa/Pt interface provides a THz enhancement up to a factor 1.33 in respect to our Co/Pt reference. This was observed for thin layers of the Heusler and we proposed a mechanism that accounts for better spin injection into the Pt layer for these thin layers. Further work here will concentrate of the self SCC from the Heusler itself using a spin sink concept. Further, realistic optimisations are possible of this scheme by the design of trilayers [35] with opposing SHA signs to fully untap the larger spin polarization and SHA of Co_2MnGa.
2) **Rashba materials** have a momentum splitting of their spin bands and are of particular interest when coupled to a ferromagnetic for large SCC efficiencies via the Inverse Edelstein Effect (IEE), a 2D interface effect. Indeed, interfaces with 2DEGs composed of the NiFe/LAO/STO and NiFe/AlO/STO Rashba platform have shown record SCC efficiencies in FMR-SP measurements, considerably larger than FM/HM systems. Here I indeed measured an ultrafast THz IEE based SCC for both systems. However, in contrast to FMR-SP, it was considerably smaller than our Co/Pt reference by a factor 10 and 100 in respect to LAO/STO and AlO/STO, respectively. This could be explained considering the barrier thickness study, that indicated a preferential hot spin-polarized carrier transport above the AlO and LAO barrier, with a higher barrier for

AlO. This is in contrast to FMR-SP that uses microwave excitations and where the electrons can tunnel through the barrier. Further cryogenic measurements on LAO/STO showed higher THz signal, and a tuneable soft phonon mode. Finally, I showed the effect of a gate as in FMR-SP experiments that have shown record SCC efficiencies. The THz electric field showed only a slight enhancement with the gate. However, the observation of the soft phonon mode indicated an effective temperature of 130K, which is not ideal for efficient the SCC. Further optimisation in the heat sink could avoid this and reach lower temperatures for enhanced THz generation. However, it should be re-mentioned that for THz generation, the excitation energy is much higher than FMR-SP, resulting in a spin orbit interaction and limiting the effect of the gate.

3) **Topological Insulators**. These are particularly interesting for highly efficient SCC through the IEE as they possess a single Fermi surface that results is no competition between spin accumulations. Here I investigated the BST family and the effect of the number of material layers. Indeed a resonance effect was found with 5 SL of BST for the THz efficiency and where the surface states should be the dominant channel. This was corroborated by ARPES measurements, that showed clear surfaces states that would permit IEE-based SCC. However bulk states are also observed owing to the difficulty of finely controlling the Sn/Bi ratio in the TI. To assess the precise contribution of surface states, bulk states and the InAs substrate, further investigations are required. The contributions could be decoupled through the using circular polarization for the excitation beam and analyzing the generated THz polarization. Other samples with constant Sn/Bi ratio would also permit a better clarification between surface and bulk states.

The THz emission of these quantum materials were investigated as a proof of concept for ultrafast SCC and further work is required to model and to fully understand the dynamics of the systems for THz pulse generation. Nonetheless this work highlights that we have only just ‘scratched the surface’ of this area with a large parameter space that can be investigated for efficient SCC. This work (Chapter III and IV) on THz spintronics showed the usefulness of THz TDS to probe and understand the physical processes of SCC at interfaces. This could be further combined with photonic concepts such as resonators, cavities for both optical and THz beams to enhance the THz efficiency. Further, as well as an interesting THz technology and in stark contrast to FMR-SP, THz emission TDS provides a relatively simple and fast **non-**

destructive technique to investigate new spintronic devices that could help in the optimization of future systems.

Chapter V is devoted to the study of resonantly pumped intersubband polaritons (ISB) for signatures of ISB polariton-polariton scattering and nonlinearities that can potentially lead to THz gain. Here, the polaritons that are investigated were based on the strong coupling of a THz intersubband transition with a THz metal-insulator-metal cavity. I introduced the notions of polaritons, BEC coherent emission and scattering channels, along with optical properties of the studied samples. A TDS setup was realized for resonant narrowband THz pumping and broadband THz probing of a polaritonic structure, and where the resonant pump angle could be tuned. Indeed, for efficient polariton-polariton scattering, a polariton branch requires to be pumped at a specific pump angle. This permits a triple resonance on the polaritonic dispersion between the pump, and the generation of the signal and the idler, whilst ensuring momentum and energy conservation. This was probed using a broadband THz pulse to monitor the reflectivity of the pumped polariton branch at normal incidence. The narrowband pump was a high power, monomode, quasi-CW THz QCL operating at 2.94 THz, especially developed for this project to pump the upper polariton (UP) branch. High powers of ~ 200 W/cm^2 were realized, estimated to be adapted to observe polariton nonlinearities and gain.

Two generation of samples were designed and investigated with differing light-matter interaction. The 1st generation showed a reduce light-matter coupling at normal incidence and resonant pumping on these showed a slight increase in the UP reflectivity under pumping. To enhance any changes in reflectivity, a second set of samples were realized for a stronger light matter coupling at normal incidence, which indeed showed a larger reflectivity change under resonant pumping. Further, a temperature dependence and an angular dependence of the pump beam on this 2nd sample generation were performed, with both revealing a clear resonant character of the reflectivity changes.

To further investigate the presence of scattering mechanisms and potential nonlinearities, another sample was designed and realized with a strong light-matter coupling combined with a Brillouin folded mode. This sample showed the strongest reflectivity changes under resonant pumping, along with important changes in the centre frequency of the UP branch, with the LP being less impacted. This pointed towards nonlinear frequency shifts

that are potentially a precursor to polariton-polariton scattering. Indeed, with support from INO-CNR, this behavior was ascribed to two effects: i) a pump inducing depolarization effect via a change of ISB plasma frequency, shifting the ISB transition towards lower frequencies, and thus expected to red-shift both the UP and LP branches and ii) a decrease of the Rabi splitting induced by the pump, blue-shifting the LP and red-shifting the UP. Combining these two effects results in UP branch strongly red-shifting with the LP virtually fixed. Furthermore, we observed evidence of an increase of the reflectivity at the folded mode frequency. To further confirm these changes observed using the THz TDS probe, I investigated the nonlinear reflectivity of the pump beam. This was done by pumping at the resonant angle and analyzing the reflected light of the pump with a pyroelectric detector. The reflectivity ratio between the sample at 20K (resonant) and at 50K (non-resonant with UP) showed a strong nonlinearity, and most importantly a saturation behavior. This indicates that the UP branch moves out of resonance of the QCL frequency owing to the induced frequency shifts. This result was reproduced by calculations from the CNR-INO using a coupled mode theory with a nonlinear g term linking the light-matter interactions to the pump. Currently the exact physics behind this g term is under active research but it would appear that depolarization effects represent a solid lead.

Together, this work has shown potential signatures of the nonlinearities and polariton-polariton scattering in ISB polaritons. Further work will provide a definite answer to this through a new generation of samples with less doping and less QWs to reduce depolarization effects and power requirements of polariton-polariton scattering threshold. This could lead then to different nonlinear behavior and potentially THz gain. The design of new higher power monomodes QCLs centered between the ISB transition and the UP could further facilitate this demonstration. Nonetheless, the ultimate proof of coherent polariton-polariton scattering lies in the characterization of the idler specific to this process. Albeit experimentally challenging, I plan to design a new experiment capable of proving the existence of this idler through angle resolved measurements. This would provide conclusive proof of THz gain from ISB polaritons and open perspectives towards the new generation of coherent THz emitters with exotic properties.

Appendix

Chapter II- Electromagnetic simulations PCS 2µm vs 2µm

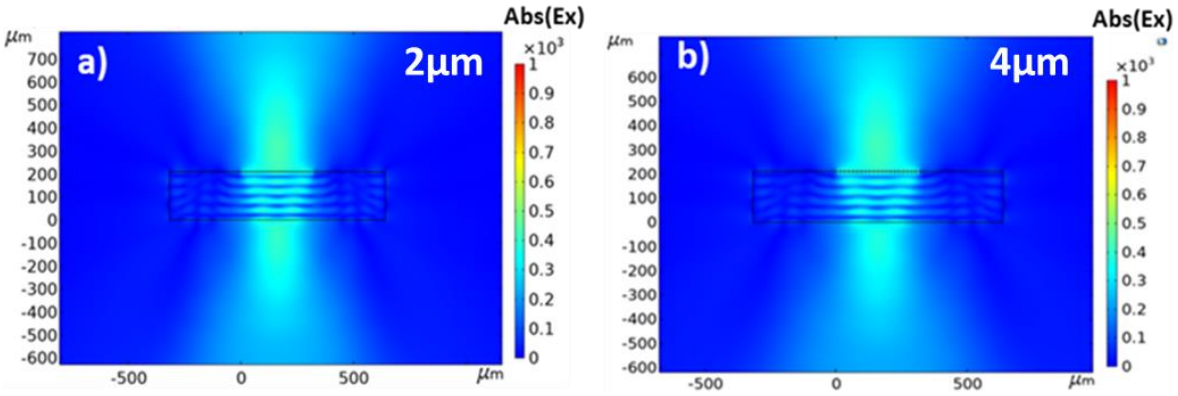

Figure A 1: 2D plot of electromagnetic distribution over a) the standard structure for the 2µm interdigit spacing b) and 4µm. In both cases, no differences in THz fields are characterized.

We note no significative difference in electric fields between a 2µm or 4µm spacing interdigitated structure.

Chapter III- Co/Pt spin resolved interfacial electronic transmission

The $k_{\parallel}$-resolved transmission function for the Co/Pt (111) interface is shown in Figure A 2 for each spin channel, at 0, 0.5, and 1.0 eV above the Fermi level. The origin of the features observed in these plots can be correlated with the density of states of bulk Co and Pt in Figure A 3, as discussed below. Note that values of the average transmissions above 1 can be observed as the average transmission is a sum of spin channels along s and d bands giving a maximum of 12 channels.

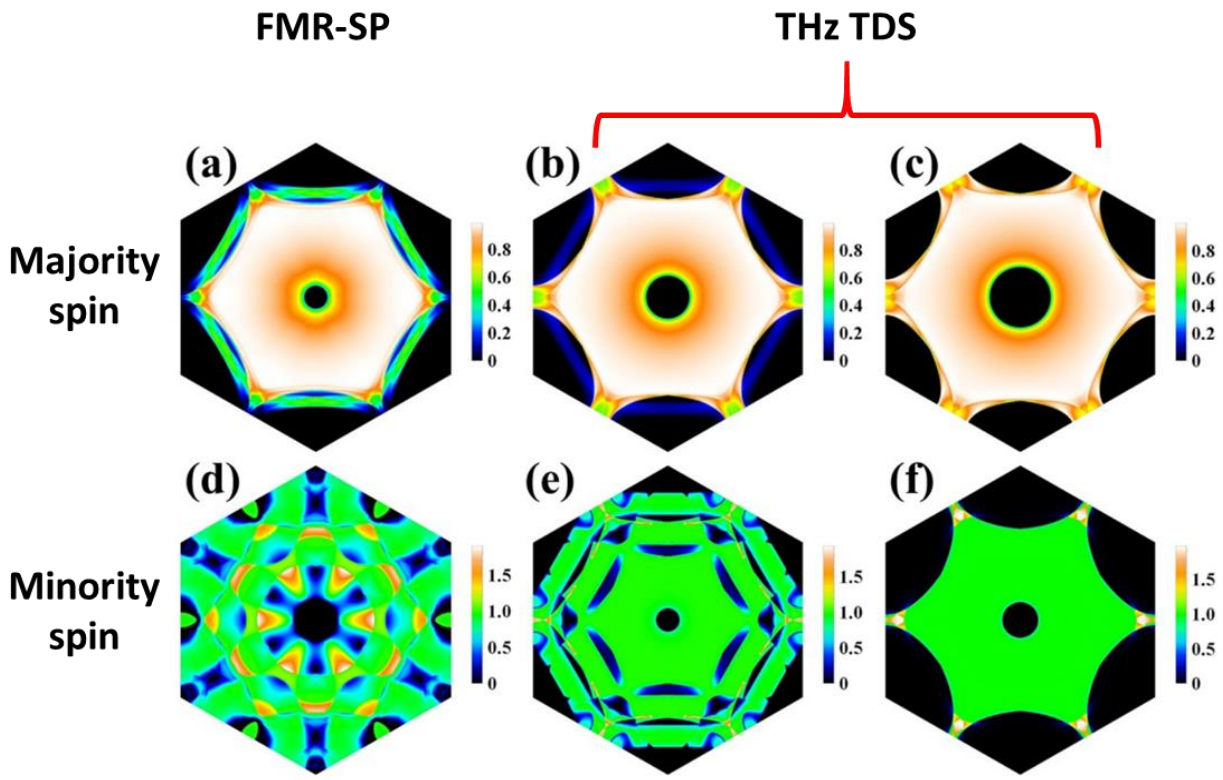

Figure A 2: Calculated energy-dependent and selected-spin transmission function for the Co/Pt (111) interface plotted as a function of $k_{\parallel}$ (projection of the wave vector on the plane of the interface, which is conserved in the scattering process) and summed in the two-dimensional Brillouin zone of the interface. (a)–(c) Majority-spin channel. (d)–(f) Minority-spin channel. (a) and (d) E-EF= 0. (b) and (e) 0.5 eV. (c) and (f) 1.0 eV. Those calculations show that near the Fermi level [(a)–(d)], the majority electrons (spins ") are more easily transmitted (on average) than the minority-spin channel, in particular near the Brillouin zone center, whereas at higher energy, 0.5 eV above the Fermi level [(e) and (f)], the electronic transmission for the minority-spin channel is larger. Calculated by the University of Nebraska.

Cobalt has one majority-spin Fermi-surface sheet with topology identical to that of Cu: the somewhat distorted free-electron-like Fermi surface does not quite fit into the first Brillouin zone forming “necks” cantered around the L points on its hexagonal faces. One of these L points projects onto the centre (Γ point) of the surface Brillouin zone of the (111) interface, resulting in a circular “hole” in the transmission function (panels (a-c) of Figure A 2) where there are no bulk states in Co. As the energy increases, the iso-energetic surface expands, and the holes become larger. Panels (a-c) of Figure A 2 show that most of the states from the majority-spin Fermi surface sheet in Co have a high probability of transmission across the interface in the entire energy window shown in Figure A 2 a). This feature is similar to the well-known case of the Co/Cu interface [244] where the band structure match in the majority-spin channel is nearly perfect. Because Pt has one electron fewer than Cu and

open 5d shells, its Fermi surface is more complicated, with one free-electron-like electronic sheet, one extended hole-like sheet that projects to the periphery of the (111) surface Brillouin zone, and one small holelike pocket around the X point. As the energy is increased, the hole-like sheets shrink and disappear at about 0.7 eV, where density of states has a van Hove singularity.

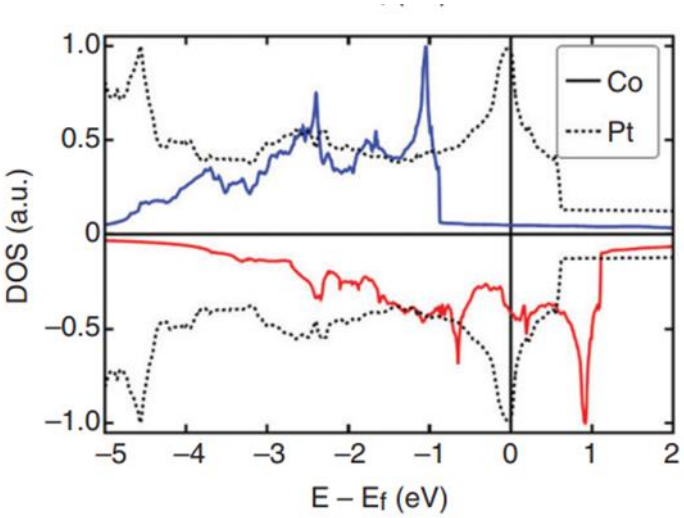

Figure A 3 : Density of states in bulk fcc Co and Pt with the lattice parameter used in the calculations for the interface. Blue (red) solid lines: majority-spin (minority-spin) electrons in fcc Co. Dotted lines: both spins in Pt. (c)

Chapter III -Theorical SML model

We define here the notations chosen able to describe the electronic wavefunction. Owing to the translation invariance in the x-y plane the propagating electronic eigenfunctions read as equation A(1).

$$\psi_{kz,k_\parallel}(r,z) = exp(ik_\parallel \rho)\, \phi_{k_z}(z) \qquad A(1)$$

where $\rho = (x, y)$ represent the in-plane coordinate and $\phi_{k_z}(z)$ are the two-component spinor scattering states along the z direction of the transport labelled by the wavevector kz of the incoming wave. In the complete set of the scattering states, one has to distinguish two orthogonal subsets of eigenfunctions: (i the states $\overleftarrow{\phi}$ incoming from the left (Co) that we will consider henceforth and (ii the incoming states $\vec{\phi}$ coming from the right (Pt) involved in the spin-orbit torque physics. One presently only considers the first class of electronic waves under optical excitation. Away from the interface defining the scattering region, the

wavefunction corresponding to the energy $\epsilon = (k^2 z + k_{\parallel}^2) = 2m^*$ have the form of equation A(2).

$$\vec{\phi}_{kz,k_{\parallel}}(r,z) = \begin{cases} \hat{\imath}_{k_{\parallel}} exp(i,k_z,z) + \hat{r}_{k_{\parallel}} exp(-i,k_z,z) & for\ z < 0\ (Co) \\ \hat{t}_{k_{\parallel}} exp\left(i,\grave{k_z},z\right) & for\ z > 0\ (Pt) \end{cases} \qquad A(2)$$

Where $\hat{r}_{k_{\parallel}}$ and $\hat{t}_{k_{\parallel}}$ are respectively the 2×2 matrix representing the reflection and transmission amplitudes corresponding to electrons of fixed energy ϵ crossing the interface from Co towards the Pt side and including the spin-orbit scattering region ($\hat{\imath}_{k_{\parallel}}$ is the incident 2×2 unity matrix). In that sense the $\hat{r}_{k_{\parallel}}$ and $\hat{t}_{k_{\parallel}}$ amplitudes may be decomposed onto the Pauli matrix basis ($\hat{\sigma}$) according to $\hat{r}_{k_{\parallel}} = r_0 \hat{I}_{2\times2} + r_{k_{\parallel}} \vec{\sigma}$ and $\hat{t}_{k_{\parallel}} = t_0 \hat{I}_{2\times2} + t_{k_{\parallel}} \vec{\sigma}$. Here the scalars r_0, t_0 and vectorial $r_{k_{\parallel}}$ and $t_{k_{\parallel}}$ find analytical expression considering i) Rashba split bands at interfaces from wavefunction matching procedures as well as ii) diffusive contributions in the bulk bands on either part of the interface. We then solve the quantum electronic transport problem sketched in Figure III-36 by matching the different electronic wavefunctions $\psi_{k_{\parallel}}(z)$ in the presence of $\hat{V}_S$. This is performed by imposing a quantum step $\frac{\hat{V}_s \Phi(0)}{\hbar^2}$ in the probability current while keeping continuous both the wavefunction and the current flux.

Moreover, we generalize the latter approach by considering spin-dependent bulk diffusion in the two bulk regions, responsible for sizeable spin-backflow. This is done by introducing a spin-dependent Boltzmann equation in the two bulk regions. We have calculated self-consistently the two spin distribution functions $\bar{n}_\sigma(z,k) = \bar{n}_\sigma^{(0)}(z,k) + \left(g_\sigma^{(1)}(z)\cos\theta_k + \Delta_{\mu\sigma}(z)\right)\delta(\epsilon - \epsilon_F)$. Here $\bar{n}_\sigma(z,k)$ is the equilibrium Fermi-Dirac, $g_\sigma^{(1)}(z)$ originates from the Fermi sphere displacement under spin current injection (the spin-dependent current writes $j_\sigma = e\mathcal{N}_F g_\sigma^{(1)}$ where $\mathcal{N}_F$ is the density of states at the Fermi level) and $\Delta_{\mu\sigma}(z)$ is the spin-accumulation term. The diffusive spin current and the spin-relaxation in the bulk regions write as equations A(3).

$$\delta j_s(z) = \frac{\sigma^*}{e}\frac{\partial \Delta\mu(z)}{\partial z}$$
$$\frac{\partial[\delta j_s(z)]}{\partial} = \frac{\sigma^*}{e\lambda_s^2}\Delta\mu(z) \qquad A(3)$$

Where δj_s denotes the spin current deviation with respect to the bulk value. We obtain the solution of these coupled equations by matching the coherent spin-current to the diffusive spin-current at the vicinity of the interface. This approach is rigorously justified only for the steady state conditions of the FMR experiment. Nonetheless, we are confident that our model can provide qualitative insights also in the superdiffusive regime of the THz emission measurements.

In the case of Co, we considered the Fermi wavevectors $k_F^{\uparrow} \approx 1\text{Å}^{-1}$, $k_F^{\downarrow} \approx 0.7\text{Å}^{-1}$ for the two spin sectors, a spin-diffusion length $l_{sf}^{Co} = 12nm$ and a mean free path $\lambda_{Co} = 3nm$. In the case of Pt, we set a Fermi wavevector $k_{Pt} \approx 1\text{Å}^{-1}$, a spin diffusion length $l_{sf}^{Pt} = 3nm$ and a mean free path $\lambda_{Pt} = 1.5nm$. Note that $k_F^{\uparrow} \approx k_{Pt}$ expresses the absence of a potential step between Co and Pt for the majority spin channel. This choice is motivated by a particularly good band matching and optimized transmission at Co/Pt interface for spin ↑ electrons [11]. In order to fit the experiments, we must consider an inverse spin-orbit length $k_{SO} = 1.5\text{Å}^{-1}$. The Rashba splitting is $\alpha_R \bar{k}_F = \frac{\hbar^2 k_{SO}}{t_I m^*}$, where $\bar{k}_F = \frac{k_F^{\uparrow} + k_F^{\downarrow}}{2}$. If we assume an interface extension of about $t_I \approx 2nm$, the previous equations give $\alpha_R \bar{k}_F \approx 0.4eV$. This Rashba splitting is in good agreement with the value predicted by ab-initio calculations for the Co/Pt interface [245] and is not far from the atomic spin-orbit strength of Pt (0.6 eV).

Chapter V- LIV QCLs

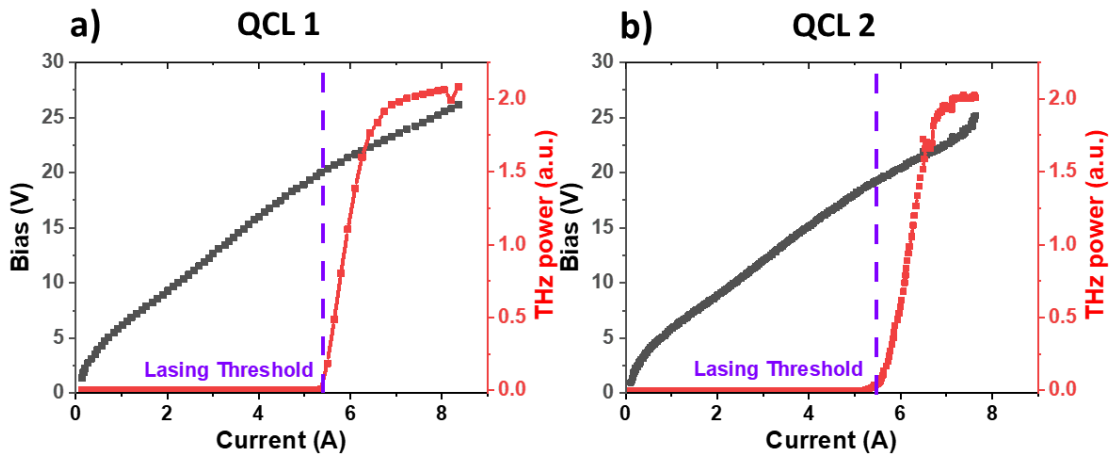

Figure A 4: LIV of a) QCL1 and b) QCL2 biased by a 50kHz 2% duty cycle modulation gated with a 20Hz modulation for pyroelectric detection. The QCL threshold is ~5.3A. Owing to the high power of these devices, the pyroelectric detector/lock-in amplifier saturates for high currents (> 6.5A).

Chapter V-Positioning of the camera procedure

This procedure is summarized in Figure A 5. Once the reflectivity on the polaritonic sample is precisely optimized, the cryostat containing the samples is replaced with the THz camera, to carefully overlap the THz probe beam from the PCs with the QCL pump beam. The positioning of the camera goes as follow: the camera is place where the spot of the PCs is tightly focused, then we take a TDS reflectivity scan on the camera (see Figure A 5). The different peak in the TDS scan corresponds to the inner structure of the THz camera where each interface reflects a part of the THz beam. The first reflection comes from the interface between ambient air and the top Si window, the second from the end of Si window and air, and finally the third reflection comes from the active area, which is the imaging area of the THz camera.

By knowing the structure of the camera, it is then possible to find the precise position of the cryostat corresponding to the image carefully adjusted. This is done by subtracting the THz time of flight induced by the Si window to the third reflection and compensating for the time delay induced by the cryostat windows and Teflon filters.

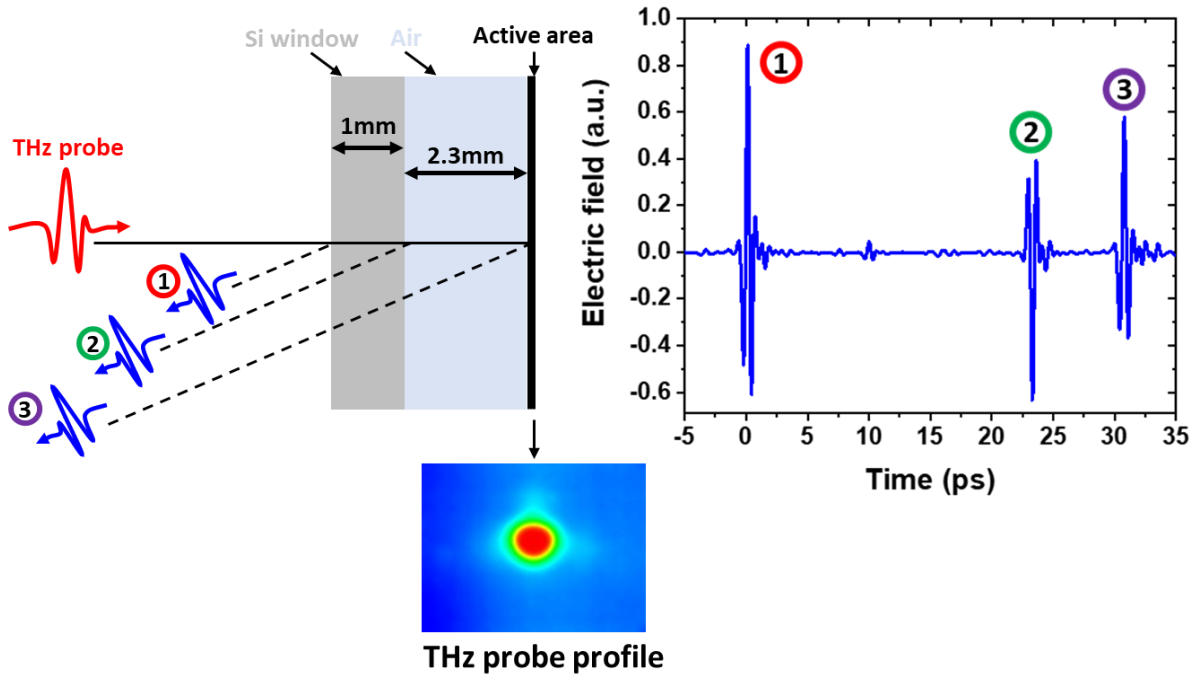

Figure A 5 : procedure of alignment of THz camera, the THz profile of the probe measured corresponds to the third reflections visible in the TDS reflectivity scan. Knowing the inner structure of the camera, it is possible to find the exact position that corresponds to the THz probe imaged (Teflon filters and cryostat windows time delays have to be compensated).

Chapter V-RCWA reflectivity of 2nd generation of sample

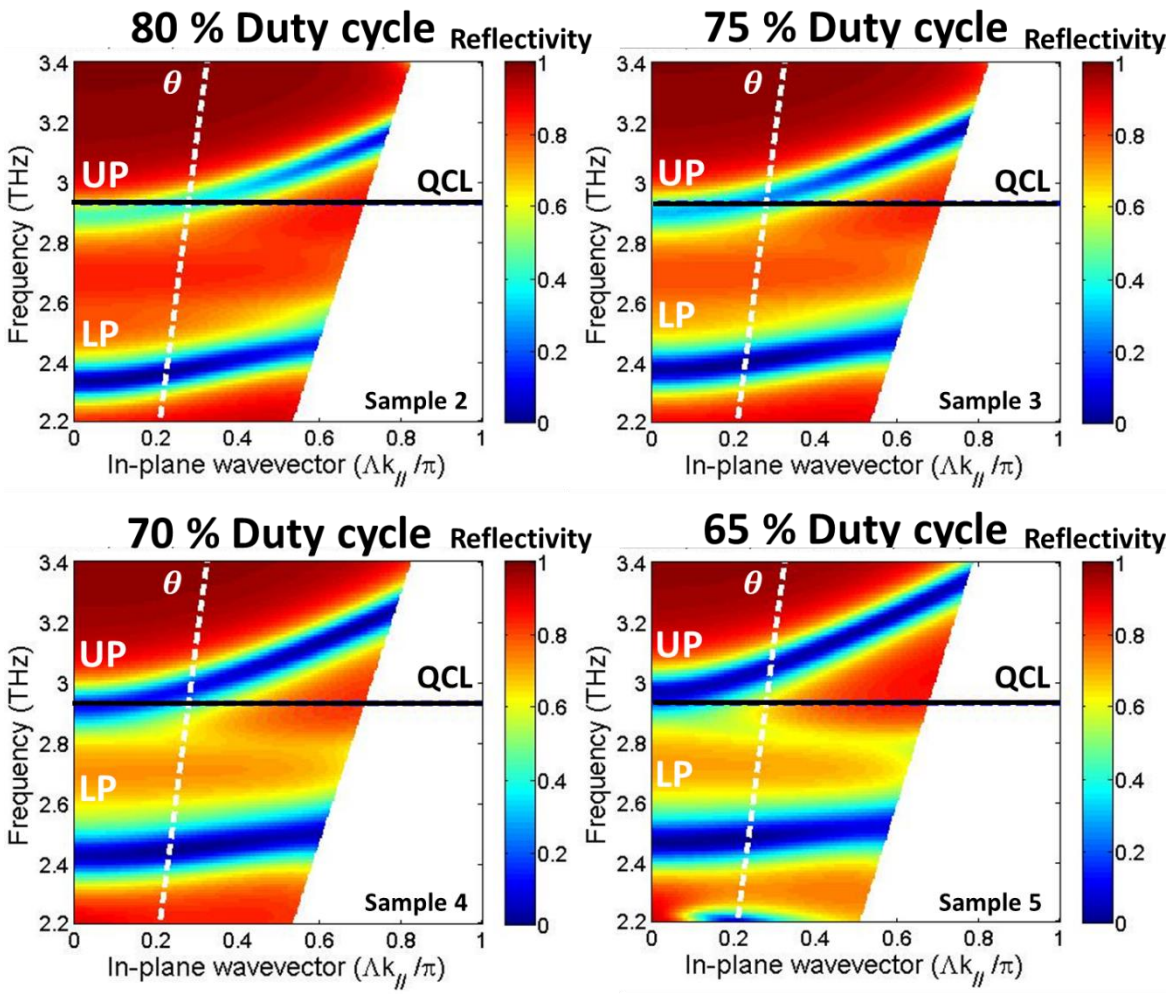

Figure A 6 : RCWA reflectivity resolved polaritonic angular dispersion of the 2nd generation of samples. The QCL pump frequency along with the resonant angle of the pump is highlighted.

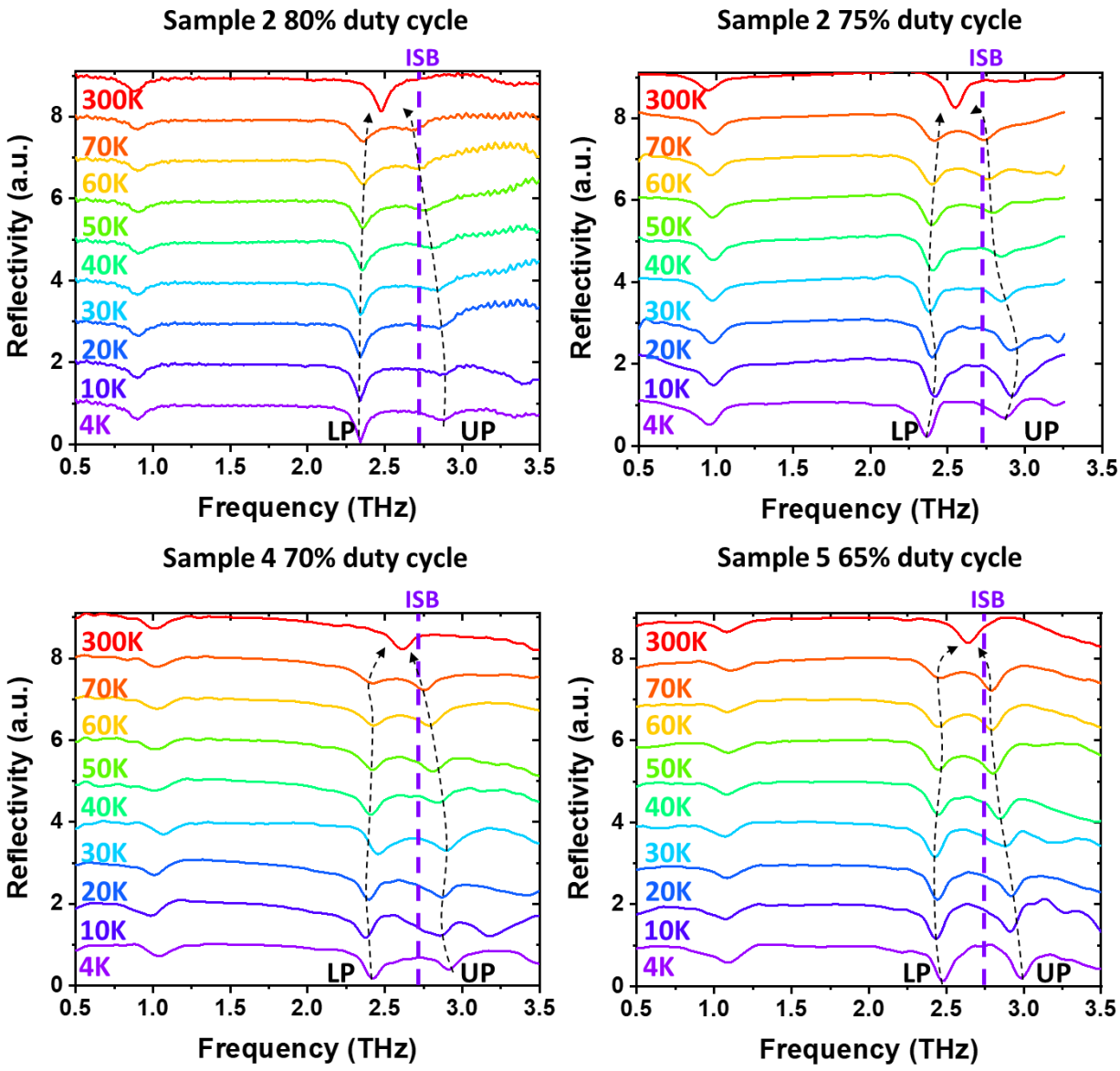

Figure A 7 : TDS reflectivity measured for the 2nd generation of samples over a temperature variation from 4K to 70K, including 300K. Dashed lines are guide to the eyes.

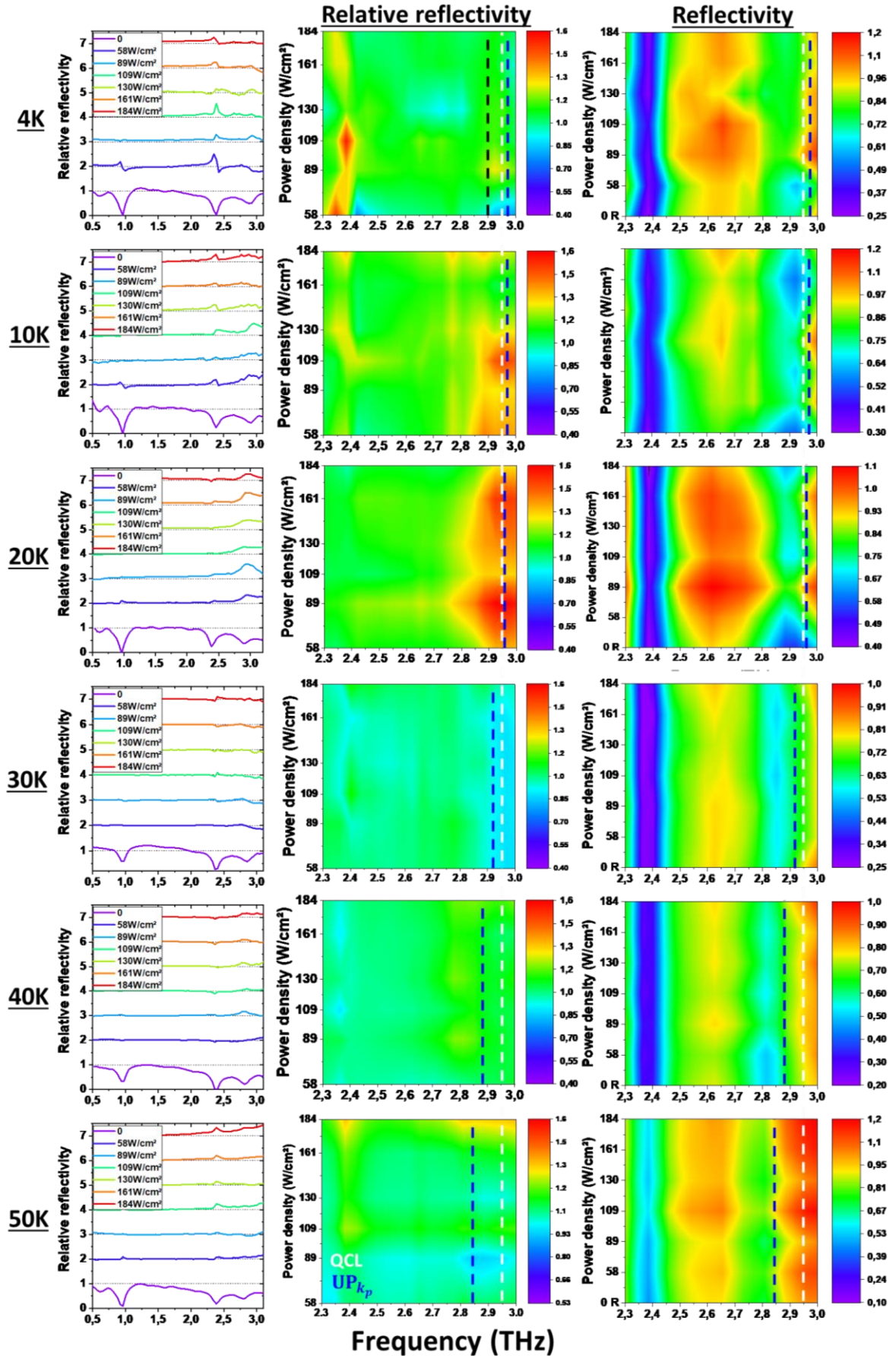

Figure A 8: Resonant pumping of sample 3 – temperature dependence

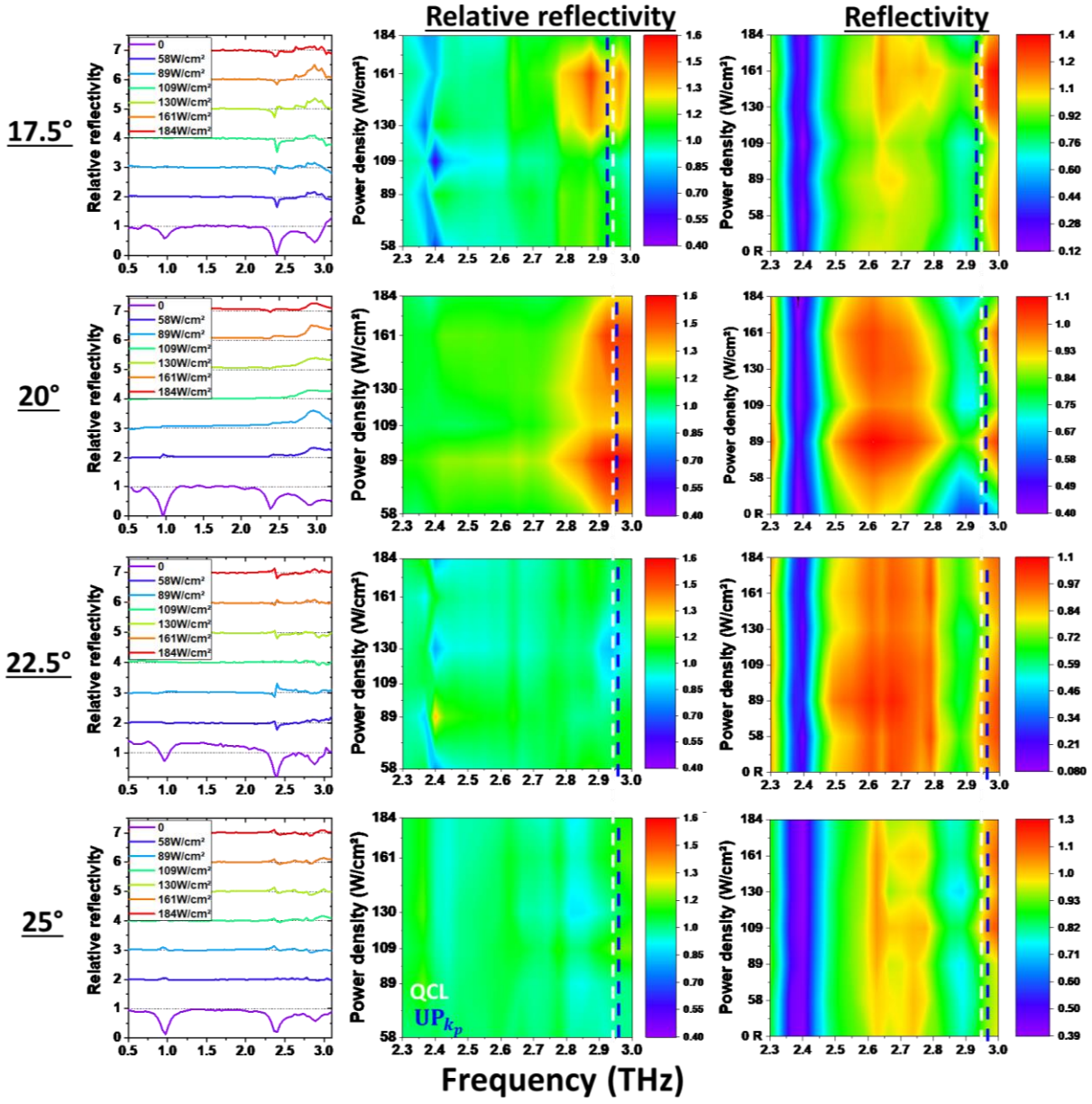

Figure A 9 : Resonant pumping of sample 3 – angular dependence.

List of publications

J. Hawecker, V. Pistore, A. Minasyan, K. Maussang, J. Palomo, I. Sagnes, J.-M. Manceau, R. Colombelli, J. Tignon, J. Mangeney, and S. S. Dhillon, "Cavity-based photoconductive sources for real-time terahertz imaging," Photonics Res. 8, 858 (2020).

M. Tsujimoto, S. Fujita, G. Kuwano, K. Maeda, A. Elarabi, **J. Hawecker**, J. Tignon, J. Mangeney, S. S. Dhillon, and I. Kakeya, "Mutually Synchronized Macroscopic Josephson Oscillations Demonstrated by Polarization Analysis of Superconducting Terahertz Emitters," Phys. Rev. Applied 13, 051001 (2020)

T. H. Dang, **J. Hawecker**, E. Rongione, G. B. Flores, J. C. Rojas-Sanchez, H. Nong, J. Mangeney, J. Tignon, F. Godel, S. Collin, P. Seneor, M. Bibes, A. Fert, M. Anane, J.-M. George, D. Dolfi, R. Lebrun, P. Bortolotti, K. Belashchenko, S. Dhillon and H. Jaffres " Ultrafast spin-currents and charge conversion at 3d-5d interfaces probed by time-domain terahertz spectroscopy" : Appl. Phys. Rev. 7, 041409 (2020)

J. Hawecker, T. H. Dang, J. Boust, S. Collin, H.-J. Drohuin, Y. Laplace, R. Grasset, and J. Dong, J. Mangeney, J. Tignon, H. Jaffres, L. Perfetti and S. S. Dhillon "THz emission, spin-mixing-conductance and spin-memory-loss in magnetic multilayers," Physical Review Letters **(under consideration Advance optical materials)**

Conferences

J. Hawecker, T. H. Dang, E. Rongione, G. B. Flores, J. C. Rojas-Sanchez, H. Nong, J. Mangeney, J. Tignon, F. Godel, S. Collin, P. Seneor, M. Bibes, A. Fert, M. Anane, J.-M. George, D. Dolfi, R. Lebrun, P. Bortolotti, K. Belashchenko, S. Dhillon and H. Jaffres "Ultrafast spin-charge interconversion in Rashba states probed by THz TDS" **Invited presentation** SPIE Optics+Photonics 2020

J. Hawecker, P.B. Vigneron, M. Salih, L.H. Li, E.H. Linfield, A.G. Davies, I.Carusotto, J. Nespolo J.-M. Manceau, R. Colombelli, J. Tignon, J. Mangeney, and S. S. Dhillon "Time resolved spectroscopy of THz intersubband polaritons at small k vector" **Oral presentation** SPIE Optics+Photonics 2020

J. Hawecker, V. Pistore, A. Minasyan, K. Maussang, J. Palomo, I. Sagnes, M. Beck, T. Plötzing, A. Bartels, J.-M. Manceau, R. Colombelli, J. Tignon, J. Mangeney, and S. S. Dhillon "Cavity based THz photoconductive switch : Real Time THz Imaging" **Oral presentation** SPIE Optics+Photonics 2020

J. Hawecker, P.B. Vigneron, M. Salih, L.H. Li, E.H. Linfield, A.G. Davies, I.Carusotto, J. Nespolo J.-M. Manceau, R. Colombelli, J. Tignon, J. Mangeney, and S. S. Dhillon "Time resolved spectroscopy of THz intersubband polaritons at small k vector" **Oral presentation** ITQW 2019, Ojai, USA

J. Hawecker, V. Pistore, F.wang, H. Nong, P.B. Vigneron, R.Colombelli, O. Parillaud, M. Riesch, C. Jirauschek, F. Mezzapesa, K. Garrasi, M. Vitiello, J,Mangeney, J. Tignon, S. S. Dhillon "Active harmonic modelocking and Self-starting harmonic emission in THz QCLs" **Oral presentation** ITQW 2019, Ojai, USA

J. Hawecker, V. Pistore, A. Minasyan, K. Maussang, J. Palomo, I. Sagnes, M. Beck, T. Plötzing, A. Bartels, J.-M. Manceau, R. Colombelli, J. Tignon, J. Mangeney, and S. S. Dhillon "Cavity based THz photoconductive switch: Real Time THz Imaging" **Oral presentation** IRMMW 2019, Paris, France

J. Hawecker, V. Pistore, A. Minasyan, K. Maussang, J. Palomo, I. Sagnes, J.-M. Manceau, R. Colombelli, J. Tignon, J. Mangeney, and S. S. Dhillon "Cavity based THz photoconductive switch:Towards real time THz imaging" Poster presentation THz GDR 2019, St-Raphaël, France

J. Hawecker, K. Maussang, J. Palomo, I. Sagnes, J.-M. Manceau, R. Colombelli, J. Tignon, J. Mangeney, and S. S. Dhillon
"Cavity based THz photoconductive switch" **Oral presentation** OTST 2019, Santa Fe, USA

J. Hawecker, V. Pistore, F.wang, H. Nong, P.B. Vigneron, R.Colombelli, O. Parillaud, J,Mangeney, J. Tignon, S. S. Dhillon "Harmonic Modelocking of THz Quantum Cascade Lasers" Poster presentation OTST 2019, Santa Fe, USA

J. Hawecker, P. Goulain, R.Colombelli, J,Mangeney, J. Tignon, S. S. Dhillon "Complex dielectric function of highly doped samples extracted by Terahertz time domain spectroscopy" Poster presentation IQCLSW 2018, Cassis, France

J. Hawecker, P. Goulain, R.Colombelli, J,Mangeney, J. Tignon, S. S. Dhillon "Complex dielectric function of highly doped samples extracted by Terahertz time domain spectroscopy" Poster presentation ICPS 2018, Montpellier, France

Bibliography

[1] E. Th. Papaioannou and R. Beigang, “THz spintronic emitters: a review on achievements and future challenges,” *Nanophotonics*, vol. 0, no. 0, Dec. 2020, doi: 10.1515/nanoph-2020-0563.

[2] Yun-Shik Lee, Ed., *Principles of Terahertz Science and Technology*. 2009.

[3] M. Tonouchi, “Cutting-edge terahertz technology,” *Nature Photon*, vol. 1, no. 2, pp. 97–105, Feb. 2007, doi: 10.1038/nphoton.2007.3.

[4] V. Pistore, “Modelocking of THz quantum cascade lasers: dispersion control and non-linearities,” LPENS, 2019.

[5] H.-J. Song and T. Nagatsuma, “Handbook of Terahertz Technologies: Devices and Applications,” p. 606.

[6] J.-L. Coutaz, F. Garet, and V. Wallace, *Principles of terahertz time-domain spectroscopy*. Singapore: Pan Stanford Publishing, 2018.

[7] H. A. Hafez, “Extremely efficient terahertz high-harmonic generation in graphene by hot Dirac fermions,” p. 20.

[8] W. Zhang, “Ultrafast terahertz magnetometry,” p. 9.

[9] H. Feng *et al.*, “A passive video-rate terahertz human body imager with real-time calibration for security applications,” *Appl. Phys. B*, vol. 126, no. 8, p. 143, Aug. 2020, doi: 10.1007/s00340-020-07496-3.

[10] H. Zhong, N. Karpowicz, and X.-C. Zhang, “Terahertz emission profile from laser-induced air plasma,” *Appl. Phys. Lett.*, vol. 88, no. 26, p. 261103, Jun. 2006, doi: 10.1063/1.2216025.

[11] T. H. Dang *et al.*, “Ultrafast spin-currents and charge conversion at 3d-5d interfaces probed by time-domain terahertz spectroscopy,” *Applied Physics Reviews*, vol. 7, no. 4, p. 041409, Dec. 2020, doi: 10.1063/5.0022369.

[12] J. Neu and C. A. Schmuttenmaer, “Tutorial: An introduction to terahertz time domain spectroscopy (THz-TDS),” *Journal of Applied Physics*, vol. 124, no. 23, p. 231101, Dec. 2018, doi: 10.1063/1.5047659.

[13] K. Maussang *et al.*, “Echo-Less Photoconductive Antenna Sources for High-Resolution Terahertz Time-Domain Spectroscopy,” *IEEE Trans. THz Sci. Technol.*, vol. 6, no. 1, pp. 20–25, Jan. 2016, doi: 10.1109/TTHZ.2015.2504794.

[14] J. Hawecker *et al.*, “Cavity-based Photoconductive sources for real time terahertz imaging,” *Photon. Res.*, May 2020, doi: 10.1364/PRJ.388219.

[15] N. M. Burford and M. O. El-Shenawee, “Review of terahertz photoconductive antenna technology,” doi: 10.1117/1.OE.56.1.010901.

[16] Q. Wu, M. Litz, and X. -C. Zhang, “Broadband detection capability of ZnTe electro-optic field detectors,” *Appl. Phys. Lett.*, vol. 68, no. 21, pp. 2924–2926, May 1996, doi: 10.1063/1.116356.

[17] S. S. Dhillon *et al.*, “The 2017 terahertz science and technology roadmap,” *J. Phys. D: Appl. Phys.*, vol. 50, no. 4, p. 043001, Feb. 2017, doi: 10.1088/1361-6463/50/4/043001.

[18] H. Guerboukha, K. Nallappan, and M. Skorobogatiy, “Toward real-time terahertz imaging,” *Adv. Opt. Photon., AOP*, vol. 10, no. 4, pp. 843–938, Dec. 2018, doi: 10.1364/AOP.10.000843.

[19] F. Simoens and J. Meilhan, “Terahertz real-time imaging uncooled array based on antenna- and cavity-coupled bolometers,” *Philosophical Transactions of the Royal Society A: Mathematical, Physical and Engineering Sciences*, vol. 372, no. 2012, p. 20130111, Mar. 2014, doi: 10.1098/rsta.2013.0111.
[20] A. W. M. Lee, Q. Qin, S. Kumar, B. S. Williams, Q. Hu, and J. L. Reno, “Real-time terahertz imaging over a standoff distance (>25meters),” *Appl. Phys. Lett.*, vol. 89, no. 14, p. 141125, Oct. 2006, doi: 10.1063/1.2360210.
[21] T. W. Crowe, W. L. Bishop, D. W. Porterfield, J. L. Hesler, and R. M. Weikle, “Opening the terahertz window with integrated diode circuits,” *IEEE Journal of Solid-State Circuits*, vol. 40, no. 10, pp. 2104–2110, Oct. 2005, doi: 10.1109/JSSC.2005.854599.
[22] D. H. Auston, “Subpicosecond electro-optic shock waves,” *Applied Physics Letters*, vol. 43, no. 8, p. 713, 1983, doi: 10.1063/1.94486.
[23] D. H. Auston, K. P. Cheung, and P. R. Smith, “Picosecond photoconducting Hertzian dipoles,” *Appl. Phys. Lett.*, vol. 45, no. 3, pp. 284–286, Aug. 1984, doi: 10.1063/1.95174.
[24] R. J. B. Dietz *et al.*, “64 μW pulsed terahertz emission from growth optimized InGaAs/InAlAs heterostructures with separated photoconductive and trapping regions,” *Applied Physics Letters*, vol. 103, no. 6, p. 061103, 2013, doi: 10.1063/1.4817797.
[25] B. Globisch *et al.*, “Absolute terahertz power measurement of a time-domain spectroscopy system,” *Opt. Lett., OL*, vol. 40, no. 15, pp. 3544–3547, Aug. 2015, doi: 10.1364/OL.40.003544.
[26] C. W. Berry, M. R. Hashemi, and M. Jarrahi, “Generation of high power pulsed terahertz radiation using a plasmonic photoconductive emitter array with logarithmic spiral antennas,” *Appl. Phys. Lett.*, vol. 104, no. 8, p. 081122, Feb. 2014, doi: 10.1063/1.4866807.
[27] D. Turan, S. C. Corzo-Garcia, N. T. Yardimci, E. Castro-Camus, and M. Jarrahi, “Impact of the Metal Adhesion Layer on the Radiation Power of Plasmonic Photoconductive Terahertz Sources,” *J Infrared Milli Terahz Waves*, vol. 38, no. 12, pp. 1448–1456, Dec. 2017, doi: 10.1007/s10762-017-0431-9.
[28] M. Tani, S. Matsuura, K. Sakai, and S. Nakashima, “Emission characteristics of photoconductive antennas based on low-temperature-grown GaAs and semi-insulating GaAs,” *Appl. Opt.*, vol. 36, no. 30, p. 7853, Oct. 1997, doi: 10.1364/AO.36.007853.
[29] A. Dreyhaupt, S. Winnerl, T. Dekorsy, and M. Helm, “High-intensity terahertz radiation from a microstructured large-area photoconductor,” *Appl. Phys. Lett.*, vol. 86, no. 12, p. 121114, Mar. 2005, doi: 10.1063/1.1891304.
[30] J. Madéo *et al.*, “Frequency tunable terahertz interdigitated photoconductive antennas,” *Electron. Lett.*, vol. 46, no. 9, p. 611, 2010, doi: 10.1049/el.2010.0440.
[31] Edward D. Palik, *Handbook of Optical Constants of Solids*. .
[32] Y. Todorov *et al.*, “Optical properties of metal-dielectric-metal microcavities in the THz frequency range,” *Opt. Express*, vol. 18, no. 13, p. 13886, Jun. 2010, doi: 10.1364/OE.18.013886.
[33] J. Oden *et al.*, “Imaging of broadband terahertz beams using an array of antenna-coupled microbolometers operating at room temperature,” *Opt. Express*, vol. 21, no. 4, pp. 4817–4825, Feb. 2013, doi: 10.1364/OE.21.004817.
[34] B. N. Behnken, G. Karunasiri, D. R. Chamberlin, P. R. Robrish, and J. Faist, “Real-time imaging using a 2.8 THz quantum cascade laser and uncooled infrared microbolometer camera,” *Opt. Lett., OL*, vol. 33, no. 5, pp. 440–442, Mar. 2008, doi: 10.1364/OL.33.000440.

[35] T. Seifert *et al.*, “Efficient metallic spintronic emitters of ultrabroadband terahertz radiation,” *Nature Photon*, vol. 10, no. 7, pp. 483–488, Jul. 2016, doi: 10.1038/nphoton.2016.91.
[36] A. Hirohata *et al.*, “Review on spintronics: Principles and device applications,” *Journal of Magnetism and Magnetic Materials*, vol. 509, p. 166711, Sep. 2020, doi: 10.1016/j.jmmm.2020.166711.
[37] E. Y. Vedmedenko *et al.*, “The 2020 magnetism roadmap,” *J. Phys. D: Appl. Phys.*, vol. 53, no. 45, p. 453001, Nov. 2020, doi: 10.1088/1361-6463/ab9d98.
[38] M. Johnson and R. H. Silsbee, “Interfacial charge-spin coupling: Injection and detection of spin magnetization in metals,” *Phys. Rev. Lett.*, vol. 55, no. 17, pp. 1790–1793, Oct. 1985, doi: 10.1103/PhysRevLett.55.1790.
[39] M. N. Baibich *et al.*, “Giant Magnetoresistance of (001)Fe/(001)Cr Magnetic Superlattices,” *Phys. Rev. Lett.*, vol. 61, no. 21, pp. 2472–2475, Nov. 1988, doi: 10.1103/PhysRevLett.61.2472.
[40] G. Binasch, P. Grünberg, F. Saurenbach, and W. Zinn, “Enhanced magnetoresistance in layered magnetic structures with antiferromagnetic interlayer exchange,” *Phys. Rev. B*, vol. 39, no. 7, pp. 4828–4830, Mar. 1989, doi: 10.1103/PhysRevB.39.4828.
[41] E. Beaurepaire, G. M. Turner, S. M. Harrel, M. C. Beard, J.-Y. Bigot, and C. A. Schmuttenmaer, “Coherent terahertz emission from ferromagnetic films excited by femtosecond laser pulses,” *Appl. Phys. Lett.*, vol. 84, no. 18, pp. 3465–3467, May 2004, doi: 10.1063/1.1737467.
[42] A. V. Chumak, V. I. Vasyuchka, A. A. Serga, and B. Hillebrands, “Magnon spintronics,” *Nature Phys*, vol. 11, no. 6, pp. 453–461, Jun. 2015, doi: 10.1038/nphys3347.
[43] S. M. Rezende, A. Azevedo, and R. L. Rodríguez-Suárez, “Introduction to antiferromagnetic magnons,” *Journal of Applied Physics*, vol. 126, no. 15, p. 151101, Oct. 2019, doi: 10.1063/1.5109132.
[44] C. Felser and G. H. Fecher, Eds., *Spintronics*. Dordrecht: Springer Netherlands, 2013.
[45] R. J. Soulen Jr., “Measuring the Spin Polarization of a Metal with a Superconducting Point Contact,” *Science*, vol. 282, no. 5386, pp. 85–88, Oct. 1998, doi: 10.1126/science.282.5386.85.
[46] E. Beaurepaire, J.-C. Merle, A. Daunois, and J.-Y. Bigot, “Ultrafast Spin Dynamics in Ferromagnetic Nickel,” *Phys. Rev. Lett.*, vol. 76, no. 22, pp. 4250–4253, May 1996, doi: 10.1103/PhysRevLett.76.4250.
[47] K. B, van K. M, K. J. T, and de J. W. J. M, “Ultrafast magneto-optics in nickel: Magnetism or optics?,” *Phys. Rev. Lett.*, vol. 85, p. 844, 2000.
[48] M. A *et al.*, “Ultrafast transport of laser-excited spin-polarized carriers in Au/Fe/MgO(001),” *Phys. Rev. Lett.*, vol. 107, p. 076601, 2011.
[49] Z. Feng *et al.*, “Highly efficient spintronic terahertz emitter enabled by metal–dielectric photonic crystal,” *Adv. Opt. Mater.*, vol. 6, p. 1800965, 2018.
[50] T. S. Seifert *et al.*, “Terahertz spectroscopy for all-optical spintronic characterization of the spin-Hall-effect metals Pt, W and Cu $_{80}$ Ir $_{20}$,” *J. Phys. D: Appl. Phys.*, vol. 51, no. 36, p. 364003, Sep. 2018, doi: 10.1088/1361-6463/aad536.
[51] G. Torosyan, S. Keller, L. Scheuer, R. Beigang, and E. Th. Papaioannou, “Optimized Spintronic Terahertz Emitters Based on Epitaxial Grown Fe/Pt Layer Structures,” *Sci Rep*, vol. 8, no. 1, p. 1311, Dec. 2018, doi: 10.1038/s41598-018-19432-9.
[52] S. S. K. V. Shanavas and Z. S. Popovic, “Theoretical model for Rashba spin-orbit interaction in d electrons,” *Physical Review B*, 2014.

[53] D. C. Vaz, “Spin-to-charge current conversion in SrTiO3-based two-dimensional electron gases,” 2018.
[54] E. H. Hall, “On a New Action of the Magnet on Electric Currents,” *American Journal of Mathematics , , No. 3 (Sep., 1879), pp. 287- 292*, vol. Vol. 2, p. 7, Sep. 1879.
[55] E. H. Hall, “XVIII. On the ‘Rotational Coefficient’ in nickel and cobalt,” *null*, vol. 12, no. 74, pp. 157–172, Sep. 1881, doi: 10.1080/14786448108627086.
[56] T. H. Dang *et al.*, “Anomalous Hall effect in 3d/5d multilayers mediated by interface scattering and nonlocal spin conductivity,” *Phys. Rev. B*, vol. 102, p. 144405, 2020.
[57] S. J, V. S. O, W. J, B. C. H, and J. T, “Spin Hall effects,” *Rev. Mod. Phys.*, vol. 87, p. 1213, 2015.
[58] N. Nagaosa, J. Sinova, S. Onoda, A. H. MacDonald, and N. P. Ong, “Anomalous Hall effect,” *Rev. Mod. Phys.*, vol. 82, no. 2, pp. 1539–1592, May 2010, doi: 10.1103/RevModPhys.82.1539.
[59] S. Lowitzer, M. Gradhand, D. Ködderitzsch, D. V. Fedorov, I. Mertig, and H. Ebert, “Extrinsic and Intrinsic Contributions to the Spin Hall Effect of Alloys,” *Phys. Rev. Lett.*, vol. 106, no. 5, p. 056601, Feb. 2011, doi: 10.1103/PhysRevLett.106.056601.
[60] Kiran Kumar Vudya Sethu, “Spin orbit torques in magnetic materials,” 2017.
[61] M. I. Dyakonov and V. I. Perel, “Current-induced spin orientation of electrons in semiconductors,” *Physics Letters A*, vol. 35, no. 6, pp. 459–460, Jul. 1971, doi: 10.1016/0375-9601(71)90196-4.
[62] Y. K. Kato, R. C. Myers, , A. C. Gossard, and D. D. Awschalom, “Observation of the Spin Hall Effect in Semiconductors,” *Science*, vol. 306, 2004.
[63] S. O. Valenzuela and M. Tinkham, “Direct electronic measurement of the spin Hall effect,” *Nature*, vol. 442, no. 7099, pp. 176–179, Jul. 2006, doi: 10.1038/nature04937.
[64] P. Laczkowski *et al.*, “Large enhancement of the spin Hall effect in Au by side-jump scattering on Ta impurities,” *Phys. Rev. B*, vol. 96, p. 140405, 2017.
[65] J.-C. Rojas-Sánchez *et al.*, “Spin Pumping and Inverse Spin Hall Effect in Platinum: The Essential Role of Spin-Memory Loss at Metallic Interfaces,” *Phys. Rev. Lett.*, vol. 112, no. 10, p. 106602, Mar. 2014, doi: 10.1103/PhysRevLett.112.106602.
[66] P. Laczkowski *et al.*, “Experimental evidences of a large extrinsic spin Hall effect in AuW alloy,” *Appl. Phys. Lett.*, vol. 104, p. 142403, 2014.
[67] K. M. Krishnan, *Fundamentals and applications of magnetic materials*, First edition. Oxford, United Kingdom: Oxford University Press, 2016.
[68] K. Dolui and B. K. Nikolić, “Spin-memory loss due to spin-orbit coupling at ferromagnet/heavy-metal interfaces: Ab initio spin-density matrix approach,” *Phys. Rev. B*, vol. 96, p. 220403, 2017.
[69] K. Gupta, R. J. H. Wesselink, R. Liu, Z. Yuan, and P. J. Kelly, “Disorder dependence of interface spin memory loss,” *Phys. Rev. Lett.*, vol. 124, p. 087702, 2020.
[70] Y.-H. Zhu, X.-X. Zhang, J. Liu, and P.-S. He, “Spin-accumulation capacitance and its application to magnetoimpedance,” *J. Appl. Phys.*, p. 10, 2017.
[71] A. Brataas, G. Bauer, and P. Kelly, “Non-collinear magnetoelectronics,” *Physics Reports*, vol. 427, no. 4, pp. 157–255, Apr. 2006, doi: 10.1016/j.physrep.2006.01.001.
[72] M. Chen *et al.*, “Current-enhanced broadband THz emission from spintronic devices,” *Adv. Opt. Mater.*, vol. 7, p. 1801608, 2019.
[73] Y. D *et al.*, “Powerful and tunable THz emitters based on the Fe/Pt magnetic heterostructure,” *Adv. Opt. Mater.*, vol. 4, p. 1944, 2016.

[74] Tom S. Seifert, “Spintronics with Terahertz Radiation: Probing and driving spins at highest frequencies,” 2017.
[75] Z. L, R. D. C, and B. R. A, “Enhancement of spin transparency by interfacial alloying,” *Phys. Rev. B*, vol. 99, p. 180404, 2019.
[76] Z. L, Z. L, S. S, S. M, R. D. C, and B. R. A, “Enhancing spin-orbit torque by strong interfacial scattering from ultrathin insertion layers,” *Phys. Rev. Appl.*, vol. 11, p. 061004, 2019.
[77] Z. L and B. R, “Maximizing spin-orbit-torque efficiency of Pt/Ti multilayers: Trade-off between intrinsic spin Hall conductivity and carrier lifetime,” *Phys. Rev. Appl.*, vol. 12, p. 051002, 2019.
[78] A. J. Berger, E. R. J. Edwards, H. T. Nembach, O. Karis, M. Weiler, and T. J. Silva, “Determination of the spin Hall effect and the spin diffusion length of Pt from self-consistent fitting of damping enhancement and inverse spin-orbit torque measurements,” *Phys. Rev. B*, vol. 98, no. 2, p. 024402, Jul. 2018, doi: 10.1103/PhysRevB.98.024402.
[79] K. D. Belashchenko, A. A. Kovalev, and M. van Schilfgaarde, “Theory of spin loss at metallic interfaces,” *Phys. Rev. Lett.*, vol. 117, p. 207204, 2016.
[80] Z. M, C. B, and L. S. T, “Interfacial electric field and spin-orbitronic properties of heavy-metal/CoFe bilayers,” *Appl. Phys. Lett.*, vol. 114, p. 012401, 2019.
[81] E. Saitoh, M. Ueda, H. Miyajima, and G. Tatara, “Conversion of spin current into charge current at room temperature: Inverse spin-Hall effect,” *Appl. Phys. Lett.*, vol. 88, no. 18, p. 182509, May 2006, doi: 10.1063/1.2199473.
[82] A. Ghosh, “Pompage de spin et absorption de spin dans des hétérostructures magnétiques.”
[83] R. Iguchi and E. Saitoh, “Measurement of spin pumping voltage separated from extrinsic microwave effects,” *J. Phys. Soc. Jpn.*, vol. 86, p. 011003, 2017.
[84] P. Noel, “Dynamical spin injection and spin to charge current conversion in oxide-based Rashba interfaces and topological insulators,” p. 182, 2019.
[85] Y. Xu, D. D. Awschalom, and J. Nitta, Eds., *Handbook of Spintronics*. Dordrecht: Springer Netherlands, 2016.
[86] A. Brataas, Y. Tserkovnyak, G. E. W. Bauer, and P. J. Kelly, “Spin Pumping and Spin Transfer,” *arXiv:1108.0385 [cond-mat]*, Mar. 2012, Accessed: Nov. 16, 2020. [Online]. Available: http://arxiv.org/abs/1108.0385.
[87] S. Maekawa, S. O. Valenzuela, and E. Saitoh, Eds., *Spin current*, Second edition. Oxford, United Kingdom: Oxford University Press, 2017.
[88] E. Y. Tsymbal and I. Žutić, *Spintronics Handbook: Spin Transport and Magnetism, Second Edition: Nanoscale Spintronics and Applications—Volume Three*, 2nd ed. Second edition. | Boca Raton : Taylor & Francis, CRC Press, 2018. |: CRC Press, 2019.
[89] D. M. Nenno *et al.*, “Modification of spintronic terahertz emitter performance through defect engineering,” *Scientific Reports*, vol. 9, no. 1, Dec. 2019, doi: 10.1038/s41598-019-49963-8.
[90] L. W.-T, Z. Y, B. M, W. Y, and Y. Z, “Interface reflectivity of a superdiffusive spin current in ultrafast demagnetization and terahertz emission,” *Phys. Rev. B*, vol. 101, p. 014435, 2020.
[91] S. Keller *et al.*, “Determination of the spin Hall angle in single-crystalline Pt films from spin pumping experiments,” *New J. Phys.*, vol. 20, no. 5, p. 053002, May 2018, doi: 10.1088/1367-2630/aabc46.

[92] T. Valet and A. Fert, “Theory of the perpendicular magnetoresistance in magnetic multilayers,” *Phys. Rev. B*, vol. 48, p. 7099, 1993.
[93] S. Kaltenborn, Y.-H. Zhu, and H. C. Schneider, “Wave-diffusion theory of spin transport in metals after ultrashort-pulse excitation,” *Phys. Rev. B*, vol. 85, p. 235101, 2012.
[94] O. Gunnarsson, O. Jepsen, and O. K. Andersen, “Self-consistent impurity calculations in the atomic-spheres approximation,” *Phys. Rev. B*, vol. 27, p. 7144, 1983.
[95] K. M. Schep, J. van Hoof, P. J. Kelly, G. E. W. Bauer, and J. E. Inglesfield, “Interface resistances of magnetic multilayers,” *Phys. Rev. B*, vol. 56, p. 10805, 1997.
[96] Y. Yafet, “g Factors and Spin-Lattice Relaxation of Conduction Electrons,” in *Solid State Physics*, vol. 14, Elsevier, 1963, pp. 1–98.
[97] L. Zhu, D. C. Ralph, and R. A. Buhrman, “Effective Spin-Mixing Conductance of Heavy-Metal–Ferromagnet Interfaces,” *Phys. Rev. Lett.*, vol. 123, no. 5, p. 057203, Aug. 2019, doi: 10.1103/PhysRevLett.123.057203.
[98] Y. Liu, Z. Yuan, R. J. H. Wesselink, A. A. Starikov, and P. J. Kelly, “Interface Enhancement of Gilbert Damping from First Principles,” *Phys. Rev. Lett.*, vol. 113, no. 20, p. 207202, Nov. 2014, doi: 10.1103/PhysRevLett.113.207202.
[99] T. S. Seifert *et al.*, “Femtosecond formation dynamics of the spin Seebeck effect revealed by terahertz spectroscopy,” *Nat Commun*, vol. 9, no. 1, p. 2899, Dec. 2018, doi: 10.1038/s41467-018-05135-2.
[100] D. M. Nenno, R. Binder, and H. C. Schneider, “Simulation of Hot-Carrier Dynamics and Terahertz Emission in Laser-Excited Metallic Bilayers,” *Phys. Rev. Applied*, vol. 11, no. 5, p. 054083, May 2019, doi: 10.1103/PhysRevApplied.11.054083.
[101] M. Walther, D. G. Cooke, C. Sherstan, M. Hajar, M. R. Freeman, and F. A. Hegmann, “Terahertz conductivity of thin gold films at the metal-insulator percolation transition,” *Phys. Rev. B*, vol. 76, no. 12, p. 125408, Sep. 2007, doi: 10.1103/PhysRevB.76.125408.
[102] L. H.-Y *et al.*, “Enhanced spin–orbit torque via interface engineering in Pt/CoFeB/MgO heterostructures,” *APL Materials*, vol. 7, p. 031110, 2019.
[103] C. O. Avci, G. S. D. Beach, and P. Gambardella, “Effects of transition metal spacers on spin-orbit torques, spin Hall magnetoresistance, and magnetic anisotropy of Pt/Co bilayers,” *Phys. Rev. B*, vol. 100, no. 23, p. 235454, Dec. 2019, doi: 10.1103/PhysRevB.100.235454.
[104] J. Hawecker *et al.*, “THz emission, spin-mixing-conductance and spin-memory-loss in magnetic multilayers,” p. 5.
[105] V. P. Amin, P. M. Haney, and M. D. Stiles, “Interfacial spin-orbit torques,” *Journal of Applied Physics*, vol. 128, no. 15, p. 151101, Oct. 2020, doi: 10.1063/5.0024019.
[106] P. M. Haney, H.-W. Lee, K.-J. Lee, A. Manchon, and M. D. Stiles, “Current-induced torques and interfacial spin-orbit coupling,” *Phys. Rev. B*, vol. 88, no. 21, p. 214417, Dec. 2013, doi: 10.1103/PhysRevB.88.214417.
[107] K.-W. Kim, K.-J. Lee, J. Sinova, H.-W. Lee, and M. D. Stiles, “Spin-orbit torques from interfacial spin-orbit coupling for various interfaces,” *Phys. Rev. B*, vol. 96, no. 10, p. 104438, Sep. 2017, doi: 10.1103/PhysRevB.96.104438.
[108] W. Han, Y. Otani, and S. Maekawa, “Quantum materials for spin and charge conversion,” *npj Quant Mater*, vol. 3, no. 1, p. 27, Dec. 2018, doi: 10.1038/s41535-018-0100-9.
[109] K. Manna, Y. Sun, L. Muechler, J. Kübler, and C. Felser, “Heusler, Weyl and Berry,” *Nat Rev Mater*, vol. 3, no. 8, pp. 244–256, Aug. 2018, doi: 10.1038/s41578-018-0036-5.

[110] E. I. Rashba and V. I. Sheka, “Symmetry of Energy Bands in Crystals of Wurtzite Type II. Symmetry of Bands with Spin-Orbit Interaction Included,” p. 16, 1959.
[111] S. Datta and B. Das, “Electronic analog of the electro-optic modulator,” *Appl. Phys. Lett.*, vol. 56, no. 7, pp. 665–667, Feb. 1990, doi: 10.1063/1.102730.
[112] A. Manchon, H. C. Koo, J. Nitta, S. M. Frolov, and R. A. Duine, “New perspectives for Rashba spin–orbit coupling,” *Nature Mater*, vol. 14, no. 9, pp. 871–882, Sep. 2015, doi: 10.1038/nmat4360.
[113] D. Bercioux and P. Lucignano, “Quantum transport in Rashba spin-orbit materials: A review,” *Rep. Prog. Phys.*, vol. 78, no. 10, p. 106001, Oct. 2015, doi: 10.1088/0034-4885/78/10/106001.
[114] L. Fu, C. L. Kane, and E. J. Mele, “Topological Insulators in Three Dimensions,” *Phys. Rev. Lett.*, vol. 98, no. 10, p. 106803, Mar. 2007, doi: 10.1103/PhysRevLett.98.106803.
[115] L. Fu and C. L. Kane, “Topological insulators with inversion symmetry,” *Phys. Rev. B*, vol. 76, no. 4, p. 045302, Jul. 2007, doi: 10.1103/PhysRevB.76.045302.
[116] C. L. Kane and E. J. Mele, “Quantum Spin Hall Effect in Graphene,” *Phys. Rev. Lett.*, vol. 95, no. 22, p. 226801, Nov. 2005, doi: 10.1103/PhysRevLett.95.226801.
[117] M. Z. Hasan and C. L. Kane, “Topological Insulators,” *Rev. Mod. Phys.*, vol. 82, no. 4, pp. 3045–3067, Nov. 2010, doi: 10.1103/RevModPhys.82.3045.
[118] M. Z. Hasan and J. E. Moore, “Three-Dimensional Topological Insulators,” *Annu. Rev. Condens. Matter Phys.*, vol. 2, no. 1, pp. 55–78, Mar. 2011, doi: 10.1146/annurev-conmatphys-062910-140432.
[119] J.-C. Rojas-Sánchez *et al.*, “Spin to Charge Conversion at Room Temperature by Spin Pumping into a New Type of Topological Insulator: a-Sn Films,” *Phys. Rev. Lett.*, vol. 116, no. 9, p. 096602, Mar. 2016, doi: 10.1103/PhysRevLett.116.096602.
[120] S.-Y. Xu *et al.*, “Topological Phase Transition and Texture Inversion in a Tunable Topological Insulator,” *Science*, vol. 332, no. 6029, pp. 560–564, Apr. 2011, doi: 10.1126/science.1201607.
[121] Edouard Lesne, “Non-Equilibrium Spin Accumulation Phenomena at the LaAlO3/SrTiO3(001) Quasi-Two-Dimensional Electron System,” 2015.
[122] B. Q. Lv *et al.*, “Experimental Discovery of Weyl Semimetal TaAs,” *Phys. Rev. X*, vol. 5, no. 3, p. 031013, Jul. 2015, doi: 10.1103/PhysRevX.5.031013.
[123] T. Matsuda, N. Kanda, T. Higo, N. P. Armitage, S. Nakatsuji, and R. Matsunaga, “Room-temperature terahertz anomalous Hall effect in Weyl antiferromagnet Mn3Sn thin films,” *Nat Commun*, vol. 11, no. 1, p. 909, Dec. 2020, doi: 10.1038/s41467-020-14690-6.
[124] Y. Sun, Y. Zhang, C. Felser, and B. Yan, “Strong Intrinsic Spin Hall Effect in the TaAs Family of Weyl Semimetals,” *Phys. Rev. Lett.*, vol. 117, no. 14, p. 146403, Sep. 2016, doi: 10.1103/PhysRevLett.117.146403.
[125] B. Yan and C. Felser, “Topological Materials: Weyl Semimetals,” *Annu. Rev. Condens. Matter Phys.*, vol. 8, no. 1, pp. 337–354, Mar. 2017, doi: 10.1146/annurev-conmatphys-031016-025458.
[126] L. X. Yang *et al.*, “Weyl semimetal phase in the non-centrosymmetric compound TaAs,” *Nature Phys*, vol. 11, no. 9, pp. 728–732, Sep. 2015, doi: 10.1038/nphys3425.
[127] K. Elphick *et al.*, “Heusler alloys for spintronic devices: review on recent development and future perspectives,” *Science and Technology of Advanced Materials*, p. 14686996.2020.1812364, Aug. 2020, doi: 10.1080/14686996.2020.1812364.

[128] Q. Wang, Z. Wen, T. Kubota, T. Seki, and K. Takanashi, “Structural-order dependence of anomalous Hall effect in Co $_2$ MnGa topological semimetal thin films,” *Appl. Phys. Lett.*, vol. 115, no. 25, p. 252401, Dec. 2019, doi: 10.1063/1.5127553.

[129] S. Zhang *et al.*, “Photoinduced terahertz radiation and negative conductivity dynamics in Heusler alloy Co_2MnSn film,” *Opt. Lett.*, vol. 42, no. 16, p. 3080, Aug. 2017, doi: 10.1364/OL.42.003080.

[130] E. Lesne *et al.*, “Highly efficient and tunable spin-to-charge conversion through Rashba coupling at oxide interfaces,” *Nature Mater*, vol. 15, no. 12, pp. 1261–1266, Dec. 2016, doi: 10.1038/nmat4726.

[131] L. Leiva *et al.*, “Giant spin Hall angle in the Heusler alloy Weyl ferromagnet Co 2 MnGa,” *Phys. Rev. B*, vol. 103, no. 4, p. L041114, Jan. 2021, doi: 10.1103/PhysRevB.103.L041114.

[132] J. C. R. Sánchez *et al.*, “Spin-to-charge conversion using Rashba coupling at the interface between non-magnetic materials,” *Nat Commun*, vol. 4, no. 1, p. 2944, Dec. 2013, doi: 10.1038/ncomms3944.

[133] D. C. Vaz *et al.*, “Mapping spin–charge conversion to the band structure in a topological oxide two-dimensional electron gas,” *Nat. Mater.*, vol. 18, no. 11, pp. 1187–1193, Nov. 2019, doi: 10.1038/s41563-019-0467-4.

[134] K. Kondou *et al.*, “Fermi-level-dependent charge-to-spin current conversion by Dirac surface states of topological insulators,” *Nature Phys*, vol. 12, no. 11, pp. 1027–1031, Nov. 2016, doi: 10.1038/nphys3833.

[135] B. B. Singh, S. K. Jena, M. Samanta, K. Biswas, and S. Bedanta, “High Spin to Charge Conversion Efficiency in Electron Beam-Evaporated Topological Insulator Bi $_2$ Se $_3$,” *ACS Appl. Mater. Interfaces*, vol. 12, no. 47, pp. 53409–53415, Nov. 2020, doi: 10.1021/acsami.0c13540.

[136] M. B. Jungfleisch *et al.*, “Control of terahertz emission by ultrafast spin-charge current conversion at Rashba interfaces,” *Phys. Rev. Lett.*, vol. 120, p. 207207, 2018.

[137] X. Wang *et al.*, “Ultrafast spin-to-charge conversion at the surface of topological insulator thin films,” *Adv. Mater.*, vol. 30, p. 1802356, 2018.

[138] M. Tong *et al.*, “Enhanced Terahertz Radiation by Efficient Spin-to-Charge Conversion in Rashba-Mediated Dirac Surface States,” *Nano Lett.*, p. acs.nanolett.0c03079, Dec. 2020, doi: 10.1021/acs.nanolett.0c03079.

[139] Y. Gao *et al.*, “Chiral terahertz wave emission from the Weyl semimetal TaAs,” *Nat Commun*, vol. 11, no. 1, p. 720, Dec. 2020, doi: 10.1038/s41467-020-14463-1.

[140] M. Tong *et al.*, “Helicity-dependent THz emission induced by ultrafast spin photocurrent in nodal-line semimetal candidate Mg3Bi2,” *Opto-Electronic Advances*, vol. 3, no. 12, pp. 20002301–20002315, 2020, doi: 10.29026/oea.2020.200023.

[141] F. de Juan, A. G. Grushin, T. Morimoto, and J. E. Moore, “Quantized circular photogalvanic effect in Weyl semimetals,” *Nature Communications*, vol. 8, no. 1, Art. no. 1, Jul. 2017, doi: 10.1038/ncomms15995.

[142] A. Johansson, J. Henk, and I. Mertig, “Edelstein effect in Weyl semimetals,” *Phys. Rev. B*, vol. 97, no. 8, p. 085417, Feb. 2018, doi: 10.1103/PhysRevB.97.085417.

[143] Yuta Sasaki , Yukiko Takahashi , Shinya Kasai, “Laser-induced terahertz emission in Co2MnSi/Pt structure,” no. Applied Physics Express, Volume 13, Number 9, doi: https://doi.org/10.35848/1882-0786/abb1c9.

[144] I. Belopolski *et al.*, “Discovery of topological Weyl fermion lines and drumhead surface states in a room temperature magnet,” *Science*, vol. 365, no. 6459, pp. 1278–1281, Sep. 2019, doi: 10.1126/science.aav2327.

[145] A. Markou *et al.*, “Thickness dependence of the anomalous Hall effect in thin films of the topological semimetal Co 2 MnGa,” *Phys. Rev. B*, vol. 100, no. 5, p. 054422, Aug. 2019, doi: 10.1103/PhysRevB.100.054422.

[146] A. Ohtomo and H. Y. Hwang, “A high-mobility electron gas at the LaAlO3/SrTiO3 heterointerface,” *Nature*, vol. 427, no. 6973, pp. 423–426, Jan. 2004, doi: 10.1038/nature02308.

[147] S. Thiel, “Tunable Quasi-Two-Dimensional Electron Gases in Oxide Heterostructures,” *Science*, vol. 313, no. 5795, pp. 1942–1945, Sep. 2006, doi: 10.1126/science.1131091.

[148] N. C. Bristowe, P. Ghosez, P. B. Littlewood, and E. Artacho, “The origin of two-dimensional electron gases at oxide interfaces: insights from theory,” *J. Phys.: Condens. Matter*, vol. 26, no. 14, p. 143201, Apr. 2014, doi: 10.1088/0953-8984/26/14/143201.

[149] A. Savoia *et al.*, “Polar catastrophe and electronic reconstructions at the LaAlO3/SrTiO3 interface: evidence from optical second harmonic generation,” *arXiv:0901.3331 [cond-mat]*, Sep. 2009, doi: 10.1103/PhysRevB.80.075110.

[150] E. Lesne *et al.*, “Suppression of the critical thickness threshold for conductivity at the LaAlO3/SrTiO3 interface,” *Nat Commun*, vol. 5, no. 1, p. 4291, Sep. 2014, doi: 10.1038/ncomms5291.

[151] A. D. Caviglia, M. Gabay, S. Gariglio, N. Reyren, C. Cancellieri, and J.-M. Triscone, “Tunable Rashba Spin-Orbit Interaction at Oxide Interfaces,” *Phys. Rev. Lett.*, vol. 104, no. 12, p. 126803, Mar. 2010, doi: 10.1103/PhysRevLett.104.126803.

[152] J.-Y. Chauleau *et al.*, “Efficient spin-to-charge conversion in the 2D electron liquid at the LAO/STO interface,” *EPL*, vol. 116, no. 1, p. 17006, Oct. 2016, doi: 10.1209/0295-5075/116/17006.

[153] H.-M. Christen, J. Mannhart, E. J. Williams, and Ch. Gerber, “Dielectric properties of sputtered SrTiO 3 films,” *Phys. Rev. B*, vol. 49, no. 17, pp. 12095–12104, May 1994, doi: 10.1103/PhysRevB.49.12095.

[154] R. Pentcheva and W. E. Pickett, “Ionic relaxation contribution to the electronic reconstruction at the n -type LaAlO 3 / SrTiO 3 interface,” *Phys. Rev. B*, vol. 78, no. 20, p. 205106, Nov. 2008, doi: 10.1103/PhysRevB.78.205106.

[155] P. Schütz *et al.*, “Band bending and alignment at the spinel/perovskite $\ensuremath{\gamma}\text{\ensuremath{-}}{\text{Al}}_{2}{\text{O}}_{3}/{\text{SrTiO}}_{3}$ heterointerface,” *Phys. Rev. B*, vol. 91, no. 16, p. 165118, Apr. 2015, doi: 10.1103/PhysRevB.91.165118.

[156] H. Wang, C. Du, P. C. Hammel, and F. Yang, “Antiferromagnonic Spin Transport from ${\mathrm{Y}}_{3}{\mathrm{Fe}}_{5}{\mathrm{O}}_{12}$ into NiO,” *Phys. Rev. Lett.*, vol. 113, no. 9, p. 097202, Aug. 2014, doi: 10.1103/PhysRevLett.113.097202.

[157] M. Kozina *et al.*, “Terahertz-driven phonon upconversion in SrTiO3,” *Nat. Phys.*, vol. 15, no. 4, pp. 387–392, Apr. 2019, doi: 10.1038/s41567-018-0408-1.

[158] P. Marsik, K. Sen, J. Khmaladze, M. Yazdi-Rizi, B. P. P. Mallett, and C. Bernhard, “Terahertz ellipsometry study of the soft mode behavior in ultrathin $SrTiO_3$ films,” *Appl. Phys. Lett.*, vol. 108, no. 5, p. 052901, Feb. 2016, doi: 10.1063/1.4940976.

[159] J. Nitta, T. Akazaki, H. Takayanagi, and T. Enoki, “Gate Control of Spin-Orbit Interaction in an Inverted In0.53Ga0.47As$\overline{\text{In}}$0.52Al0.48As Heterostructure,” *PHYSICAL REVIEW LETTERS*, vol. 78, no. 7, p. 4, 1997.

[160] J. Biscaras *et al.*, “Limit of the electrostatic doping in two-dimensional electron gases of LaXO3(X = Al, Ti)/SrTiO3,” *Sci Rep*, vol. 4, no. 1, p. 6788, May 2015, doi: 10.1038/srep06788.
[161] A. Joshua, S. Pecker, J. Ruhman, E. Altman, and S. Ilani, “A universal critical density underlying the physics of electrons at the LaAlO3/SrTiO3 interface,” *Nat Commun*, vol. 3, no. 1, p. 1129, Jan. 2012, doi: 10.1038/ncomms2116.
[162] S. Fragkos *et al.*, “Topological surface states in epitaxial (Sn Bi 2 Te 4) n (Bi 2 Te 3) m natural van der Waals superlattices,” *Phys. Rev. Materials*, vol. 5, no. 1, p. 014203, Jan. 2021, doi: 10.1103/PhysRevMaterials.5.014203.
[163] M. Reid, I. V. Cravetchi, and R. Fedosejevs, “Terahertz radiation and second-harmonic generation from InAs: Bulk versus surface electric-field-induced contributions,” *Phys. Rev. B*, vol. 72, no. 3, p. 035201, Jul. 2005, doi: 10.1103/PhysRevB.72.035201.
[164] C. Weisbuch, M. Nishioka, A. Ishikawa, and Y. Arakawa, “Observation of the coupled exciton-photon mode splitting in a semiconductor quantum microcavity,” *Phys. Rev. Lett.*, vol. 69, no. 23, pp. 3314–3317, Dec. 1992, doi: 10.1103/PhysRevLett.69.3314.
[165] D. Dini, R. Köhler, A. Tredicucci, G. Biasiol, and L. Sorba, “Microcavity Polariton Splitting of Intersubband Transitions,” *Physical Review Letters*, vol. 90, no. 11, Mar. 2003, doi: 10.1103/PhysRevLett.90.116401.
[166] R. Colombelli and J.-M. Manceau, “Perspectives for Intersubband Polariton Lasers,” *Physical Review X*, vol. 5, no. 1, Mar. 2015, doi: 10.1103/PhysRevX.5.011031.
[167] E. T. Jaynes and F. W. Cummings, “Comparison of quantum and semiclassical radiation theories with application to the beam maser,” *Proc. IEEE*, vol. 51, no. 1, pp. 89–109, 1963, doi: 10.1109/PROC.1963.1664.
[168] Pierre-Baptiste Vigneron, “Mid-Infrared Detectors and THz Devices Operating in the Strong Light-Matter Coupling Regime,” 2019.
[169] N. L. Tran, “Mid-Infrared Intersubband Polaritonic Devices.”
[170] J.-M. Manceau *et al.*, “Mid-infrared intersubband polaritons in dispersive metal-insulator-metal resonators,” *Appl. Phys. Lett.*, vol. 105, no. 8, p. 081105, Aug. 2014, doi: 10.1063/1.4893730.
[171] Y. Todorov *et al.*, “Strong Light-Matter Coupling in Subwavelength Metal-Dielectric Microcavities at Terahertz Frequencies,” *Phys. Rev. Lett.*, vol. 102, no. 18, p. 186402, May 2009, doi: 10.1103/PhysRevLett.102.186402.
[172] M. Geiser *et al.*, “Strong light-matter coupling at terahertz frequencies at room temperature in electronic LC resonators,” *Appl. Phys. Lett.*, vol. 97, no. 19, p. 191107, Nov. 2010, doi: 10.1063/1.3511446.
[173] C. Ciuti, G. Bastard, and I. Carusotto, “Quantum vacuum properties of the intersubband cavity polariton field,” *Phys. Rev. B*, vol. 72, no. 11, p. 115303, Sep. 2005, doi: 10.1103/PhysRevB.72.115303.
[174] G. Günter *et al.*, “Sub-cycle switch-on of ultrastrong light–matter interaction,” *Nature*, vol. 458, no. 7235, pp. 178–181, Mar. 2009, doi: 10.1038/nature07838.
[175] E. Dupont, J. A. Gupta, and H. C. Liu, “Giant vacuum-field Rabi splitting of intersubband transitions in multiple quantum wells,” *Phys. Rev. B*, vol. 75, no. 20, p. 205325, May 2007, doi: 10.1103/PhysRevB.75.205325.
[176] A. A. Anappara *et al.*, “Signatures of the ultrastrong light-matter coupling regime,” *Phys. Rev. B*, vol. 79, no. 20, p. 201303, May 2009, doi: 10.1103/PhysRevB.79.201303.

[177] P. Jouy *et al.*, “Transition from strong to ultrastrong coupling regime in mid-infrared metal-dielectric-metal cavities,” *Appl. Phys. Lett.*, vol. 98, no. 23, p. 231114, Jun. 2011, doi: 10.1063/1.3598432.
[178] Y. Todorov *et al.*, “Ultrastrong Light-Matter Coupling Regime with Polariton Dots,” *Phys. Rev. Lett.*, vol. 105, no. 19, p. 196402, Nov. 2010, doi: 10.1103/PhysRevLett.105.196402.
[179] M. Porer *et al.*, “Nonadiabatic switching of a photonic band structure: Ultrastrong light-matter coupling and slow-down of light,” *Phys. Rev. B*, vol. 85, no. 8, p. 081302, Feb. 2012, doi: 10.1103/PhysRevB.85.081302.
[180] V. M. Muravev, I. V. Andreev, I. V. Kukushkin, S. Schmult, and W. Dietsche, “Observation of hybrid plasmon-photon modes in microwave transmission of coplanar microresonators,” *Phys. Rev. B*, vol. 83, no. 7, p. 075309, Feb. 2011, doi: 10.1103/PhysRevB.83.075309.
[181] G. Scalari *et al.*, “Ultrastrong Coupling of the Cyclotron Transition of a 2D Electron Gas to a THz Metamaterial,” *Science*, vol. 335, no. 6074, pp. 1323–1326, Mar. 2012, doi: 10.1126/science.1216022.
[182] A. Bayer *et al.*, “Terahertz Light–Matter Interaction beyond Unity Coupling Strength,” *Nano Lett.*, vol. 17, no. 10, pp. 6340–6344, Oct. 2017, doi: 10.1021/acs.nanolett.7b03103.
[183] A. Frisk Kockum, A. Miranowicz, S. De Liberato, S. Savasta, and F. Nori, “Ultrastrong coupling between light and matter,” *Nat Rev Phys*, vol. 1, no. 1, pp. 19–40, Jan. 2019, doi: 10.1038/s42254-018-0006-2.
[184] P. Forn-Díaz, L. Lamata, E. Rico, J. Kono, and E. Solano, “Ultrastrong coupling regimes of light-matter interaction,” *Rev. Mod. Phys.*, vol. 91, no. 2, p. 025005, Jun. 2019, doi: 10.1103/RevModPhys.91.025005.
[185] P. Jouy *et al.*, “Intersubband electroluminescent devices operating in the strong-coupling regime,” *Phys. Rev. B*, vol. 82, no. 4, p. 045322, Jul. 2010, doi: 10.1103/PhysRevB.82.045322.
[186] R. Colombelli, C. Ciuti, Y. Chassagneux, and C. Sirtori, “Quantum cascade intersubband polariton light emitters,” *Semicond. Sci. Technol.*, vol. 20, no. 10, pp. 985–990, Oct. 2005, doi: 10.1088/0268-1242/20/10/001.
[187] D. Chastanet *et al.*, “Surface emitting thermally assisted polaritonic light-emitting device,” *Appl. Phys. Lett.*, vol. 110, no. 8, p. 081108, Feb. 2017, doi: 10.1063/1.4976585.
[188] L. Sapienza *et al.*, “Electrically Injected Cavity Polaritons,” *Phys. Rev. Lett.*, vol. 100, no. 13, p. 136806, Apr. 2008, doi: 10.1103/PhysRevLett.100.136806.
[189] A. Delteil *et al.*, “Optical phonon scattering of cavity polaritons in an electroluminescent device,” *Phys. Rev. B*, vol. 83, no. 8, p. 081404, Feb. 2011, doi: 10.1103/PhysRevB.83.081404.
[190] S. De Liberato and C. Ciuti, “Quantum theory of electron tunneling into intersubband cavity polariton states,” *Phys. Rev. B*, vol. 79, no. 7, p. 075317, Feb. 2009, doi: 10.1103/PhysRevB.79.075317.
[191] A. A. Anappara, A. Tredicucci, G. Biasiol, and L. Sorba, “Electrical control of polariton coupling in intersubband microcavities,” *Appl. Phys. Lett.*, vol. 87, no. 5, p. 051105, Aug. 2005, doi: 10.1063/1.2006976.
[192] A. A. Anappara, A. Tredicucci, F. Beltram, G. Biasiol, and L. Sorba, “Tunnel-assisted manipulation of intersubband polaritons in asymmetric coupled quantum wells,” *Appl. Phys. Lett.*, vol. 89, no. 17, p. 171109, Oct. 2006, doi: 10.1063/1.2367664.

[193] S. Pirotta *et al.*, “Fast amplitude modulation up to 1.5 GHz of mid-IR free-space beams at room-temperature,” *Nat Commun*, vol. 12, no. 1, p. 799, Dec. 2021, doi: 10.1038/s41467-020-20710-2.
[194] A. Benz *et al.*, “Strong coupling in the sub-wavelength limit using metamaterial nanocavities,” *Nat Commun*, vol. 4, no. 1, p. 2882, Dec. 2013, doi: 10.1038/ncomms3882.
[195] M. Malerba *et al.*, “Towards strong light-matter coupling at the single-resonator level with sub-wavelength mid-infrared nano-antennas,” *Appl. Phys. Lett.*, vol. 109, no. 2, p. 021111, Jul. 2016, doi: 10.1063/1.4958330.
[196] B. Paulillo, J.-M. Manceau, L. H. Li, A. G. Davies, E. H. Linfield, and R. Colombelli, “Room temperature strong light-matter coupling in three dimensional terahertz meta-atoms,” *Appl. Phys. Lett.*, vol. 108, no. 10, p. 101101, Mar. 2016, doi: 10.1063/1.4943167.
[197] M. Jeannin *et al.*, “Ultrastrong Light–Matter Coupling in Deeply Subwavelength THz LC Resonators,” *ACS Photonics*, vol. 6, no. 5, pp. 1207–1215, May 2019, doi: 10.1021/acsphotonics.8b01778.
[198] J. Keller *et al.*, “Few-Electron Ultrastrong Light-Matter Coupling at 300 GHz with Nanogap Hybrid LC Microcavities,” *Nano Lett.*, vol. 17, no. 12, pp. 7410–7415, Dec. 2017, doi: 10.1021/acs.nanolett.7b03228.
[199] L. P. Pitaevskiĭ and S. Stringari, *Bose-Einstein condensation and superfluidity*, First edition. Oxford, United Kingdom: Oxford University Press, 2016.
[200] A. Einstein, “Quantentheorie des einatomigen idealen Gases.,” 1925.
[201] Bose, “Plancks Gesetz und Lichtquantenhypothese,” *Zeitschrift für Physik*, vol. 26, no. 1, pp. 178–181, Dec. 1924, doi: 10.1007/BF01327326.
[202] M. H. Anderson, J. R. Ensher, M. R. Matthews, C. E. Wieman, and E. A. Cornell, “Observation of Bose-Einstein Condensation in a Dilute Atomic Vapor,” *Science*, vol. 269, no. 5221, pp. 198–201, Jul. 1995, doi: 10.1126/science.269.5221.198.
[203] H. Deng, H. Haug, and Y. Yamamoto, “Exciton-polariton Bose-Einstein condensation,” *Rev. Mod. Phys.*, vol. 82, no. 2, pp. 1489–1537, May 2010, doi: 10.1103/RevModPhys.82.1489.
[204] A. Imamog¯lu, R. J. Ram, S. Pau, and Y. Yamamoto, “Nonequilibrium condensates and lasers without inversion: Exciton-polariton lasers,” *Phys. Rev. A*, vol. 53, no. 6, pp. 4250–4253, Jun. 1996, doi: 10.1103/PhysRevA.53.4250.
[205] H. Deng, G. Weihs, C. Santori, J. Bloch, and Y. Yamamoto, “Condensation of Semiconductor Microcavity Exciton Polaritons,” *Science*, vol. 298, no. 5591, pp. 199–202, Oct. 2002, doi: 10.1126/science.1074464.
[206] J. Kasprzak *et al.*, “Bose–Einstein condensation of exciton polaritons,” *Nature*, vol. 443, no. 7110, pp. 409–414, Sep. 2006, doi: 10.1038/nature05131.
[207] M. Richard, J. Kasprzak, R. Romestain, R. André, and L. S. Dang, “Spontaneous Coherent Phase Transition of Polaritons in CdTe Microcavities,” *Phys. Rev. Lett.*, vol. 94, no. 18, p. 187401, May 2005, doi: 10.1103/PhysRevLett.94.187401.
[208] C. Schneider *et al.*, “An electrically pumped polariton laser,” *Nature*, vol. 497, no. 7449, pp. 348–352, May 2013, doi: 10.1038/nature12036.
[209] A. Rahimi-Iman, *Polariton Physics: From Dynamic Bose–Einstein Condensates in Strongly-Coupled Light–Matter Systems to Polariton Lasers*, vol. 229. Cham: Springer International Publishing, 2020.

[210] S. De Liberato and C. Ciuti, “Stimulated Scattering and Lasing of Intersubband Cavity Polaritons,” *Phys. Rev. Lett.*, vol. 102, no. 13, p. 136403, Mar. 2009, doi: 10.1103/PhysRevLett.102.136403.

[211] J.-M. Manceau *et al.*, “Resonant intersubband polariton-LO phonon scattering in an optically pumped polaritonic device,” *Appl. Phys. Lett.*, vol. 112, no. 19, p. 191106, May 2018, doi: 10.1063/1.5029893.

[212] P. G. Savvidis, J. J. Baumberg, R. M. Stevenson, M. S. Skolnick, D. M. Whittaker, and J. S. Roberts, “Angle-Resonant Stimulated Polariton Amplifier,” *Phys. Rev. Lett.*, vol. 84, no. 7, pp. 1547–1550, Feb. 2000, doi: 10.1103/PhysRevLett.84.1547.

[213] R. M. Stevenson *et al.*, “Continuous Wave Observation of Massive Polariton Redistribution by Stimulated Scattering in Semiconductor Microcavities,” *Phys. Rev. Lett.*, vol. 85, no. 17, pp. 3680–3683, Oct. 2000, doi: 10.1103/PhysRevLett.85.3680.

[214] C. Ciuti, P. Schwendimann, and A. Quattropani, “Theory of polariton parametric interactions in semiconductor microcavities,” *Semicond. Sci. Technol.*, vol. 18, no. 10, pp. S279–S293, Oct. 2003, doi: 10.1088/0268-1242/18/10/301.

[215] P. G. Savvidis, J. J. Baumberg, R. M. Stevenson, M. S. Skolnick, D. M. Whittaker, and J. S. Roberts, “Asymmetric angular emission in semiconductor microcavities,” *Phys. Rev. B*, vol. 62, no. 20, pp. R13278–R13281, Nov. 2000, doi: 10.1103/PhysRevB.62.R13278.

[216] L. Nguyen-thê, S. De Liberato, M. Bamba, and C. Ciuti, “Effective polariton-polariton interactions of cavity-embedded two-dimensional electron gases,” *Phys. Rev. B*, vol. 87, no. 23, p. 235322, Jun. 2013, doi: 10.1103/PhysRevB.87.235322.

[217] J. Nespolo and I. Carusotto, “Generalized Gross-Pitaevskii model for intersubband polariton lasing,” *Phys. Rev. B*, vol. 100, no. 3, p. 035305, Jul. 2019, doi: 10.1103/PhysRevB.100.035305.

[218] I. Carusotto and C. Ciuti, “Quantum fluids of light,” *Rev. Mod. Phys.*, vol. 85, no. 1, pp. 299–366, Feb. 2013, doi: 10.1103/RevModPhys.85.299.

[219] Z. Wang, R. Gogna, and H. Deng, “What is the best planar cavity for maximizing coherent exciton-photon coupling,” *Appl. Phys. Lett.*, vol. 111, no. 6, p. 061102, Aug. 2017, doi: 10.1063/1.4997171.

[220] R. Dingle, W. Wiegmann, and C. H. Henry, “Quantum States of Confined Carriers in Very Thin Al x Ga 1 − x As -GaAs- Al x Ga 1 − x As Heterostructures,” *Phys. Rev. Lett.*, vol. 33, no. 14, pp. 827–830, Sep. 1974, doi: 10.1103/PhysRevLett.33.827.

[221] L. A. Coldren, S. W. Corzine, and M. Mashanovitch, *Diode lasers and photonic integrated circuits*, 2nd ed. Hoboken, N.J: Wiley, 2012.

[222] R. Paiella, Ed., *Intersubband transitions in quantum structures*. New York: McGraw-Hill, 2006.

[223] G. Bastard, *Wave mechanics applied to semiconductor heterostructures*. 1992.

[224] T. Ando, A. B. Fowler, and F. Stern, “Electronic properties of two-dimensional systems,” *Rev. Mod. Phys.*, vol. 54, no. 2, pp. 437–672, Apr. 1982, doi: 10.1103/RevModPhys.54.437.

[225] Capasso, *Intersubband transitions in quantum wells: Physics and device applications*. .

[226] J. D. Joannopoulos, Ed., *Photonic crystals: molding the flow of light*, 2nd ed. Princeton: Princeton University Press, 2008.

[227] L. Li, “Use of Fourier series in the analysis of discontinuous periodic structures,” *J. Opt. Soc. Am. A*, vol. 13, no. 9, p. 1870, Sep. 1996, doi: 10.1364/JOSAA.13.001870.

[228] D. M. Whittaker and I. S. Culshaw, “Scattering-matrix treatment of patterned multilayer photonic structures,” *Phys. Rev. B*, vol. 60, no. 4, pp. 2610–2618, Jul. 1999, doi: 10.1103/PhysRevB.60.2610.
[229] M. Załużny and C. Nalewajko, “Coupling of infrared radiation to intersubband transitions in multiple quantum wells: The effective-medium approach,” *Phys. Rev. B*, vol. 59, no. 20, pp. 13043–13053, May 1999, doi: 10.1103/PhysRevB.59.13043.
[230] J. Faist, F. Capasso, D. L. Sivco, C. Sirtori, A. L. Hutchinson, and A. Y. Cho, “Quantum Cascade Laser,” *Science*, vol. 264, no. 5158, pp. 553–556, Apr. 1994, doi: 10.1126/science.264.5158.553.
[231] R. Köhler *et al.*, “Terahertz semiconductor-heterostructure laser,” *Nature*, vol. 417, no. 6885, pp. 156–159, May 2002, doi: 10.1038/417156a.
[232] L. Li *et al.*, “Terahertz quantum cascade lasers with >1 W output powers,” *Electronics Letters*, vol. 50, no. 4, pp. 309–311, Feb. 2014, doi: 10.1049/el.2013.4035.
[233] L. Bosco, M. Franckié, G. Scalari, M. Beck, A. Wacker, and J. Faist, “Thermoelectrically cooled THz quantum cascade laser operating up to 210 K,” *Appl. Phys. Lett.*, vol. 115, no. 1, p. 010601, Jul. 2019, doi: 10.1063/1.5110305.
[234] M. A. Kainz *et al.*, “Thermoelectric-cooled terahertz quantum cascade lasers,” *Opt. Express*, vol. 27, no. 15, p. 20688, Jul. 2019, doi: 10.1364/OE.27.020688.
[235] J. Faist, *Quantum Cascade Lasers*. 2013.
[236] M. S. Vitiello, “Physics and technology of Terahertz quantum cascade lasers,” p. 32.
[237] B. S. Williams, “Terahertz quantum-cascade lasers,” *Nature Photon*, vol. 1, no. 9, pp. 517–525, Sep. 2007, doi: 10.1038/nphoton.2007.166.
[238] F. Zhao *et al.*, “Sampled grating terahertz quantum cascade lasers,” *Appl. Phys. Lett.*, vol. 114, no. 14, p. 141105, Apr. 2019, doi: 10.1063/1.5066310.
[239] D. Bachmann *et al.*, “Short pulse generation and mode control of broadband terahertz quantum cascade lasers,” *Optica*, vol. 3, no. 10, p. 1087, Oct. 2016, doi: 10.1364/OPTICA.3.001087.
[240] Raed Hussain S Alhathlool, L. Li, P. Dean, Linfield Edmund, and A. G. Davies, “The Development and Applications of Terahertz Quantum Cascade Lasers,” OSA, San Jose, California, 2014.
[241] J.-M. Manceau, G. Biasiol, N. L. Tran, I. Carusotto, and R. Colombelli, “Immunity of intersubband polaritons to inhomogeneous broadening,” *Phys. Rev. B*, vol. 96, no. 23, p. 235301, Dec. 2017, doi: 10.1103/PhysRevB.96.235301.
[242] S. Zanotto, R. Degl’Innocenti, J.-H. Xu, L. Sorba, A. Tredicucci, and G. Biasiol, “Ultrafast optical bleaching of intersubband cavity polaritons,” *Phys. Rev. B*, vol. 86, no. 20, p. 201302, Nov. 2012, doi: 10.1103/PhysRevB.86.201302.
[243] J. Raab, “Ultrafast terahertz saturable absorbers using tailored intersubband polaritons,” p. 8.
[244] I. Turek, V. Drchal, J. Kudrnovsky, M. Sob, and P. Weinberger, *Electronic Structure of Disordered Alloys, Surfaces and Interfaces*. 1997.
[245] S. Grytsyuk *et al.*, “k -asymmetric spin splitting at the interface between transition metal ferromagnets and heavy metals,” *Phys. Rev. B*, vol. 93, no. 17, p. 174421, May 2016, doi: 10.1103/PhysRevB.93.174421.

Spectroscopie térahertz résolue en temps de polaritons intersous-bandes et de sources térahertz basées sur des phénomènes spintroniques

Résumé : Le domaine térahertz (THz) inclut une riche variété d'applications pratiques et fondamentales où la basse énergie des photons permettent l'investigation de nouveaux phénomènes d'interaction lumière-matière. Ces travaux se focalisent sur deux thématiques émergentes où la spectroscopie THz ultra-rapide représente un outil particulièrement adapté à l'étude de phénomènes fondamentaux ainsi qu'à la conception de nouvelles sources THz. La première thématique concerne la spintronique THz capable de générer des ondes THz équivalentes à celles obtenues au sein des cristaux non-linéaires. Cette technologie est basée sur des hétérostructures constituées de matériaux ferromagnétiques – métaux de transitions possédant des épaisseurs nanométriques permettant une émission THz par excitation ultra-rapide de la structure, induisant un courant de spin et via l'effet Hall de spin, une conversion de courant de spin en courant de charge. Au-delà de ces structures métalliques, des matériaux « quantiques » faisant intervenir des phénomènes tel que l'effet inverse Edelstein au sein des isolants topologiques sont également étudiés. La seconde thématique abordée est celle des polaritons intersous-bandes dans le domaine THz. Les polaritons sont des quasi-particules résultant d'un couplage lumière-matière fort provenant d'un mode de cavité couplé à une transition intersous-bande. Leur nature bosonique représente une perspective pertinente à long terme pour développer de nouvelles sources THz lasers basées sur le principe de condensat de Bose-Einstein. Dans ces travaux, nous étudions le pompage optique monofréquence et résonant d'une branche polaritonique par une sonde large bande constituée d'impulsions THz. Cette investigation révèle de fortes indications d'effets non-linéaires et potentiellement des signatures de diffusions polaritoniques. Enfin, nous présentons également des optimisations technologiques de sources THz existantes utiles à l'études des deux thématiques abordées. Notamment de sources THz de type antennes photoconductrices haute puissance en cavités, qui ont permis la première démonstration d'imagerie THz en temps réel obtenue avec de tel dispositifs.

Mots clés : [Térahertz, Spectroscopie THz résolue en temps, Spintronique, Transitions intersous-bandes, Polaritons intersous-bandes, antenne photoconductrice]

Terahertz time resolved spectroscopy of Intersubband Polaritons and Spintronic Emitters

Abstract: The terahertz (THz) domain provides a rich playground for many practical and fundamental applications, where the low energy of THz photons permits to probe novel light-matter interactions. This work investigates two recent and emerging scientific areas where ultrafast THz spectroscopy can be used as a probe of fundamental phenomena, as well as potentially enabling the conception of new THz sources. In the first case, ultrafast THz spintronics are studied where ultrafast excitations of spintronic heterojunctions result in efficient pulse generation. These structures consist of nanometer thick ferromagnetic - heavy metal junctions, where an optically generated spin-charge in the former is converted to a charge-current in the latter via the Inverse Spin Hall Effect. Beyond these metal-based junctions, ultrafast THz spintronics based on "quantum" materials is also investigated, where THz pulses are generated using quantum phenomena such as the Inverse Edelstein Effect in Topological Insulators, shown to be a promising research direction. The second subject area is focused on THz intersubband polaritons, quasi-particles that emerge from the strong light-matter coupling of a THz photonic cavity and an intersubband transition. Here we are interested in the bosonic nature of the intersubband polaritons, as a long-term aim of realizing a novel THz laser based on Bose-Einstein condensation. In this work, we investigate resonant narrowband pumping of a polariton branch and probe using spectrally broad THz pulses. This shows strong indications of nonlinear effects and potential signatures of scattering processes that could eventually lead to the demonstration of THz polaritonic gain. Finally, to support our work in the above subject areas, technological developments were made in existing THz sources. This included high power THz photoconductive switches using cavities, which permitted the first demonstrations of real time THz imaging with such devices, and high power THz quantum cascade lasers as narrowband laser pumps.

Keywords: [Terahertz, time domain spectroscopy, THz Spintronic, Intersubband transitions, Intersubband polaritons, photoconductive switch]